UNIVERSIDADE FEDERAL DE MINAS GERAIS
Instituto de Geociências
Programa de Pós-Graduação em Geologia

Janaina Rodrigues de Paula

PALEOENVIRONMENTAL RECONSTRUCTION AND IRON FORMATION GENESIS IN THE MINAS BASIN (QUADRILÁTERO FERRÍFERO, BRAZIL): insights from geochemistry, stable isotopes, and provenance analysis

Belo Horizonte
2025

Janaina Rodrigues de Paula

PALEOENVIRONMENTAL RECONSTRUCTION AND IRON FORMATION GENESIS IN THE MINAS BASIN (QUADRILÁTERO FERRÍFERO, BRAZIL): insights from geochemistry, stable isotopes, and provenance analysis

Tese apresentada ao Programa de Pós-Graduação em Geologia da Universidade Federal de Minas Gerais como requisito parcial para obtenção do título de doutora em Geologia Econômica e Aplicada.

Orientador(a): Prof. Dr. Fabrício de Andrade Caxito

Coorientador(a): Prof. Dr. Kurt Konhauser

Belo Horizonte
2025

P324p
2025

Paula, Janaina Rodrigues de.
Paleoenvironmental reconstruction and Iron formation genesis in the Minas Basin (Quadrilátero Ferrífero, Brazil) [manuscrito] insights from geochemistry, stable isotopes, and provenance analysis / Janaina Rodrigues de Paula. – 2025.
185 f., enc. il. (principalmente color.)

Orientador: Fabrício de Andrade Caxito.
Coorientador: Kurt Konhauser.
Tese (doutorado) – Universidade Federal de Minas Gerais, Instituto de Geociências, 2025.
Área de concentração: Geologia Econômica e Aplicada.
Bibliografia: f. 160-182.

1. Geologia econômica – Teses. 2. Isótopos estáveis – Teses. 3. Geoquímica – Teses. 4. Tempo geológico – Teses. 5. Quadrilátero Ferrífero (MG) – Teses. I. Caxito, Fabrício de Andrade. II. Konhauser, Kurt. III. Universidade Federal de Minas Gerais. Instituto de Geociências. IV. Título.

CDU: 553 (815.1)

Ficha catalográfica elaborada por Graciane Aparecida de Paula – CRB-6/3404
Biblioteca "Vitória Pedersoli", Instituto de Geociências da UFMG

UNIVERSIDADE FEDERAL DE MINAS GERAIS

PROGRAMA DE PÓS-GRADUAÇÃO EM GEOLOGIA DO IGC-UFMG

FOLHA DE APROVAÇÃO

PALEOENVIRONMENTAL RECONSTRUCTION AND IRON FORMATION GENESIS IN THE MINAS BASIN (QUADRILÁTERO FERRÍFERO, BRAZIL): INSIGHTS FROM GEOCHEMISTRY, STABLE ISOTOPES, AND PROVENANCE ANALYSIS

JANAINA RODRIGUES DE PAULA

Tese submetida à Banca Examinadora designada pelo Colegiado do Programa de Pós-Graduação em GEOLOGIA (PPGeol), do Instituto de Geociências (IGC), da Universidade Federal de Minas Gerais (UFMG), como **REQUISITO PARCIAL** para obtenção do grau de Doutor(a) em GEOLOGIA, área de concentração GEOLOGIA ECONÔMICA E APLICADA, pelo Programa de Pós-graduação em Geologia do IGC/UFMG.

Aprovada em 28 de abril de 2025, pela banca constituída pelos membros:

Prof(a). Dr(a). Fabrício de Andrade Caxito – Orientador(a)
UFMG

Documento assinado digitalmente
gov.br ROSALINE CRISTINA FIGUEIREDO E SILVA
Data: 07/05/2025 18:17:53-0300
Verifique em https://validar.iti.gov.br

Prof(a). Dr(a). Rosaline Cristina Figueiredo e Silva
UFMG

Prof(a). Dr(a). Gabriel Jubé Uhlein
UFMG

Prof(a). Dr(a). Flávia Cristina Silveira Braga
UFMG

Documento assinado digitalmente
gov.br LUCAS PEREIRA LEAO
Data: 15/05/2025 09:45:05-0300
Verifique em https://validar.iti.gov.br

Prof(a). Dr(a). Lucas Pereira Leão
UFOP

Belo Horizonte, 28 de abril de 2025.

À minha Mãe, por ser uma mulher pioneira em nossa família.

AGRADECIMENTOS

Agradeço a todos que, de alguma forma, me ajudaram a realizar este trabalho, em especial:

À Pró-Reitoria de Pós-Graduação da UFMG e ao Programa de Pós-Graduação em Geologia do Instituto de Geociências da Universidade Federal de Minas Gerais por terem proporcionado minha formação desde a graduação em 2007 até o doutorado, além de fornecerem o apoio técnico e administrativo necessário para o desenvolvimento desta pesquisa.

Ao meu orientador, Prof. Dr. Fabrício de Andrade Caxito, por me oferecer oportunidades de crescimento acadêmico e por viabilizar o financiamento desta pesquisa.

Ao meu supervisor internacional, Prof. Kurt Konhauser, por me receber em Edmonton e por incentivar o pensamento crítico e a excelência acadêmica.

Às agências de fomento CAPES, CAPES PrINT, CNPq (408815/2021-3 e 304509/2021-3), FAPEMIG (PPM-00618-18), pelos recursos financeiros destinados à minha bolsa de estudos e as análises laboratoriais, e ao Instituto Serrapilheira pelo apoio financeiro durante o estágio na Universidade de Alberta através do bônus diversidade do projeto MOBILE (Serra-1912-31510).

Agradeço à empresa VALE S.A., pela disponibilização de amostras para estudo e apoio financeiro, especialmente por meio do projeto colaborativo ADIMB: VALE – UNIVERSIDADES – INSTITUIÇÕES.

Agradeço, ainda, à equipe do Centro de Pesquisa Manoel Teixeira da Costa (CPMTC - UFMG), Laboratório de Isótopos Estáveis (NEG-LABISE - UFPE), e do Laboratório de Geoquímica (UFOP), pela preparação de amostras e análises. E ao Prof. Erik Sperling e à equipe do *Sedimentary Geochemistry Laboratory da Stanford Doerr School of Sustainability*, pelo apoio na obtenção e interpretação dos dados de especiação de ferro.

Aos amigos da salinha da Pós-Graduação – UFMG pela amizade, colaboração e inúmeras doses de café e ao secretário William Campos por sua paciência e dedicação.

Por fim, àqueles de Edmonton que tornaram nossa experiência internacional ainda mais enriquecedora, em especial Katrina e família, Taiwo Kassim, Luiza, e todo o grupo de pesquisa da UofA.

ACKNOWLEDGEMENTS

I would like to express my gratitude to everyone who, in some way, contributed to the completion of this work, especially:

To the Pró-Reitoria de Pós-Graduação at UFMG and the Graduate Program in Geology at the Institute of Geosciences of the Federal University of Minas Gerais for supporting my academic journey from my undergraduate studies in 2007 to my doctoral research, as well as for providing the technical and administrative support necessary for the development of this research.

To my advisor, Prof. Dr. Fabrício de Andrade Caxito, for offering me opportunities for academic growth and securing funding for this research.

To my international supervisor, Prof. Kurt Konhauser, for welcoming me to Edmonton and for encouraging critical thinking and academic excellence.

To the funding agencies CAPES, CAPES PrINT, CNPq (408815/2021-3 and 304509/2021-3), and FAPEMIG (PPM-00618-18) for the financial resources that supported my scholarship and laboratory analyses, and to the Serrapilheira Institute for the financial support during the internship at the University of Alberta through the diversity bonus of the MOBILE project (Serra-1912-31510)."

I am grateful to VALE S.A. for providing study samples and financial support, particularly through the collaborative ADIMB project: VALE – UNIVERSITIES – INSTITUTIONS.

I also extend my appreciation to the teams at the Manoel Teixeira da Costa Research Center (CPMTC - UFMG), the Stable Isotope Laboratory (NEG-LABISE - UFPE), and the Geochemistry Laboratory (UFOP) for sample preparation and analyses. Special thanks to Prof. Erik Sperling and the team at the Sedimentary Geochemistry Laboratory at the Stanford Doerr School of Sustainability for their support in obtaining and interpreting iron speciation data.

To my friends from the Graduate Study Room at UFMG for their friendship, collaboration, and countless coffee breaks, and to the secretary William Campos for his patience and dedication.

Finally, those in Edmonton who enriched our international experience, especially Katrina and her family, Taiwo Kassim, Luiza, and the entire University of Alberta research group.

RESUMO

As Formações Ferríferas (Iron Formation, IF) são um registro geológico das transformações geodinâmicas ocorridas no Pré-Cambriano, especialmente relacionadas ao Grande Evento de Oxigenação (~2,4-2,1 Ga). No Brasil, o Quadrilátero Ferrífero, sudeste do Cráton São Francisco, abriga um depósito de ferro (Fe) de classe mundial. As rochas do Supergrupo Minas (~2,5-2,2 Ga) registram a evolução de uma bacia de margem passiva, litoestratigraficamente representadas da base para o topo, pelos grupos: Caraça, Itabira e Piracicaba. Este estudo concentra-se nas rochas metassedimentares silicilásticas de granulação fina dessas unidades litoestratigráficas, bem como, na Formação Cauê - hospedeira do minério de (Fe) de alto teor do Quadrilátero Ferrífero, com foco em contribuir com a reconstrução paleoambiental da Bacia Minas. Amostras de IF, rochas carbonáticas e filitos, coletadas no Sinclinal Gandarela, foram analisadas quanto à geoquímica elementar, isótopos estáveis de carbono (C), nitrogênio (N) e oxigênio (O), além da especiação de Fe. Adicionalmente, foram revisitados e organizados para publicação dados geoquímicos e isotópicos (C-O) do Grupo Itabira e geocronologia de proveniência (U-Pb) da sucessão metassedimentar do Sinclinal Dom Bosco. Os resultados confirmam o modelo deposicional dos Fe-minerais mediados por atividade microbiana, em uma paleobacia estratificada. Além disso, a reconstrução paleoambiental da bacia revela a evolução da paleosalinidade e das condições redox, evidenciando mudanças biogeoquímicas significativas.

Palavras-chave: isótopos estáveis; paleoredox; paleo-salinidade; geoquímica; paleoproterozoico.

ABSTRACT

Iron Formation (IF) is a geological record of geodynamic transformations that occurred through the Precambrian, particularly related to the Great Oxygenation Event (~2.4-2.1 Ga). In Brazil, the Quadrilátero Ferrífero province, southeastern portion of the São Francisco Craton, hosts one of the world's largest Fe deposits. The Minas Supergroup (~2.5–2.2 Ga) records the evolution of a passive margin basin lithostratigraphically represented from base to top by the Caraça, Itabira, and Piracicaba groups. This study focuses on the fine-grained metasedimentary rocks of these lithostratigraphic units, as well as, on the Cauê Formation, which host high-grade Fe ore deposits in the province, aiming to contribute to the paleoenvironmental reconstruction of the Minas paleobasin. Samples of IF, carbonate rock, and phyllite, collected in the Gandarela Syncline, were analyzed for major and trace element chemistry, stable isotopes of carbon (C), nitrogen (N), and oxygen (O), as well as Fe speciation. Additionally, geochemical and stable isotopic data (C-O) from the Itabira Group and U-Pb provenance geochronology from the metasedimentary succession in the Dom Bosco Syncline were revisited and organized for publication. The results confirm the depositional model of Fe minerals mediated by microbial activity in a stratified paleobasin. Furthermore, the paleoenvironmental reconstruction of the basin reveals the evolution of paleosalinity and redox conditions, highlighting significant biogeochemical changes.

Keywords: stable isotope; paleoredox; paleosalinity; geochemistry*;* Paleoproterozoic

LIST OF ILLUSTRATIONS

LIST OF TABLES

SUMMARY

1 INTRODUCTION

1.1 General Considerations

This doctoral thesis investigates the biogeochemical processes underlying the genesis of the Fe-mineral precursors of the world-class Fe deposits in the Quadrilátero Ferrífero province, Brazil (Figure 1.1). The genesis of this mineral province, as other giant worldwide IF-hosted Fe systems (e.g. Hamersley, Transvaal, Sokoman provinces), integrates biogenic, sedimentary, and geological factors directly linked to Earth's paleoenvironmental and paleogeochemical evolution (Spier et al. 2007; Rosière et al. 2008; Bekker et al., 2010; Mendes et al. 2016; Konhauser et al., 2017). Advancing knowledge of this mineral province elevates the Quadrilátero Ferrífero to a research significance comparable to other globally recognized IF-hosted Fe systems, such as the Hamersley Basin in Australia (Morris, 1993; Pecoits et al., 2009; Morris and Kneeshaw, 2011; Li et al., 2023).

This thesis extends the master's research, which applied chemostratigraphy and geochronology techniques to the Paleoproterozoic succession of the Segredo Mine, southeastern Quadrilátero Ferrífero province (De Paula, 2020). The study focused on multi-element geochemistry, C-O isotopic composition and U-Pb provenance geochronology of detrital zircon crystals extracted from metasedimentary rocks. During the initial phase of the doctoral research, the previously unpublished master's paper was refined into a more concise and structured version, leading to the first paper published in the *Journal of South American Earth Sciences* (De Paula et al., 2023).

In the next phase, multi-element geochemistry, stable isotope (C, N, and O), and Fe speciation analyses were conducted on samples from both outcrops and drill cores within the Gandarela Syncline, eastern Quadrilátero Ferrífero province. These studies led to the second paper, submitted and accepted to *Chemical Geology*, which investigates the changes in paleosalinity and paleoredox conditions of the Minas sedimentary basin. The third paper, currently in preparation, examines the biogeochemical processes influencing the deposition of the mineral precursor of the BIF in the province. Collectively, these three papers contributed to previous work developed in the region (e.g., Bekker et al., 2003; Spier et al., 2007; Morgan et al., 2013; Mendes et al., 2016; Hensler et al., 2017; and Teixeira et al., 2017).

Figure 1.1 — Global map showing the main Fe formations worldwide, categorized by age and deposit size. The Quadrilátero Ferrífero province is highlighted as the study area.

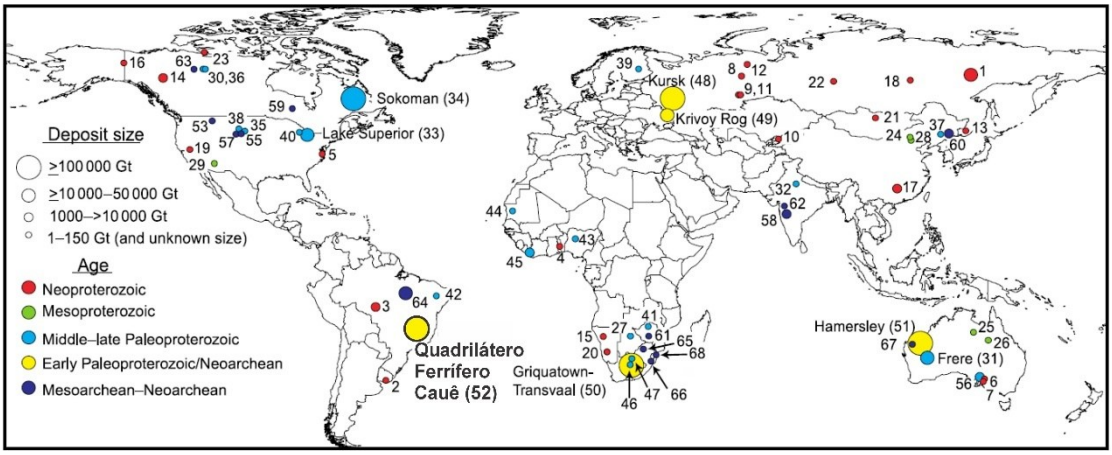

Legend: 1. Maly Khinghan Formation, Russia (560 Ma); 2. Yerbel Formation, Uruguay (600 Ma); 3. Jacadigo Group (Urucum district), Brazil (600 Ma); 4. Bisokpabe Group, Togo (600 Ma); 5. Chestnut Hill Formation, USA (600 Ma); 6. Holowilena Ironstone, Australia (650 Ma); 7. Braemar IF, Australia (650 Ma); 8. Vil'va and Koyva Formations, Russia (650 Ma); 9. Bakeevo (Tolparovo) Formation, Russia (650 Ma); 10. Dzhetymtau Suite, Kyrgyzstan (650 Ma); 11. UK Formation, Russia (700 Ma); 12. Yamata Formation, Russia (700 Ma); 13. Lake Khanka Formation, Russia (700 Ma); 14. Rapitan Formation, Canada (715 Ma); 15. Chuos Formation, Namibia (715 Ma); 16. Tindir Group, USA (715 Ma); 17. Fulu Formation, China (741 Ma); 18. Medvezhevo Formation, Russia (700-750 Ma); 19. Kingston Peak Formation, USA (700-750 Ma); 20. Numees Formation, Namibia (700-750 Ma); 21. Mugur Formation, Mongolia (767 Ma); 22. Nizhne-Angara Formation, Russia (800 Ma); 23. Aok Formation (Shaler Supergr.), Canada (840 Ma); 24. Xiamaling Formation, China (1368 Ma); 25. Roper Group, Australia (1490 Ma); 26. South Nicholson Group, Australia (1500 Ma); 27. Shoshong Formation, Botswana (1600 Ma); 28. Chuanlinggou IF, China (1650-1600 Ma); 29. Pike's Peak Iron-Formation, USA (1728 Ma); 30. Gibraltar Formation, Canada (1880 Ma); 31. Frere Formation, Australia (1890 Ma); 32. Alwar Group (North Delhi fold belt), India (1850-2000 Ma); 33. Lake Superior region, USA + CAN (1880-1850 Ma); 34. Sokoman IF, Canada (1877 Ma); 35. Rochford Formation, USA (1884 Ma); 36. Basile Formation, Canada (1930 Ma); 37. Liaohe Group, China (1950-2050 Ma); 38. Estes Formation, USA (2020-2100 Ma); 39. Pääkkö IF, Finland (2080 Ma); 40. Glen Township Formation, USA (2100 Ma); 41. Lomagundi Group, Zimbabwe (2100-2200 Ma); 42. Caldeirão belt, Brazil (>2078-<2687 Ma); 43. Malumfashi, Maru, Birnin Gwari,, Nigeria (2100 Ma); 44. Ijil Group, Mauritania (2200 Ma); 45. Nimba Itabirite, Liberia (>2100-<2615 Ma); 46. Hotazel IF, South Africa (2200 Ma); 47. Timeball Hill Formation, South Africa (2320 Ma); 48. Kursk Supergroup, Russia (2450 Ma); 49. Krivoy Rog Supergroup, Ukraine (2450 Ma); 50. Transvaal Province, South Africa (2480-2431 Ma); 51. Hamersley Basin, Australia (2597-2445 Ma); 52. Cauê Formation, Brazil (2450 Ma); 53. Indian Creek Metamorphic Suite, USA (2470-2750 Ma); 54. Ruker Series, Antarctica (2450-2480 Ma); 55. Benchmark IF, USA (2480-2560 Ma); 56. Hutchison Group (Middleback), Australia (2500 Ma); 57. Nemo IF, USA (2560-2890 Ma); 58. Chitradurga Group, India (2614 Ma); 59. Beardmore-Geraldton assemblage, Canada (2700 Ma); 60. Anshan IF, China (2700 Ma); 61. Manjeri IF, Zimbabwe (2700-2830 Ma); 62. Bababudan Group, India (2720 Ma); 63. Central Slave Cover Group, Canada (2730-2920 Ma); 64. Carajäs Formation, Brazil (2740-2750 Ma); 65. West Rand Group, South Africa (2960 Ma); 66. Pongola Supergroup, South Africa (2960 Ma); 67. Jack Hills belt, Australia (>3080 Ma); 68. Moodies Group, South Africa (3230 Ma).

Source: Konhauser et al. 2017

This doctoral research is part of the MOBILE (Mountain Belt Inception Life on Earth) project, supported by the Serrapilheira Institute (Serra-1912-31510), which seeks to understand how global tectonic processes, shifts in the ocean-atmosphere chemical composition, and dramatic climate events (e.g., Snowball Earth) influenced the emergence and development of complex life on Earth. Additionally, this research

is part of the collaborative VALE-UNIVERSITIES-INSTITUTIONS project, funded by the mining company VALE S.A., which aims to advance the understanding of the Quadrilátero Ferrífero, one of the world's most significant mineral provinces.

1.2 Characterization of the problem

The IF consists of an alternation of layers rich in Fe-oxides and layers of quartz, carbonates, and silicates (James, 1954), playing a pivotal role in understanding the geological and environmental evolution of the ancient Earth (Bekker et al., 2010; Konhauser et al., 2017). These rocks, which host the giant Fe ore deposits worldwide, were developed during specific geological intervals and potentially recorded biogeochemical shifts in the ocean-atmosphere system that directly impacted the evolution of life on Earth (Cloud, 1973; Lyons et al., 2014).

Several key factors influencing the formation of IF-hosted Fe systems, including (i) Fe sources in oceans, with a consensus that hydrothermal vents contributed significantly more than detrital input (Ohmoto et al., 2006; Hagemann et al., 2016); (ii) paleogeographic model for ancient oceans propose a density-stratified ocean system was a predominant feature, with oxic surface water and anoxic bottom water enrichment in dissolved Fe(II) (Klein and Beukes, 1989; Klein et al., 1992; Klein 2005); (iii) biotic (Konhauser et al., 2002; Konhauser et al., 2011; Teixeira et al., 2017) and abiotic (Rasmussen et al., 2014) mechanisms driving Fe mineral precipitation and its transformation into reduced mineral assemblages; and iv) processes responsible for the characteristic alternating Fe- and silica (Si)-rich bands, such as seasonal upwelling of Fe-rich hydrothermal fluids (Morris, 1993); density currents and turbiditic fluxes (Krapež et al., 2003), and the seasonal interactions between temperature variations and microbial activity (Schad et al., 2019). Despite extensive studies, these topics remain a subject of ongoing debate.

Gross (1965, 1973, 1980) proposed a classification of IF based on their depositional environment: (1) Algoma-type, associated with submarine volcanic environments, and (2) Lake Superior-type, deposited in passive margin settings on continental platforms. Finally, Rapitan-type IF is associated with glacial deposits from Snowball Earth events and submarine volcanism (Hoffman et al., 1998). In Brazil, IF vary in age and genesis (Figure 1.1), from the Archean Algoma-type deposits in the Carajás Mineral Province (PA), to Paleoproterozoic Lake Superior-

type formations in the Quadrilátero Ferrífero (MG) and Neoproterozoic Rapitan-type IF in the Urucum province (MS) (Rosière and Chemale, 2000).

This study focuses on the Quadrilátero Ferrífero, a globally significant metallogenetic province for gold (Au), Fe, and manganese (Mn) occurrences. This province has played a major role in Brazil's geology, history, and economy since Feore extraction began in the early 19th century with Baron von Eschwege, who is recognized as the founder of Brazilian geology due to his contributions to economic geology (Machado, 2009). Iron exploitation increased during World War II, reaching 7 Mt/a (Lima et al., 2019), and today, Vale S.A. extracts 148 Mt/a from both primary IFs and supergene-enriched deposits (Vale, 2024).

Therefore, a detailed study of the Minas metasedimentary succession is essential for refining paleoenvironmental reconstruction models of the Minas paleobasin, enhancing the understanding of IF deposition, and providing knowledge for establishing links between the Quadrilátero Ferrífero and global Paleoproterozoic giant BIF-hosted Fe systems, potentially linking them to events such as the Great Oxidation Event (GOE) and Snowball Earth.

Seeking to improve the reconstruction of the paleoenvironmental model of the Minas sedimentary paleobasin in the Quadrilátero Ferrífero, the following **questions** arise:

- What were the biogeochemical conditions involved in the deposition of the Fe-mineral precursors of the IF?
- What was the evolution of salinity and redox conditions in the Minas paleobasin?
- Do the rocks preserve a geochemical and isotopic signature that reflects primary (seawater) conditions?

1.3 Main Goals

The objective of this study is to reconstruct the paleoenvironment by investigating the paleo-conditions that controlled the deposition of the Minas Supergroup, with a particular focus on the precursor Fe-minerals associated with the formation of the IF-hosted Fe system in the Quadrilátero Ferrífero province, southeast Brazil.

The specific objectives are:

- Conduct novel geochemical investigations, including bulk rock elemental chemistry, isotopic analyses (C, N, and O), and Fe speciation, focusing on IF, carbonate rocks and phyllites from the Minas Supergroup.

- Through the geochemical and isotopic proxy's indicative of paleo-redox and paleosalinity conditions, reconstruct the paleoenvironment of the Minas stratigraphic succession.

- Assess the applicability of geochemical and isotopic techniques and proxies, originally developed and calibrated for more recent rocks, to the Paleoproterozoic stratigraphic section of the Minas Supergroup.

- Contextualize the Quadrilátero Ferrífero province and its significant IF-hosted Fe system concerning major global events (e.g. GOE).

1.4 Study area location and access

The studied areas are in the Quadrilátero Ferrífero province, in Minas Gerais state, Brazil (Figure 1.2). This research primarily focuses on two distinct regions within this province: the Gandarela Syncline in the northeastern Quadrilátero Ferrífero and the Dom Bosco Syncline in its southwest portion.

The Gandarela Syncline (Figure 1.2) lies approximately 40 km southeast of Belo Horizonte and includes the municipalities of Caeté, Barão de Cocais, Santa Bárbara, and São Gonçalo do Rio Abaixo. Access from Belo Horizonte is via the federal highway BR-356, followed by MG-30. From Rio Acima, an unpaved road extends east for about 20 km, leading to the Mirante do Parque Gandarela.

The Dom Bosco Syncline is situated in the southern Quadrilátero Ferrífero (Figure 1.2) and is delimited by the Belo Vale, Congonhas, and Ouro Preto municipalities. Access from Belo Horizonte follows the BR-040 south for about 60 km toward Rio de Janeiro state.

Figure 1.2 — A) Map of Brazil showing the limits of the São Francisco Craton and Quadrilátero Ferrífero province. B) Enlarged map of Quadrilátero Ferrífero highlighting area shown in Figure C. C) Location map of the studied areas (blue rectangles) within the Quadrilátero Ferrífero.

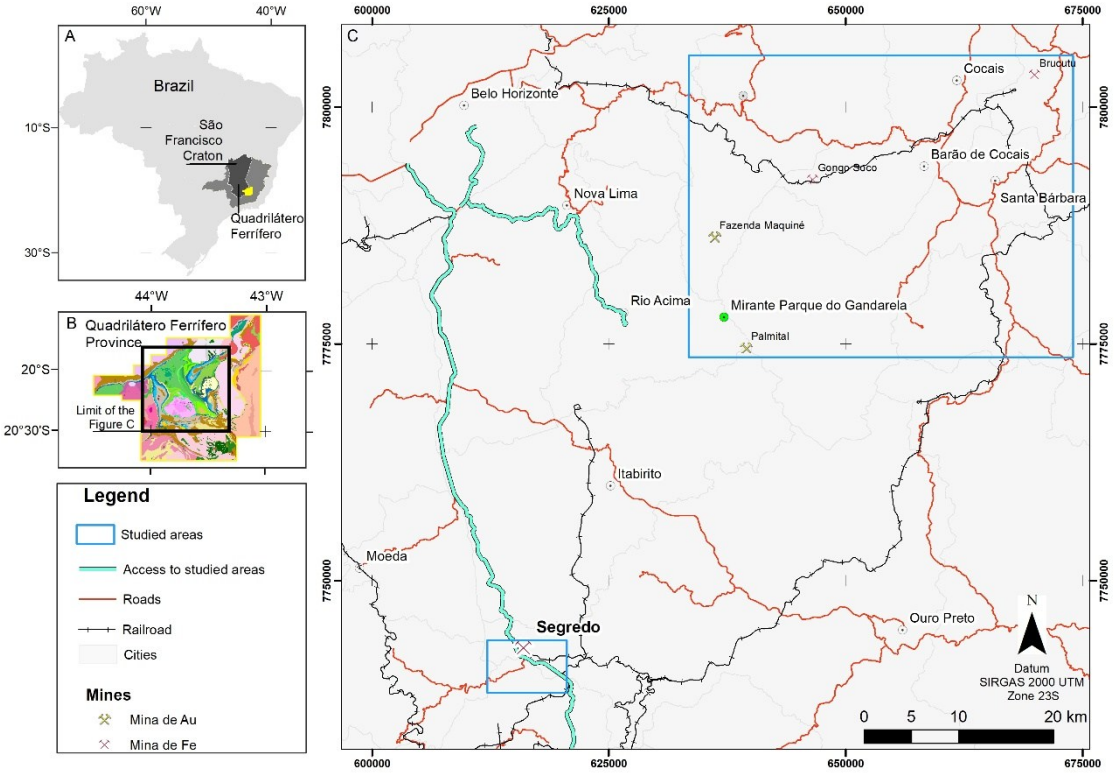

Source: Elaborated by the author

1.5 Thesis outline

This thesis presents detailed geochemical and isotopic data from the Quadrilátero Ferrífero, southeastern Brazil. It incorporates petrographic analyses, mineral characterization, elemental geochemistry, C-O-N isotopic compositions and geochronologic data to investigate the depositional conditions and evolutionary pathways of the giant IF-hosted Fe system in the Quadrilátero Ferrífero province. The thesis is structured as a series of integrated scientific papers, organized as follows:

Chapter 1: Introduction, outlining the significance of this study, research questions, objectives and study area.

Chapter 2: Background information on the Earth's historical evolutionary through the Paleoproterozoic, the formation of the IF-hosted iron systems, and the

geological setting of the Quadrilátero Ferrífero, providing both regional and local geological context.

Chapter 3: Methodology, describing the fieldwork, sample selection and analytical techniques used in the study.

Chapter 4: Published paper titled "*Trace elements, C-O isotopes and U-Pb geochronology of the Minas Supergroup in the Segredo deposit, Quadrilátero Ferrífero, Brazil" (Journal of South American Earth Sciences*). This study presents a lithostratigraphic review and the reconstruction of the ancient environmental conditions, contributing to the understanding of the genesis of the IF-hosted Fe system in the Quadrilátero Ferrífero.

Chapter 5: Accepted paper entitled "*Trace element and iron speciation analysis of Paleoproterozoic phyllite from the Gandarela syncline: implications for salinity and redox conditions in the Quadrilátero Ferrífero, Brazil (Chemical Geology).* This work reconstructs the evolution of redox and salinity conditions during the deposition of fine-grained sediments of the Minas Supergroup.

Chapter 6: Upcoming paper presenting novel stable isotope (C-O-N) and elemental geochemical data from IF in the Gandarela Syncline. This study evaluates redox conditions and the influence of microbial activity in Fe (oxyhydr)oxide precipitation and the formation of reduced Fe-mineral assemblages.

Chapter 7: Conclusions and perspectives, summarizing the main findings and outlining future research directions.

References: section provides a complete list of all sources cited in this study.

Appendix: additional photomicrographs of the thin sections.

2 OVERVIEW

2.1 Earth's evolution through the Paleoproterozoic era

The Precambrian time registered substantial environmental transformations associated with shifts in the global redox state of the ocean and the atmosphere (Cloud, 1973; Lyons et al., 2014). Reconstructions of paleo-ocean chemistry suggest an anoxic, ferruginous, and Si-rich water column (Poulton and Canfield, 2011; Konhauser et al., 2007, 2017) with circumneutral pH values (Cloud, 1965, 1973) was a dominant feature. Such chemical conditions facilitated the formation of giant IF-hosted Fe systems globally, including those in the Hamersley Province (Australia), Quadrilátero Ferrífero Province (Brazil), Kaapvaal/Griqualand West Craton (South Africa), Krivoy Rog (Ukraine) and others, as demonstrated in Figure 1.1.

Concerning the Fe source, it is widely accepted that the high abundance of dissolved Fe in the Precambrian water column is related to the transportation of dissolved Fe(II), as Fe(III) is insoluble under circumneutral pH (e.g. Konhauser et al. 2017). Two main processes can provide Fe(II) to the seawater:

Hydrothermal source

The upwelling of Fe(II)-rich deep waters in near-coastal areas is considered the primary source of Fe for precipitation of Fe-mineral precursors (Holland, 1973; Morris and Horwitz, 1983; Konhauser et al., 2017). During the Paleoproterozoic, this process was closely linked to the emplacement of large igneous provinces (LIPs) (Isley and Abbott, 1999) responsible for the formation of large continental masses and widespread mafic magmatic activity on a global scale (Klein and Beukes, 1992; Bekker et al., 2010). As a modern analogue, submarine hydrothermal systems are estimated to contribute approximately 75% of the dissolved Fe in deep ocean waters (German and Seyfried, 2014). This dissolved Fe can be transported over long distances, dispersing up to 2000 km (Fitzsimmons et al., 2017), demonstrating the potential scale and reach of hydrothermal inputs during IF deposition (Konhauser et al., 2017).

Geochemical evidence highlights the dominant role of hydrothermal fluids, as reflected in Rare Earth Elements (REE)+ yttrium (Y) patterns normalized to shale standards like the PAAS (Post-Archean Australian Shale). These patterns typically

show heavy REE (HREE) enrichment over light REE (LREE) and a positive Y anomaly, resembling marine signatures (Bau and Möller, 1993; Konhauser et al., 2017; Spier et al., 2007; Sampaio et al., 2018). Additionally, a positive europium (Eu) anomaly indicates a strong hydrothermal influence (Derry and Jacobsen, 1990; Planavsky et al., 2010, 2012; Mendes et al., 2016), while a strongly positive lanthanum (La) anomaly is typically associated with marine conditions (Bau and Dulski, 1996; Lawrence et al., 2006).

Continental source

It is attributed to the detrital input carrying Fe(II) in the absence of atmospheric oxygen - to prevent its oxidation (James, 1954; Holland, 1984). However, the detrital influence on most IF is considered minimal, as indicated by the low concentrations of detrital elements like aluminum (Al), niobium (Nb), titanium (Ti), zirconium (Zr), and a low amount of total REEY, which are markers of detrital contribution (e.g. Bau and Dulski, 1996; Pecoits et al., 2009; Tong et al., 2021; De Paula et al., 2023). As an example, quantitative studies in IF from the Hamersley Province, Australia, estimate an Fe deposition rate of approximately 10^{31} g/year (Trendall and Blockley, 1970). It requires riverine systems comparable to or larger than the modern Amazon (Brazil) to deliver significantly higher Fe loads than present (Konhauser et al., 2017).

In terms of the high silica saturation in ancient oceans, it is widely accepted as a result of the absence of silica-secreting microorganisms, such as diatoms, which are highly efficient in modern oceans (e.g. Cloud, 1973; Schad et al., 2019; Dreher et al., 2021). During the Precambrian, amorphous silica was precipitated abiotically, its estimated saturation level being 2.2 mM (~62 ppm) (Maliva et al., 2005), significantly higher than the modern ocean's silica concentration of ~1 ppm (Siever, 1992).

In the Precambrian context, oxygen levels were negligible (Holland, 2002; Olson et al., 2013) except in surface ocean waters close to coastal regions where cyanobacteria produced oxygen through photosynthesis (Cloud, 1973; Bekker et al. 2010). Estimates of oxygen concentration in these regions range between 5 μM and 100 μM (~0.16–3.2 ppm) (Kendall et al., 2010; Planavsky et al., 2010), far below modern levels of approximately 21% by volume (Fischer and Valentine, 2019). The GOE (Great Oxidation Event) at ~ 2.4 Ga marked a transition in Earth’s redox

system, characterized by a significant increase in atmospheric O_2 levels (Holland, 1984). During this time, shallow ocean waters became partially oxygenated, in contrast to deeper waters that remained anoxic (Holland, 2006). This period closely coincides with the cessation of BIF deposition, which reappeared approximately 350 Ma later (Bekker et al., 2010 Holland, 2006).

2.2 Iron Formation

Iron Formation is an iron-rich chemical sedimentary rock (15 – 40 wt.% Fe) (James, 1954; Gross, 1980) that precipitated from marine water during specific geological intervals between 2.8 and 1.85 Ga. Typically, IF shows low detrital input as supported by the low abundance of detrital components (Al_2O_3, Ti, Zr, Th) (Konhauser et al., 2017). Texturally, the IF exhibits a typical rhythmic textural feature which can be classified as Banded Iron Formation (BIF) and Granular Iron Formation (GIF), as shown in Figure 2.1.

Figure 2.1 — IF's texture in the Quadrilátero Ferrífero. A and B) Thick section showing GIF displaying ooids and intraclast of Fe oxide cemented by dolomite, sericite and chlorite in a thick section (Spier et al. 2007) and C) Photo of thin section of dolomitic BIF showing irregular thick Fe-rich and dolomite layers and D) Photo of drill core, highlighting the laminated structure.

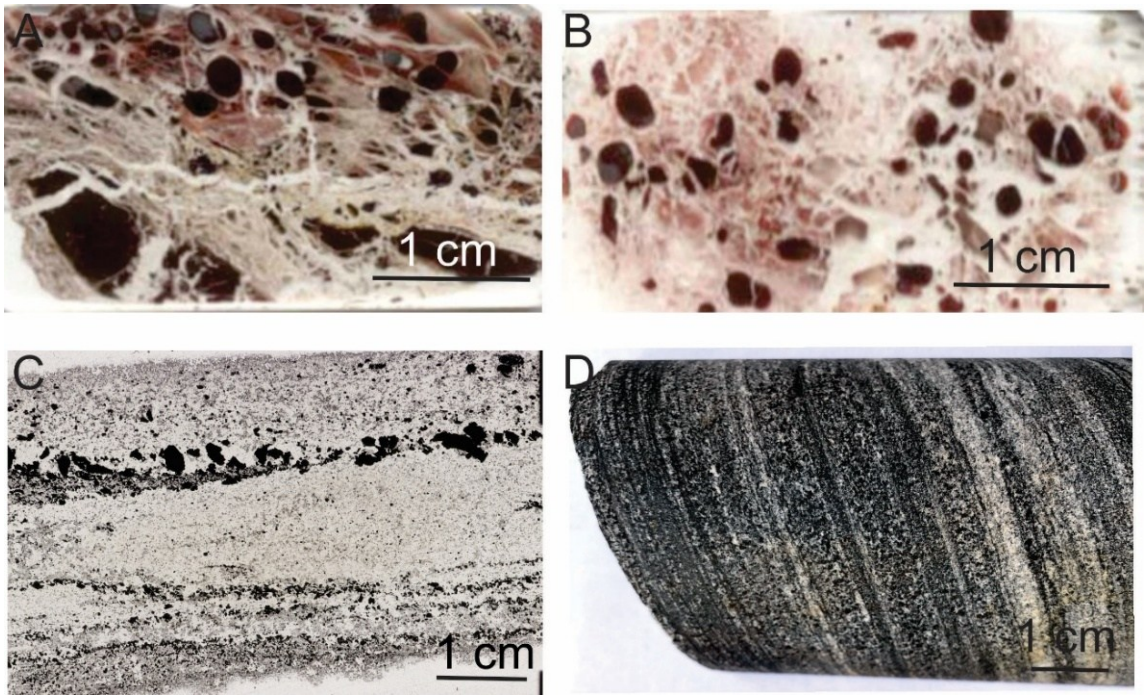

Source: Spier et al. 2007 (A and B) and elaborated by the author (C and D)

Granular IF was restricted to Paleoproterozoic successions and is associated with sedimentary reworking of iron-rich mudstones and arenites in shallow marine environments (Simonson and Goode, 1989; Bekker et al., 2010). On the other hand, BIF, common from the Archean to early Paleoproterozoic, is characterized by micro or meso-banding, formed through sedimentary and/or post-depositional processes (Krapež et al., 2003; Konhauser et al., 2002; Schad et al., 2019). Several genetic models have been proposed to explain the origin of the repetitive iron-rich bands, as summarized following:

- Cloud (1973) proposed that the formation of iron-rich bands in IF is driven by cyclical variations in prokaryotic populations, fluctuations in Fe(II) supply rates, or a combination of both processes.

- Klein and Beukes (1989) proposed a model for a stratified ocean in which relative sea-level fluctuations and changes in the position of the photic zone relative to the basin floor controlled the precipitation of carbonates or BIF types and chert. According to this model, during regressive events, the photic zone reached the seafloor on the deep shelf, facilitating primary productivity and the carbonate's deposition. In contrast, transgressive events caused the photic zone to move up relative to the seafloor, inhibiting the deposition of carbonates and favouring the deposition of BIF types and chert in the paleobasin.

- Krapež et al. (2003) proposed that microbands could form due to sedimentary density currents.

- More recently, Schad et al. (2019), based on experiments with marine photoferrotroph cultures, have suggested that varve-like deposition influenced by seasonal temperature fluctuations and microbial activity may be responsible for the band formation (Figure 2.2). In contrast, mesobands rich in Fe were likely formed during periods of intense hydrothermal input, lasting years to decades, while silica-rich mesobands formed during hydrothermal quiescence (Morris, 1993; Konhauser et al., 2002).

The formation of iron-bearing minerals involves Fe(II) oxidation and Fe(III) reduction (Bekker et al., 2010; Konhauser et al., 2017). However, the mechanisms driving Fe-mineral transformations remain debated (e.g., Konhauser et al., 2002, 2017; Rasmussen et al., 2013, 2016, 2017). The Fe(II) oxidation has been proposed to occur through two main pathways: biotic mediation (e.g., Klein and Beukes, 1989;

Konhauser et al., 2002, 2017; Bekker et al., 2010) or abiotic processes (Cairns-Smith, 1978), as illustrated in Figure 2.3.

Figure 2.2 — Seasonal model for BIF banding, illustrating Fe(III) and Si precipitation linked to temperature and microbial activity.

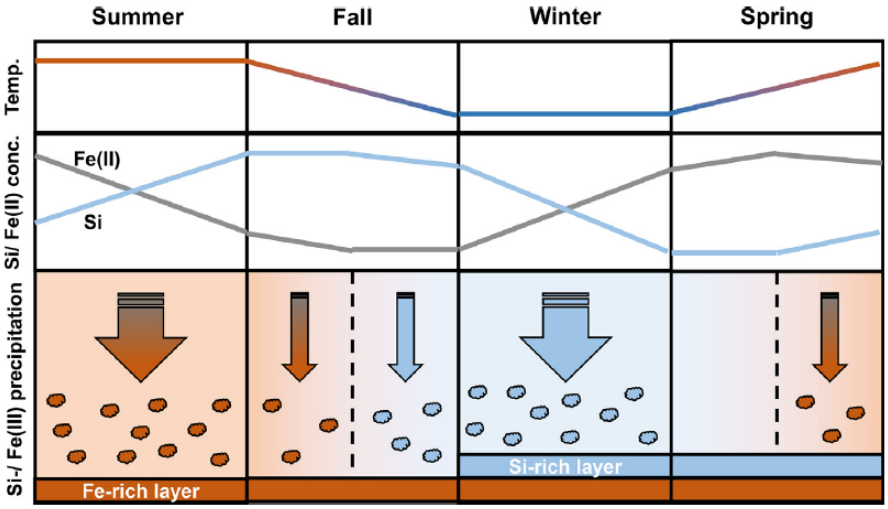

Source: Schad et al. (2019)

Figure 2.3 — Biological and abiological mechanisms involved in Fe-mineral precipitation and reduction of Fe-bearing mineral assemblages.

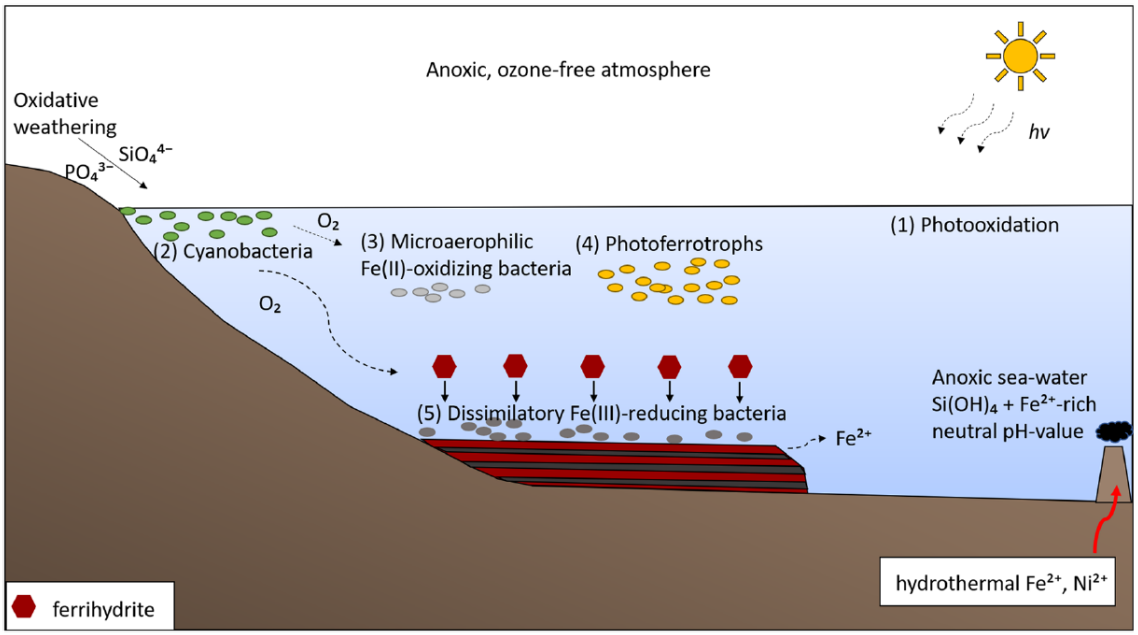

Source: Dreher et al. (2021)

Biological Pathways:

Indirect biologically mediated

Chemical Oxidation by Cyanobacteria-derived Oxygen (Figure 2.3): This traditional model suggests indirect Fe(II) oxidation driven by oxygen produced by cyanobacteria (Cloud, 1965, 1973; Konhauser et al., 2007). Oxygen, concentrated above the redoxcline as localized oases or within stratified oceans (e.g., Klein and Beukes, 1989; Poulton and Canfield, 2011), facilitated the process in nutrient-enriched near-coastal waters, restricted to the photic zone and influenced by upwelling Fe-rich deep waters (Bekker et al., 2010). However, the role of cyanobacteria remains debated due to potential negative influences, including exposure to UV radiation (Mloszewska et al., 2018), Fe(II) toxicity (Swanner et al., 2015), and nutrient limitations, particularly phosphorus scarcity (Jones et al., 2015).

Direct biologically mediated

Metabolic Fe Oxidation by autotrophs: autotrophic microorganisms synthesize their organic components and derive energy by oxidizing dissolved Fe(II) through redox reactions (Figure 2.3). This process may involve distinct bacterial types that inhabit deeper layers of the photic zone than cyanobacteria, each associated with different redox reactions (Konhauser et al., 2002, 2007; Dreher et al., 2021). One process is oxygenic Fe(II) oxidation, driven by microaerophilic bacteria (Figure 2.3). This occurs in the presence of oxygen, where these bacteria utilize the limited oxygen produced by cyanobacteria to oxidize Fe(II) under near-neutral pH conditions, resulting in the formation of ferrihydrite (Silverman and Lundgren, 1959; Konhauser et al., 2011). Another pathway is photoferrotrophy, which corresponds to direct Fe(II) oxidation (Figure 2.3). Photoferrotrophic bacteria perform anoxygenic redox reactions, oxidizing dissolved Fe(II) while producing ferrihydrite and organic matter (Garrels et al., 1973; Hartman, 1984; Bryce et al., 2018). This process occurs below the redoxcline, at depths of up to 100 meters (Kappler et al., 2005).

Metabolic Fe Reduction by heterotrophic bacteria: these microorganisms, which were part of seafloor microbial communities, consume freshly deposited phytoplankton biomass and Fe(III) (oxyhydr)oxides, such as ferrihydrite, through DIR – Dissimilatory Iron Reduction (Konhauser et al., 2005, 2011; Bekker et al. 2010). The DIR facilitated the active recycling of Fe (e.g., Konhauser et al., 2005) via

metabolic activity that reduced Fe(III) to Fe(II), leading to the formation of mixed-valence Fe(II)-Fe(III) minerals (Lovley and Phillips, 1987). As a consequence, crystalline minerals such as hematite, magnetite, and Fe(III)-rich clay minerals could form (Konhauser et al., 2007, 2011, 2017).

Abiotically mediated

Two models of abiotic process are discussed below, however, their significance in Paleoproterozoic IF-hosted Fe system have been questioned in numerous studies (e.g., Bekker et al. 2010; Konhauser et al., 2002, 2017 and references therein; Schad et al. 2019).

Primary Fe(II)-Silicate Formation: Rasmussen et al. (2013, 2014, 2017, 2021) proposed that precursors of Fe minerals in IF were Fe(II/III) silicates, such as greenalite, which formed through purely abiotic pathways. This model suggests that the Fe(III) oxidation occurred during post-depositional events such as diagenesis, metamorphism, or weathering (Rasmussen et al., 2021). However, this hypothesis has several challenges. One of them is the high pH required for Fe-silicate formation (Beukes and Gutzmer, 2008). In addition, isotopic constraints, particularly $\delta^{18}O$ values ranging from 1 to 7‰ suggest that hematite formed under low-temperature conditions (Konhauser et al., 2017).

Photochemical Oxidation of Fe(II): Cairns-Smith (1978) proposed that Fe(II) oxidation in the Precambrian ocean could have been driven by ultraviolet (UV) radiation. This hypothesis suggests that UV light facilitated the conversion of dissolved Fe(II) into Fe(III) minerals. Experimental studies (e.g., Konhauser et al., 2007) indicate that photochemical oxidation was likely not a dominant mechanism in ancient environments. However, recent work by Liu et al. (2020) demonstrates the potential importance of anoxic photochemical oxidation of Mn-oxide during the Archaean, which has led to the discussion about the relevance of this mechanism in the formation of transition metal oxides

In conclusion, biotic mechanisms, supported by isotopic evidence, are considered the dominant pathway for the formation and accumulation of precursor Fe-minerals in an anoxic Paleoproterozoic water column with negative carbon isotope fractionation in IF interpreted as driven by DIR (Baur et al., 1985; Beukes and Klein, 1990; Fischer et al., 2009; Sial et al., 2000; Teixeira et al., 2017). Although the absence of convincing microfossil records (Konhauser et al., 2002) and the low

organic matter content (<0.5 wt.%) (Gole and Klein, 1981) may raise questions, the latter is primarily attributed to the consumption of biomass during Fe(III) reduction and organic matter oxidation via fermentation or methanogenesis (Konhauser et al., 2005), or it may have been removed by post-depositional processes (Köehler et al., 2010).

2.3 Minas Supergroup – Depositional Systems of the Minas paleobasin

The Minas Supergroup (Figure 2.4) corresponds to a Paleoproterozoic succession of metasedimentary rocks deposited between approximately 2.5-2.2 Ga in the Quadrilátero Ferrífero province (Babinsky et al., 1995; Machado et al., 1996; Hartmann et al., 2006; Koglin et al., 2014; Nunes, 2016; Dopico et al., 2017; Rossignol et al., 2020). The succession represents the tectonic evolution of a Minas paleobasin from an intra-continental rift system to a passive continental margin in a platform setting (Canuto, 2010; Alkmim and Martins Neto, 2012).

Figure 2.4 — Simplified geological map of the Quadrilátero Ferrífero province, highlighting the studied areas.

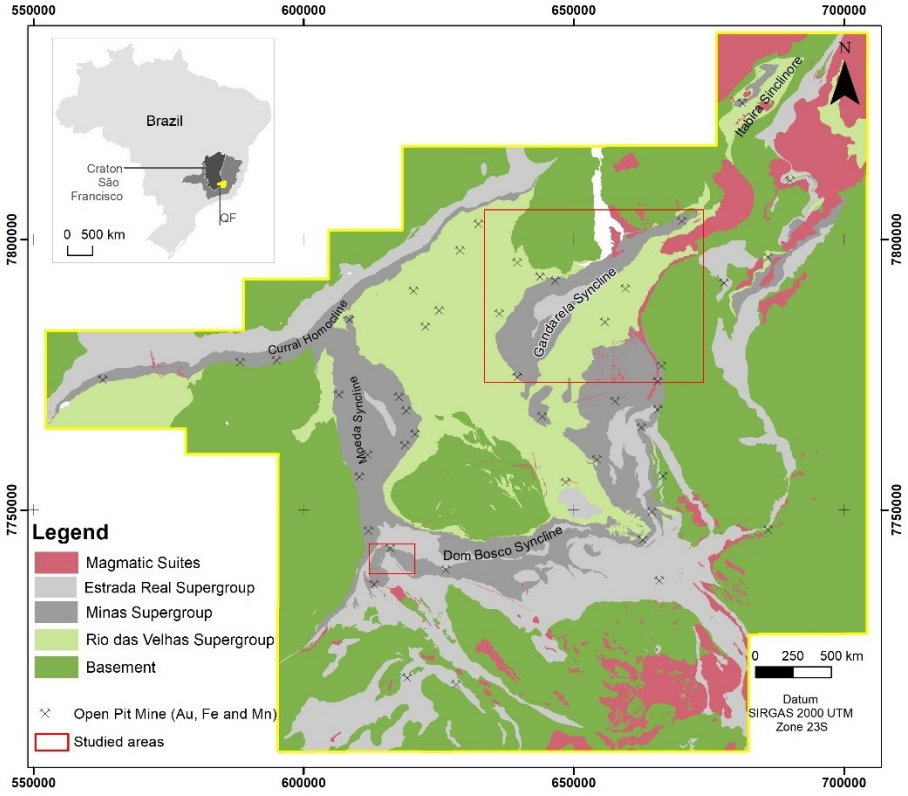

Source: Modified by Endo et al. (2019)

The Minas Supergroup records a regional transgressive sequence with three cycles of transgression and regression (Gonçalves and Uhlein, 2022), which led to sediment accumulation in a tectonically controlled basin (Dorr, 1969; Canuto, 2010). The Minas Supergroup unconformably overlies the Archean greenstone belt of the Rio das Velhas Supergroup (Dorr et al., 1969; Farina et al., 2016). At the top, a regional unconformity separates it from a subsequent basin inversion phase, resulting in a foreland basin (Dorr, 1969; Noce, 1995; Reis et al., 2002; Gonçalves and Uhlein, 2022), recently classified as the Estrada Real Supergroup by Endo et al. (2019, 2020).

The Minas succession comprises approximately 3.5 km of clastic and chemical sedimentary rocks (Alkmim and Marshak, 1998; Endo et al. 2019, 2020) and is divided into four lithostratigraphic units (Figure 2.5), from base to top: the Caraça/Tamanduá, Itabira, and Piracicaba groups (Dorr, 1969; Endo et al., 2019, 2020).

At the base, the Caraça group records the evolution of the alluvial, fluvial, lacustrine, deltaic, and marine environments (Figure 2.6), comprising conglomerate, quartzite, phyllite, minor, BIF and carbonate rocks (Dorr, 1969; Madeira et al., 2019; Madureira, 2021; Gonçalves and Uhlein, 2022). The maximum depositional age is estimated at 2.5 Ga for the Caraça Group, based on the youngest U-Pb detrital zircon populations (Machado et al., 1996; Hartmann et al., 2006; Nunes, 2016; Dopico et al., 2017; Rossignol et al., 2020; Madureira et al., 2021). In contrast, the equivalent basal unit, the Tamanduá Group, remains a subject of debate due to uncertainties regarding its extent, timing, and stratigraphic context (e.g., Simmons and Maxwell, 1961; Marshak and Alkmim, 1989; Daher et al., 2020; Dutra et al., 2020).

The Itabira Group marks the phase of chemical sedimentation within the passive margin basin (Dorr, 1969; Alkmim and Marshak, 1998). At its base, the Cauê Formation comprises a thick IF layer (~350 m) (Dorr, 1969), indicative of deposition on the continental shelf (Klein and Ladeira, 2000). Overlying this, the Gandarela Formation consists of carbonate rocks (dolostone, limestone, dolomitic BIF), along with minor phyllite and intraformational breccia (Dorr, 1969; Souza and Müller, 1984), reflecting a shallow marine environment (Dorr, 1969; Gonçalves and Uhlein, 2022). A Pb/Pb whole-rock isochron indicates an age of 2,420 ± 19 Ma for the stromatolitic facies of the Gandarela Formation (Babinsky et al., 1995). Conversely,

Cabral et al. (2012) reported a U-Pb zircon age of 2,655 ± 6 Ma for a proposed meta-volcanic layer overlying the Cauê Formation. However, the significance of this age remains debated, as it is coeval with the closure of the Archean Rio das Velhas basin, and may be related to an inherited zircon population (Koglin et al., 2014; Farina et al., 2016; Dopico et al., 2017).

Figure 2.5 — Lithostratigraphic column of Quadrilátero Ferrífero province.

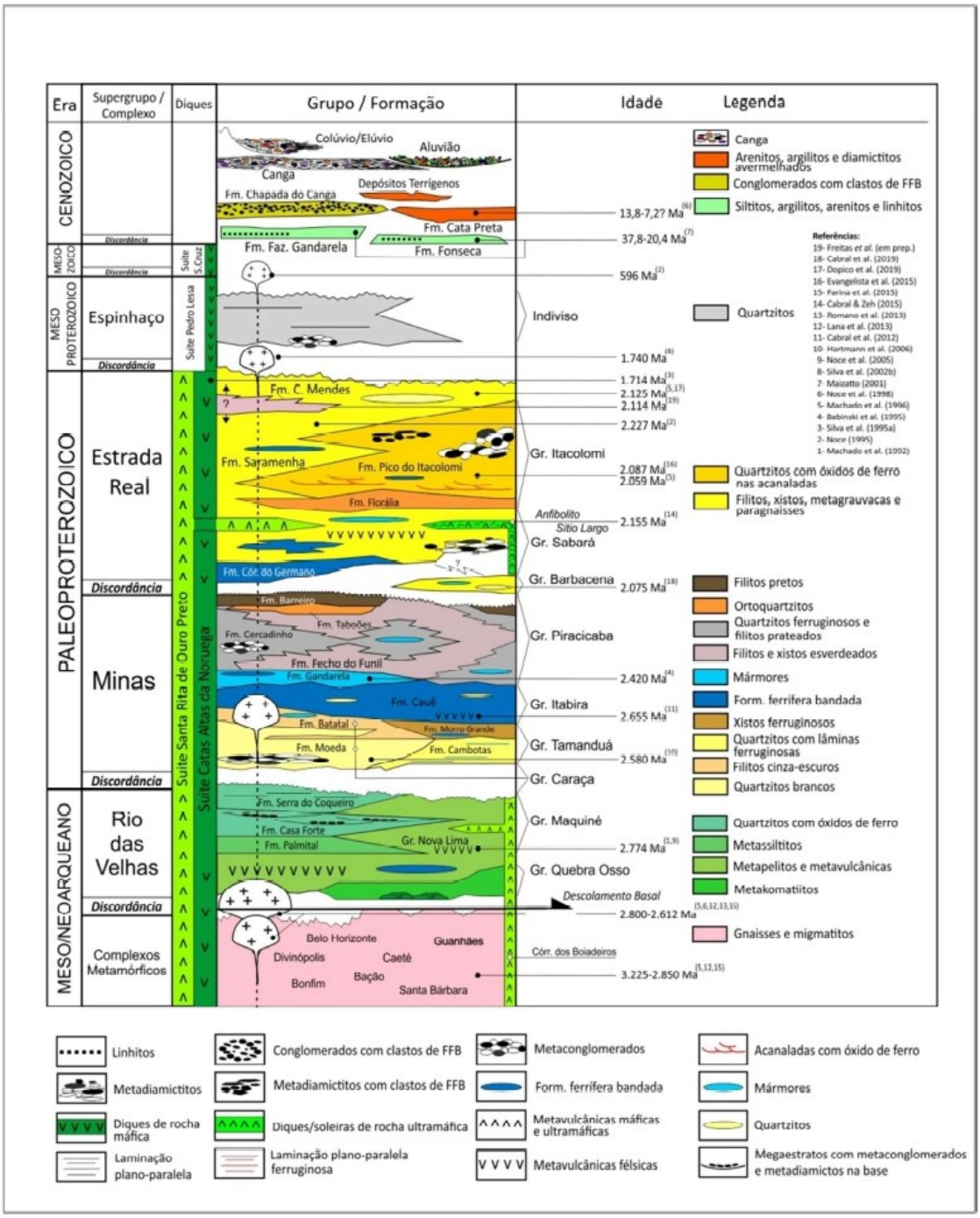

Source: Endo et al. (2019)

The top stratigraphic unit, the Piracicaba Group, consists predominantly of clastic sedimentary rocks, including phyllite, quartzite and minor carbonates rocks, deposited in a shallow marine environment (Dorr, 1969). This group reflects the evolution of depositional systems such as shallow marine, delta, and continental shelf settings (Gonçalves and Uhlein, 2022). The minimal depositional age of 2,180Ma is based on U-Pb crystallization dating of garnet-hosted zircon obtained from the Sitio Largo amphibolite, which is on top of the Cauê Formation, as reported by Cabral and Zeh (2015), along with chemostratigraphy data from Bekker et al. (2003) and a 2110 ± 10 Ma Pb-Pb whole-rock carbonate isochron from the Fecho do Funil Formation (Babinski et al., 1995), indicates that the deposition of the Piracicaba Group occurred before the Minas accretionary orogeny and may extend into the Rhyacian.

Figure 2.6 – Tectono-sedimentary model for the continental sedimentation of the Caraça Group in the Gandarela and Ouro Fino synclines, showing the variation of depositional systems from alluvial (ALG1, ALG2, ALOF2) to fluvial systems (ALG3, ALOF1, ALOF3).

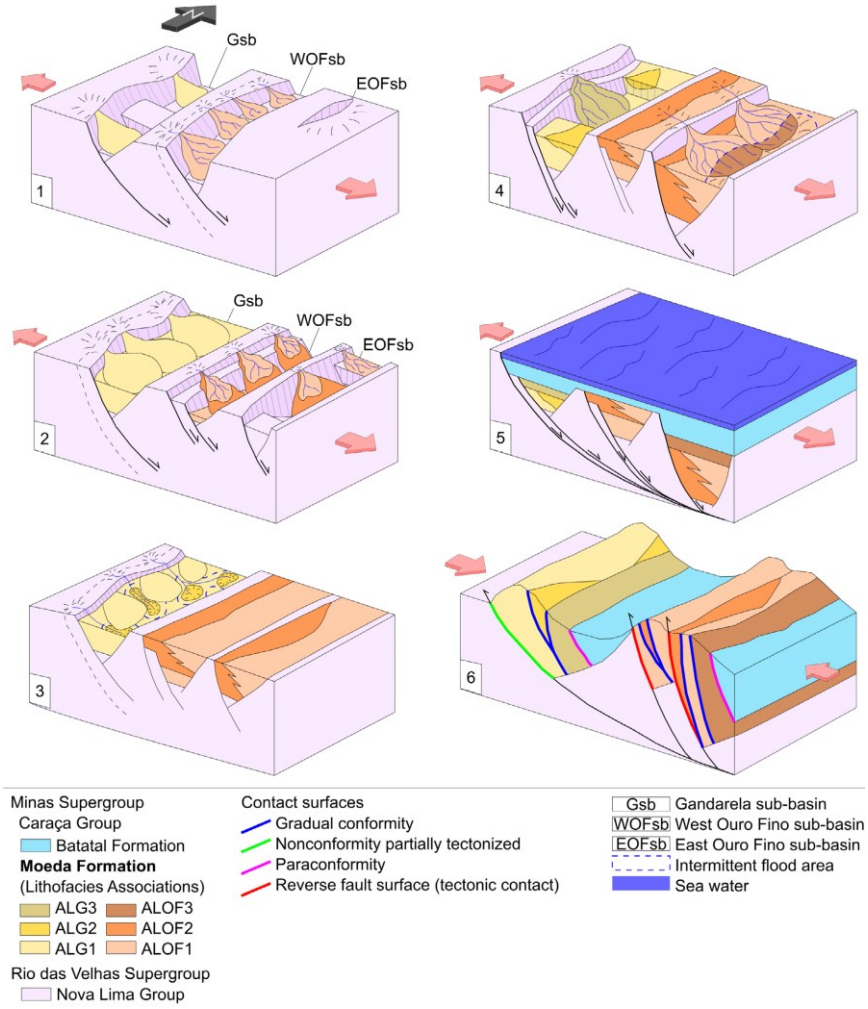

Source: Madureira et al. (2021)

2.4 Gandarela Syncline

The Gandarela Syncline (Figure 2.7) holds significant economic importance within the Quadrilátero Ferrífero province due to the concentration and extraction of mineral resources such as Fe, gold (Au), limestone, and coal. Additionally, it has geological, speleological, and environmental relevance, featuring well-preserved rare outcrops, numerous caves, and the conservation area of the Serra do Gandarela National Park (PARNA).

In this region, Paleoproterozoic rocks of the Minas and Estrada Real supergroups are surrounded by Archean rocks from the metamorphic complex and the Rio das Velhas Supergroup. Furthermore, post-Minas magmatic intrusions, including the Peti Granite and the Cocais Suite, are also present (Figure 2.7).

The lithostratigraphy of the Minas Supergroup (Figure 2.5) consists, at its base, of the Tamanduá and Caraça groups (Dorr, 1969; Endo et al. 2019). The Tamanduá Group, named after its type locality in the Serra do Tamanduá, has an uncertain stratigraphic continuity across the Quadrilátero Ferrífero (Simmons and Maxwell, 1961; Marshak and Alkmim, 1989; Daher et al., 2020; Dutra et al., 2020). According to Endo et al. (2019, 2020), the Tamanduá Group occurs in the northeastern portion of the Gandarela Syncline and consists of quartzite from the Cambotas Formation, along with dolomitic schists, dolomitic BIF, dolostone, ferruginous quartzite, and carbonaceous phyllite from the Morro Grande Formation. Given the inconsistencies in the lithostratigraphic classification of the Tamanduá Group within the province, the basal lithostratigraphic unit, which transitions gradually into the chemical rocks of the Itabira Group, has been considered compositional variations of the Caraça Group, as also discussed by Dorr (1969). In contrast, the Caraça Group (Figure 2.8 A, B and C) is subdivided into the Moeda Formation at its base, characterized predominantly by quartzite with intercalations of conglomerate and phyllite (Dorr, 1969). Above it, the Batatal Formation consists mainly of phyllite (, with lenses of metachert and dolostone (Dorr, 1969).

Above the gradual contact, the Itabira Group consists of chemically precipitated rocks with remarkable continuity (Figure 2.7), including well-preserved BIF units that shape the Gandarela range, reaching elevations over 1,600 meters. At its base, the Cauê Formation is composed of quartz-BIF (Figure 2.8 D), dolomite-BIF (Figure 2.8 F and G), and amphibolitic-BIF (Figure 2.8 E), with minor

occurrences of phyllite and dolostone lenses (Dorr et al., 1957). The overlying Gandarela Formation comprises a carbonate rocks succession (Figure 2.8 H, I and J) that transitions both laterally and vertically, featuring dolostones—locally containing spheroids and stromatolites (Figure 2.8 J)—along with ferruginous and argillaceous dolostone, dolomitic BIF, and carbonate breccia (e.g., Bekker et al., 2003; Almeida and Sousa Jorge, 2022).

Figure 2.7 – Geological map of the Gandarela Syncline with a schematic vertical profile illustrating the fold geometry.

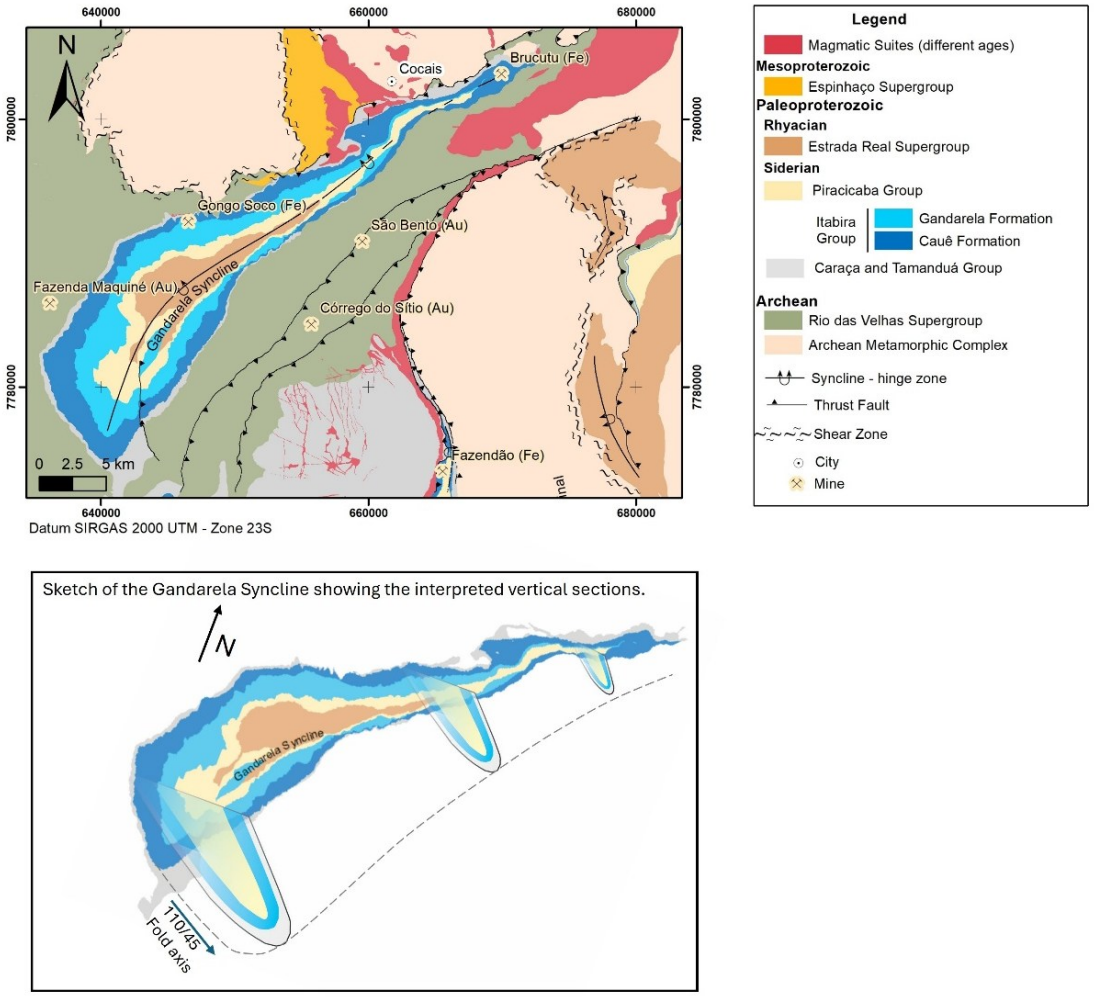

Source: Modified from Endo et al. 2019 and elaborated by the author.

The Piracicaba Group conformably overlies the Itabira Group (Dorr et al., 1957). Within the Gandarela Syncline, the Cercadinho Formation consists of quartzite, ferruginous quartzite, schist, and phyllite (Figure 2.8 L).

Lastly, the metasedimentary succession of the Estrada Real Supergroup (Figure 2.5 and 2.7), was deposited unconformably over the Minas Supergroup

(Endo et al., 2019, 2020), and is composed of phyllite, quartzite, metagraywacke, BIF, and metaconglomerates of the Sabará Group, primarily concentrated in the central portion of the regional fold.

Figure 2.8 – Photos of representative rock types from the Gandarela Syncline. (A) Sericitic phyllite and (B, C) Carbonaceous phyllite from the Batatal Formation. (D) Quartz-BIF, (E) Altered amphibolitic-BIF and (F, G) Dolomitic BIF from the Cauê Formation. (H) Outcrop of dolostone, (I) Laminated dolostone and (J) stromatolitic dolostone from Gandarela Formation. (L) Drill core displaying quartzite with discrete phyllite lenses from Cercadinho Formation.

Source: Elaborated by the author.

The geometry of the Gandarela Syncline has been studied by several authors (e.g. Dorr, 1969; Franco and Endo, 2004; Endo et al., 2004; Oliveira et al., 2005).

Recent works characterize it as a reclined fold with an NE-SW oriented axial trace and a hinge zone dipping southeastward (Endo et al., 2004; Oliveira et al., 2005). Its structural evolution resulted from progressive deformation through three main phases (Endo et al., 2004). The first phase, associated with the Rhyacian orogeny (~2.0 Ga), resulted in a recumbent fold, a nappe with SSW vergence (Endo et al., 2020). This was followed by the development of the Gandarela and Ouro Fino antiformal syncline (Dorr, 1969). Subsequently, the emplacement of intrusive bodies - Borrachudos suite, linked to post-Minas magmatism, further deformed the Gandarela syncline (Endo et al., 2020). Finally, the Brasiliano orogeny (~0.5 Ga) overprinted the syncline, particularly affecting its eastern portion (Endo et al., 2004; Oliveira et al., 2005).

In addition, the southern region of the reverse flank is intercepted by the Fundão fault system (Endo and Fonseca 1992), following an N-S trend and vergence for the west (Figure 2.7).

3 METHODS AND TECHNIQUES

This research included fieldwork, selection of drill cores, sample collection, petrographic description, chemical and isotopic (C, N, and O) analyses, and Fe speciation to characterize the Minas Supergroup sedimentary succession. Additionally, a bibliographic compilation of trace elements abundance and stable isotopic data (C and O) was conducted for regional analysis and interpretation within the project's scope.

3.1 Survey and Sampling

Fieldwork was conducted in the study area in January 2022 (Figure 3.1 A) when twenty-four fresh rock samples of carbonate rocks, phyllites, and quartzites from the Caraça, Itabira, and Piracicaba groups were collected. The primary purposes were to identify well-preserved outcrops of metasedimentary rocks, to examine their compositional variation and structures, and to collect representative samples. Fortunately, the fieldwork took place during the summer, following intense rainfall that triggered block sliding and exposed well-preserved rock surfaces.

Figure 3.1 — A) Outcrop of Batatal Formation in the Gandarela Syncline (UTM coordinates: 637470E, 7777341N; elevation: 1514 m; Datum: SIRGAS 2000) B) Collection of core samples.

Source: Elaborated by the author

Drill cores, gently provided by Vale S.A, were selected from the company's dataset based on the following criteria:

- the geographical location, including their position on a map and vertical profile, depth and lithostratigraphic units intercepted by the drill hole,
- their availability — since many had been previously used for geochemical analyses, quality control sampling, metallurgical tests or disposed of the core and,
- the state of preservation of the drill core and its core box.

Based on recent exploratory surveys (2020/2021) conducted in the Serra do Tamanduá area, located in the northeastern portion of the Gandarela Syncline, this region was identified as the target for this study. Four drill holes were initially selected, with subsequent focus on three of them, as the STM-FD00218 showed evidence of post-depositional alteration. Table 3.1 summarizes the main information of the selected drill cores.

Table 3.1 — Location and data of the studied drill core.

Drill Hole ID	East	North	Elevation	Depth (m)	Azimuth	Dip
STM-FD00155	663076	7800065	858	591	330	-80
STM-FD00205	663997	7800938	935	376	347	-78
STM-FD00218	664501	7801323	925	301	336	-80
STM-FD00233	666686	7801702	895	266	330	-75

Source: Elaborated by the author

Drill core STM-FD00155 is a stratigraphic drill hole, while STM-FD00205 is notable for containing well-preserved dolomitic BIF. Drill core STM-FD00233 was selected for its compositional variation, featuring quartz-rich BIF. Conversely, STM-FD00218 was excluded from detailed analysis due to the presence of pseudomorphs of amphiboles and goethite, indicating alteration processes likely driven by hydrothermal or meteoric fluids.

The geological description and sampling of seventy-four core samples took place at the Ferrous Technical Center (CDM - Centro Tecnológico de Ferrosos, also known as Miguelão), Nova Lima, Minas Gerais (Figure 3.1 B). Table 3.2 and Table 3.3 provide detailed information on the sampled samples, as well as the analytical methods applied in this research.

Table 3.2 — List of core samples collected and analyzed in this study.

Drillcore ID	Sample ID	Depth (m)	Lithology	Stratigraphy	Thin Section	Geochemical Analyses	$\delta^{13}C$ - $\delta^{18}O$	$\delta^{15}N$	Iron Speciation
STM-FD00155	155-A01	155	Quartzite/Phyllite	Cercadinho Fm.	-	x	-	-	x
	155-A02	159	Quartzite	Cercadinho Fm.	-	-	-	-	-
	155-A03	178	Quartzite	Cercadinho Fm.	-	-	-	-	-
	155-A04	202	Quartzite/Phyllite	Cercadinho Fm.	-	x	-	-	x
	155-A05	208	Quartzite/Phyllite	Cercadinho Fm.	-	-	-	-	-
	155-A06	215	Quartzite/Phyllite	Cercadinho Fm.	-	x	-	-	-
	155-A07	233	Quartzite	Cercadinho Fm.	-	-	-	-	-
	155-A08	296	Quartzite	Cercadinho Fm.	-	-	-	-	-
	155-A09	308	Quartzite	Cercadinho Fm.	-	-	-	-	-
	155-A10	383	Gabbro	Intrusive Igneous	-	x	-	-	-
	155-A11	412	BIF	Cauê Fm.	-	x	-	x	-
	155-A12	456	BIF	Cauê Fm.	-	x	-	-	-
	155-A13	492	BIF	Cauê Fm.	-	x	-	x	-
	155-A15	505	BIF	Cauê Fm.	-	x	-	-	-
	155-A16	521	BIF	Cauê Fm.	x	x	-	-	-
	155-A17	534	BIF	Cauê Fm.	x	x	-	x	-
	155-A18	541	Impure carbonate	Batatal Fm.	x	x	-	-	-
	155-A19	543	Phyllite	Batatal Fm.	-	x	-	-	x
	155-A20	551	BIF	Batatal Fm.	x	x	-	-	-
	155-A21	558	Impure carbonate	Batatal Fm.	-	x	-	-	-
	155-A22	562	BIF	Batatal Fm.	-	x	-	-	-
	155-A23	569	BIF	Batatal Fm.	x	x	-	x	-
	155-A24	571	Phyllite	Batatal Fm.	-	x	-	-	x
	155-A25	575	Phyllite	Batatal Fm.	-	x	-	-	x
	155-A26	578	Phyllite	Batatal Fm.	-	x	-	-	x
	155-A27	581	Impure carbonate	Batatal Fm.	-	x	-	-	-
	155-A28	582	Phyllite	Batatal Fm.	-	x	-	-	-
	155-A29	583	Phyllite	Batatal Fm.	x	x	-	-	-
	155-A30	590	Impure carbonate	Batatal Fm.	-	-	-	-	-
STM-FD00205	205-A01	158	BIF	Cauê Fm.	-	x	-	-	-
	205-A02	164	BIF	Cauê Fm.	x	x	x	x	-
	205-A03	166	Phyllite	Cauê Fm.	x	x	-	-	-
	205-A04	172	BIF	Cauê Fm.	-	x	x	x	-
	205-A05	176	Phyllite	Cauê Fm.	-	x	-	-	-
	205-A06	184	BIF	Cauê Fm.	-	x	-	-	-
	205-A07	190	BIF	Cauê Fm.	-	x	x	x	-
	205-A08	192	Phyllite	Cauê Fm.	x	x	x	x	-
	205-A09	242	Dolostone	Cauê Fm.	-	x	x	-	-
	205-A10	247	Dolostone	Cauê Fm.	-	x	x	-	-
	205-A11	252	BIF	Cauê Fm.	-	x	x	-	-
	205-A12	256	BIF	Cauê Fm.	-	x	x	-	-
	205-A13	266	BIF	Cauê Fm.	-	x	x	-	-
	205-A14	270	BIF	Cauê Fm.	-	x	x	-	-
	205-A15	274	BIF	Cauê Fm.	-	x	x	-	-
	205-A16	279	BIF	Cauê Fm.	-	x	x	x	-
	205-A17	284	BIF	Cauê Fm.	-	x	x	x	-
	205-A18	289	Dolostone	Cauê Fm.	-	x	x	-	-

Drillcore ID	Sample ID	Depth (m)	Lithology	Stratigraphy	Thin Section	Geochemical Analyses	$\delta^{13}C$ - $\delta^{18}O$	$\delta^{15}N$	Iron Speciation
	205-A19	293	Dolostone	Cauê Fm.	-	x	x	-	-
	205-A20	297	Dolostone	Cauê Fm.	-	x	x	-	-
	205-A21	302	BIF	Cauê Fm.	-	x	x	-	-
	205-A22	307	Dolostone	Cauê Fm.	-	x	x	-	-
	205-A23	311	BIF	Cauê Fm.	-	x	x	-	-
	205-A24	362	Carbonaceous phyllite	Batatal Fm.	-	x	-	-	-
	205-A25	366	Carbonaceous phyllite	Batatal Fm.	x	x	-	-	-
	205-A26	369	Carbonaceous phyllite	Batatal Fm.	-	x	-	-	-
	205-A27	373	Phyllite	Batatal Fm.	x	x	-	-	-
STM-FD00233	233-A01	98	BIF	Cauê Fm.	-	x	-	x	-
	233-A02	130	BIF	Cauê Fm.	-	x	-	-	-
	233-A03	146	BIF	Cauê Fm.	x	x	-	x	-
	233-A04	159	BIF	Cauê Fm.	-	x	-	-	-
	233-A05	166	BIF	Cauê Fm.	-	x	-	x	-
	233-A06	207	Phyllite	Batatal Fm.	-	x	-	-	x
	233-A07	212	Quartzite	Batatal Fm.	-	-	-	-	-
	233-A08	218	Quartzite	Batatal Fm.	-	-	-	-	-
	233-A09	225	Phyllite	Batatal Fm.	-	x	-	-	
	233-A10	227	Carbonaceous phyllite	Batatal Fm.	x	x	-	-	x
	233-A11	236	Phyllite	Batatal Fm.	-	x	-	-	x
	233-A12	244	Phyllite	Batatal Fm.	-	x	-	-	x
	233-A13	248	Phyllite	Batatal Fm.	-	x	-	-	-
	233-A14	253	Phyllite	Batatal Fm.	-	x	-	-	x
	233-A15	257	Phyllite	Batatal Fm.	-	x	-	-	-
	233-A16	262	Phyllite	Batatal Fm.	-	x	-	-	x

Source: Elaborated by the author

Table 3.3 — List of outcrop samples collected and analyzed in this study.

Sample	East	North	Lithology	Stratigraphy	Thin Section	Geochemical Analyses	$\delta^{13}C$ - $\delta^{18}O$	Iron Speciation
AC02A	637470	7777341	Phyllite	Batatal Fm.	-	x	-	x
AC02B	637300	7777582	Phyllite	Batatal Fm.	-	x	-	x
AC02C	637101	7777815	Phyllite	Batatal Fm.	-	x	-	x
AC03	638949	7781499	Phyllite	Batatal Fm.	-	x	-	x
AC04	637101	7777815	Phyllite	Batatal Fm.	-	x	-	-
AC5-00	638949	7781499	Dolostone	Gandarela Fm.	-	x	x	-
AC5-01	638949	7781499	Dolostone	Gandarela Fm.	-	x	x	-
AC5-02	638949	7781499	Dolostone	Gandarela Fm.	-	x	x	-
AC5-03	638949	7781499	Dolostone	Gandarela Fm.	-	x	x	-
AC5-03A	638949	7781499	Dolostone	Gandarela Fm.	x	-	x	-
AC5-04	638949	7781499	Dolostone	Gandarela Fm.	-	x	x	-
AC5-05	638949	7781499	Dolostone	Gandarela Fm.	-	x	x	-
AC5-06	638949	7781499	Ferruginous dolostone	Gandarela Fm.	-	x	x	-
AC5-07	638949	7781499	Ferruginous dolostone	Gandarela Fm.	-	x	x	-
AC5-08	638949	7781499	Dolostone	Gandarela Fm.	x	-	x	-
AC5-09	638949	7781499	Dolostone	Gandarela Fm.	-	x	x	-
AC5-10	638949	7781499	Dolostone	Gandarela Fm.	-	x	x	-
AC5-11	638949	7781499	Dolostone	Gandarela Fm.	-	x	x	-
AC5-12	638949	7781499	Dolostone	Gandarela Fm.	-	x	x	-
AC5-13	638949	7781499	Dolostone	Gandarela Fm.	-	x	x	-
AC5-14	638949	7781499	Ferruginous dolostone	Gandarela Fm.	-	x	x	-
AC5-15	638949	7781499	Ferruginous dolostone	Gandarela Fm.	-	x	x	-
AC06	642120	7787537	Phyllite	Cercadinho Fm.	-	x	-	x
AC016	638923	7781030	Dolostone	Gandarela Fm.	-	-	x	-

Source: Elaborated by the author

3.2 Petrographic Description and Mineralogy

3.2.1 Principles

Petrographic analysis was conducted to characterize the mineralogical composition, textural relationships, and structural features of the studied rocks. This examination provides insights into their geological evolution.

3.2.2 Sample Preparation, Data Acquisition and Recording

Fifteen thin sections (Figure 3.2), of which ten were polished laminae, of IF, dolostones and phyllite were prepared in the CPMTC laboratory and by an external professional technician.

Figure 3.2 — Scan of the thin section representing a carbonaceous phyllite.

Source: Elaborated by the author

These observations were performed using an optical microscope, specifically the Zeiss Axioskop 40 model (Microscopy Laboratory, Federal University of Minas Gerais - Brazil) and Zeiss (Microscopy Laboratory, University of Alberta - Canada).

3.3 X-ray diffraction (XRD)

3.3.1 Principles

X-ray diffraction was applied to identify crystalline and mineral phases. It is a non-destructive technique that evaluates the interaction between X-rays and the atomic lattice of minerals, generating unique diffraction patterns used for phase identification (Figure 3.3 A). When an incident X-ray beam strikes a crystalline sample, it excites electrons within the atomic lattice (Figure 3.3 B), and as the

electrons return to their ground state, they emit X-rays, producing diffraction patterns (Pecharsky and Zavalij, 2003).

Figure 3.3 — (A) XRD instrumentation configuration. (B) Interaction of X-rays with the crystalline lattice, producing diffracted energy.

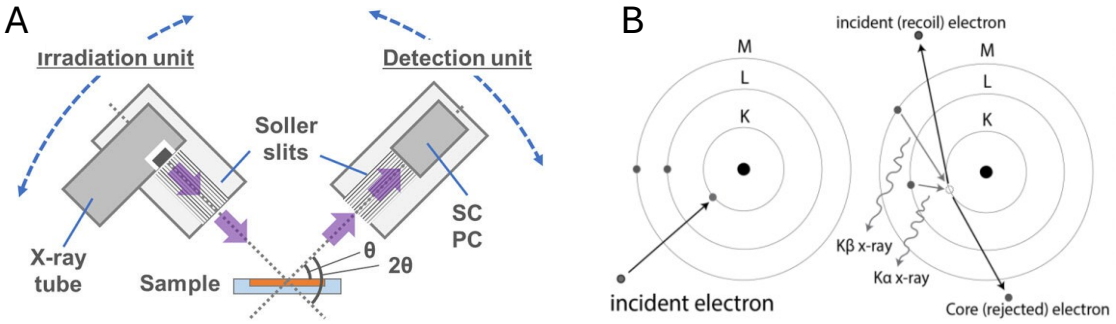

Source: Pecharsky and Zavalij (2003).

3.3.2 Sample Preparation, Data Acquisition and Recording

Sixteen samples, including IF, dolostone, and phyllite, were pulverized to a fine powder (< 40 microns) using an agate mortar and pestle or a SPEX sample prep shatter box, a ring and puck mill.

The XRD analyses were conducted in two laboratories: CPMTC Research Center at the Federal University of Minas Gerais (Brazil) and X-Ray Diffraction Laboratory at the University of Alberta (Canada). At the CPMTC, the analysis was performed using the Panalytical X'Pert PRO diffractometer, equipped with a Cu anode. The scan was set at 40 kV and 45 mA. The HighScore Plus (HPS) software was used to process the XRD raw data and identify the mineral phases. On the other hand, the X-Ray Diffraction Laboratory utilized the Bruker D8 Advance X-ray diffractometer, equipped with a cobalt radiation source (35 kV and 40 mA). The DIFFRAC.EVA software was used for data processing.

In both laboratories, the main mineral phases were identified by comparing the peak sequences in the calculated scans with reference patterns from ICDD (International Center for Diffraction Data) and COD (Crystallographic Open Database).

3.4 Scanning Electron Microscope (SEM)

3.4.1 Principles

The SEM analyses were conducted to obtain high-magnification images of select areas, refine the mineral paragenesis, and detail the intergranular texture at a microscale.

The SEM operates by emitting a focused electron beam that interacts with the sample, generating various signals (Figure 3.4). These signals allow detailed imaging and compositional analysis at both the micro- and nano-scale.

Different detectors capture the emitted signals, which are subsequently processed to generate images or spectra. The Secondary Electron (SE) detector produces high-resolution images of the surface, while the Backscattered Electron (BSE) detector reveals compositional contrasts in the crystal structure, Cathodoluminescence (CL) detector aids in identifying mineral zoning, crystal defects and evidence of alteration in the crystal. Additionally, Energy Dispersive X-ray Spectroscopy (EDS) technique allows for elemental analysis by detecting X-rays emitted from the sample.

Figure 3.4 — The interactions of the electron beam in a SEM with different signals that provide detailed information about the sample.

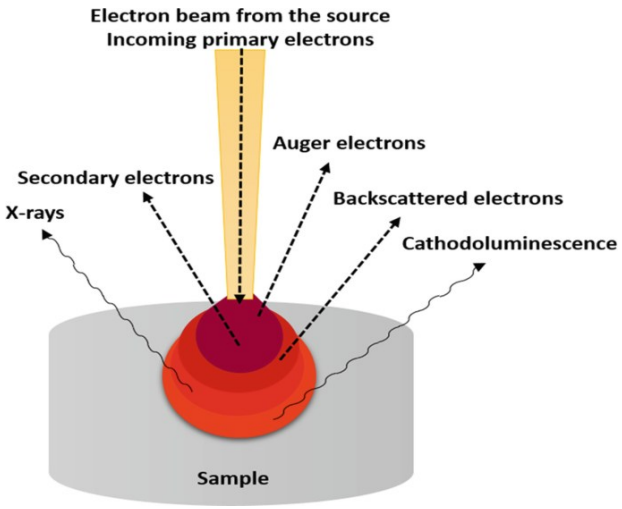

Source: Thermo Fisher (2024)

3.4.2 Sample Preparation, Data Acquisition and Recording

Sample preparation involved selecting three polished thin sections and defining the target area for analysis. These sections correspond to IF and dolostone

samples analyzed at the Scanning Electron Microscope Laboratory, University of Alberta (Canada) - Figure 3.5.

The analyses were performed using a Zeiss Sigma Field Emission SEM equipped with SE, BSE and CL detectors and a high-resolution Bruker dual detector energy dispersive X-ray spectroscopy (EDS) system.

Figure 3.5 — Scanning Electron Microscope Laboratory, University of Alberta (Canada)

Source: Scanning Electron Microscope Laboratory (2024)

3.5 Geochemical analyses

3.5.1 Principles

Geochemical analyses were performed to determine the abundance of major elements (e.g. Al_2O_3, CaO, Fe_2O_3, MgO) and trace elements, including REE + yttrium (Y) and RSE. Major elements are critical for characterizing compositional variations at high resolution within the studied section, identifying localized elemental enrichments or contaminations, and aiding in identifying minerals and processes involved in the formation and transformation of the rocks.

The REEY patterns are a valuable tool for investigating biochemical processes in ancient aquatic systems (Lawrence et al. 2006). For IF, the REEY signature can reflect the influence of hydrothermal fluids on seawater and indicate the primary source of Fe (Gross, 1993; Bekker et al., 2010). In contrast, RSE abundances (e.g., Cr, Mo, V, U) are typically indicative of a change in local redox conditions in paleo-watermass, potentially providing evidence of euxinic or

ferruginous conditions in the anoxic sinks or the oxygenation within the water column (Tostevin et al., 2020).

The analytical techniques employed for multielement chemical determination were inductively coupled plasma mass spectrometry (ICP-MS) or optical emission spectrometry (ICP-OES). Both techniques utilize high-temperature plasma, composed of argon – an inert gas for sample ionization. The plasma temperatures can reach approximately 8,0000 K, comparable to the surface temperature of the Sun. The main characteristics of each analytical technique are presented following:

ICP-MS – This technique operates on the principle that each element has a specific mass. After ionization, the ionized atoms are filtered based on their mass or mass-to-charge ratio (Tyler and Yvon, 1995). The concentration of the elements is directly measured by a mass spectrometer, with the intensity of the signal used for quantification (Figure 3.6). This method offers lower detection limits than other techniques, making it particularly suitable for trace element analysis (Olesik, 1991).

Figure 3.6 —The main components of an ICP-MS instrument

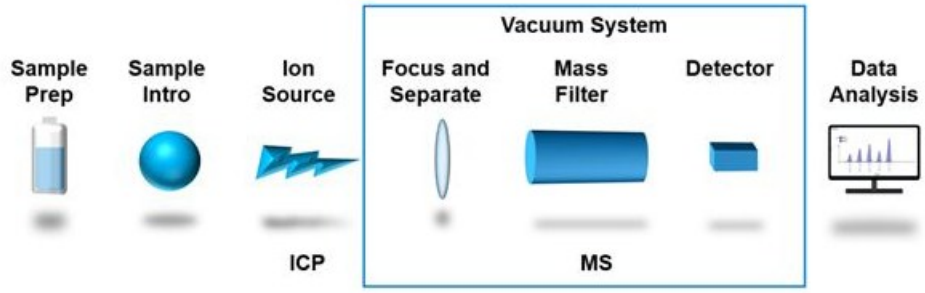

Source: Agilent Technologies (2024)

ICP-OES - This technique is based on the principle that atoms and ions absorb energy, causing their electrons to transition from a ground state to an excited state. When the electrons return to their lower energy state, electromagnetic radiation is emitted (Figure 3.7). The intensity of this emitted light is measured by an optical spectrometer, and elemental concentrations are determined through calibration curves

Figure 3.7 —Schematic representation of ICP-OES.

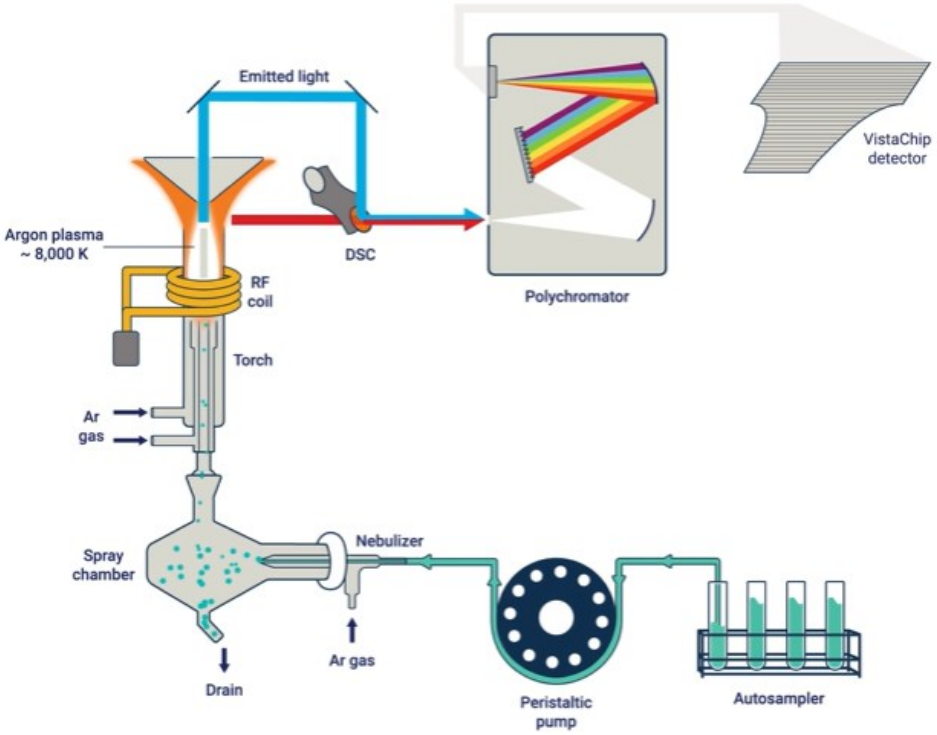

Source: Agilent Technologies (2024).

3.5.2 Sample Preparation, Data Acquisition and Recording

Sample preparation involved several steps: drying, crushing, homogenization, and pulverization using a ring and puck mill to achieve a 150# mesh size. The samples were pulverized using a Shatter Box at SPEX Sample Prep (Figure 3.8), University of Alberta, or in the Centro de Pesquisa Manoel Teixeira da Costa (CPMTC), Universidade Federal de Minas Gerais or at the Geosol Lab.

The powdered aliquots were subjected to digestion processes using lithium metaborate fusion or multi-acid digestion (nitric, hydrochloric, hydrofluoric, and perchloric acids). For the Total organic carbon (TOC) analysis, the samples were acidified through successive additions of 50 µL of 1M HCl, followed by overnight drying at 70°C.

A total of 84 samples of IF, phyllite, and carbonate rocks were analyzed at SGS Geosol Laboratory Ltd., Brazil, and 22 samples, by Bureau Veritas Mineral Laboratories, Canada. Loss on ignition (LOI) values were determined based on the

relative mass difference after heating the samples to 1000 °C. Analytical errors for most major oxides were below 5%, while errors for most trace elements ranged between 10% and 15%. The detection limit for major oxides is 0.01 wt.%. At the same time, trace elements range from 0.01 ppm to 20 ppm—for example, the lowest detection limit applies to certain rare earth elements such as lutetium (Lu). In contrast, the highest is associated with elements like nickel (Ni).

Figure 3.8— Sample preparation laboratory, University of Alberta

Source: Elaborated by the author.

Additionally, boron (B) abundance was analyzed in 12 phyllite samples at the University of Alberta using an ICP-MS/MS (Agilent 8800). The analytical deviation for these measurements was less than 5%. Total organic carbon (TOC) analysis for the same 12 samples was performed at the Natural Resources Analytical Laboratory, University of Alberta, Canada. The TOC abundance determination was obtained using a Thermo FLASH 2000 Organic Elemental Analyzer (analytical precision of 0.4 wt.% and detection limit for carbon is 0.10 wt.%).

3.6 Stable Isotopes (C-O-N)

Stable isotope analysis of carbon and oxygen is a tool for chemostratigraphy, offering insights into local and regional biogeochemical carbon cycles, the reconstruction of watermass conditions in ancient basins, and depositional and post-depositional processes (Sial et al., 2016; Caxito et al., 2019) On the other hand, the N-isotopic composition serves as a valuable proxy for reconstructing redox

conditions and primary productivity in marine environments (Thomazo et al., 2009; Stüeken et al., 2016; Wei et al., 2021; Pellerin et al., 2023).

3.6.1 Principles

Carbon and Oxygen

The principle assumes that chemical rocks such as carbonate rocks and BIF may retain a composition of the dissolved inorganic carbon (DIC) pool during the precipitation (Halverson et al., 2010). Oxygen isotopic composition is useful for identifying temperature-driven fractionation (Urey, 1947), providing insights into post-depositional processes that may alter the primary isotopic signature.

The preservation of the carbon-oxygen isotopic signature in Paleoproterozoic rocks has been investigated in BIF-hosted Fe systems worldwide, including regions in Australia, Brazil, Guinea, India, and South Africa (Hagemann et al., 2016, and references therein). Studies in the Quadrilátero Ferrífero by Hoefs et al. (1982), Bekker et al. (2003), Spier et al. (2007), Morgan et al. (2013), Hensler et al. (2017), Nogueira et al. (2019), and de Paula et al. (2023) have shown that these proxies are reliable tools for chemostratigraphy and paleoenvironmental reconstruction.

Nitrogen

Nitrogen abundance in sedimentary and metamorphic rocks can be determined because the molecule NH_4^+ can replace K^+ ions in the lattice structure of K-bearing minerals, such as biotite, muscovite, K-feldspar, plagioclase, by substituting for K^+ ions (Honma and Itihara 1981; Boyd and Philippot, 1998).

The N cycle is closely linked to bioproductivity, as autotrophic microorganisms realize nitrogen fixation from the atmosphere through photosynthetic activity (Thomazo et al., 2009). Additionally, the redox state of the ocean and atmosphere strongly influences the nitrogen cycle due to the redox reactivity of nitrogen species (Stüeken et al., 2016), (Figure 3.9).

Under oxic conditions, nitrate (NO_3^-), the most oxidized nitrogen species, is stabilized through nitrification, a process that results in significant isotopic fractionation (Thomazo et al., 2009). Nitrification occurs in the presence of free oxygen and takes place at higher redox potentials than ferric Fe or sulfate reduction, highlighting the sensitivity of nitrogen species to redox shifts (Stüeken et al., 2016).

However, the largest isotopic fractionation occurs during denitrification (Sigman et al., 2009). This process involves nitrate recycling through uptake or assimilation and/or the activity of heterotrophic bacteria under suboxic conditions, resulting in the enrichment of the heavy isotope in the ocean relative to atmospheric concentrations (Thomazo et al., 2009).

Figure 3.9 — Illustration of the reconstructed N- cycle across several geological times, highlighting the evolution of N-biogeochemical processes in Earth's history.

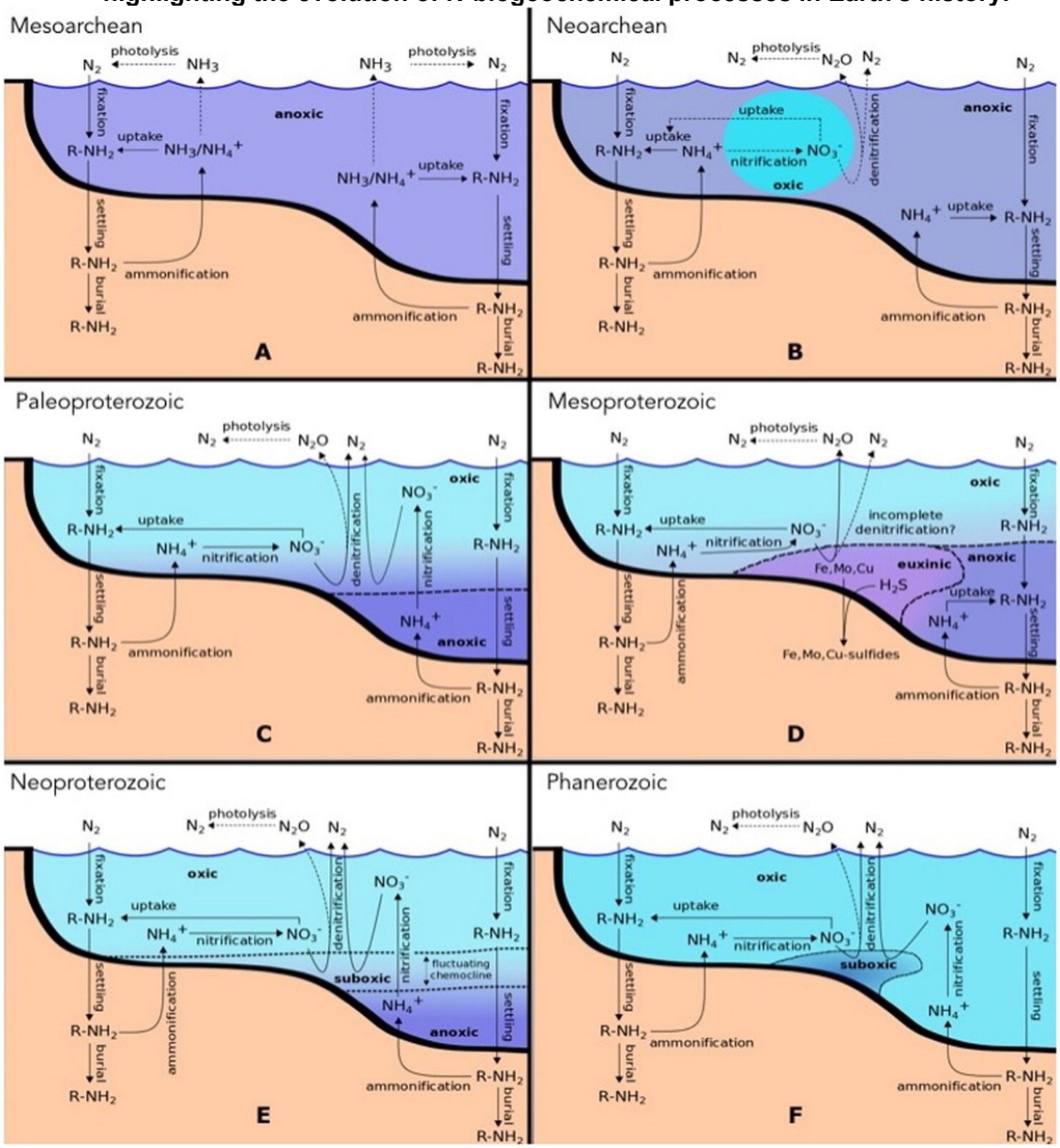

Source: Stüeken et al. 2016

3.6.2 Sample Preparation, Data Acquisition and Recording

Carbon and Oxygen

Seventy-six carbon and oxygen isotope measurements were obtained from dolomitic BIF and dolostones. Samples were collected from drill cores and field outcrops using a micro-drilling technique with a 4 mm diameter drill bit, ensuring avoidance of strongly deformed zones to mitigate the effects of metamorphism or other post-depositional alterations.

The C-O-isotopic ratio analyses were carried out in three laboratories: the NEG-LABISE Laboratory at the Federal University of Pernambuco (UFPE), the Geochemistry Laboratory at the Federal University of Ouro Preto (UFOP), and the Stable Isotope Laboratory at the University of Alberta, Canada.

At NEG-LABISE (UFPE) CO_2 gas extraction was performed using high-vacuum lines (Figure 3.10 A). Approximately 20 mg of powdered sample was reacted with 100% orthophosphoric acid at 25°C over three days, tailored to the Ca-Mg carbonate composition of the samples. The liberated CO_2 was analyzed for carbon and oxygen isotopic compositions using a Thermo Finnigan Delta V Advantage mass spectrometer.

Figure 3.10 — Different instruments for purification and extraction of C and O gases. A) high-vacuum lines (NEG-LABISE Laboratory) and B) online techniques (UFOP Geochemistry Laboratory).

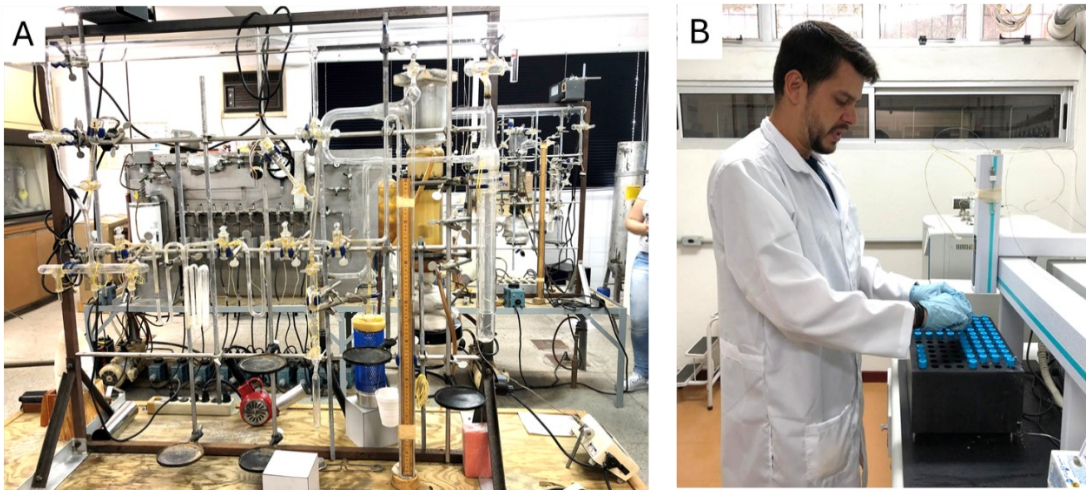

Source: Elaborated by the author

At the UFOP Geochemistry Laboratory, CO_2 extraction was performed online (Figure 3.10 B). In this method, 500 µg of powdered sample was reacted with 100% orthophosphoric acid at 72°C for one hour in a closed-tube system. The released CO_2 was analyzed using a Thermo Finnigan Delta V Advantage mass spectrometer coupled to a GasBench II system.

At the Stable Isotope Lab, the powdered samples were reacted with 100% orthophosphoric acid overnight at 50°C under a vacuum. The released CO2 gas, was cryogenically purified, collected and measured using the dual-inlet mode in a Thermo Finnigan MAT 253 isotope ratio mass spectrometer.

Isotopic ratios for carbon and oxygen are reported in δ-notation (‰) relative to the Vienna Pee Dee Belemnite (VPDB) standard. Measurement accuracy is better than ±0.1‰ for NEG-LABISE and UFOP and Stable Isotope Lab ±0.2‰.

Nitrogen

Twenty BIF samples, representing specific intervals (<5 cm) of finely banded IF from a drill core, were prepared for nitrogen extraction and isotopic analysis. Sample preparation involved pulverization with an agate mortar and pestle to achieve a uniform granulometry of <200 mesh.

The analyses were performed at the Stable Isotope Lab, University of Alberta, Canada (Figure 3.11), using a sealed-tube offline combustion method (Li et al., 2021). However, due to equipment maintenance, only partial results from 10 samples are presented in this study.

The procedure for N-extraction and analyses involves two combustion stages: the first at 1,200°C for 2 hours and the second at 900°C for 8 hours, followed by cooling at 600°C for 2 hours. A CUxOx reagent is added during the second combustion to remove contaminants like atmospheric nitrogen and organic matter while converting ammonium ($NH4^+$) into nitrogen gas (N_2). The quartz tube containing the sample is then connected to an analytical line under high vacuum, cracked to release the purified N_2, and cryogenically collected (Figure 3.12 and 3.13). The nitrogen is subsequently analyzed using a GasBench II interface and a Thermo MAT 253 isotope ratio mass spectrometer, with measurements performed at nitrogen concentrations.

Figure 3.11 — Equipment of the Stable Isotope Lab . A) instruments utilized for grinding the IF samples (< 200 mesh); B) Precision balance; C) Prepared samples; D) Custom-made ultrahigh-vacuum metal line (left side) and isotope ratio mass spectrometer (right side); E) GasBench II interface.

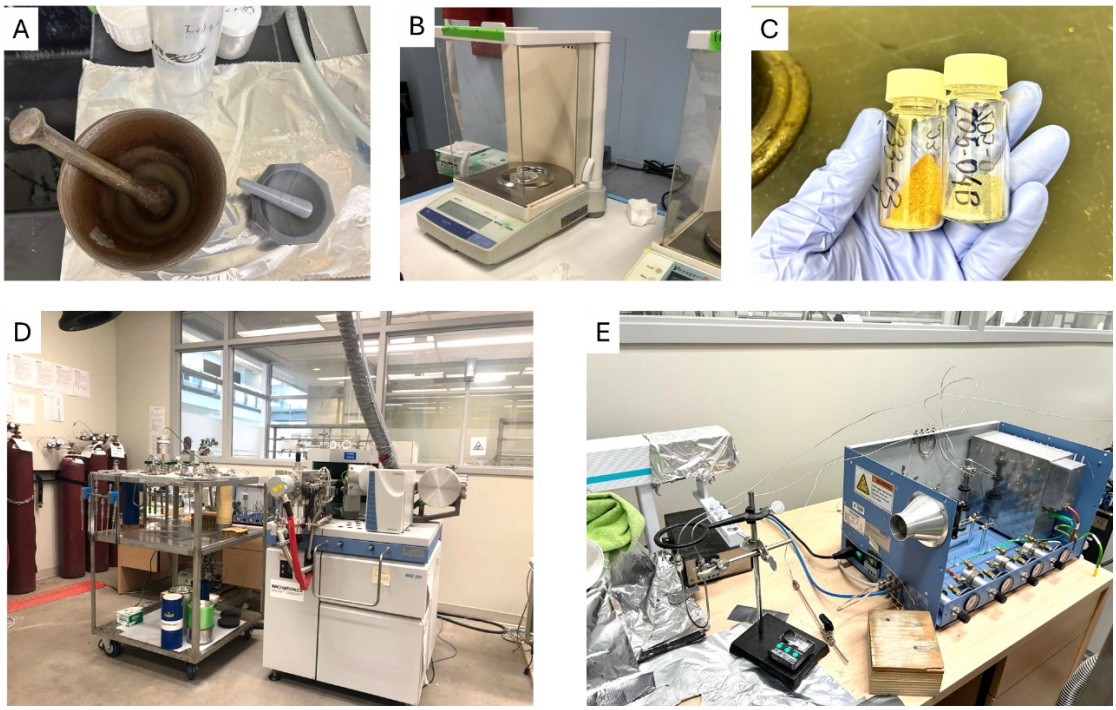

Source: Elaborated by the author

Figure 3.12 — Diagram of the manifold used for nitrogen extraction from combusted quartz tube for quantification and isotopic measurement.

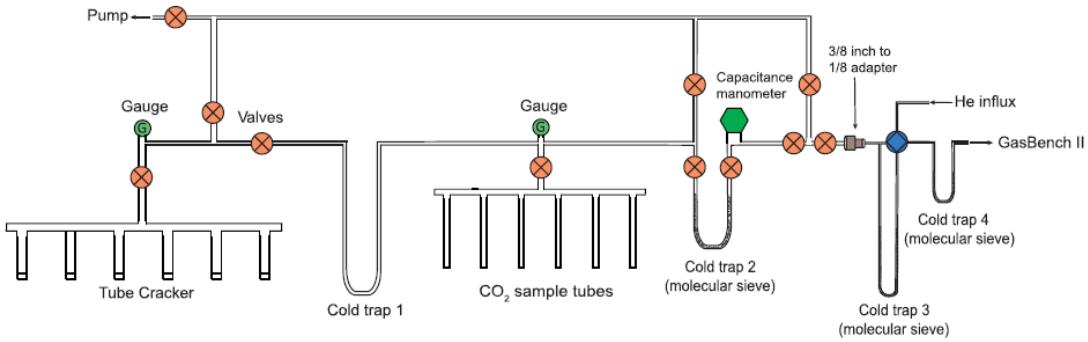

Source: Li et al., 2021

Figure 3.13 — The main steps for nitrogen extraction in the Stable Isotope Lab (sequential number 1 – 4).

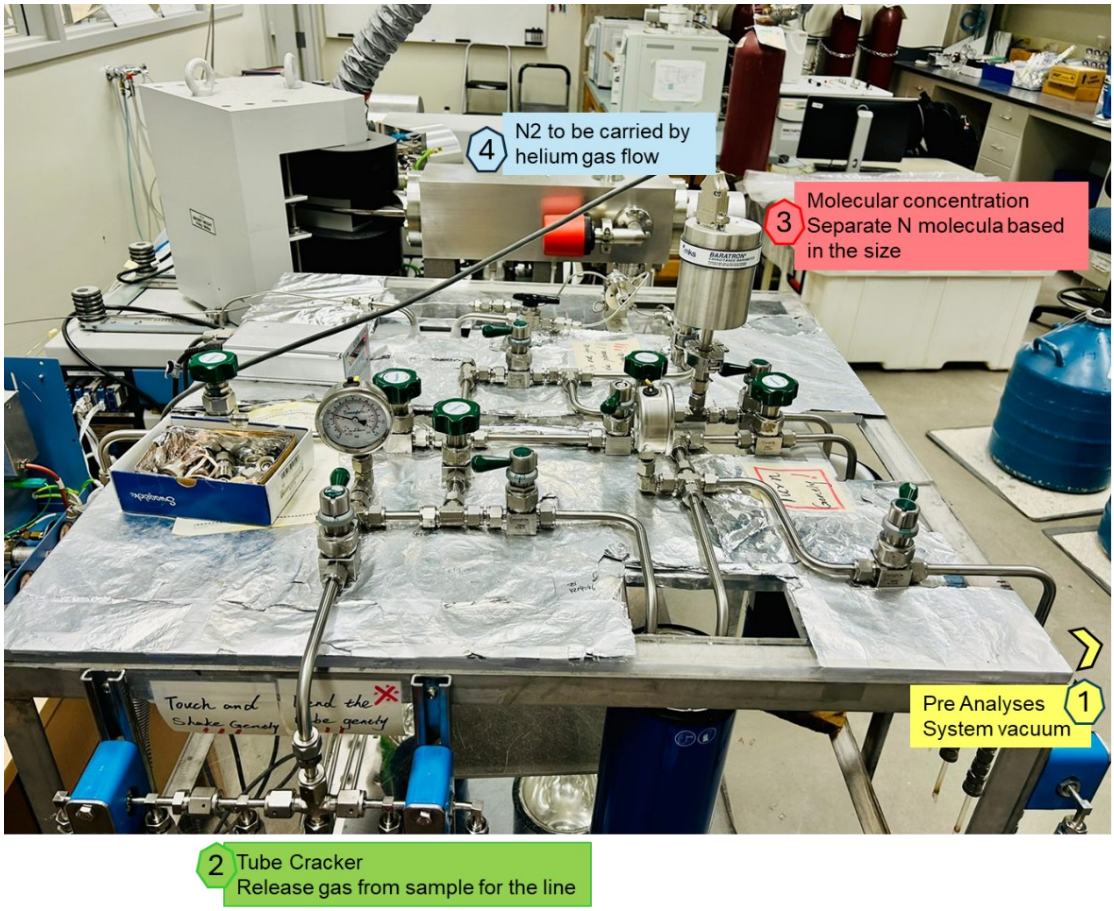

Source: Elaborated by the author

3.7 Iron Speciation

3.7.1 Principles

Iron speciation was employed as a paleoredox proxy to differentiate the oxidation state of ancient ocean bottom water directly above the sediments accumulated in the sedimentary basin (Tostevin and Mills, 2020). Anoxic conditions were prevalent during the Paleoproterozoic, with ferruginous environments dominating the oceans (Poulton and Canfield, 2011; Poulton, 2021) and the upwelling of Fe-rich deep waters was the primary source of highly reactive iron (Fe_{HR}) enrichment (Poulton and Canfield, 2011; Wood et al., 2015; Poulton et al., 2021).

The technique used for Fe speciation analyses determines the abundance of specific mineral phases, such as Fe-carbonates, Fe-oxides, Fe-sulfides, and Fe-silicates, in fine-grained siliciclastic marine rocks (Alcott et al., 2020; Poulton, 2021).

The abundance of highly reactive Fe (Fe_{HR}) is calculated as the sum of its fractions ($Fe_{HR} = Fe_{carb} + Fe_{ox} + Fe_{mag} + Fe_{py}$), while total Fe ($Fe_T$), includes unreactive forms, such as those found in Fe-silicates (Fe_U). The Fe_{HR}/Fe_T ratio differentiates anoxic from oxic environments, while the Fe_{py}/Fe_T ratio indicates the extent of sulfidic conditions, distinguishing ferruginous from euxinic settings (Poulton & Canfield, 2011) (Figure 3.14).

Figure 3.14 — Criteria for classification of redox conditions based on the contents of Fe_{HR}, Fe_T and Fe_{py}.

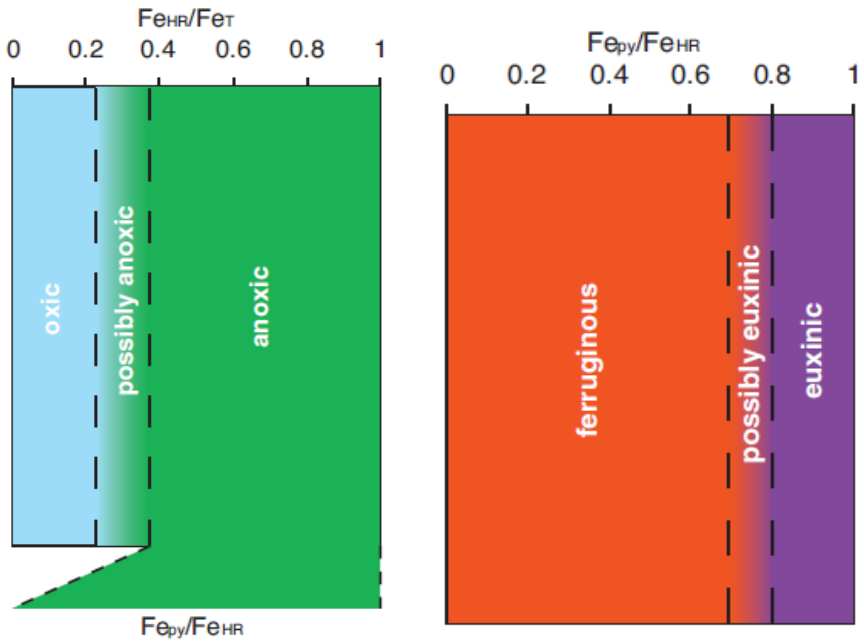

Source: Poulton & Canfield, 2011

3.7.2 Sample Preparation, Data Acquisition and Recording

In this study, twenty-four phyllite samples were analyzed at the Sedimentary Geochemistry Laboratory, Stanford Doerr School of Sustainability, to determine the iron-bearing mineral phases.

Sample preparation involved crushing with a ring and puck mill to achieve a clay-sized granulometry, conducted at the CPMTC laboratory, Universidade Federal de Minas Gerais. The sequential extraction methods followed the protocols established by Canfield et al. (1986), Poulton & Canfield (2005, 2011), and Alcott et al. (2020) (Table 3.4).

Table 3.4 — Protocol for the sequential extractions.

Method	Target phase	Terminology
Ia) Na acetate, pH 4.5, 48 h, 50 °C	Carbonate Fe, including siderite and ankerite	Fe_{carb}
Ib) Dithionite, 2 h	Ferric oxides, including ferrihydrite, haematite and goethite	Fe_{ox}
Ic) Oxalate, 6 h	Magnetite Fe	Fe_{mag}
II) Chromous chloride	Pyrite Fe	Fe_{py}
III) Boiling concentrated HCl	Reactive Fe, poorly reactive sheet silicate Fe	Fe_R, Fe_{prs}
IV) XRF	Total Fe, unreactive silicate Fe	Fe_T, Fe_U

Source: Alcott et al., 2020

The sequential extractions begin with the Fe_{car}, extracted using a 48-hour sodium acetate treatment at 50ºC, while Fe_{ox} was obtained through a 2-hour reaction with sodium dithionite at room temperature. Femag was isolated via a 6-hour ammonium oxalate reaction at room temperature, and Fe_{py} was determined using the chromium reduction of sulfur (CRS) method, following Canfield et al. (1986) (Figure 3.15). The Fe concentrations in each fraction were measured using the ferrozine spectrophotometric method (Stookey, 1970), whereas Fe_{py} was quantified through gravimetric analysis. For detailed procedures and precision estimates, refer to the Supplementary Material in Sperling et al. (2021). Total iron content (Fe_T) was analyzed by SGS Geosol, as previously described.

Figure 3.15 — Steps for Fepy extraction in the Sedimentary Geochemistry Laboratory: A) Weighing the sample. B) Preparation of CRS flasks, including acidification of the sample with 6N HCl. C) Experiment setup with the addition of nitrogen gases, to maintain an anoxic environment, condenser tube and tube for Fe-sulfide distillation. D) Addition of chromium chloride to initiate distillation. E) Take down of distillate followed by the addition of silver nitrate to precipitate pyrite. F) Pyrite precipitation.

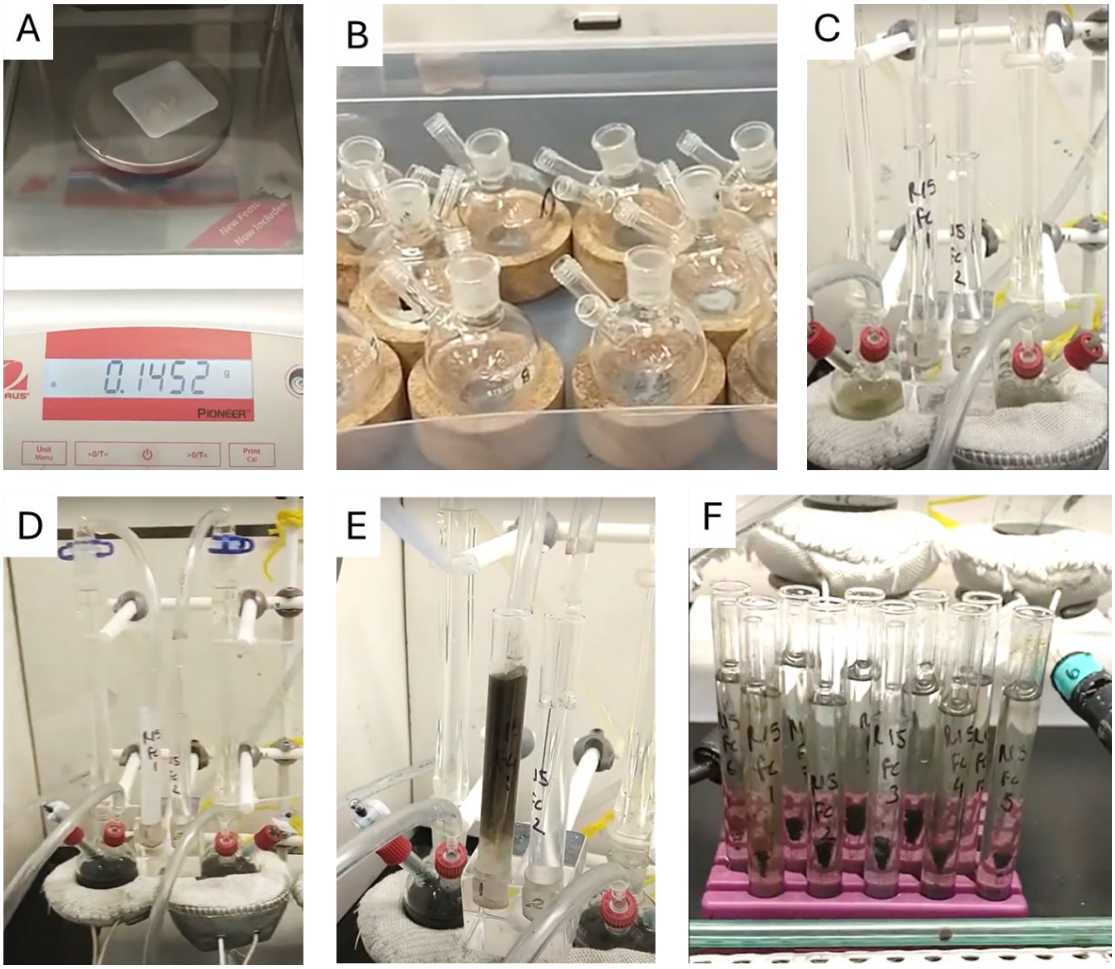

Source: https://www.youtube.com/watch?v=Z3pov90ibf0

4 SCIENTIFIC CONTRIBUTIONS I

This paper presents a lithostratigraphic revision of the chemical and sedimentary rocks located in the Segredo Mine, based on geological mapping and novel data, including elemental geochemistry, stable isotope ratios (C and O), and radiogenic isotopes (U-Pb). It was published by the Journal of South American Earth Sciences (https://doi.org/10.1016/j.jsames.2023.104525)

TRACE ELEMENTS, C-O ISOTOPES AND U-Pb GEOCHRONOLOGY OF THE MINAS SUPERGROUP IN THE SEGREDO DEPOSIT, QUADRILÁTERO FERRÍFERO, BRAZIL

Janaina Rodrigues De Paula[1]*, Fabricio A. Caxito[1], Alcides N. Sial[2], Diniz T. Ribeiro[3], Ana Ramalho Alkmim[4], Cristiano Lana[4] And Issamu Endo[4]

[1] Federal University of Minas Gerais, Belo Horizonte, Brazil, janainarpaula@gmail.com* and caxito@ufmg.br
[2] Federal University of Pernambuco – LABISE, Recife, Brazil, alcides.sial@ufpe.br
[3] Independent consultant, Belo Horizonte, Brazil, diniztribeiro@gmail.com
[4] Federal University of Ouro Preto, Ouro Preto, Brazil, ana_alkmim@yahoo.com.br, cristiano.lana@ufop.edu.br and issamu.endo@gmail.com
*Corresponding author.

4.1 Abstract

The metasedimentary succession of the Minas Supergroup in the Quadrilátero Ferrífero (QFe) region, eastern Brazil, contains important, up to 400m thick Lake Superior-type Banded Iron Formation (BIF) of the Cauê Formation. These are superposed by dolomitic carbonates of the Gandarela Formation, deposited ca. 2.4 Ga ago and thus probably registering the Great Oxygenation Event (GOE) of the Paleoproterozoic.

The Segredo BIF deposit is located in the SW part of the QFe. The structural complexity and the discontinuity of layers challenge local studies on the sedimentary evolution of the Minas Basin. In the Segredo deposit, the stratigraphic sequence of

the Minas Supergroup is exposed in the overturned limb of Fábrica Synform, that refold the Dom Bosco Synform.

Based on the geological mapping and the study of a 480-m deep drill core, a lithostratigraphic review of the area is proposed, with stacking of the Itabira, Piracicaba, Sabará and Itacolomi groups, from the bottom up.

The Itabira Group comprises BIF, intraformational metaconglomerate and dolostone with lateral and vertical interlayering. The chemical and isotopic data from the Cauê and Gandarela formations are defined by variations of the trace element and C-isotopic signatures. The intraformational metaconglomerate is interpreted as gravity flow products at the edges of the carbonate platform.

Dolomitic BIFs show positive Eu anomalies and low terrigenous content, thus confirming the contribution of seawater hydrothermal fluids during the precipitation of BIF and carbonates. Negative Ce anomalies reflect a locally oxygenated ocean during precipitation of the Gandarela Formation carbonates.

The carbon isotope stratigraphy is marked by $\delta^{13}C$ values from around -1.5‰ in the Cauê BIF and around 0‰ in the Gandarela dolomites, indicating normal seawater conditions and deposition probably before the global Lomagundi event. The negatively fractionated values obtained for the Cauê BIF are consistent with previous studies suggesting the operation of microbial Dissimilatory Iron Reduction as an important process in BIF formation.

Above the Gandarela carbonate rocks, the occurrence of the Sabará Group through an angular unconformity is for the first time confirmed in the region by the occurrence of detrital sedimentary facies and by U-Pb geochronological data (younger detrital zircon at ca. 2.1 Ga).

Keywords: Great Oxygenation Event (GOE), Carbon and Oxygen Isotope Stratigraphy, Paleoproterozoic BIF, Cauê Formation, Gandarela Formation, Detrital zircon U-Pb geochronology, São Francisco Craton

4.2 Introduction

Paleoproterozoic Banded Iron Formations record geochemical changes of the Earth's systems, mainly marked by the increase of atmospheric oxygen during the Great Oxygenation Event (GOE) at ca. 2.4 Ga. The GOE shows a permanent change in the concentration of atmospheric oxygen contents, in the volatile

composition of the atmosphere-ocean system and an increase of the oxidizing potential (Holland, 2006; Lyons et al., 2014). Increasing oxygen levels led to changes in atmospheric CH4/CO2 ratios and a decrease in greenhouse warming by CH4, H2S and H2 reduced gases (Pavlov et al., 2000; Kopp et al., 2005). Furthermore, Hoffman (2013) and Gumsley et al. (2017) postulated that the rise of atmospheric oxygen was not monotonic, but characterized by oscillations that may have contributed as triggers for climate instability and cyclical global glacial events.

A useful tool for understanding the prevailing geochemical conditions on ancient Earth is the application of stable isotopes, codified in ratios and presented as factors such as $\delta^{13}C$, $\delta^{53}Cr$, $\delta^{56}Fe$, $\delta^{18}O$ and $\delta^{33}S$. Stable isotope proxies contribute to determining stratigraphic correlations worldwide (Beukes et al., 1990; Veizer et al., 1992; Sial et al., 2000; Maheshwari et al., 2010). Although currently it has been well accepted that the C-isotopic data in chemically precipitated sediments echoes the original composition of seawater during sedimentary deposition (provided post-depositional alteration have not altered that signal), several discussions have also been conducted about the preservation of the original isotopic composition in Paleoproterozoic BIF (e.g., Veizer et al., 1989; Sial et al., 2000; Bekker et al., 2003; Morgan et al., 2013).

Another issue concerns the source of iron in the genesis of large BIF deposits during the Precambrian (Klein and Beukes, 1992; Bekker et al., 2010). Two main genetic models for BIF formation have been discussed. The first advocates mobilization of Fe under continental weathering conditions (Borchert, 1960). The second and more accepted model discussed by several authors (Isley, 1995; Barley et al., 1997) invokes an iron-rich hydrothermal solution generated at mid-ocean ridges through episodic magmatism related to intensified plume activity, testified by ancient Large Igneous Provinces (LIPs). LIPs contributed to increase the expansion rate of oceanic crust leading to the production of flood basalts, dike swarms and layered intrusions (Bekker et al., 2010) and could represent one of the main sources for dissolved ferrous iron for BIF deposition, as well as contribute to variations in the oceanic redox state (Isley and Abbott, 1999).

The world's largest Paleoproterozoic iron ore deposits are in Brazil, Australia, South Africa, Russia and Ukraine (Klein and Beukes, 1992). In Brazil, the main deposits are hosted in different BIFs which are significantly different in genesis and age, such as the Archean Algoma-type BIFs of the Carajás Province in northern

Brazil, the Paleoproterozoic Lake Superior-type deposits of the Quadrilátero Ferrífero (QFe) in southeastern Brazil, and the Neoproterozoic Rapitan-like iron formation of the Urucum district in western Brazil.

In the QFe, the Minas Supergroup records a passive margin setting, starting with a regional marine transgression stage and superposed by a foreland cycle of the Minas Basin (Dorr, 1969; Alkmim and Marshak, 1998; Canuto, 2010; Gonçalves and Uhlein, 2022). The BIF deposits hosted at Itabira Group were interpreted by Gonçalves and Uhlein (2022) as a part of a first depositional sequence of the Minas Basin formed by transgressive and highstand system tracts. The Itabira Group is composed of BIF from the Cauê Formation overlain by carbonate rocks belonging the Gandarela Formation. The metasedimentary succession has experienced greenschist facies metamorphism and deformation related to Rhyacian (ca. 2.0 Ga) and Ediacaran/Cambrian (Brasiliano, ca. 0.5 Ga) orogenesis (e.g., Marshak and Alkmim, 1989).

The Segredo deposit in the SW QFe (Figure 4.1) offers opportunities to increase the geological understanding of the province, specifically by considering its structural and stratigraphic features. In this study, we propose a lithostratigraphic review of the Segredo deposit based on mapping, chemostratigraphy (trace elements and C-O isotopes) and geochronological (detrital zircon) data obtained from a 480 meters deep drill core. Finally, in the light of new chemical and geochronological results obtained in this work, we expect to contribute to the knowledge of environmental reconstruction of the Minas Basin and the changes of oxidation state of the atmosphere–ocean system over Paleoproterozoic time.

4.3 Geological Setting

Regional Geology

The QFe, located in southeastern Brazil, is an important polymetallic province and contains economically important deposits of gold, iron and manganese. The regional geomorphological features exhibit an approximately square geometric arrangement framed by Paleoproterozoic BIF (Figure 4.1). The metallogenic district is situated at the southernmost São Francisco Craton (Almeida, 1977), where four regional lithostratigraphic units are recognized (Figure 4.2): i) Metamorphic

Complex: Archean gneisses, migmatites and granitoids; ii) Rio das Velhas Supergroup: Archean greenstone belt; iii) Minas Supergroup: Paleoproterozoic rocks composed of clastic and chemical metasedimentary rocks; and iv) Itacolomi Group: Paleoproterozoic supracrustal sequence of rudaceous and arenaceous metasedimentary rocks.

Figure 4.1 — Location of Segredo mine in the geologic map of the Quadrilátero Ferrífero.

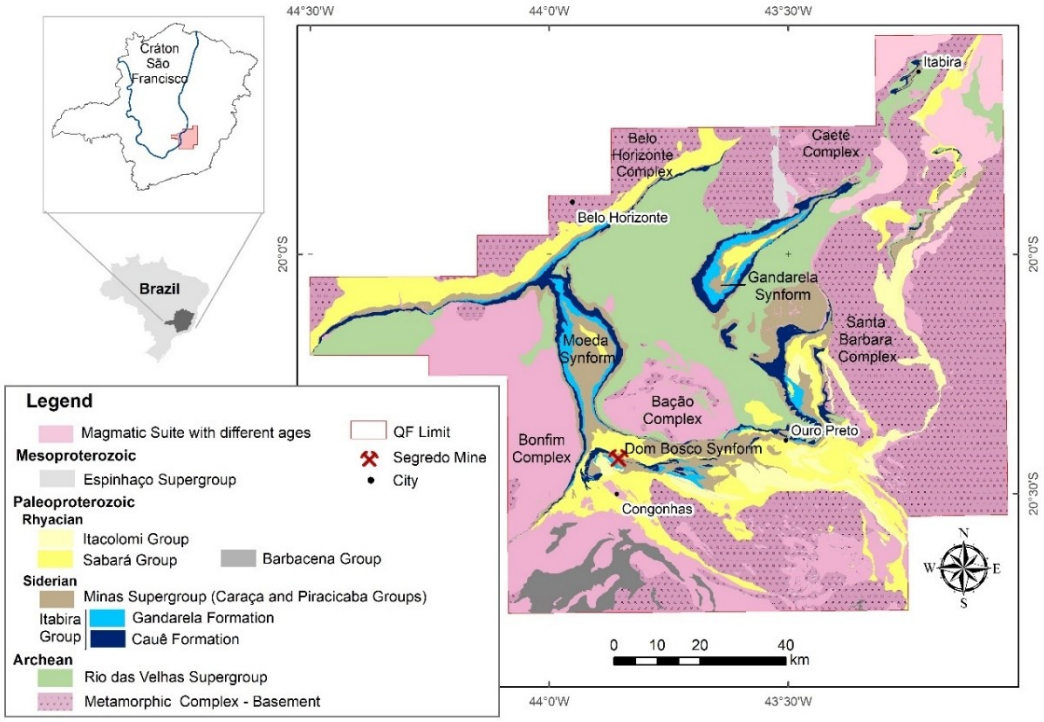

Source: modified from Endo et al., 2019

The Minas Supergroup comprises metasedimentary rocks, approximately 6 km thick (Alkmim and Marshak, 1998), deposited from ca. 2550 to 2100 Ma (Renger et al., 1994; Machado et al., 1996; Babinski et al., 1995; Hartmann et al., 2006; Mendes et al., 2014). The initial opening of the basin is marked by the intrusion of the Lavras dyke swarm at ca. 2.55 Ga (Caxito et al., 2020). The sedimentary rocks unconformably overlie the Archean basement and record a complete Wilson Cycle (Alkmim and Marshak, 1998). As a consequence, the stages of evolution of the Minas basin include the installation of passive margin followed by the development of syn-orogenic basin during a Rhyacian accretionary orogeny (Alkmim and Marshak, 1998; Canuto, 2010).

The QFe was subjected to a complex deformation pattern, with superposition of at least two orogenic events: i) Rhyacian Orogeny, acting from 2.1 to 1.8 Ga, and ii) Brasiliano Orogeny, comprising the period between 0.63 and 0.56 Ga. Regional metamorphism ranges from greenschist to amphibolite facies (Herz, 1978; Hoefs et al., 1982; Pires and Bertolino, 1991; Neri, 2012).

Figure 4.2 — Stratigraphic column of the Minas Supergroup. References for ages are from: (i) Machado et al. (1992) (younger detrital zircon U-Pb age) and (ii) Babinski et al. (1995) (Pb-Pb whole-rock isochron).

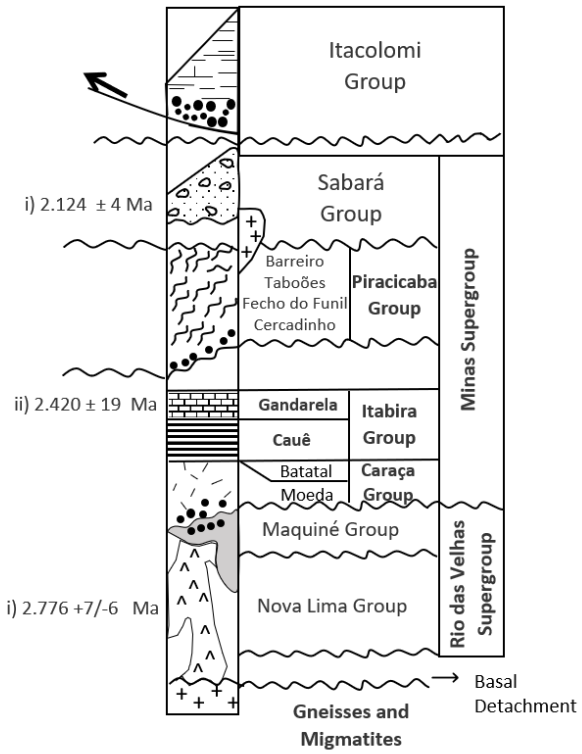

Source: modified from Dorr (1969), Renger et al. (1994); Rosière et al. (2008) and Morgan et al. (2013)

Segredo Deposit Geology

The Segredo BIF deposit, located in the southwest QFe (Figure 4.1), comprises part of an allochthonous succession placed between the Dom Bosco and Moeda synclines (Dorr, 1969; Endo et al., 2019). The lithostratigraphic record, from the bottom up, of the Itabira, Piracicaba, Sabará and Itacolomi groups is recognized (Figure 4.3), but some lithostratigraphic uncertainties remain under discussion (e.g., Guild et al., 1957; Endo et al., 2019).

Figure 4.3 — Geological map of the Segredo deposit and region, showing the lithostratigraphy of the Fábrica Synform.

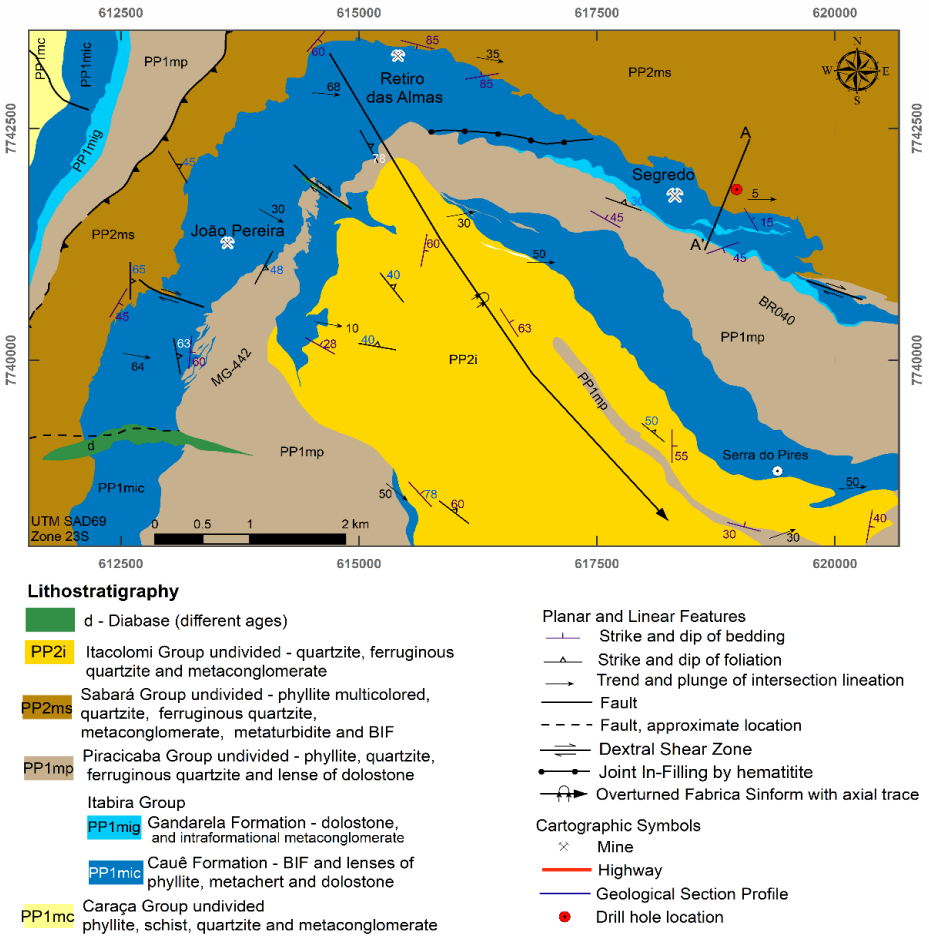

Source: modified from Endo et al., 2019

The Caraça Group, the basal unit of the Minas Supergroup, is a siliciclastic succession subdivided into the Moeda Formation, composed of quartzites and phyllites and the Batatal Formation, represented by phyllites and quartz-muscovite schist with minor black shale lenses (Dorr, 1969). The unit is restricted to the extreme west of Figure 4.3.

The Itabira Group conformably overlies the Caraça Group and is dominantly composed of chemical sedimentary rocks, subdivided into the Cauê and Gandarela formations (Dorr, 1969). It is distributed throughout the study area along the structural framework and in the extreme eastern part. The basal unit, Cauê Formation, is mainly composed of metamorphosed quartz-rich, dolomitic and amphibolitic BIFs known as quartz itabirites, dolomitic itabirites and amphibolitic itabirites, respectively and it has economic importance due to the supergene iron

enrichment. Lenses of phyllite, metachert and dolostone are common. The thickness of the BIF ranges from 100 to 900 meters, the maximum thickness being found in the hinge zone of regional-scale folds (Figure 4.3). Furthermore, the variation in thickness is due both to syn-depositional factors and the high degree of deformation. In the eastern part of the Segredo deposit, the proto-ore is dolomitic BIF intercalated with dolostone in a structurally controlled system, and its main supergene products include high-grade iron ore (> 64% wt. Fe_2O_3). Through a lateral and vertical transition lies the Gandarela Formation, which consists mostly of carbonate rocks, predominantly of dolomitic composition. An unsolved issue is the delimitation of these two formations, due to the intergradational characteristic and the effects of weathering on their contact zone.

The Piracicaba Group is characterized by shallow to deep sea metasedimentary rocks overlying the Itabira Group over an erosional unconformity (Dorr, 1969). It has significant spatial distribution and continuity in the Segredo deposit. It comprises grey phyllite, quartzite, ferruginous quartzite, iron formation and dolostone lenses from Cercadinho formation.

The Sabará Group is positioned on top of the Minas Supergroup and overlies the Piracicaba Group through an erosive surface. The clastic metasedimentary rocks of the Sabará Group represent flysch-type deposits (Alkmim and Marshak, 1998). In the Segredo deposit, this unit is predominant at the northern part of the Fábrica Synform. The lithotypes are composed of phyllite, chlorite-schist, quartz-schist, metagreywacke, metaconglomerate, quartzite, metadiamictite, and BIF (Almeida et al., 2005). The metaconglomerate exhibits granite and gneiss pebbles, indicating important changes in paleogeography, with the emergence of new source areas, increased erosion and transport gradient (Renger et al., 1994). There is still no consensus on the extension of the unit in the region.

The younger unit, the Itacolomi Group, overlies the lower units through an angular unconformity (Dorr, 1969) and it is located in the southern part of Fábrica Synform. The sedimentary rocks represent erosion of the Minas Supergroup and re-deposition in a marine to continental environment (Dorr, 1969). Quartzite and ferruginous quartzite are common, while lenticular phyllites and metaconglomerates occur in restricted areas.

Subsequent studies conducted by Endo et al. (2019) grouped the younger units (Sabará and Itacolomi groups) into the Estrada Real Supergroup. This was

proposed in the geological map of Endo et al., (2019) and will be clarified in future investigations.

Normally, the Paleoproterozoic rocks are partially covered by Cenozoic sediments or by a thick layer of weathered rock that can reach hundreds of meters.

The origin and tectonic evolution of the Segredo deposit are still the subject of debate by several authors (e.g., Trzaskos et al., 2011; Endo et al., 2019). Despite the different evolution models, it is a matter of consensus that the region is defined by a km-scale fold called Fábrica Synform (Figures 4.3 and 4.4), that refolds the Dom Bosco Synform (e.g., Endo et al., 2019).

Figure 4.4 — Schematic profile of the Fábrica Synform (refolding Dom Bosco Synform) where, Segredo deposit (SEG) is situated in the inverse limb, the João Pereira mine (JPE) is located in the normal limb with the hinge zone in Retiro das Almas region.

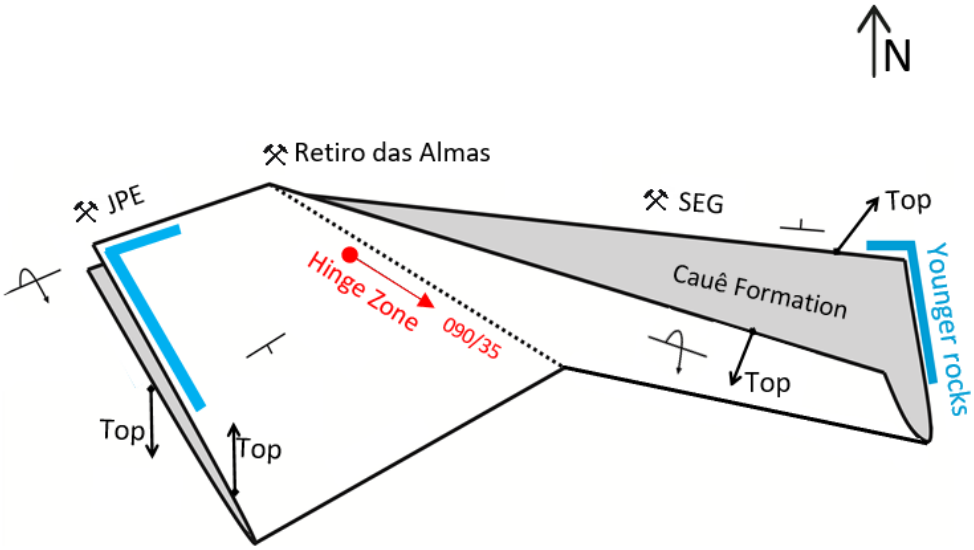

Source: modified from Endo et al., 2019

This structural framework contains an asymmetric fold with the hinge line dipping towards E (095/35) and verging SW. The fold geometry (Figure 4.4) exhibits the overturned limb of the Fábrica Synform in the Segredo deposit. Consequently, the Paleoproterozoic units are arranged in an inverted stratigraphic sequence. The bedding plane strikes to ESE and dip 30° to the NNE or sub vertical. The hinge is exposed in Retiro das Almas region. The normal limb of the Fábrica Synform is in the João Pereira (JPE) mine, where the direction of the layers inflects to NE-SW. The rocks show penetrative regional schistosity.

4.4 Sampling and analytical Methods

4.4.1 Drill Core Samples

A 480 meters deep drill hole (FDSP0046) was selected for sampling in the Segredo deposit. The drill core intercepts an overturned lithostratigraphic sequence of Minas Supergroup. At 110 meters, the rocks are well preserved from weathering, and black shale, intraformational metaconglomerate, dolostone, dolomitic BIF, metaconglomerate, phyllite and quartzite have been identified (Figure 4.5). The rocks were submitted to greenschist facies metamorphism and, in parts of the drill core, subsequently hydrothermally altered (e.g., carbonation). Samples selected for geochemical and isotopic analysis avoided those hydrothermally areas, unless specified otherwise. Sixty-four samples were selected for petrographic, chemical and geochronological analysis.

Figure 4.5 A — Regional NNE-SSE cross section of the Segredo deposit demonstrating the inverse stratigraphy succession. The red polygon delimits the area from figure 3.5 - B, where detailed cross section and the black line indicates the studied drill hole. Key: PP2ms – Sabará Group undivided, conglomerate (co), quartzite (qt), phyllite (phy); PP1mic – Cauê Formation, hematite (he), dolomitic BIF (BIF), dolostone (do); PP1mig – Gandarela Formation: dolostone, intraformational metaconglomerate (imc) e manganese zone (mn) e PP1mip – Piracicaba Group: phyllite and quartzite.

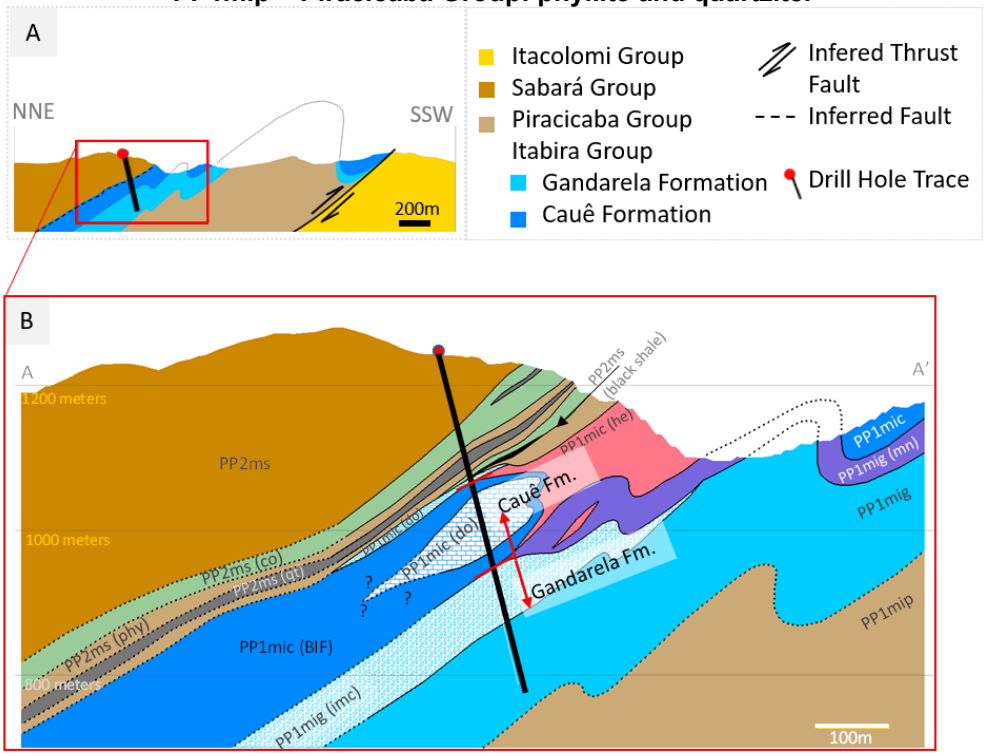

Source: Elaborated by the author

4.4.2 Analytical Methods

A total of 29 thin polished sections from the drill hole were studied by optical microscopy (Zeiss, model Imager Z1 - reflected and transmitted light). Analyses of microstructures and mineral composition were performed on four thin sections through a HITACHI SU3500 SEM (scanning electron microscopy). The images were obtained by Back-Scattering Electron Technique (BSE) with a 20.0 kV beam at the CDM - Vale Mineralogy Laboratory, Minas Gerais, Brazil.

For qualitative analysis of the mineral phases, 11 samples were analyzed by X-ray diffraction. The Bruker D8 Advance diffractometer with Linxeye XE cobalt radiation detector was used through the powder method in the CDM - Vale Mineralogy Laboratory. The collected diffractograms were treated by Diffrac.EVA software and database, PDF2-2003.

Major, trace and rare earth elements analysis were conducted at the SGS Geosol Laboratory Ltd., Minas Gerais, Brazil. A total of 22 samples were analyzed for major oxide and trace elements by ICP-MS or ICP-OES after fusion with lithium metaborate or multi acid digestion (nitric, hydrochloric, hydrofluoric and perchloric acid). The volatile content (Loss On Ignition - LOI) was determined by the mass difference after ignition at 1000 °C. Analytical errors are within 5% for most of the major oxides and 10–15% for most of the trace and rare earth elements.

Stable isotope analyses of C and O were performed on 74 aliquots of dolomite from dolostone, intraformational metaconglomerate (clast and matrix) and dolomitic rich layers of the BIF, as well as 05 samples of dolomite from hydrothermal veins. Samples were collected at each five meters. The pulverized material was collected through micro-drilling (4mm diameter drill) in the selected areas (e.g., banding, clasts, matrix or veins). The analyses were conducted at the NEG-LABISE Laboratory at the Federal University of Pernambuco (UFPE/Brazil). For extraction of CO2 gas in a high vacuum line, 20 mg of powdered carbonates were attacked with 100% orthophosphoric acid at 25°C for three days. The duration of the reaction is due to the Ca-Mg carbonate composition of most samples. The obtained CO_2 gas was analyzed for O and C isotopes in a ThermoFinnigan Delta V Advantage mass spectrometer. Results are expressed in the notation δ in permil (‰) relative to the Vienna Pee Dee Belemnite (VPDB) standard, with accuracy better than ± 0.1‰.

For detrital zircon dating, samples were collected from different intervals of metaconglomerate (drill hole depth ranges: 106.05 to 106.23, 114.53 to 114.85, 117.15 to 117.50 and 146.20 to 146.42 meters deep). Nearly 65 zircon grains were acquired through heavy mineral concentration at the SEPURA laboratory, CPMTC Research Center, at the Federal University of Minas Gerais (UFMG/Brazil). The analysis of cathodoluminescence images enabled the investigation of internal structures of the zircon grains. Uranium-Pb isotope determinations by LA-SF-ICP-MS, in a ThermoFinningan Element 2 coupled to a CETAC laser 213nm, were carried out at the laboratories of the Federal University of Ouro Preto (UFOP/Brazil). For the complete U-Pb analytical procedures followed in this study and machine parameters, see Lana et al. (2017).

4.5 Results

4.5.1 Local Geology

The Paleoproterozoic succession at the Segredo deposit integrates an overturned limb of the Fábrica Synform, where the overturned stratigraphic succession strikes to ESE and dips towards NNE. The cross-section (Figures 4.3 and 4.5) shows a 30° dip of the stratigraphy to the NNE. The weathering horizon can be about 300 m deep.

The Minas Supergroup succession is incomplete at the Fábrica Synform, due to the absence of the basal unit, the Caraça Group. The base of Itabira Group comprises the Cauê Formation sedimentary rocks, characterized principally by BIF, although dolostone, chert and phyllite lenses are observed. Compositionally, different BIF types are recognized: hematitite (hard hematite), quartz-itabirite (Figure 4.6A), dolomite-quartz-itabirite and dolomitic itabirite. The main supergenic product corresponds to friable iron ore, where the quartz content is lower (<5%) and Ca-Mg carbonates are absent.

Figure 4.6 A — Folded quartz-itabirite layers from Cauê Formation; B - Drill core sample of brecciated dolostone; C – Intraformational metaconglomerate with cobble of carbonates immersed in matrix ferruginous and carbonate; D – Different shapes and size of carbonate clasts in matrix-supported conglomerate (intraformational metaconglomerate); highlighted dolostone megaclast; E - Matrix-supported metaconglomerate with diversified and deformed clasts associated with the Sabará Group; F - Drill core sample of metaconglomerates imbricated clasts of quartzite (black lines) and BIF (red lines) from Itacolomi Group.

Source: Elaborated by the author

In a transitional contact, the chemical sedimentary rocks of Gandarela Formation are gradually interlayered with the Cauê BIF, both laterally and vertically. Apart from that, the contact is generally covered by sediments of Cenozoic basins that can reach 150 meters thick. Dolostone (Figure 4.6B) and intraformational

metaconglomerate (Figures 4.6C and 4.6D) comprise the Gandarela Formation. Besides these, irregular layers of dolomitic phyllite and manganesiferous phyllite are recognized. Its main weathering products have different levels of iron hydroxide, quartz and aluminosilicates, but the presence of Mn oxides is common and characterizes a typical brown color known as "coffee grounds" (“borra de café”). Locally, the discontinuity of carbonate layers promotes an unconformable contact between BIF (Cauê Formation) and metasedimentary rocks of the Piracicaba Group.

The Piracicaba Group displays wide areal distribution and consists of monotonous sericitic phyllite strata with rare quartzite, ferruginous quartzite and dolostone. Unfortunately, the metasedimentary rocks are severely weathered.

The upper part of Minas Supergroup stratigraphy, related to the Sabará Group, is restricted to the N-NE portion of the Segredo deposit, and it overlies the Cauê Formation through an unconformity. Lithologies are composed by green phyllite, quartzite, ferruginous quartzite and polymictic metaconglomerate constitute this unit. Phyllite is a characteristic rock of the group, and when not weathered, it shows green color due to the presence of chlorite. In fact, the lithostratigraphic classification of this phyllite is difficult, because it is a common rock of both the Sabará and Piracicaba groups and their weathered products are very similar. For these reasons, the polymictic metaconglomerate is used as guide for the definition of the Sabará Group. In many places, polymictic metaconglomerate is matrix-supported, poorly sorted and shows deformed clasts of quartzite, BIF, granite and gneiss (Figure 4.6E) immersed in a fine-grained matrix.

The younger unit in the area is characterized by the clastic sedimentary rocks of Itacolomi Group, restricted to the southern portion of the Segredo deposit. The clastic sedimentary rocks unconformably overlie the Piracicaba Group. The most abundant rock is quartzite and, locally, minor lenses of phyllite and monomict metaconglomerate are observed (Figure 4.6F).

4.5.2 Petrography

The drill hole intercepts the overturned limb of Segredo deposit, where the part of the lithostratigraphic succession of Minas Supergroup was recognized. Figures 4.7A and B shows two lithological domains defined as: i) clastic and ii) chemical (dolomitic BIF and dolostone).

Figure 4.7 — A) Stratigraphic column of the Itabira Group, drill hole FDSP0046 (Segredo iron deposit), with plots of C and O isotopes, Al2O3, Fe2O3, SiO2 and Mg/Ca ratios. Abbreviations for grain-size scale: (M) mud, (S) sand and (G) gravel. B) Section showing the succession exposed at the overturned limb of Fábrica Synform, intercepted by the studied drill hole. The position of the section shown in the previous figure is indicated, as well as the stratigraphic location of the detrital zircon sample shown in Figure 3.15.

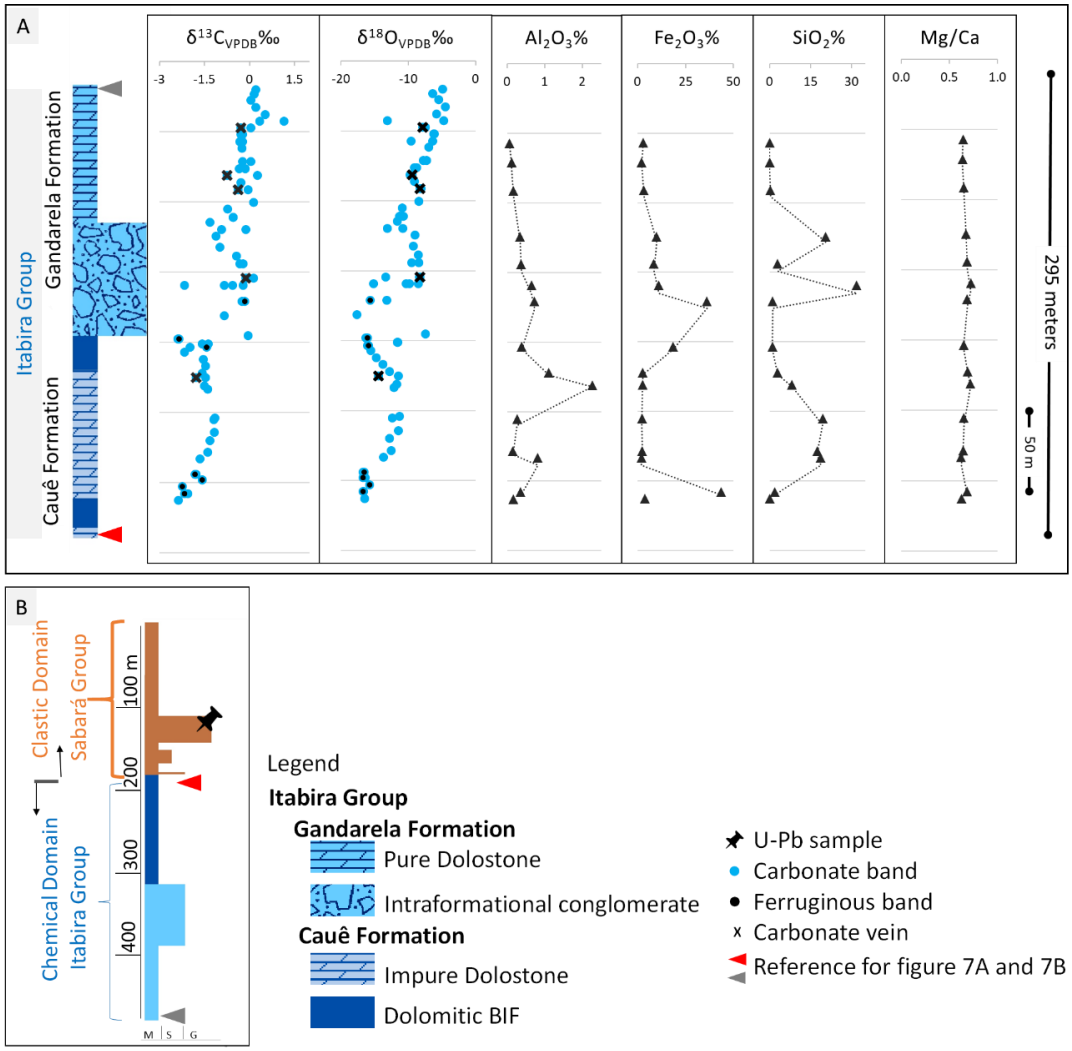

Source: Elaborated by the author

4.5.2.1 Clastic Domain

The clastic domain is predominantly composed of phyllite reaching 185m thick (Figure 4.7B), where approximately 60% is weathered. The mineralogy consists mainly of chlorite, quartz and muscovite (Figure 4.8A). The green phyllite layer displays uniform color, fine lamination, lepidoblastic texture and pervasive schistosity. Discrete levels of oligomictic metaconglomerate with quartzite fragments are interbedded. Two folding phases are recognized, with a crenulation cleavage, pressure shadows and associated quartz veinlets.

Figure 4.8 — X-ray diffraction analysis. A) clastic domain represented by phyllite (sample A005) composed mainly of chlorite, muscovite and quartz and B) chemical domain with dolomite as the main phase (samples: A011, A022, A023, A026, A029, A031, A035, A060 and A063).

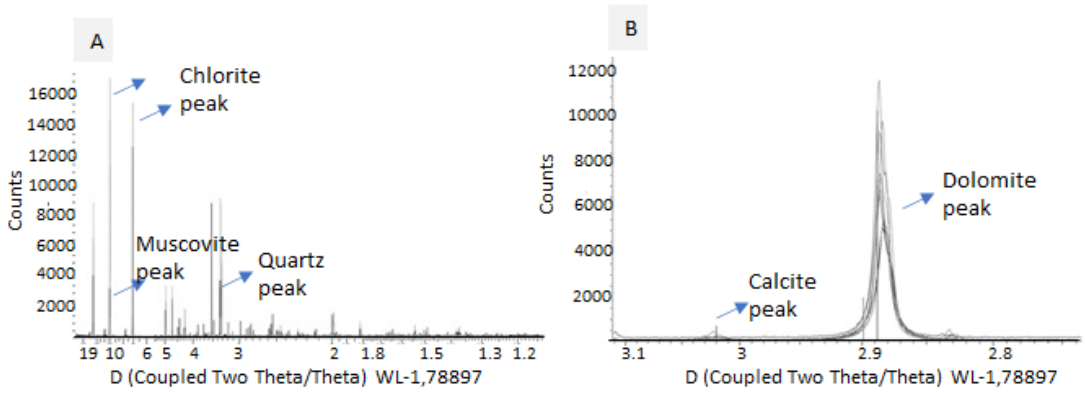

Source: Elaborated by the author

From 114 m, the drill core exhibits a 30-meter-thick matrix-supported metaconglomerate (Figures 4.9A and 4.9B) with rounded and low-sphericity clasts composed mostly of quartzite, although BIF clasts and other lithic fragments are found elsewhere (Figures 4.9 A and B). The clasts are poorly sorted, and the size ranges from sand to pebble, occasionally larger than the diameter of the drill core (6.3 cm). The matrix maintains the same composition and texture of green phyllite. Crenulated lepidoblastic texture is pervasive in the interval.

Phyllite with magnetite porphyroblasts occurs over an angular discordance at 145m depth (Figures 4.9 C and D). Fine lamination is formed by the alternation of chlorite-rich phyllite and quartz-rich laminae. Porphyroblasts of euhedral magnetite with millimetre size with pressure shadow and discrete rutile grains are found. Deformational structures such as crenulated to anastomosed foliation are displayed.

An impure quartzite bed (17 meters thick) occurs interleaved with the phyllite (Figure 4.7B), where gradational contact is observed. The rock is mainly composed of coarse-grained quartz and chlorite-rich laminae exhibiting a planar foliation.

Up to 290m, there are discrete lenses of matrix-supported metaconglomerate (maximum thick 2 meters). Generally, marked by gradational appearance of gravel to sand-size clasts, composed by quartzite and conglomeratic quartzite, immersed in a quartz-chlorite-phyllite matrix.

Finally, the last part of the clastic domain comprises a thin black shale stratum (0.65 meters thick) over the metaconglomerate through an angular discordance (Figures 4.9 E and F). Mineralogically, the black shale is composed by carbonaceous

matter, and it shows a brecciated texture. Quartz and muscovite fill the fragment's interstices and disseminated microcrystals of kaolinite, chlorite, goethite, hematite, Ti oxide and pyrite occur as accessory phases. The fractures are filled by quartz with granoblastic texture and Fe-hydroxide.

Figure 4.9 —A) Drill core of metaconglomerate (132m depth); B) Photomicrograph of crenulated matrix composed by chlorite (clo) and quartz (qtz). Cross-polarized transmitted light. C) Chlorite-phyllite (174m depth); D) Photomicrograph of magnetite porphyroblast (mag) and rutile (rut). Reflected light. E) Contact of phyllite, quartz vein and black shale; F) Monazite (mnz), kaolinite (cau), chlorite (clo), iron hydroxide (hid Fe), quartz (qtz), titanium oxide (ox Ti) in black shale layer (SEM–EDX).

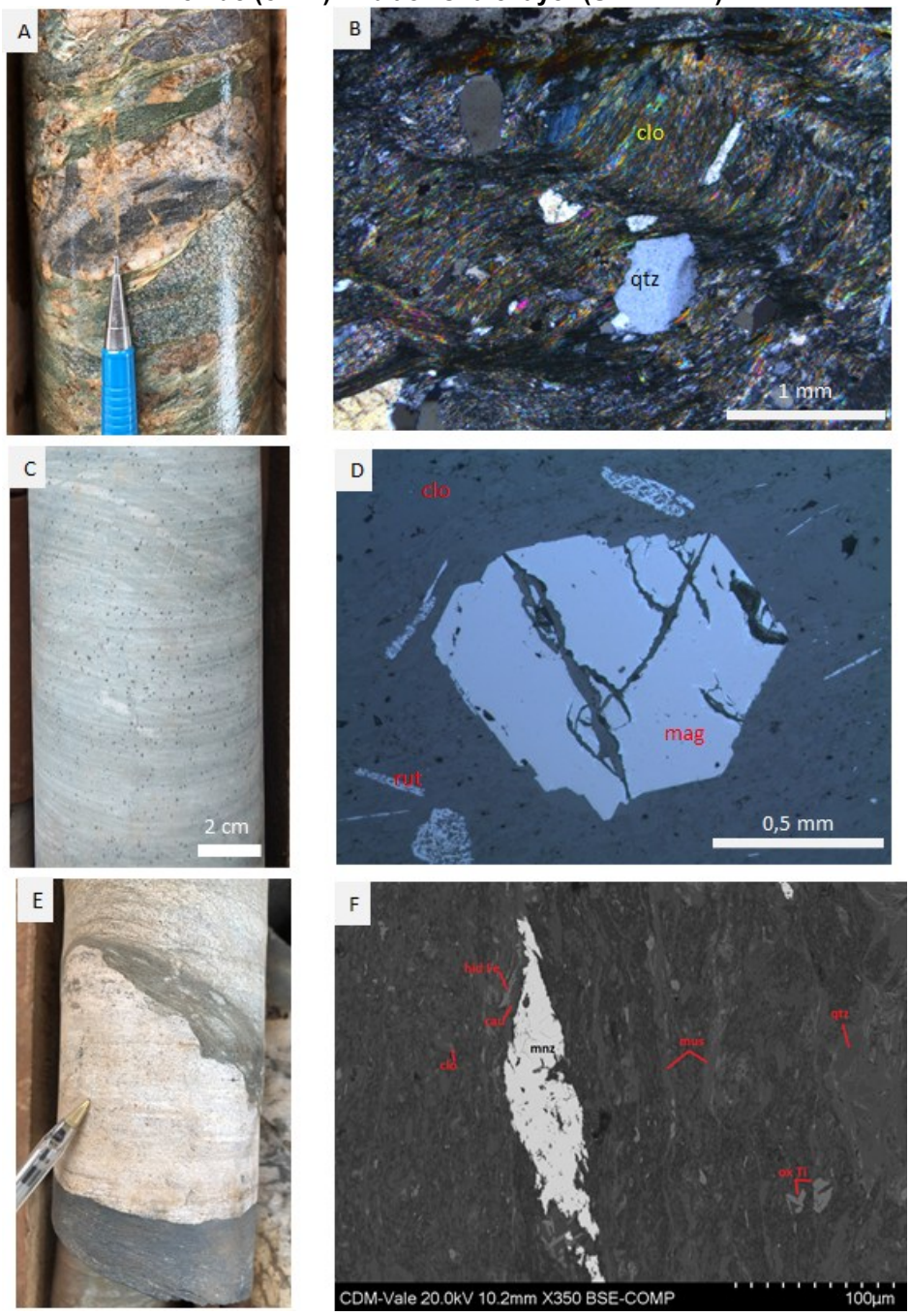

Source: Elaborated by the author

4.5.2.2 Chemical Domain: dolomitic BIF, dolostone and intraformational metaconglomerate

The carbonate succession comprises at least 295 meters (Figures 4.7A and B). The uncertainty of thickness is due to the drill hole not having crosscut the top contact of the carbonate rocks. Dolostone, intraformational metaconglomerate and dolomitic BIF are the predominant rocks in the interval. Dolomite is the main carbonate mineral (Figures 4.7A and 4.8B) and mostly displays triple junctions (120°) at grain boundaries.

From 185 to 316 meters, impure dolostone strata alternate with dolomitic BIF (Figure 4.7A), where the dolomitic BIF corresponds to approximately 30% of this thickness. Veins of various compositions (dolomite, calcite, quartz, chlorite and Fe oxide) crosscut the strata.

Impure dolostone strata exhibits white to red color, the variation corresponding to the amount of iron oxide. Commonly, quartz crystals are dispersed in the rocks. Chlorite laminae and rare solution surfaces (stylolite) are found. Hematite appears as an accessory mineral, as well as in micrometric inclusions in the impure dolostone. Texturally, impure dolostone displays fine-grained and locally banded textures.

In contrast, dolomitic BIF is characterized by mesobands of iron oxide and dolomite (Figures 4.10 A and B). Microscopically, grey iron-oxide bands comprise hematite microcrystalline, whereas micritic dolomite defines the carbonate bands. Generally, dolomite is in close association with the ferruginous bands (Figure 4.10B). Accessory minerals include talc, apatite and calcite (Figure 4.11A). All the strata are highly deformed and have undergone folding and shearing (Figure 4.10B).

From a gradual contact, given by the appearance of intraclasts in the dolomitic BIF, the intraformational metaconglomerate is formed (Figures 4.7A and 4.7B). The intraformational metaconglomerate layer is 74m thick and it is the only strata with clastic contribution from chemical domain, representing the sedimentary reworking of the chemical rocks in this domain. The matrix is thin (Figure 4.10C) and is composed mainly of dolomite and Fe oxide. The rock is poorly sorted, and clast size is mostly millimeters in length, rarely ≥5 centimeters. Compositionally, it is oligomictic and is mainly formed by intraclasts of the dolomite. Locally, beds contain quartz clasts (Figure 4.10D) and lithoclasts as BIF are rare. Some clasts borders are associated with overgrowths of chlorite or hematite, indicating local hydrothermal

alteration. Two different carbonates can be identified by SEM–EDX: a brighter Fe-Mn dolomite associated with recrystallized borders, and a darker, pure dolomite, preserved in crystal cores (Figure 4.11C).

Figure 4.10 — A) Dolomitic BIF from the studied drill core. The banding is defined by alternating layers of dolomite and iron oxide. B) Photomicrograph of superposed folding and internal shearing strata of dolomite (dol) and hematite (hem). Cross-polarized transmitted light. C) Drill core of intraformational metaconglomerate. D) Photomicrography by cross-polarized transmitted light of dolomite clasts (dol clast) and quartz (qtz) immersed in dolomitic matrix (dol). E) Contact between Intraformational metaconglomerate, phyllite and dolostone in drill core. And F) Different texture between dolostone (dol) and vein composed by carbonate (carb) and quartz (qtz). Photomicrography under parallel-polarized transmitted light.

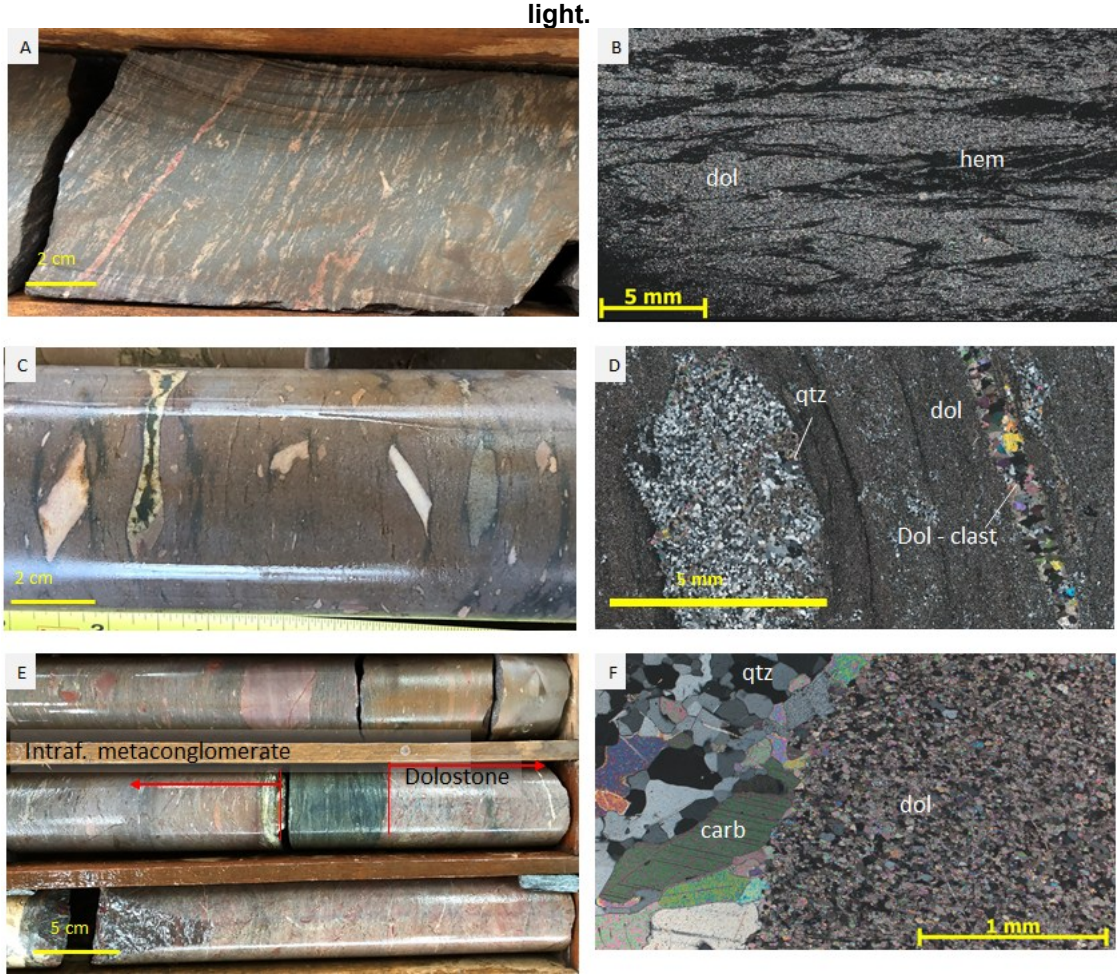

Source: Elaborated by the author

Figure 4.11 — SEM and backscattered electron (BSE) images. A) Hematite (hem) and dolomite (dol) in the groundmass, talc veinlet (tlc) and overgrown apatite (apa). B) Calcite vein as a hydrothermal carbonate. C) Different composition of dolomite crystals: core: pure dolomite - dol and borders: Fe and Mn-dolomites. D) Hematite laminas (ox Fe) and calcite veins in dolostone.

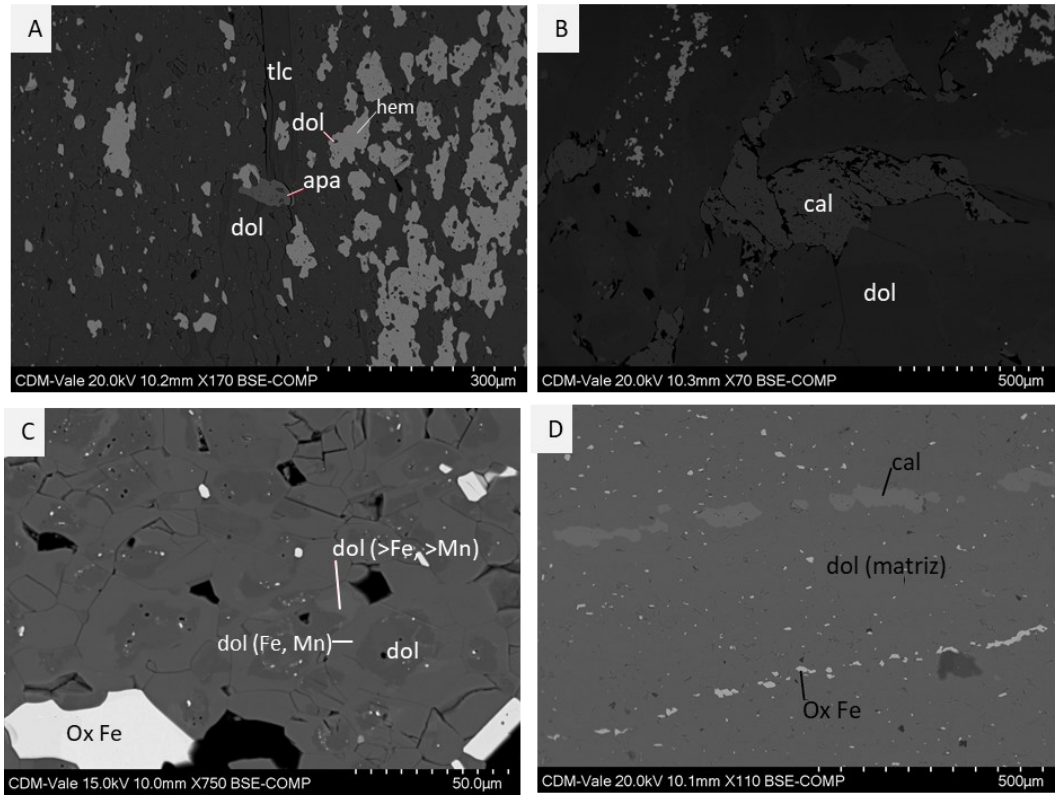

Source: Elaborated by the author

Overlying in sharp contact, in the 390m of depth, there is a discrete chlorite-phyllite layer (0.7m thick), composed mainly of chlorite and hematite (Figure 4.10 E). Whitish dolostone concordantly overlies the chlorite-phyllite. Representing the topmost Gandarela Formation, the dolostone occurs for more than 90 meters in the drill core (Figures 4.7A and 4.7B), but the maximum thickness is not known due to the end of the drill hole at 480m, not cross cutting the whole layer. The dolostone is composed of dolomite and it is thus characterizing distinct facies compared to impure dolostone logged between 185 to 316 meters deep. In terms of texture, the dolostone is locally brecciated and banded. The color varies between white, rose and gray, caused by concentrations of iron oxides or chlorite. Generally, millimetric veins of carbonates and quartz crosscut the dolostone (Figure 4.10 F). Accessory minerals include biotite, calcite and hematite dispersed throughout the dolomite matrix (Figure 4.11D).

4.5.2.3 Geochemistry

4.5.2.4 Major oxides and trace elements

The geochemical analyses relative to the major oxide and trace elements for each sedimentary rock domain (clastic and chemical) are presented in Table 4.1.

Clastic Domain

The oxides SiO_2, Al_2O_3 and Fe_2O_3 make up most of the composition of these rocks of the clastic domain (Figure 4.12), and MgO can reach a maximum value of 3.33 wt.% (sample A010). Low contents of Ca (0.04 to 0.90 wt.%) and Mn (0.03 to 0.10 wt.%) were obtained for metaconglomerate, phyllite, quartzite and black shale. The latter shows high LOI; the maximum value is 15.50 wt.% due to the presence of carbonaceous matter. The metaconglomerate sample (sample A001) displays anomalously high NaO values (2.62 wt.%). Rocks from the clastic domain are characterized by a high content of terrigenous components, expressed by $Al_2O_3 \leq$ 18.23 wt.%, $TiO_2 \leq$ 1.03 wt.%, Hf ≤ 4.26 ppm, Nb ≤ 11.46ppm, Th ≤ 14.6 ppm and Zr ≤ 172 ppm (Figure 4.13).

The metaconglomerate, phyllite, quartzite and black shale are relatively enriched in incompatible elements compared to the dolomitic rocks from the chemical domain, e.g., K ≤ 2.96%, Ba ≤ 1,348 ppm, Ce ≤ 159.9 ppm, Rb ≤ 135.4 ppm, V ≤ 265 ppm, Cr ≤ 157 ppm (except sample A073) and U ≤ 11.7 ppm.

Table 4.1 — Chemical analyses of rock samples from the Segredo deposit.

	Clastic Domain						Chemical Domain															
Sample	A001	A005	A073	A008	A009	A010	A011	A012	A022	A023	A026	A029	A031	A035	A042	A044	A046	A050	A074	A056	A060	A063
Depht (m)	106.1	151.9	165.0	183.5	183.6	184.0	187.2	192.2	216.9	221.6	244.7	269.0	277.9	296.6	329.1	340.8	356.0	375.8	390.0	408.9	429.0	443.0
Lithology	Metacon-glomerate	Phyllite	Quartzite	Black Shale	Black Shale	Black Shale	Dolostone	Dolomitic BIF	Dolostone	Dolostone	Dolostone	Dolostone	Dolostone	Dolomitic BIF	Dolomitic BIF	Int. Meta Conglom.	Int. Meta Conglom.	Int. Meta Conglom.	Chlorite Phyllite	Dolostone	Dolostone	Dolostone
Major Elements (%)																						
Al_2O_3	15.94	17.45	8.44	18.23	12.34	14.06	0.16	0.35	0.81	0.15	0.26	2.26	1.1	0.38	0.72	0.64	0.37	0.34	15.82	0.16	0.11	0.06
CaO	0.22	0.12	0.9	0.05	0.04	0.16	28.71	14.22	23.89	24.23	23.93	25.71	27.38	23.95	15.98	15.05	23.88	18.04	0.17	28.79	29.12	29.59
Fe_2O_3	8.44	9.42	3	6.12	4.21	11.04	3.66	43.61	1.98	2.39	2.3	2.54	2.67	18.58	36.19	11	8.38	9.87	24.32	3.23	2.03	2.86
K_2O	1.99	3.23	1.9	3.56	2.28	1.49	0.06	<0.01	0.11	0.06	0.08	0.13	0.07	0.05	<0.01	<0.01	0.01	<0.01	<0.01	<0.01	0.07	0.06
LOI	3.16	3.64	3.31	15.5	11.74	4.32	45.2	22.76	36.71	37.93	37.4	40.35	43.61	37	26.88	26.31	34.37	37.48	10	45.49	46.25	45.96
MgO	2.88	2.53	1.78	1.09	0.15	3.33	18.03	9.73	14.81	15.55	15.57	18.46	18.88	15.52	10.92	10.85	16.35	12.13	22.52	18.67	18.51	19
MnO	0.09	0.04	0.1	0.04	0.03	0.06	0.98	0.4	0.32	0.36	0.28	0.34	0.26	0.64	0.46	0.44	0.58	0.69	0.08	0.25	0.43	0.27
Na_2O	2.62	0.47	0.27	0.34	0.2	0.16	<0.01	<0.01	<0.01	<0.01	0.01	0.04	0.02	<0.01	<0.01	<0.01	<0.01	<0.01	<0.01	<0.01	<0.01	<0.01
P_2O_5	0.15	0.09	0.03	0.09	0.13	0.1	0.02	0.24	0.06	0.05	0.07	0.06	0.01	0.11	<0.01	<0.01	<0.01	<0.01	0.11	<0.01	0.01	<0.01
S	<0.01	<0.01	<0.01	0.01	0.01	0.01	<0.01	<0.01	<0.01	<0.01	<0.01	<0.01	<0.01	<0.01	<0.01	<0.01	0.01	<0.01	<0.01	<0.01	<0.01	<0.01
SiO_2	62.56	61.23	77.48	44.9	55.98	62.89	0.16	1.84	18.75	17.42	19.37	8.17	2.95	0.99	1.09	31.83	2.97	20.53	24.44	0.27	<0.01	<0.01
TiO_2	0.67	0.75	0.18	1.03	0.64	0.88	<0.01	0.04	0.06	<0.01	<0.01	0.13	0.05	0.08	0.04	0.05	0.03	0.03	0.77	0.03	<0.01	<0.01
Trace Elements (ppm)																						
Ag	<0.02	0.08	<0.02	<0.02	<0.02	<0.02	0.17	0.62	0.26	0.27	0.16	0.13	0.31	0.65	0.5	<0.02	<0.02	<0.02	0.59	0.22	0.32	0.45
As	14	<1	1	11	17	23	<1	1	<1	<1	<1	<1	<1	3	1	1	1	1	4	<1	<1	<1
Ba	428	873	574	1348	844	689	<10	<10	214	<10	17	47	<10	22	<10	<10	<10	<10	13	<10	<10	<10
Be	1.3	2.2	0.4	3.4	2.9	1.8	0.2	0.2	0.5	0.2	0.2	0.7	0.6	1.1	0.6	0.2	0.3	0.3	2.1	0.1	0.1	0.2
Bi	0.13	0.11	0.11	0.25	0.11	0.15	<0.04	0.04	0.04	0.05	0.06	<0.04	<0.04	0.07	0.07	<0.04	0.07	0.13	0.15	<0.04	<0.04	<0.04
Cd	0.18	0.07	0.11	<0.02	0.05	0.03	0.14	0.18	0.06	0.12	0.07	0.1	0.1	0.38	0.13	0.08	0.06	0.03	0.04	0.04	0.03	0.12
Co	29.5	37.6	199.6	35.6	78.9	71.7	6.3	46.3	229.6	109.3	108.6	35.8	33.2	47.9	39.4	94.1	21.2	44.9	67.5	12	1.3	1.6
Cr	125	134	19	157	101	106	2	<1	2	<1	2	3	1	<1	<1	3	7	<1	977	4	3	3
Cs	3.98	6.36	4.86	9.99	5.65	2.31	<0.05	0.08	1.15	0.17	0.33	0.44	0.06	<0.05	<0.05	<0.05	0.09	<0.05	0.73	<0.05	<0.05	<0.05
Cu	61.4	12.4	7.9	37.9	55.1	15.1	4.9	13	<0.5	0.7	1.2	2.7	1	<0.5	8.6	15.5	15.4	24.2	13.9	4	<0.5	0.7
Ga	18.4	22.4	11.6	27	17.5	20.3	1.5	2.5	1.7	0.8	0.9	3.1	1.4	2.1	4.6	2.1	3.2	2.1	24.5	1.6	0.7	0.5
Ge	0.4	0.3	<0.1	<0.1	<0.1	<0.1	<0.1	0.2	<0.1	<0.1	<0.1	<0.1	<0.1	0.3	0.2	<0.1	<0.1	<0.1	0.6	<0.1	<0.1	<0.1
Hf	3.23	3.17	2.94	4.26	2.58	3.25	0.11	0.17	0.51	0.1	0.17	0.71	0.37	0.43	0.28	0.22	0.13	0.14	4.22	0.09	0.07	0.11
In	0.06	0.09	0.03	0.08	0.07	0.05	<0.02	<0.02	<0.02	<0.02	<0.02	0.02	<0.02	<0.02	<0.02	<0.02	<0.02	<0.02	0.06	<0.02	<0.02	<0.02
Li	68	72	28	20	5	58	<1	2	16	4	4	28	14	2	3	6	5	4	140	6	4	<1
Mo	1.28	1.94	0.73	0.63	0.83	0.23	0.46	1.62	0.19	0.19	0.22	0.18	0.22	1.07	0.58	0.3	0.34	0.45	0.73	0.16	0.32	0.26
Nb	9.98	11.4	10.63	11.46	6.95	7.84	1.13	0.55	1.7	0.47	0.89	2.07	0.92	2.14	0.62	0.61	0.29	0.34	22.59	0.06	0.24	0.22
Ni	111.5	115.3	43.5	25.3	12.3	121.8	4.3	<0.5	2.8	2.5	1.6	3.6	4.8	6.4	<0.5	0.9	<0.5	0.9	194	<0.5	1.5	2.5
Pb	50.1	41.3	4.9	5.2	4.3	3.1	12	3.8	5.2	4.1	6.9	8.2	10.3	10.5	1.7	1	1.7	2.3	<0.5	1.7	6.8	29.6
Rb	80.4	120.3	77	135.4	84.7	49.6	0.4	<0.2	2.8	0.9	1.1	3.3	0.5	<0.2	0.2	<0.2	1	<0.2	1	0.3	0.9	<0.2
Sb	1.14	2.82	4.76	5.47	23.23	4.08	0.47	7.64	5.2	0.17	0.45	13.7	6.98	4.4	4.75	1.13	1.42	2.03	6.69	0.71	0.65	0.83
Sc	11.1	15.7	3.9	28.4	21	19.9	0.8	1	1.5	<0.5	0.5	3.2	3	3.8	2.5	1.3	1	1	15.7	<0.5	<0.5	<0.5
Se	<2	<2	<2	<2	<2	<2	<2	<2	<2	<2	<2	<2	<2	<2	<2	<2	<2	<2	<2	<2	<2	<2
Sn	<0.3	<0.3	0.9	4.1	2.4	2.3	<0.3	<0.3	<0.3	<0.3	<0.3	<0.3	<0.3	<0.3	<0.3	0.7	<0.3	<0.3	2.1	<0.3	<0.3	<0.3
Sr	97	80	65	45	25	19	93	<10	76	65	57	78	62	59	52	31	40	32	<10	<10	40	49
Ta	0.71	1.23	0.28	0.96	0.67	0.72	<0.05	0.09	0.22	0.1	0.07	0.25	<0.05	0.11	0.16	0.13	<0.05	<0.05	1.21	0.12	<0.05	<0.05
Te	0.1	0.09	0.08	0.25	0.09	0.06	<0.05	<0.05	<0.05	<0.05	<0.05	<0.05	<0.05	<0.05	<0.05	<0.05	<0.05	<0.05	0.2	<0.05	<0.05	<0.05
Th	9.1	13.5	10.2	14.6	7.6	7.9	2.5	0.4	1.2	0.5	0.5	1.9	0.7	1.2	0.7	0.7	0.4	0.4	10.1	0.2	0.2	0.2
Tl	<0.5	<0.5	<0.5	<0.5	<0.5	<0.5	<0.5	<0.5	<0.5	<0.5	<0.5	<0.5	<0.5	<0.5	<0.5	<0.5	<0.5	<0.5	0.8	<0.5	<0.5	<0.5
U	1.7	6.5	2.1	8	9.7	11.7	2.7	3	1	0.5	0.8	1.4	0.9	4.4	9.9	1.4	1.6	1.2	7.5	0.4	0.3	0.4
V	110	141	57	265	172	166	<5	55	<5	<5	<5	<5	26	9	59	<5	<5	5	157	28	<5	<5
W	10	12.3	712.4	100.4	304.6	161.4	2.6	145.7	378.2	326.8	285.3	115.4	96.4	102.5	110.2	462.5	68.6	165	12.5	39	1.9	2.2
Zn	150	120	43	43	22	120	17	35	12	7	10	20	24	33	22	24	12	13	129	5	11	28
Zr	128	130	80	172	93	131	13	36	38	13	18	38	20	29	26	11	20	23	148	28	14	14

Source: Elaborated by the author

Figure 4.12 — Composition of major oxides in samples from the studied drill core. A – Clastic domain (samples: A001, A005, A073 and average of: A008, A009, A010). B – Chemical domain shows different contributions of hematite and quartz. The plot shows the average of the lithological groups: Impure dolostone (samples A011, A022, A023, A026, A029 and A031), Dolomitic BIF (samples: A012, A035 and A042), Intraformational metaconglomerate (sample: A044, A046 and A050), Chlorite-phyllite (sample: A074) and Pure dolostone (sample: A056, A060 and A063).

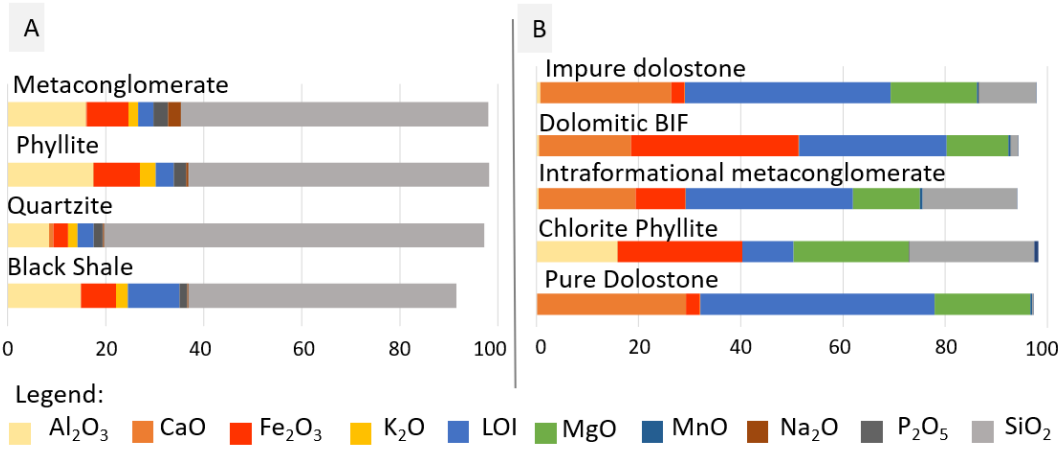

Source: Elaborated by the author

Figure 4.13 — Plot of Nb, Ti and Zr versus Al for all samples and domains: clastic (orange circles) and chemical (blue circles). The studied samples present positive correlations in the cross-plots, and the terrestrial contribution is significant only in rocks from the clastic domain.

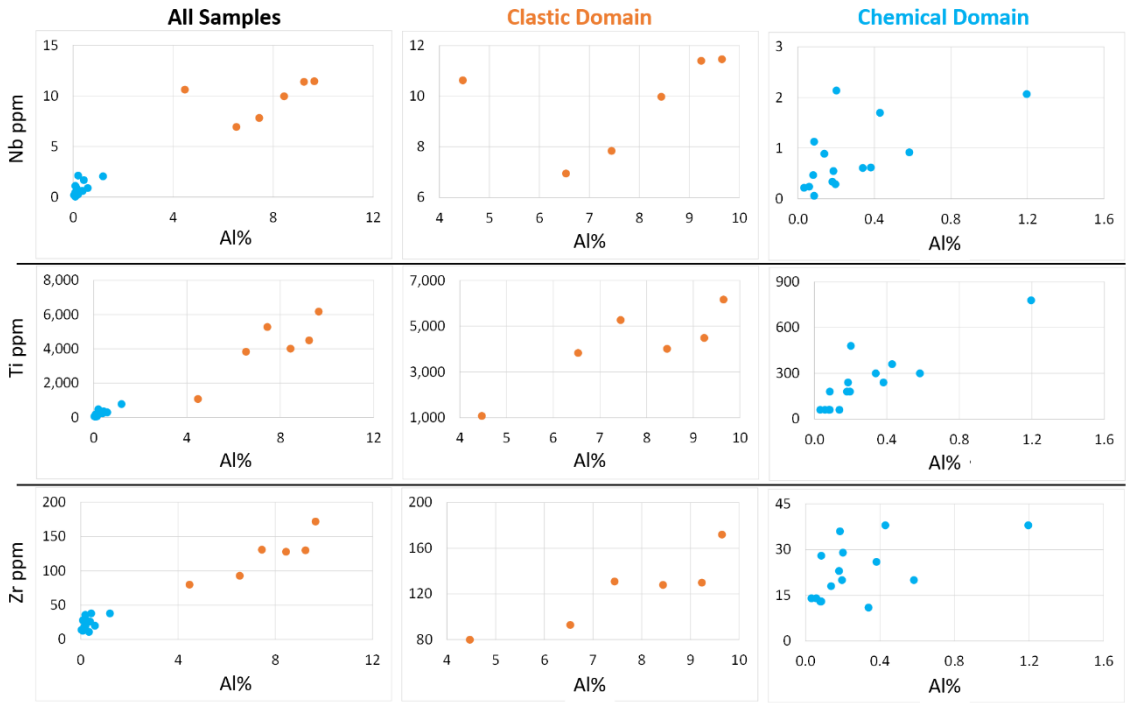

Source: Elaborated by the author

Chemical Domain: carbonate rocks and Intraformational metaconglomerate

The main mineral in the chemical domain is dolomite (Figure 4.8B), while the presence of calcite is associated with secondary veins. Chemical analyses identified the average content of LOI, CaO and MgO at 37.58, 23.50 and 15.53 wt.%, respectively, except for the chlorite-phyllite. The chemical domain was subdivided into impure dolostone, dolomitic BIF, intraformational metaconglomerate, chlorite-phyllite, and pure dolostone (Figure 4.12B). The samples show low contents of terrigenous elements (Figure 4.13).

Impure dolostone displays an average 11.14 wt.% SiO_2. Samples A022, A023, A026 and A029 have higher SiO_2 concentrations, reaching a maximum of 19.37 wt.% SiO_2. In addition, they have low $Fe_2O_3 \leq 2.59$ wt.% and average values of 0.42wt% MnO and 0.08 wt.% K_2O.

Samples of dolomitic BIF display a high percentage of carbonates (from 46.71 to 76.47 wt.% sum of the CaO, MgO and LOI contents). They contain $Fe_2O_3 \leq 43.61$ wt.%, $SiO_2 \leq 1.84$ wt.%, $Al_2O_3 \leq 0.72$ wt.%, MnO ≤ 0.64 wt.% and $P_2O_5 \leq 0.24$ wt.%.

In the intraformational metaconglomerate, the signature of the major oxides shows variations due to the heterogeneous composition of the matrix and clasts. The level with the highest contribution of quartz clasts has $SiO_2 \leq 31.83$ wt.%, whereas the levels with the highest carbonate intraclasts display a minimum value of 2.97 wt.% SiO_2. The iron content in the matrix shows average values of 9.75 wt.% of Fe_2O_3. The carbonate composition (CaO + MgO + LOI) ranges from 52.21 to 74.60 wt.% and the MnO content is less than 0.69 wt.%.

Sample A074 was collected from chlorite-phyllite (0.65 meters thick) and showed Fe_2O_3 (24.32 wt. %), SiO_2 (24.44 wt.%), MgO (22.52 wt%) and Al_2O_3 (15.82 wt.%) as main constituents. Among the trace elements, the sample shows relatively high levels of Cr, Ga, Hf, Li, Nb, Ni, Ti and Th.

Pure dolostone collected from samples A056, A060 and A063 shows a homogeneous carbonate composition, exceeding 92.95% wt. of CaO + MgO + LOI. These rocks are characterized by low $Fe_2O_3 \leq 3.23$ wt.%, MnO ≤ 0.43 wt.%, $SiO_2 \leq$ 0.27 wt.% and $Al_2O_3 \leq 0.16$ wt.%.

Dolostone and dolomitic BIF show low contents of Ba (except sample A22 with Ba = 214ppm), Hf, K, Na, Ni Th and Zr. Additionally, they display an average U/Th ratio of 3.09 with one outlier (sample A042) of 14.14.

4.5.2.5 Rare Earth Elements and Yttrium

The Rare Earth Elements and Yttrium (REEY) values, normalized to Post Archean Average Australian Shale (PAAS; Taylor and McLennan, 1985), are shown in Table 4.2. Generally, rocks are depleted in REE but can reach an anomalous value of 159.9 ppm Ce in sample A008 (black shale). Distinct REEY signatures were identified in the rocks from both domains, as shown in Figures 4.14A and 4.14B.

The clastic domain samples show relatively flat, NASC-like REEY patterns (Figure 4.14 A), except for samples A008 and A073, which correspond to black shale and quartzite, respectively, and show slight heavy REE depletion. Values below the detection limit (<0.05) were not plotted in the figures.

In the chemical domain, all samples show enrichment in the heavier REE with respect to light REE (Figure 4.14B). The mean values of impure dolostone present intermediate REEY composition between dolomitic BIF and dolostone associated with the Gandarela Formation. In addition, the Gandarela Formation dolostone is more depleted in the REEY in relation to the chemical domain. On the other hand, the chlorite-phyllite (390m deep in the drill core) has a different REEY pattern and enrichment in the heavy REE is more prominent (Figure 4.14C).

A positive Eu anomaly (average 1.25) characterizes the dolomitic BIF and dolostone. This anomaly is calculated as $Eu/Eu^* = [Eu]_{PAAS} / ([Sm]_{PAAS} \times [Gd]_{PAAS})0.5$, where Eu* is the hypothetical concentration of Eu^{+3} (Taylor and McLennan, 1985). The Ce anomalies calculated from the formula $Ce/Ce^* = [Ce]_{PAAS} /(([Pr]^2_{PAAS})/[Nd]_{PAAS})$, developed by Tostevin et al. (2016), display negative Ce anomalies in pure dolostones from the Gandarela Formation, the values range from 0.57 to 0.87. Additionally, dolomitic BIF and dolostone show Y/Ho ratios ranging from 31.0 to 46.0, within the typical range of Archean and Paleoproterozoic iron-rich sedimentary rocks (Planavsky et al., 2010).

Table 4.2 — REE + Y data and relevant ratios for drill core samples in the Segredo deposit.

	Clastic Domain						Chemical Domain														
Sample	A001	A005	A073	A008	A009	A010	A011	A012	A022	A023	A026	A029	A031	A035	A042	A044	A046	A050	A074	A056	A060	A063
Depht (m)	106.1	151.9	165.0	183.5	183.6	184.0	187.2	192.2	216.9	221.6	244.7	269.0	277.9	296.6	329.1	340.8	356.0	375.8	390.0	408.9	429.0	443.0
Lithology	Metacon-glomerate	Phyllite	Quartzite	Black Shale	Black Shale	Black Shale	Dolostone	Dolomitic BIF	Dolostone	Dolostone	Dolostone	Dolostone	Dolostone	Dolomitic BIF	Dolomitic BIF	Int. Meta Conglom.	Int. Meta Conglom.	Int. Meta Conglom.	Chlorite Phyllite	Dolostone	Dolostone	Dolostone
Rare Earth Elements + Y (ppm)																						
Ce	49.6	64.9	46.2	159.9	41.9	55.1	12.1	4.2	5.2	5	4.1	6.5	5.7	17.4	12.2	3.2	3	3.3	2.4	1.5	2	2
Dy	3.47	4.34	1.49	5.69	3.45	4.2	0.66	1.24	0.52	0.36	0.28	0.67	0.57	1.24	1.11	0.69	0.67	0.48	0.74	0.21	0.12	0.14
Er	2.07	2.57	0.76	3.13	2.37	2.59	0.38	0.89	0.32	0.21	0.15	0.49	0.4	0.91	0.83	0.48	0.5	0.34	0.94	0.16	0.09	0.07
Eu	1.06	1.04	0.83	2.35	0.67	0.89	0.15	0.24	0.1	0.12	0.07	0.13	0.14	0.39	0.33	0.12	0.15	0.1	0.05	<0.05	<0.05	<0.05
Gd	3.7	4.35	1.91	9.64	3.22	4.4	0.62	0.81	0.6	0.49	0.39	0.6	0.59	1.51	1.15	0.44	0.48	0.41	0.36	0.15	0.16	0.21
Ho	0.68	0.9	0.3	1.13	0.71	0.93	0.12	0.27	0.11	0.07	0.07	0.14	0.13	0.29	0.3	0.15	0.18	0.1	0.22	<0.05	<0.05	<0.05
La	26.4	35.1	25.7	85.9	22.7	26.3	11.1	1.3	6.1	5.6	6.3	6	11.1	13.1	5	1.1	2.4	2.8	1	0.3	3.2	2.9
Lu	0.29	0.38	0.12	0.49	0.34	0.38	<0.05	0.14	<0.05	<0.05	<0.05	0.06	<0.05	0.14	0.15	0.06	0.09	<0.05	0.26	<0.05	<0.05	<0.05
Nd	21.9	25.8	14.3	74.2	17.2	22.2	3.7	2.5	2.3	2.2	1.6	2.7	2.3	9.4	5.1	1.9	1.6	1.4	0.1	0.7	0.8	0.9
Pr	5.78	7.04	4.5	19.49	4.66	6.02	1.28	0.61	0.56	0.52	0.44	0.7	0.6	2.42	1.36	0.53	0.44	0.48	<0.05	0.23	0.23	0.26
Sm	4.1	4.8	2.3	13.5	3	4.4	0.6	0.6	0.5	0.3	0.3	0.6	0.4	1.6	0.8	0.4	0.4	0.4	0.3	<0.1	0.1	0.2
Tb	0.55	0.7	0.29	1.14	0.51	0.69	0.09	0.16	0.09	0.07	0.05	0.1	0.1	0.19	0.17	0.09	0.11	0.07	0.09	<0.05	<0.05	<0.05
Tm	0.29	0.37	0.13	<0.05	<0.05	<0.05	<0.05	<0.05	<0.05	<0.05	<0.05	0.07	<0.05	0.14	<0.05	<0.05	<0.05	<0.05	0.17	<0.05	<0.05	<0.05
Y	17.11	23.83	7.02	30.06	21.35	24.99	5.48	11.2	3.49	3.22	2.17	4.37	4.32	11.73	9.95	5.7	7.38	4.97	7.26	2.68	1.61	1.33
Yb	2	2.5	0.8	3.1	2.3	2.5	0.3	0.8	0.3	0.1	0.1	0.4	0.3	0.8	0.8	0.4	0.5	0.3	1.4	0.2	<0.1	<0.1
Σ REE + Y	139	178.62	106.65	409.72	124.38	155.59	36.58	24.96	20.19	18.26	16.02	23.53	26.65	61.26	39.25	15.26	17.9	15.15	15.29	6.13	8.31	8.01
Relevant Ratios [1] Normalized to PAAS (McLennan, 1989)																						
Cr/Ti	0.03	0.03	0.02	0.03	0.03	0.02	<LD	<LD	0.01	<LD	<LD	0.00	0.00	<LD	<LD	0.01	0.04	<LD	0.21	0.02	<LD	<LD
U/Th	0.19	0.48	0.21	0.55	1.28	1.48	1.08	7.50	0.83	1.00	1.60	0.74	1.29	3.67	14.14	2.00	4.00	3.00	0.74	2.00	1.50	2.00
Y/Ho	25.16	26.48	23.40	26.60	30.07	26.87	45.67	41.48	31.73	46.00	31.00	31.21	33.23	40.45	33.17	38.00	41.00	49.70	33.00	<LD	<LD	<LD
Eu/Eu*	-	-	-	-	-	-	1.16	1.62	0.86	1.47	0.96	1.02	1.36	1.18	1.62	1.35	1.61	1.16	0.72	<LD	<LD	<LD
Ce/Ce*	-	-	-	-	-	-	0.79	0.82	1.10	1.18	0.98	1.03	1.05	0.81	0.97	0.63	0.72	0.58	<LD	0.57	0.87	0.77
Pr/Pr*	-	-	-	-	-	-	1.11	1.09	0.95	0.92	1.01	0.98	0.97	1.11	1.01	1.25	1.17	1.31	<LD	1.32	1.07	1.14

Source: Elaborated by the author

Figure 4.14 — PAAS-normalized REEY data (Taylor and McLennan, 1985) for (A) clastic domain, (B) chemical domain, and (C) chlorite phyllite. The elements that yielded values lower than the detection limit were omitted from the graphs.

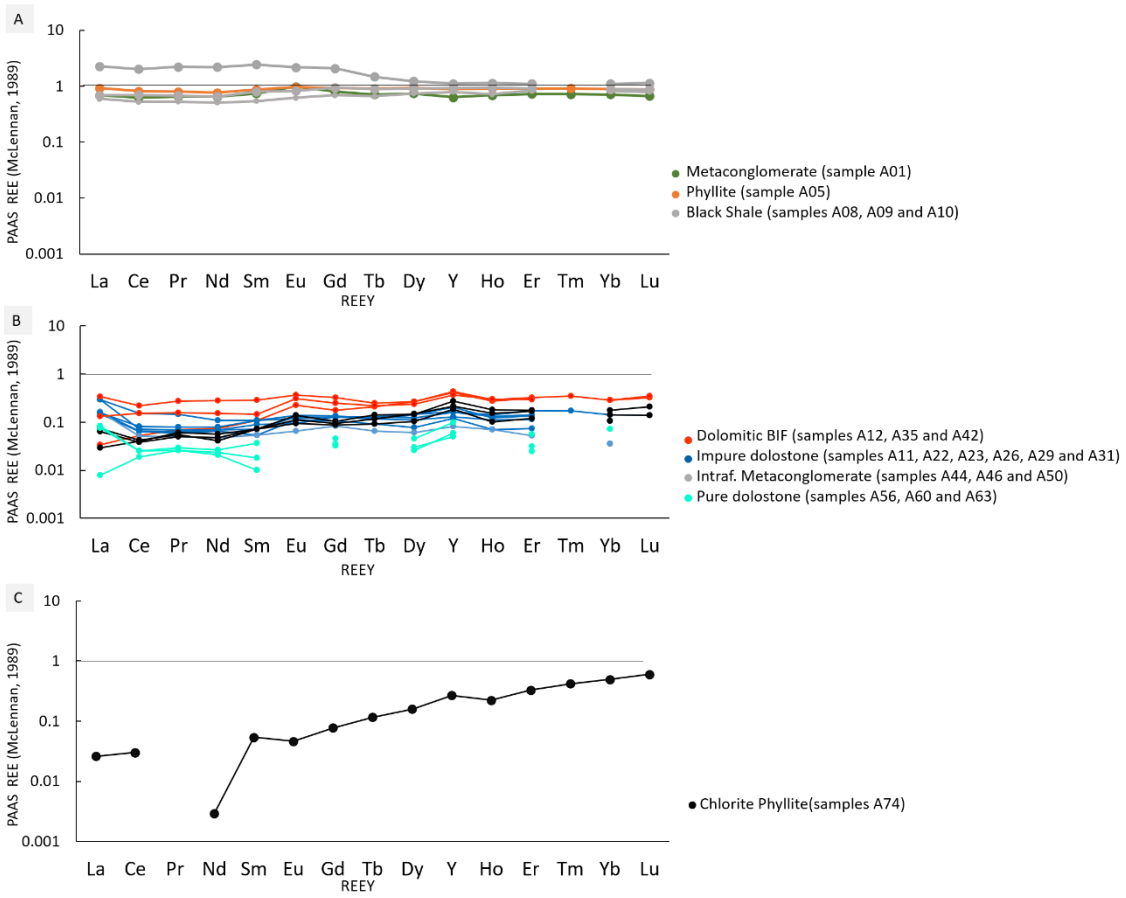

Source: Elaborated by the author

4.5.3 Carbon and Oxygen Isotopes

The overall isotopic data, summarized in Table 4.3, shows the variation of $\delta^{13}C$ and $\delta^{18}O$ values for the Cauê and Gandarela formations and veins of carbonate. Isotopic data were calibrated to the Vienna PeeDee Belemnite (VPDB), an international marine carbonate standard.

Seventy-four aliquots collected from dolostone, dolomitic BIF, intraformational metaconglomerate and carbonate veins show $\delta^{13}CV_{PDB}$ values ranging from -2.4 to 1.1‰ and negative values of $\delta^{18}OV_{PDB}$ ranging between -17.6 to -4.5‰. With increasing drill hole depth. from the Cauê dolomitic BIF and dolostone to Gandarela dolostone and

intraformational metaconglomerate, the O-isotopic ratio becomes less negatively fractionated and $\delta^{13}C$ V_{PDB} values approach zero (Figure 4.7A).

Dolomitic BIF and dolostones from the Cauê Formation display $\delta^{13}C$ values from -2.4 to 0.0‰ and the oxygen isotope ratio shows values between -17.6 to -7.4‰. Thus, the Cauê Formation is more depleted in ^{13}C and ^{18}O than the Gandarela dolostone and intraformational metaconglomerate (bottom of the drill core) which shows $\delta^{13}C$: -2.2 to 1.1‰ and $\delta^{18}O$: -15.1 to -4.5‰.

The results obtained in the carbonate veins vary in depth, with $\delta^{13}C$ values from -1.78 to -0.13‰ and $\delta^{18}O$ values between -9.40 and -7.89‰ with one outlier at -14.46‰. Remarkably, these values of carbon and oxygen isotope ratio exhibit a similar pattern to the whole-rock samples of the Cauê Formation towards the Gandarela Formation, in other words, C-O-values decrease with increasing drill hole depth.

Table 4.3 – Whole rock carbon and oxygen isotope values for samples from drill hole FDSP0046. The precision of isotopic measurements is better than ± 0.1‰.

Samp	Depth (i	$\delta^{13}C_{VPDB}$	$\delta^{18}O_{VPDB}$	Analized Rock	Lithostratigraphy
A011	187.2	-2.38	-16.52	Dolostone	Cauê Formation
A012-C	192.2	-2.06	-16.66	Dolomitic BIF - Carbonate band	Cauê Formation
A012-F	192.2	-2.18	-16.76	Dolomitic BIF - Ferruginous band	Cauê Formation
A019-F	197.2	-2.24	-15.72	Dolomitic BIF - Ferruginous band	Cauê Formation
A020-C	202.1	-1.59	-16.37	Dolomitic BIF - Carbonate band	Cauê Formation
A020-F	202.1	-1.59	-16.75	Dolomitic BIF - Ferruginous band	Cauê Formation
A021-C	206.1	-1.78	-16.71	Dolomitic BIF - Carbonate band	Cauê Formation
A021-F	206.1	-1.83	-16.6	Dolomitic BIF - Ferruginous band	Cauê Formation
A022	216.9	-1.66	-13.67	Dolostone	Cauê Formation
A023	221.6	-1.39	-12.52	Dolostone	Cauê Formation
A024	230.0	-1.33	-12.77	Dolostone	Cauê Formation
A025	235.7	-1.17	-11.51	Dolostone	Cauê Formation
A026	244.7	-1.19	-12.39	Dolostone	Cauê Formation
A027	245.9	-1.16	-11.3	Dolostone	Cauê Formation
A028	266.7	-1.4	-12.13	Dolostone	Cauê Formation
A029	269.0	-1.5	-11.75	Dolostone	Cauê Formation
A030-C1	275.0	-1.47	-11.46	Dolostone	Cauê Formation
A030-C2	275.0	-1.78	-14.46	Carbonate Vein	Vein
A031	277.9	-1.59	-12.82	Dolostone	Cauê Formation
A032	283.0	-1.48	-13.74	Dolostone	Cauê Formation
A033	287.9	-1.55	-14.75	Dolostone	Cauê Formation
A034-C	292.9	-2.17	-15.56	Dolomitic BIF - Carbonate band	Cauê Formation
A035-C	296.6	-1.98	-16.04	Dolomitic BIF - Carbonate band	Cauê Formation
A035-F	296.6	-1.43	-15.88	Dolomitic BIF - Ferruginous band	Cauê Formation
A036-M	298.8	-1.38	-11.59	Dolostone	Cauê Formation
A036-C	298.8	-1.58	-11.62	Dolostone	Cauê Formation
A037-C	302.2	-2.4	-16.28	Dolomitic BIF - Carbonate band	Cauê Formation
A037-F	302.2	-2.36	-16.05	Dolomitic BIF - Ferruginous band	Cauê Formation
A038	304.8	-0.06	-7.44	Dolostone	Cauê Formation
A041-C	318.8	-0.84	-17.6	Dolomitic BIF - Carbonate band	Cauê Formation
A042-C	329.1	-0.25	-13.17	Dolomitic BIF - Carbonate band	Cauê Formation
A042-F	329.1	-0.17	-15.66	Dolomitic BIF - Ferruginous band	Cauê Formation
A044-M	340.8	-0.84	-8.49	Intraf. metaconglomerate - Matrix	Gandarela Formation
A044-C1	340.8	-2.18	-15.13	Intraf. metaconglomerate - Siliciclastic Clast	Gandarela Formation
A044-C2	340.8	-0.57	-9.82	Intraf. metaconglomerate - Siliciclastic Clast	Gandarela Formation
A044-C3	340.8	-0.22	-10.3	Intraf. metaconglomerate - Dolomitic BIF Clast	Gandarela Formation
A045-C1	345.7	-0.106	-8.39	Intraf. metaconglomerate - Matrix	Gandarela Formation
A045-C2	345.7	0.14	-13.39	Intraf. metaconglomerate - Matrix	Gandarela Formation
A045-V	345.7	-0.13	-8.31	Carbonate Vein	Vein
A046-M	356.0	-0.32	-9.5	Intraf. metaconglomerate - Matrix	Gandarela Formation
A046-C	356.0	-0.22	-8.48	Intraf. metaconglomerate - Carbonate Clast	Gandarela Formation
A047	361.3	-0.44	-8.54	Intraf.metaconglomerate - Matrix	Gandarela Formation
A049	367.8	-0.99	-9.27	Intraf. metaconglomerate - Matrix	Gandarela Formation
A050-C	375.8	-1.12	-8.99	Intraf. metaconglomerate - Siliciclastic Clast	Gandarela Formation
A051-M	380.2	-0.93	-10.8	Intraf. metaconglomerate - Matrix	Gandarela Formation
A051-C	380.2	-0.13	-13.12	Intraf. metaconglomerate - Carbonate Clast	Gandarela Formation
A052	385.7	-1.33	-11.68	Intraf. metaconglomerate - Matrix	Gandarela Formation
A053-M	389.1	-0.54	-11.31	Intraf. metaconglomerate - Matrix	Gandarela Formation
A053-C	389.1	-0.54	-10.75	Intraf. metaconglomerate - Carbonate Clast	Gandarela Formation
A054	395.0	-0.74	-10.87	Dolostone	Gandarela Formation
A055	399.9	0.14	-8.44	Dolostone	Gandarela Formation
A056-C1	408.9	-0.06	-8.1	Dolostone	Gandarela Formation
A056-C2	408.9	-0.39	-8.25	Carbonate Vein	Vein
A057	413.9	-0.29	-9.1	Dolostone	Gandarela Formation
A058-C1	418.9	0.27	-9.73	Dolostone	Gandarela Formation
A058-C2	418.9	-0.76	-9.4	Carbonate Vein	Vein
A059-C1	423.8	-0.14	-8.79	Dolostone	Gandarela Formation
A059-C2	423.8	-0.34	-9.13	Dolostone	Gandarela Formation
A060-C1	429.0	-0.23	-7.33	Dolostone	Gandarela Formation
A060-C2	429.0	0.05	-7.79	Dolostone	Gandarela Formation
A062	438.4	-0.25	-6.99	Dolostone	Gandarela Formation
A063-C1	443.0	-0.24	-6.36	Dolostone	Gandarela Formation
A063-C2	443.0	-0.33	-9.58	Dolostone	Gandarela Formation
A064-C1	448.0	-0.29	-6.16	Dolostone	Gandarela Formation
A064-C2	448.0	-0.23	-6.23	Dolostone	Gandarela Formation
A065-C1	452.7	0.05	-7.46	Dolostone	Gandarela Formation
A065-C2	452.7	-0.29	-7.89	Carbonate Vein	Vein
A066-C1	457.5	0.33	-4.78	Dolostone	Gandarela Formation
A066-C2	457.5	1.15	-13.08	Dolostone	Gandarela Formation
A067	462.4	0.53	-5.82	Dolostone	Gandarela Formation
A068	467.4	0.21	-4.47	Dolostone	Gandarela Formation
A069	472.5	0.04	-5.49	Dolostone	Gandarela Formation
A070	477.0	0.16	-6.41	Dolostone	Gandarela Formation
A071	480.1	0.2	-4.94	Dolostone	Gandarela Formation

Source: Elaborated by the author

4.5.4 Detrital zircon U-Pb dating

From the metaconglomerate belonging to the clastic domain (Figure 4.7B), a total of 65 zircon crystals (sample AC01) were recovered. Images of zircon grains obtained by cathodoluminescence (CL) are shown in Figure 4.15. The grain sizes range from 65 to 260 μm in length and exhibit anhedral to euhedral prismatic shapes.

Figure 4.15 — Representative cathodoluminescence images with the location of some of the spots performed by LA-SF-ICPMS in concordant zircon grains (within 90-110% concordance) and the measured $^{207}Pb/^{206}Pb$ ages.

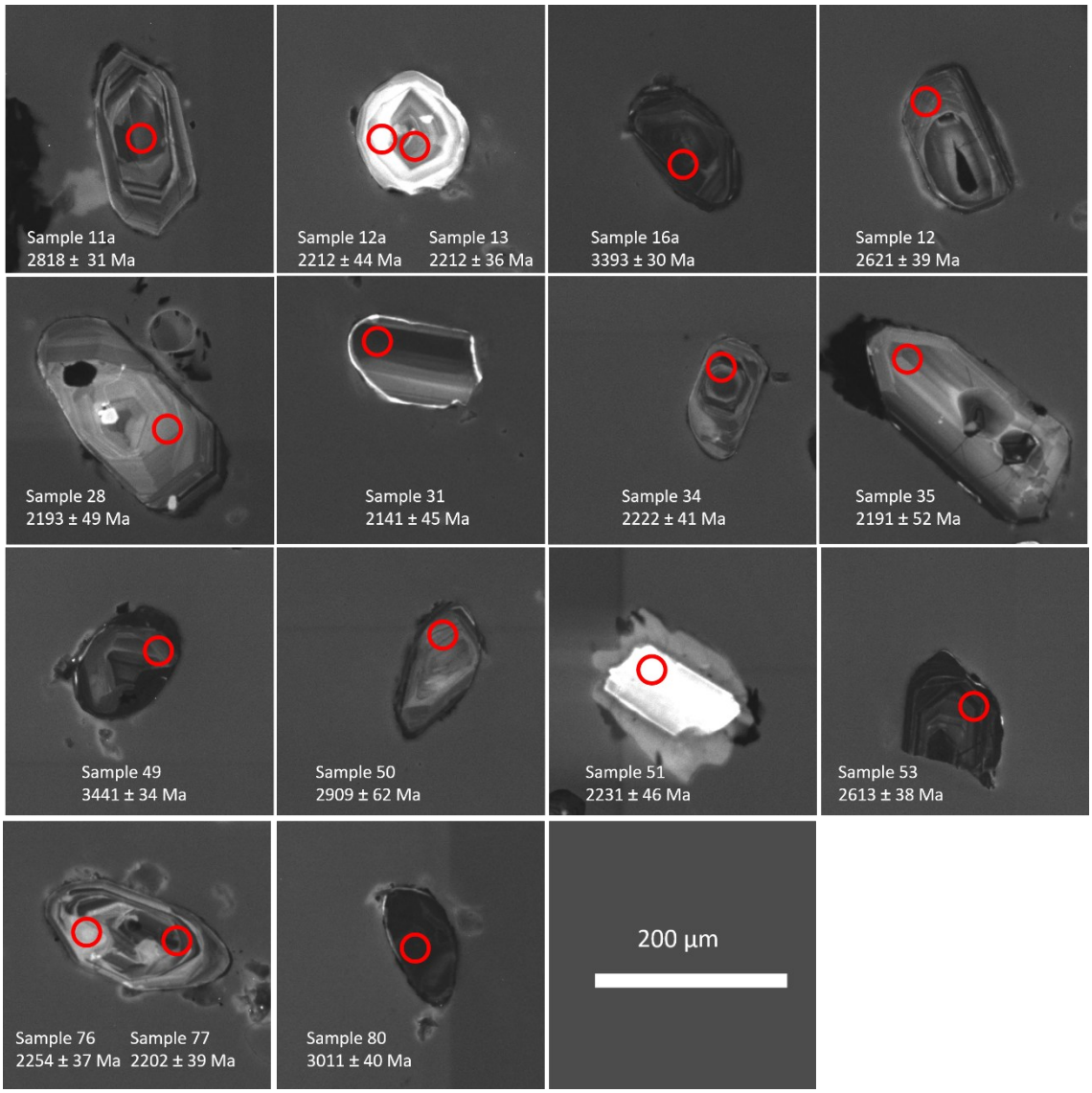

Source: Elaborated by the author

Measurements were obtained from 71 spots, avoiding microfractures and other heterogeneous areas. Among the measures obtained, 17 yielded concordant ages within 90-110%. The complete dataset is provided in table 4.4. The results are shown in $^{207}Pb/^{206}Pb$ age histograms (bin size: 40 Ma) and probability density plots (Figure 4.16A), calculated using the Isoplot 3.6 software by Ludwig (2008).

Table 4.4 — U-Pb data for detrital zircons of the metaconglomerate sample number AC01. Concordance is calculated as (^{206}Pb-^{238}U age/^{207}Pb-^{206}Pb age)*100. Total systematic uncertainties (ssys): $^{206}Pb/^{238}U$ = 2.0%, 207Pb/206Pb = 0.55% (2sigma). The blue lines indicate concordant dates; the yellow lines show the dates utilized in the Discordia regression, and the green line shows a sample used in both diagrams.

					Ratios							Ages (Ma)						
Spot Number	f^{206}	^{206}Pb cps	U ppm	Th/U	$^{207}Pb/^{206}Pb$	2s (%)	$^{207}Pb/^{235}U$	2s (%)	$^{206}Pb/^{238}U$	2s (%)	Rho	$^{207}Pb/^{206}Pb$	2s ±	$^{206}Pb/^{238}U$	2s ±	$^{207}Pb/^{235}U$	2s ±	% conc
07a	0.12	2367549	635.7897	0.60	0.1304	2.02	5.2889	2.67	0.2941	1.74	0.65	2104	35	1662	26	1867	23	89
08a	0.10	2016384	533.807	2.46	0.1238	1.96	5.0935	2.63	0.2983	1.74	0.66	2012	35	1683	26	1835	23	92
09a	0.28	1958229	459.0961	1.83	0.1352	2.23	6.2812	2.95	0.3369	1.93	0.66	2167	39	1872	32	2016	26	93
10a	0.23	1574618	851.8338	3.52	0.1033	2.42	2.0799	2.95	0.1460	1.68	0.57	1685	45	878	14	1142	21	77
11a	0.16	1888376	275.3773	1.65	0.1990	1.90	14.8577	2.67	0.5416	1.88	0.70	2818	31	2790	43	2806	26	100
12a	1.00	510183.1	99.70736	0.66	0.1388	2.56	7.7326	3.13	0.4041	1.79	0.57	2212	44	2188	34	2200	29	100
13a	0.00	410220	79.70513	0.76	0.1388	2.07	7.7790	2.72	0.4065	1.75	0.64	2212	36	2199	33	2206	25	100
14a	0.27	2059849	767.8102	2.41	0.1197	1.97	3.4971	2.72	0.2119	1.87	0.69	1952	35	1239	21	1527	22	82
15a	3.29	2079148	3067.527	1.36	0.2901	3.09	2.1414	12.64	0.0535	12.26	0.97	3418	48	336	41	1162	92	29
16a	0.01	2379240	274.8946	2.99	0.2855	1.93	26.9088	2.67	0.6836	1.84	0.69	3393	30	3358	49	3380	26	100
07	5.67	1966293	1245.475	1.36	0.4010	4.51	17.5008	6.09	0.3165	4.09	0.67	3913	68	1773	63	2963	60	60
08	0.49	1484571	1591.549	1.43	0.1214	2.09	3.1311	2.87	0.1870	1.97	0.69	1977	37	1105	20	1440	22	77
09	1.00	1756928	2717.729	0.83	0.1144	2.72	2.0449	3.63	0.1296	2.41	0.66	1871	49	786	18	1131	25	69
10	3.95	1407782	1109.837	1.80	0.3135	3.50	10.9933	5.04	0.2543	3.63	0.72	3538	54	1461	47	2523	48	58
11	0.66	1072553	674.9201	0.94	0.1297	2.11	5.6982	2.92	0.3186	2.01	0.69	2094	37	1783	31	1931	25	92
12	1.00	873160.5	346.4124	2.05	0.1766	2.36	12.3023	3.04	0.5054	1.92	0.63	2621	39	2637	41	2628	29	100
13	1.00	171045.8	75.24873	2.44	0.1736	2.40	10.9085	3.09	0.4557	1.94	0.63	2593	40	2421	39	2515	29	96
14	0.07	744970.9	504.2569	0.97	0.1285	2.24	5.2490	2.90	0.2962	1.84	0.64	2078	39	1672	27	1861	25	90
15	1.78	1531072	1868.107	0.98	0.2136	2.69	4.8395	3.92	0.1643	2.85	0.73	2933	44	981	26	1792	33	55
16	1.42	852322.7	1530.352	2.82	0.1415	2.80	2.1781	4.25	0.1117	3.19	0.75	2245	48	682	21	1174	30	58
17	0.40	1542301	1352.861	0.72	0.1633	2.20	5.1456	2.88	0.2286	1.87	0.65	2490	37	1327	22	1844	25	72
18	1.16	1249016	1755.684	3.06	0.1479	2.51	2.9089	3.55	0.1426	2.52	0.71	2322	43	860	20	1384	27	62
19	2.10	699735.4	437.1664	0.43	0.2630	2.76	11.6375	3.58	0.3209	2.27	0.64	3265	43	1794	35	2576	34	69
20	0.96	1492847	1564.589	1.19	0.1475	2.30	3.8911	3.21	0.1913	2.23	0.70	2317	39	1128	23	1612	26	70
27	0.90	1330235	1549.505	0.99	0.1417	2.37	3.3624	3.24	0.1721	2.20	0.68	2248	41	1024	21	1496	26	68
28	1.00	179089.1	88.73375	1.84	0.1373	2.84	7.6590	3.46	0.4047	1.99	0.57	2193	49	2190	37	2192	32	100
29	0.13	577693.5	479.4644	2.19	0.1217	1.93	4.0542	2.74	0.2416	1.94	0.71	1982	34	1395	24	1645	23	85
30	0.52	355394.3	202.7906	1.74	0.1335	2.35	6.4656	3.02	0.3514	1.90	0.63	2144	41	1941	32	2041	27	95
31	1.00	498812.1	252.1849	2.38	0.1332	2.56	7.2835	3.22	0.3966	1.96	0.61	2141	45	2153	36	2147	29	100
32	0.47	1110303	708.2636	1.59	0.1306	2.08	5.6596	2.88	0.3143	1.99	0.69	2106	36	1762	31	1925	25	91
33	0.84	370747.7	262.622	2.43	0.1761	2.32	6.8719	3.12	0.2830	2.09	0.67	2616	39	1607	30	2095	28	76
34	0.19	681428	327.9661	1.54	0.1396	2.39	8.0166	3.08	0.4166	1.94	0.63	2222	41	2245	37	2233	28	100
35	0.50	262527.9	128.2043	2.23	0.1371	2.96	7.7629	3.55	0.4106	1.95	0.55	2191	52	2217	36	2204	32	100
36	4.97	327283.9	264.1939	3.73	0.3993	3.29	13.6738	5.55	0.2484	4.47	0.81	3906	49	1430	57	2727	54	52
37	0.17	1395503	1204.967	0.26	0.1250	1.85	4.0010	2.76	0.2322	2.05	0.74	2028	33	1346	25	1634	23	82
38	1.00	219994.1	160.586	1.70	0.1597	2.39	6.0482	3.26	0.2747	2.22	0.68	2453	41	1564	31	1983	29	79
39	0.32	667790.6	368.0409	2.14	0.1356	1.99	6.8019	2.85	0.3638	2.04	0.72	2172	35	2000	35	2086	25	96
40	0.02	1649409	726.6904	1.18	0.1728	1.98	10.8441	2.80	0.4551	1.98	0.71	2585	33	2418	40	2510	26	96
47	0.02	700596.6	460.374	2.19	0.1350	2.12	5.6811	2.86	0.3051	1.92	0.67	2165	37	1717	29	1929	25	89
48	0.00	231446	105.0306	2.14	0.1731	1.99	10.5447	2.86	0.4418	2.05	0.72	2588	33	2359	40	2484	27	95
49	0.01	1345943	377.2558	2.87	0.2944	2.21	29.0351	2.93	0.7153	1.92	0.65	3441	34	3478	52	3455	29	100
50	1.00	359886.7	125.8378	1.69	0.2104	3.85	16.6365	4.38	0.5734	2.10	0.48	2909	62	2922	49	2914	43	100
51	1.00	368094.1	177.8925	1.33	0.1403	2.68	8.0257	3.36	0.4149	2.02	0.60	2231	46	2237	38	2234	31	100
52	0.50	866134	724.055	1.69	0.1289	2.13	4.2624	2.99	0.2398	2.10	0.70	2083	37	1386	26	1686	25	82
53	0.20	726823.1	289.0991	1.50	0.1758	2.26	12.2157	2.96	0.5041	1.90	0.64	2613	38	2631	41	2621	28	100
54	2.26	1747592	2878.776	0.53	0.1669	3.33	2.8007	5.42	0.1217	4.28	0.79	2527	56	740	30	1356	41	54
55	0.38	1270666	642.6569	2.08	0.2166	1.97	11.8390	2.79	0.3964	1.97	0.71	2956	32	2153	36	2592	26	83
56	0.11	1028962	841.0188	1.40	0.1296	2.18	4.3820	2.93	0.2453	1.95	0.67	2092	38	1414	25	1709	24	82
57	0.53	477408.2	509.34	3.91	0.1401	2.27	3.6295	3.04	0.1879	2.02	0.67	2228	39	1110	21	1556	24	71
58	0.43	1079619	1839.673	1.52	0.0993	2.18	1.6114	3.03	0.1177	2.11	0.70	1612	41	717	14	975	19	73
59	0.37	726557.5	1370.725	3.62	0.0925	2.55	1.3550	3.32	0.1063	2.13	0.64	1477	48	651	13	870	20	75
60	0.15	1237412	1586.374	1.21	0.1373	2.08	2.9597	2.86	0.1564	1.97	0.69	2193	36	937	17	1397	22	67
67	0.26	287258.9	175.6452	2.27	0.1383	2.36	6.2504	3.16	0.3279	2.11	0.67	2205	41	1828	33	2012	28	91
68	0.46	560096.7	248.6652	4.85	0.2492	2.14	15.5190	2.91	0.4516	1.97	0.68	3180	34	2402	39	2848	28	84
69	1.66	1070468	1635.02	1.54	0.1867	3.03	3.3793	4.40	0.1313	3.20	0.73	2713	50	795	24	1500	35	53
70	0.16	514889.9	392.1644	2.59	0.1311	2.06	4.7576	2.87	0.2632	1.99	0.70	2112	36	1506	27	1777	24	84
71	0.19	1104091	391.5197	1.30	0.1797	2.27	14.0126	3.00	0.5654	1.97	0.65	2651	38	2889	46	2751	29	105
72	0.34	1231415	955.8345	1.62	0.1284	2.17	4.5742	2.95	0.2583	2.01	0.68	2077	38	1481	26	1745	25	85
73	0.63	999689.2	1824.591	0.57	0.0960	2.71	1.4533	3.54	0.1099	2.28	0.64	1547	51	672	14	911	21	74
74	0.67	721218.2	1279.935	0.98	0.0910	2.50	1.4179	3.48	0.1130	2.42	0.70	1447	48	690	16	896	21	77
75	0.68	1355628	787.3516	0.52	0.1878	2.12	8.9401	2.97	0.3452	2.09	0.70	2723	35	1912	34	2332	27	82
76	0.07	427408.1	215.685	1.36	0.1422	2.13	7.7905	2.92	0.3973	2.00	0.69	2254	37	2157	37	2207	27	97
77	0.16	204055	99.93639	1.43	0.1380	2.23	7.7868	3.00	0.4094	2.01	0.67	2202	39	2212	37	2207	27	100
78	0.42	1242908	832.7164	0.88	0.1808	2.03	7.4601	2.91	0.2993	2.08	0.72	2660	34	1688	31	2168	26	78
79	0.84	939396	528.0744	1.23	0.1396	2.30	6.8655	3.16	0.3567	2.17	0.69	2222	40	1966	37	2094	28	94
80	1.00	1582554	529.0929	1.95	0.2242	2.48	18.5388	3.17	0.5997	1.98	0.62	3011	40	3029	48	3018	31	100
87	0.47	1238282	1664.953	0.67	0.1409	3.28	2.8979	3.91	0.1491	2.14	0.55	2239	57	896	18	1381	30	65
88	0.42	1549132	2946.626	1.30	0.0737	2.34	1.0712	3.26	0.1054	2.27	0.70	1033	47	646	14	739	17	87
89	0.00	606585	183.2607	2.34	0.2626	2.65	24.0246	3.37	0.6636	2.09	0.62	3262	42	3281	54	3269	33	100
90	0.00	169913	367.4624	0.48	0.0584	2.71	0.7464	3.46	0.0927	2.15	0.62	544	59	572	12	566	15	101
91	0.00	177735	381.5993	0.47	0.0588	2.31	0.7566	3.08	0.0934	2.03	0.66	558	50	576	11	572	13	100

Source: Elaborated by the author

The probability density plot displays one main cluster at 2.1-2.2 Ga, whereas secondary grains are spread between Archean ages at 2.6 Ga, 2.8-3.0 Ga and 3.2-3.4 Ga. Thorium/U ratios range from 0.66 to 2.99.

Although only the concordant grains are used in the provenance analysis and relative probability density plot of Figure 4.16A, it is noteworthy that some of the discordant grains align in a Discordia (Figure 4.16B) with an upper intercept at ca. 2.9 Ga and a lower intercept at 573 ± 39 Ma (MSWD 6.9).

Figure 4.16 — A) Relative probability density plot of U–Pb detrital zircon ages obtained from a metaconglomerate (sample AC01). For comparison, the age distributions of different tectonic-magmatic events in the QFe region are marked (Farina et al. 2016; Aguilar et al. 2017). B) Concordia diagram for metaconglomerate (sample AC01) showing discordant zircon grains that align in a Discordia with an upper intercept at ca. 2.9 Ga and a lower intercept at 573 Ma.

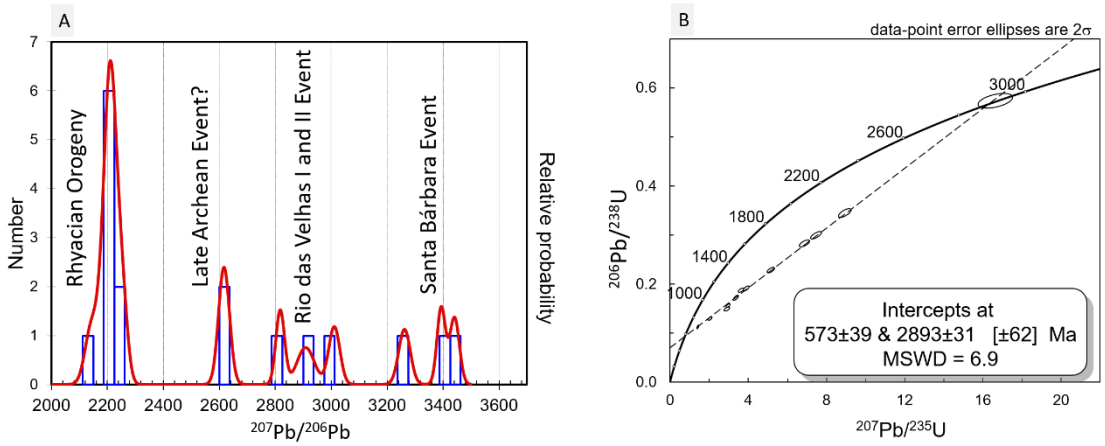

Source: Elaborated by the author

4.6 Discussion

4.6.1 Assessment of lithochemical and C-O isotope data as seawater geochemistry proxies

The discussion about the preservation of original seawater chemical and isotopic composition is important to Precambrian carbonates because ancient rocks may have been subject to post-depositional changes during diagenesis, metamorphism, weathering

and/or hypogene hydrothermal alteration (Kaufman and Knoll, 1995; Maheshwari et al., 2010; Caxito et al., 2019).

There are various proxies that can be used to infer the extent and intensity of post-depositional alteration. For example, very negatively fractionated O-isotope compositions are commonly interpreted as due to interaction with post-depositional fluids, although the cutoff limits are somewhat arbitrarily set in different works. This could suggest that the upper part of the studied drill core, where dolomitic BIF prevails, would show the highest degree of alteration, due to the lower $\delta^{18}O$, generally below -10‰. In comparison, the dolomites of the Gandarela Formation show higher $\delta^{18}O$ values around -5‰, which could indicate a more preserved original seawater signature.

Indeed, in the $\delta^{18}O$ versus $\delta^{13}C$ diagram proposed by Hudson (1977) and modified by Nelson and Smith (1996), where the identification of different origins of carbonates is assessed, the dolostone samples from the Gandarela Formation plot within the marine limestone field. This is consistent with the regional understanding of evolution of the depositional systems in the carbonate precipitation of the Gandarela Formation (e.g., Nogueira et al., 2019). It is important to notice that the definition of the marine limestone field suggests that dolomite was formed diagenetically, as a product of dolomitization processes. Alternative explanations for mechanisms of dolomite formation are argued by several authors, for example, reactions with seawater (Machel, 2003), bacterial mediation (Warren, 2000; Spier et al., 2007) or primary abiotic precipitation from a CO_2-rich hydrothermal-seawater fluid (Morgan et al., 2013).

Although the dolomitic BIFs show generally more negatively fractionated carbon and oxygen isotope values than the dolomites, cross-plotting of the whole dataset shows, however, that although generally speaking higher $\delta^{18}O$ values are associated with higher $\delta^{13}C$, the correlations are not so perfectly defined, and a high degree of scattering can be observed, both within each unit and in comparison, to the entire stratigraphic dataset. Figure 4.17 also compares the data obtained in the Segredo deposit in this study with data obtained for metamorphosed but relatively unaltered QFe rocks from other works (Bekker et al., 2003; Spier et al., 2007; Morgan et al., 2013; Teixeira et al., 2017). The data obtained from the Segredo deposit is shown to be consistent with the amassed dataset for the whole QFe.

Figure 4.17 — Carbon and oxygen isotopes of BIF, dolostones and intraformational metaconglomerate of the Segredo deposit. For comparison, data collected in the QFe by other works are also plotted. Key: Carbonate Rocks – Qfe: calcites, dolomites, limestones and dolomitic limestones from Extramil Quarry, Hargreaves Quarry, Gandarela Farm and Socorro Quarry (Bekker et al., 2003; Morgan et al., 2013). BIF – Qfe: results obtained in Águas Claras and Alegria mines (Spier et al., 2007; Morgan et al., 2013; Teixeira et al., 2017).

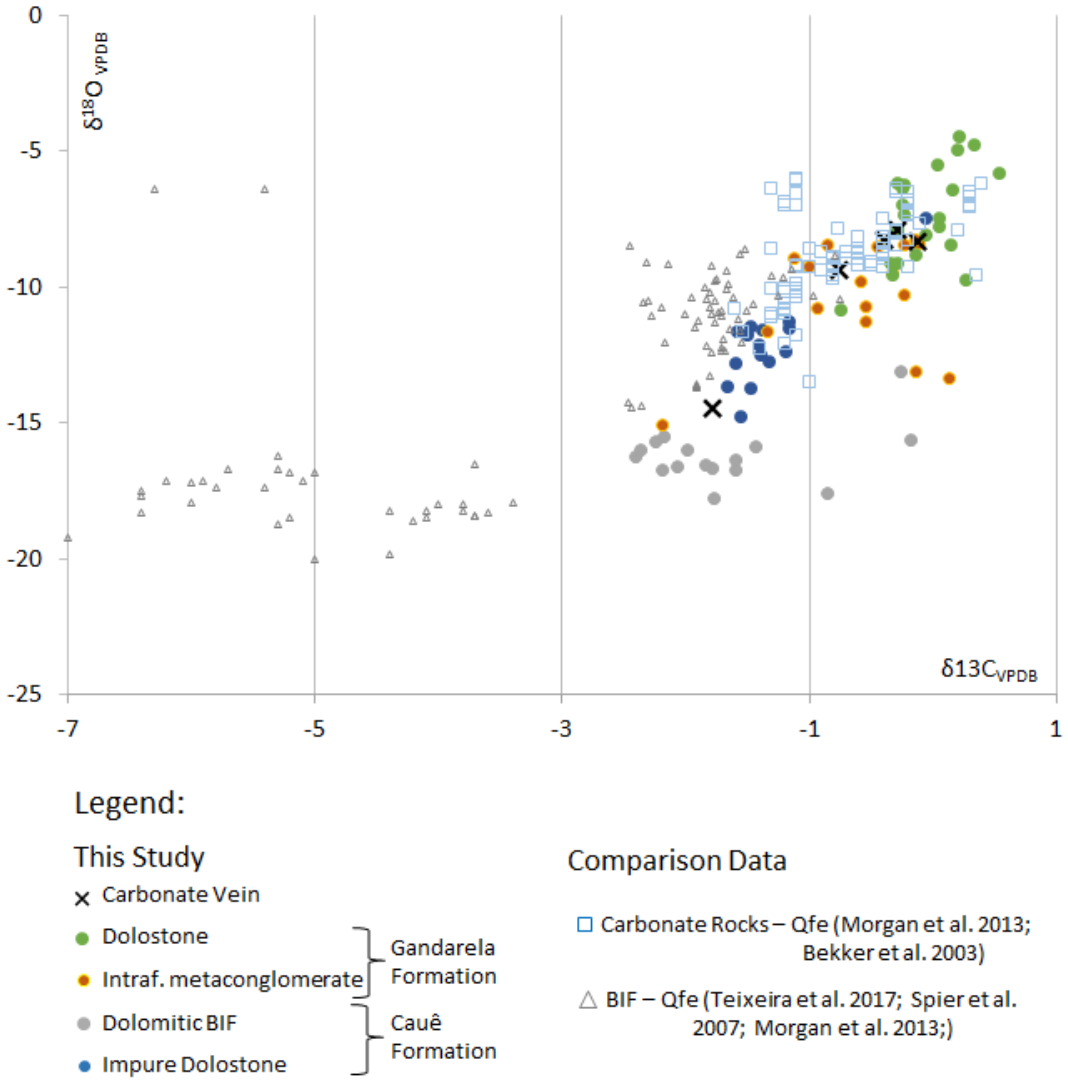

Source: Elaborated by the author

Figure 4.17 illustrates that data from carbonate rocks of the Gandarela Formation normally cluster around $\delta^{13}C$ = -2‰ to 1‰ and $\delta^{18}O$ from -15‰ to -5‰, with increasing up section values. The repetition of this pattern in various works conducted in different

areas of the QFe indicates that this is probably a regional and primary signature of the Gandarela dolostones.

On the other hand, dolomitic BIFs of the Cauê Formation show variable values, either clustering along with the Gandarela rocks or defining a very distinct pattern with scattered lower $\delta^{13}C$ around -1 to -7‰ defining a horizontal array around roughly the same $\delta^{18}O$, between -20 and -15‰. Thus, dolomitic BIFs of the Cauê Formation regularly show lower negatively fractionated C and O isotope signatures, indicating that the signal obtained in this study is not exclusive of the Segredo deposit and is probably also a primary signature of the BIF. An explanation for the consistently lower C-O values of the dolomitic BIF is presented by Teixeira et al. (2017), which detected a correlation of the negatively fractionated C-isotopic values with positively fractionated $\delta^{56}Fe$ values occurring in the same stratigraphic interval, and interpreted this double signal as generated by the influence of microorganism activity in the dissimilatory iron reduction (DIR) of the precursor ferric oxides. To test for this hypothesis in other locations, including the Segredo deposit, further iron isotope determinations in conjunction with C-O isotope systematics are necessary.

The main evidence of local hydrothermal alteration in the Segredo deposit is the calcite or quartz veins and subordinately, chlorite veinlets. The last may result from hydrothermal alteration related to decarbonation reactions, a process responsible for the formation of Ca-Mg silicates in the presence of siliciclastic rocks and ^{12}C rich - CO_2 release due to kinetic fractionation (Kaufman and Knoll, 1995). Besides that, the abundance of chlorite as thin blades parallel to the bedding suggests the formation of the mineral as a product of the greenschist facies metamorphism at the Segredo deposit. However, the isotopic composition of postdepositional carbonate veins obtained in this study is variable in depth and displays $\delta^{18}O$ ratios similar to the dolostones intercepted by veins. Likely, the succession of rocks from the Itabira Group and carbonate veins attained close to isotopic equilibrium with the adjacent rocks. Furthermore, the $\delta^{13}C$ values define identical trends of the BIF and dolostones. This reinforces that processes of carbonate formation and their interaction with fluids did not promote extensive exchange of the isotopic composition in the Segredo deposit.

Finally, the $\delta^{18}O$ reaching a minimum of -17.6‰ and maximum -4.47‰ in the Segredo mine are also consistent with other well-preserved Paleoproterozoic carbonate rocks from South Africa and Australia (Veizer et al., 1989, 1992; Bekker et al., 2003).

Regarding the trace element composition, the chemical rocks of the studied drill core show Y/Ho ratios which are typical of Archean and Paleoproterozoic iron-rich sedimentary rocks (Planavsky et al., 2010), indicating a generally good preservation of seawater signals. Kaufman and Knoll (1995) suggest the Mn/Sr index to analyze the degree of alteration of the rocks by weathering. The results may indicate the representativeness of the isotopic results, in relation to primary C-isotope values. The dolostone in the Segredo deposit shows Mn/Sr ratios >32 and no significant correlations were shown between Mn/Sr and $\delta^{13}C$ as well as $\delta^{18}O$.

According to the authors, the Mn/Sr ratios <10 in carbonates demonstrates the substitution of Sr by Mn due to percolation of meteoric fluid. However, authors do not recommend the use of the index rigorously, as the substitution of Sr by Mn may not change the chemistry of the major elements. Nevertheless, the index of alteration is not easily applied to Paleoproterozoic rocks (Veizer et al., 1992; Bekker, 2003).

All dolomitic BIF and dolostone present in the Segredo deposit exhibit a uniform average Mg/Ca ratio of 0.7 (Figure 4.7A) and $CaMgCO_3$ (dolomitic) composition (Figure 4.8B). Some alteration halos composed of Fe-Mn dolomite were identified in the intraformational metaconglomerate. The hydrothermal alteration is restricted to the clast borders and probably results from limited hydrothermal fluid flow in the reactive surface of the clasts. In addition, dolomites have a homogeneous texture, in contrast to the granular texture of the dolomite veins.

Beukes et al., (2003) proposed that BIF - banded carbonate-hematite rock, from the Águas Claras mine (QFe), results from a local hydrothermal metasomatism responsible for the replacement of chert bands by hydrothermal dolomite. Based on the chemical results and field evidence obtained in this study, the presence of dolomite in the BIF is interpreted as a variation of the sedimentary facies (James, 1954). Moreover, similar ideas are presented in the regional investigations about the BIF mineralogy in the QFe (Spier et al., 2007; Rosière et al., 2008; Teixeira et al., 2017).

4.6.2 Implications for depositional conditions and the global Paleoproterozoic BIF, oxygenation and climatic records

As demonstrated in the discussion above, despite complex deformation and greenschist facies metamorphism of the host rock in the Segredo deposit, the carbon isotope variations (Figure 4.17), the content of major oxide elements, mainly SiO_2 and Al_2O_3 (Figure 4.7A) and the REEY signatures (Figure 4.14 B) suggest that the isotopic and chemical signals can be conservatively interpreted as representative of primary signature, albeit post-depositional alteration, especially for the samples with the more negatively fractionated oxygen isotope compositions, can not be completely ruled out. There is no clear evidence that metamorphic reactions that could have been responsible for loss of CO_2 and oxygen isotope fractionation, could significantly alter the REEY abundance in the studied rock units. The distribution of the total REEY contents seems to be more clearly related to the lithology/mineralogical content to possible metamorphic overprints, as shown in Figure 4.14B. Additionally, distinctive signatures of chemical rocks of the Cauê and Gandarela formations indicate that they show different geochemical and isotopic features that can be used to recognize their limits and transition in the field and drill cores.

Accordingly, syngenetic processes for this lithological arrangement are interpreted. The dolomitic BIF intercalated with impure dolostones at the intervals of 184.75 to 316.45 meters deep in the drill hole are grouped into the Cauê Formation (Figure 4.7A), whereas the pure carbonates (from 390.70 meters up to the bottom of the hole) are attributed to the Gandarela Formation. This lithostratigraphic framework, with distinctive isotopic signatures and precipitation of distinct mineral phases, is a result of precipitation in a shallow-water basin under changing geochemical conditions. During deposition of the Cauê BIF, microbial DIR was an important process in the bottom sediment, converting amorphous iron-rich phases such as ferrihydrite to reduced iron minerals and impinging a biological-related negatively fractionated carbon isotope signature to the dolomitic matrix (Teixeira et al., 2017). Shutting down of the iron shuttle then caused an iron famine and microbial DIR was not able to operate during the deposition of the overlying Gandarela dolomites, which display carbon and oxygen isotope compositions which are

progressively closer to the original seawater, not being altered by microbial processes. Following this interpretation, the carbon biological pump operated under “normal” conditions during the deposition of the Gandarela Formation, with carbon isotope signatures close to the value of the standard Vienna Pee Dee Belemnite. The progressively higher $\delta^{18}O$ towards the top of the unit could indicate the progressive shallowing of the basin, with higher evaporation rates.

Several studies (Hoffman et al., 1998; Bekker et al., 2003; Gumsley et al., 2017) use stable isotope proxies to investigate the drastic climate changes during the Proterozoic eon. These studies include the discussion about the coexistence of cap carbonates and glacial events in low latitude terrains around the world. In Brazil, isotopic composition obtained at the QFe region reveals that the Minas Supergroup may record a global glaciation during Paleoproterozoic evolution (Bekker et al., 2003, Nogueira et al., 2019). Bekker et al. (2003) argued that isotopic changes are correlated with North American glacial events, although no evidence of glaciation has been identified in the Minas Basin. The lack of evidence was associated with erosional processes. On the other hand, the ranges of C isotopes in the Segredo deposit shows no evidence of glacial events concurrently with the formation of the Itabira Group.

The discussion of REE signatures, considering variations in the Ce (III and IV) and Eu (III and II) elements, contributes to the analysis of marine redox conditions and fluid-rock interaction in the Minas Basin. Contributions of Graf (1977), Fryer et al. (1979), Viehmann et al. (2015), Uhlein et al. (2021) indicate that the REEY pattern of chemical precipitates is subject to change by terrigenous contamination, furthermore, Nothdurft et al. (2004) mentioned that <1-2% of terrigenous inputs (e.g., Al, Zr, Th, and Sc) can influence the seawater pattern recorded in rocks. In the Segredo deposit, the sum of Al, Zr, Th, and Sc contents ranges between 0.04% and 0.61% with one outlier at 1.22%. The low detrital input demonstrated that chemical sediments from Segredo deposit is devoid of significative detrital input. It should be noted that the intraformational metaconglomerate matrix, belonging to the chemical domain, shows no clastic contribution, being composed of carbonate itself. This characteristic, associated with their oligomictic composition and C-isotope pattern, suggests that their formation results from

sediment-gravity flow in a slope wedge, reworking the platformal carbonate itself. Therefore, no evidence was found for glacial records.

The behavior of Y/Ho, Ce/Ce* and Pr/Pr* ratios in BIF and dolostones at the Cauê Formation is compatible with Paleoproterozoic and Archean BIF. The positive Eu anomaly found in some rocks of the Segredo deposit is consistent with the reference values of most Early Proterozoic and Archean BIFs (Isley, 1995; Bekker et al., 2010; Rosière et al., 2008). This is interpreted as resulting from a mixing of seawater and submarine hydrothermal iron-bearing fluids. Fryer et al. (1979) discussed whether the anomaly is derived from a local hydrothermal input related to BIF precipitation or is reflected in marine chemistry in ancient times. Negative Ce anomalies reflect a locally oxygenated ocean during carbonate precipitation of the Gandarela Formation. The dolomitic BIF Ce/Ce* ratios of the Cauê Formation are, on the other hand, scattered and not conclusive.

Finally, the chlorite-phyllite (sample A074) is restricted to a cm-thin layer in the contact of the intraformational metaconglomerate and dolostones (Gandarela Formation). It is rich in Fe_2O_3 (24.32%), MgO (22.52%) and Cr_2O_3 (977ppm). Analyses of petrogenetic diagrams indicates correlation between Cr and Ti contents and might be interpreted as similar to the geochemical signature of an oceanic floor basalt protolith for the sample. Thus, this rock could tentatively be interpreted as a metamorphosed mafic volcanic rock, but this possibility must be assessed through further studies.

4.6.3 Interpretation of Detrital Zircon data

In the studied drill core, the initial rock sequence reaches 184.75 meters and exhibits various levels of polymictic conglomerate directly in contact with the dolostones of the Cauê Formation. The provenance of zircon crystals recovered from this conglomerate was based on the U/Pb frequency histogram and probability density plot (Figure 4.16A), which shows ages related to Archean basement (ages at 2.6 Ga, 2.8-3.0 Ga and 3.2-3.4 Ga) and to the magmatism (age 2.1-2.2 Ga) formed during supercontinent amalgamation in Paleoproterozoic times. Thus, we interpret this conglomerate as related to the final stages of the Wilson cycle in the Minas Basin, represented by the inversion of

the basin and deposition of the Sabará Group. This supracrustal sequence was deposited in a synorogenic foreland basin related to the Rhyacian accretionary orogeny.

The age of metamorphism dated in the metaconglomerate of the Sabará Group, in the Segredo deposit, is determined to be 573 ± 39 Ma, as suggested by the lower intercept of the Discordia line in the Concordia diagram in Figure 4.16B, corresponding to the linear regression of 14 discordant zircon crystals obtained in this study, interpreted as due to the effects of partial lead loss due to irregularities in the crystalline structure, such as microfractures or micro-capillary network of zircon crystals.

This age is consistent with the regional thermal event known as Brasiliano Orogeny, related to western Gondwana amalgamation. Thus, the results provide evidence for the importance of the last significant disturbance in the rocks of the QFe registered at the Brasiliano collage, responsible for greenschist facies metamorphism and probable hydrothermal effects (e.g., Dias et al., 2022).

Other post-depositional processes, such as hypogene hydrothermal alteration and Fe ore mineralization to which the Minas Supergroup rocks were submitted may have promoted iron enrichment of the BIF. At Segredo deposit, near the surface high grade iron ore was developed, while underneath the zone of weathering, dolostones and dolomitic BIF are predominant (Figure 4.5). This suggests that weathering alteration may be responsible for leaching of carbonate and, consequently, residual iron oxide concentration. Ribeiro et al. (2002) and Ribeiro et al. (2021) elucidate the role of weathering in the enrichment of BIF, through the processes of dissolution, transport and collapse of the residual layers.

4.7 Conclusions

Based on new lithostratigraphic, petrographic, elemental geochemistry and isotopic data, we characterized detrital and chemical sedimentary rocks of the Minas Supergroup in the Segredo deposit and proposed depositional and paleoenvironmental settings. The Itabira Group is marked by the transition of dolomitic BIF and dolostone of the Cauê Formation to pure dolostones of the Gandarela Formation. Those are capped, above an unconformity, by conglomerates of the Sabará Group, with detrital zircon U-Pb

data indicating provenance areas that sourced the main Archean and Paleoproterozoic igneous rocks of the QFe, with main sources located in Rhyacian orogenic rocks (ca. 2.2 Ga).

The Cauê and Gandarela formations show devoid of significative detrital input and the REEY signatures of these chemical rocks with local Ce and Eu anomalies indicating the importance of oxygenation pulses and hydrothermal input of iron to seawater.

The carbon isotopic composition of the Itabira Group in the Segredo is marked by a gradual increase of $\delta^{13}C$ and $\delta^{18}O$ values from the dolomitic itabirites of the Cauê Formation towards the dolostones of the Gandarela Formation, from slightly negatively to slightly positively fractionated values for carbon and from ca. -15 to ca. -4 per mil for oxygen. Comparison with literature data for both units indicates very similar results throughout the QFe, suggesting the values reflect the regional fluid composition and a probable syndepositional origin for the isotopic signatures. The negatively fractionated values obtained for the Cauê Formation are consistent with previous works that suggested the operation of microbially induced processes such as DIR in the deposition of the iron-rich sediments, while an iron famine during the deposition of the Gandarela Formation leads to values that are closer to the original seawater signatures.

The deposition of intraformational metaconglomerate at ca. ~ 2.4 Ga in the Itabira Group was associated with debris flows in areas of slope resedimentation at the edges of the carbonate platform. Thus, no evidence of glaciation was yet identified in the Minas Supergroup.

4.8 Acknowledgments

The authors would like to thank the mining company VALE S.A. for its collaboration and financial support, especially through ADIMB collaborative project: VALE - UNIVERSITIES - INSTITUTIONS. FAC, ANS and CL are recipients of Research Productivity Grants from the Conselho Nacional de Pesquisa Científica (CNPq) and acknowledge for the support received. We thank the funding agency FAPEMIG for supporting the research through grant nb. PPM-00618-18. This is a contribution to Project MOBILE (geolifemobile.com), supported by Instituto Serrapilheira, Brazil (grant nb Serra-

1912-31510). We would like to express our gratitude to the staff of the Stable Isotope Laboratory (NEG-LABISE – UFPE), High Purity Mineral Separation Laboratory (CPMTC – UFMG) and Radiogenic Isotope Laboratory (UFOP). We thank everyone that somehow contributed to accomplish this study. An original version was improved after comments and suggestions by Gabriel Uhlein and an anonymous reviewer.

5 SCIENTIFIC CONTRIBUTIONS II

This paper proposes a paleo-salinity and -redox reconstruction of the Minas Basin that reveals a transition of the watermass, from freshwater to marine conditions and a redox state during the sedimentation through the Paleoproterozoic. The paper was submitted to *Chemical Geology* (Paper number: CHEMGE18144) on February 28, 2025 and it was accepted for publication on May 8, 2025.

TRACE ELEMENT AND IRON SPECIATION ANALYSIS OF PALEOPROTEROZOIC PHYLLITE FROM THE GANDARELA SYNCLINE: IMPLICATIONS FOR SALINITY AND REDOX CONDITIONS IN THE QUADRILÁTERO FERRÍFERO, BRAZIL

Janaina Rodrigues de Paula[1], Wei Wei[2, 3]*, Fabricio A. Caxito[1], Katherine N. Snihur[3], Cody N. Lazowski[3], Kurt O. Konhauser[3], Erik A. Sperling[4], Daniel S. Alessi[3]

[1] Universidade Federal de Minas Gerais, Programa de Pós-graduação em Geologia, Instituto de Geociências, Departamento de Geologia, CPMTC-IGC, Brazil, 31270-901

[2] School of Earth Science, China University of Geosciences (Wuhan), Wuhan, Hubei Province, China 430074

[3] Department of Earth and Atmospheric Sciences, University of Alberta, 1-26 Earth Sciences Building, Edmonton, Alberta, Canada T6G 2E3

[4] Department of Geological Sciences, Stanford University, Stanford, CA, USA, 94305-2115

*Corresponding author: Wei Wei

Email address: weiwei910911@163.com

5.1 Abstract

The Quadrilátero Ferrífero, Brazil, is among the most significant iron ore provinces. This study utilizes geochemical proxies, including elemental paleosalinity ratios (B/Ga, Sr/Ba, S/TOC), redox-sensitive elements (RSE), and iron speciation, to investigate water mass evolution. Samples were analyzed from three drill cores and four outcrops in the Gandarela Syncline, providing new insights into the Paleoproterozoic phyllites associated with the Cauê BIF. Although metamorphism of these rocks might affect the application of

the proxy, consistent directional trends in proxy results indicate a refined and/or robust paleoenvironmental reconstruction of the Minas Basin. Paleosalinity data indicate a transition from freshwater to low-brackish conditions during early sedimentation (Caraça Formation), followed by predominantly marine conditions during the deposition of the Cauê, Gandarela, and Cercadinho Formations. This model revises earlier interpretations suggesting an initial dominance of marine facies during fine sediment deposition in the Batatal Formation. Elevated concentrations of trace elements (Cu, Ni, and Zn) in carbonaceous phyllites highlight the role of microbial activity in bioproductivity before BIF deposition. Additionally, the decreasing enrichment factor (EF) of Mo_{EF}/U_{EF} ratio and RSE concentrations toward younger rocks, coupled with variations in Fe_{HR} (highly reactive iron), suggest that the early basin waters were characterized by anoxic to suboxic conditions, with free O_2 likely present in surface waters. These results point to a stratified water column, featuring an oxic surface layer overlying ferruginous, anoxic water. This study advances understanding of the paleoenvironmental evolution of the Minas Basin and the depositional processes that facilitated the formation of the Quadrilátero Ferrífero's giant BIF-hosted iron systems. It also underscores the value of paleosalinity proxies for reconstructing environmental conditions in Paleoproterozoic systems, while also highlighting the need for more studies of how paleoenvironmental proxies behave during metamorphism.

Key-words: Paleosalinity, Redox-sensitive elements, Cauê BIF, Minas Supergroup, Paleoenvironmental reconstruction

5.2 Introduction

The Quadrilátero Ferrífero is among Brazil's most important iron ore deposits (Dorr, 1969; Rosière and Chemale, 2000; Hagemann et al., 2016). In addition to the economic benefits, Banded Iron Formation (BIF) are chemical archives of Precambrian seawater and therefore integral for understanding the evolution of early Earth (Spier et al., 2007; Konhauser et al., 2017). Previous research has suggested that the Paleoproterozoic rocks in this region were primarily deposited in a partially oxidized ocean (e.g. Spier et al., 2007; Rosière et al., 2008; Mendes et al., 2016). Several studies have been carried

out on trace elements and stable isotopes such as carbon (C), iron (Fe), chromium (Cr), and oxygen (O2) in BIF and associated carbonate rocks. Studies by Bekker et al. (2003), Morgan et al. (2013), Teixeira et al. (2017), Sampaio et al. (2018), and de Paula et al. (2023) have discussed the role of dissimilatory iron reduction (DIR) in the diagenesis of the primary iron-rich mineral phases comprising BIF. These studies have also correlated the iron deposits of the Quadrilátero Ferrífero with other Paleoproterozoic giant BIF-hosted iron systems in South Africa and Western Australia. Despite these advances, no investigations have focused on paleo-salinity and its relationship with redox conditions within the Quadrilátero Ferrífero. This gap underscores the limited understanding of paleo-water mass evolution in this region, obscuring the formation mechanism of the BIF developed in this area. Therefore, an integrated approach is imperative to obtain more insight into the depositional reconstruction of this geological region and improve our knowledge of the Paleoproterozoic biogeochemical process.

Salinity and redox conditions are intrinsic water mass properties that can provide insights into the geochemical evolution of ancient sedimentary environments over time (Wei and Algeo, 2020; Gilleaudeau et al., 2021; Song et al., 2021; Remírez et al., 2024). The temporal and spatial distribution patterns of these properties in the water column are associated with various factors, including watershed morphology, detrital input, connectivity with the open ocean, and other related processes (Algeo and Tribovillard, 2009; Zhang et al., 2017; Wei et al., 2018; Gilleaudeau et al., 2021). Thus, water mass properties such as density, salinity, redox state and temperature may relate closely to the formation of mineral resources, including Fe, manganese (Mn), and hydrocarbons, and is therefore of economic significance (e.g. Xu et al., 2015; Konhauser et al., 2017; Wei et al., 2024). Specifically, paleo-salinity and paleo-redox proxies may help link the evolution of the atmosphere, hydrosphere and biosphere to regional and global events (e.g. Tribovillard et al., 2006; Konhauser et al., 2017; Wei and Algeo, 2020), such as the Great Oxidation Event (GOE) at ~2.5 billion years ago (Large et al., 2022).

This study investigates the paleoenvironmental evolution of the Minas Basin using geochemical and iron speciation analyses of Paleoproterozoic phyllites from the Gandarela Syncline, northeastern Quadrilátero Ferrífero, Brazil. The analyzed samples, deposited before and after the giant BIF-hosted iron systems (Cauê BIF), provide insights

into paleoenvironmental reconstruction of the study area. The dynamic of paleosalinity and paleo-redox conditions influenced the geochemical cycles within the basin which contributed to iron ore genesis. Samples from three drill cores and outcrops were analyzed for paleosalinity proxies: boron (B)/ gallium (Ga), strontium (Sr)/ barium (Ba) and sulfur (S)/ total organic carbon (TOC), Fe speciation and RSE enrichment (e.g. molybdenum (Mo), nickel (Ni), uranium (U)). Although all proxies are likely affected by regional greenschist metamorphism (see below), the consistent trends in geochemical data can be interpreted as reflecting changes in the original seawater composition. The integrated geochemical data indicate a progressive transition from freshwater-brackish conditions during deposition of the Caraça Group to marine facies (Itabira and Piracicaba groups) within a predominantly ferruginous, anoxic basin. These findings revise the previous model, that suggests marine facies were widely established in the Minas Basin during the early stages of BIF deposition.

5.3 Geologic Background

The Quadrilátero Ferrífero province, which covers approximately 15,000 km^2, is situated within the São Francisco Craton in southeastern Brazil (Figure 5.1). It is renowned for its world-class gold and iron deposits (Lobato et al., 2001; Rosiere et al., 2008). Despite more than 80 years of iron mining, the giant Paleoproterozoic iron deposit, the Cauê BIF, still contains over 25 Gt, with an average grade of 43% Fe, as reported resources (Vale, 2024). The present study is focused in the Gandarela area, which resides in the northeastern region of the Quadrilátero Ferrífero (Figures 5.1 and 5.2). The area's structural framework is defined by the Gandarela syncline, a reclined fold with an NE-SW striking axial trace and an SE-plunging hinge line (Chemale et al., 1994; Oliveira et al., 2005).

The study area is dominated by the Paleoproterozoic strata from the Minas Supergroup and our research focuses on the phyllite layers deposited before, and after, the Cauê BIF layer (~2.4 Ga) (Figure 5.2). The metasedimentary rocks of the Minas Supergroup record repeating transgressions-regressions marine cycles in the Minas Basin (Dorr, 1969; Canuto, 2010; Gonçalves and Uhlein, 2022) and are classified into

three units from the base to top, named the Caraça, Itabira and Piracicaba groups (Figure 5.2), according to the subdivision proposed by Endo et al. (2019, 2020), based on Dorr (1969). At the stratigraphic base, the Caraça Group is composed of conglomerate and quartzite overlain by phyllite, minor BIF and carbonate rocks, all of which are interpreted to reflect the depositional evolution from alluvial to fluvial, lacustrine and deltaic to marine environments (Dorr, 1969; Madeira et al., 2019; Gonçalves and Uhlein, 2022). Detrital zircon $^{207}Pb/^{206}Pb$ dates constrain the maximum sedimentation age for the Caraça Group to 2.5 Ga (Machado et al., 1996; Hartmann et al., 2006; Koglin et al., 2014; Nunes, 2016; Dopico et al., 2017; Rossignol et al., 2020). In the northeastern portion of the study area, some authors (e.g., Dorr, 1969; Endo et al., 2019) have distinguished the Tamanduá Group as the basal unit of the Minas Supergroup. However, its extent, timing, and stratigraphic context remain controversial (e.g. Simmons and Maxwell, 1961; Marshak and Alkmim, 1989; Daher et al., 2020; Dutra et al., 2020). In this study, basal fine-grained sedimentary rocks which were deposited earlier than the BIF from the Itabira Group, have been attributed to the Batatal Formation (Figure 5.2) (e.g. Gonçalves and Uhlein, 2022).

The Itabira Group records chemical precipitation within a passive margin basin (Dorr, 1969; Alkmim and Marshak, 1998). At the base, the Cauê Formation features BIF deposition on the continental shelf (Klein and Ladeira, 2000). Overlying this, the Gandarela Formation comprises carbonate rock, including dolostone and limestone, locally stromatolitic, dolomitic BIF, and minor phyllite and intraformational breccia (Dorr, 1969; Souza and Müller, 1984; de Paula, 2023). The carbonate rocks were deposited in a shallow marine environment (Dorr, 1969; Babinsky et al., 1995) within a tidal depositional system characterized by high-energy intertidal to shallow subtidal zones (Bekker et al., 2003). They were deposited ca. 2,420 ±19 Ma, according to a Pb/Pb whole rock isochron age dating of stromatolitic facies from the Gandarela Formation (Babinsky et al., 1995). Furthermore, Cabral et al. (2012) obtained a U-Pb zircon age of 2,655 ± 6 Ma for a purported meta-volcanic layer overlying the Cauê Formation, proposing an Archean age for it. However, this interpretation is contentious as it contradicts published detrital zircon data for the underlying Moeda Formation, which suggests a maximum depositional age of around 2.5 Ga and could represent an inherited population (Koglin et al., 2014; Farina et al., 2016; Nunes, 2016; Dopico et al., 2017).

Figure 5.1 — Geological map of the Quadrilátero Ferrífero Province, with the inset showing the location of the São Francisco Craton within Brazil. Additional symbols: red polygon: studied area, red stars: reference data, white circle, city's name.

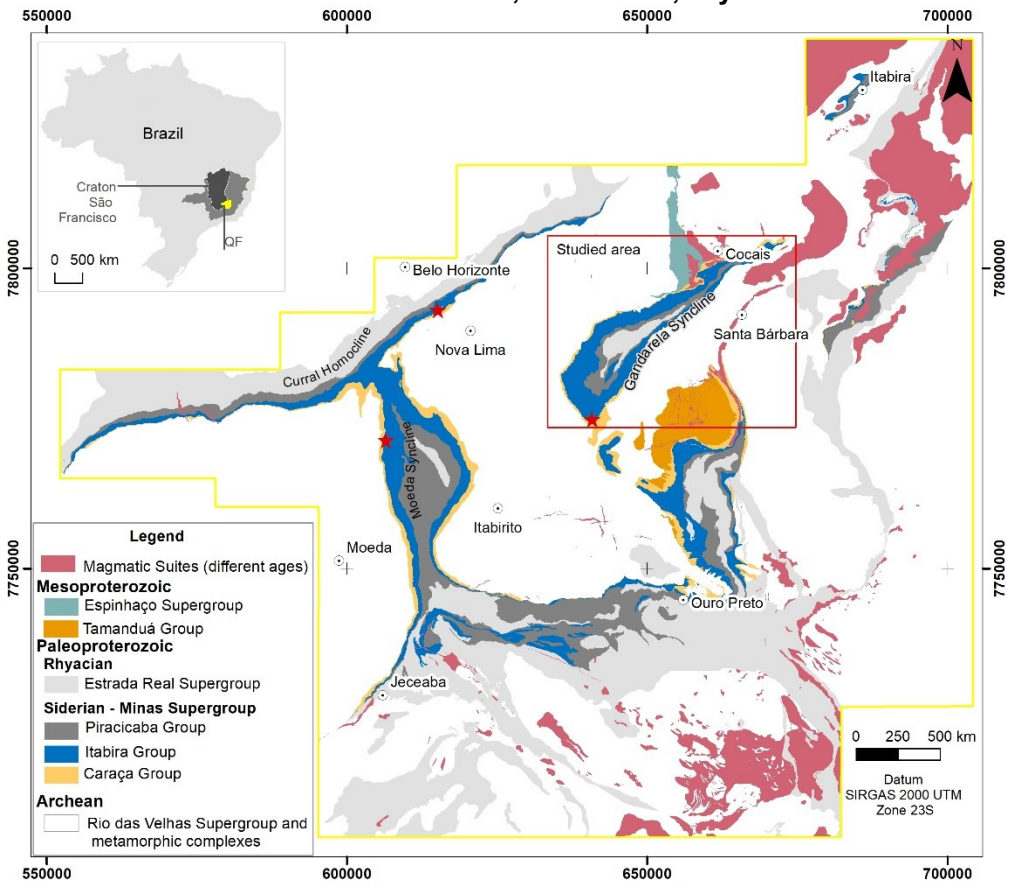

Source: modified from Endo et al., 2019 and Dutra et al., 2020

The uppermost stratigraphic unit, the Piracicaba Group, consists of clastic sedimentary rocks (phyllite, quartzite and minor carbonates rocks) interpreted to represent marine deposition (Dorr, 1969). Detrital zircon $^{207}Pb/^{206}Pb$ dates constrain the maximum sedimentation age for the lowermost Cercadinho Formation to 2.6 Ga (Mendes et al., 2014; Dopico et al., 2017; Dutra et al., 2020). However, based on chemostratigraphy (Bekker et al., 2003) and a 2,110 ± 10 Ma Pb-Pb carbonate whole rock isochron for the Fecho do Funil Formation (Babinski et al., 1995), the age of deposition of the Piracicaba Group could be younger than that, straddling the Rhyacian. The Quadrilátero Ferrífero Province underwent greenschist metamorphism associated with Rhyacian (2.2-2.0 Ga) and Ediacaran/Cambrian (Brasiliano, 570-480 Ma)

orogenesis (Chemale et al., 1994; Alkmim and Marshak, 1998; Oliveira et al., 2010; Seixas et al., 2013; Gonçalves-Dias et al., 2022).

Figure 5.2 — (A) Geological map of Gandarela Syncline showing drill holes and field sample locations. The outcrop location GAD-SW includes AC02A, AC02B, AC02C, AC-03 and AC-04 samples; GAD-Central is associated with the AC06; and GAD-NE includes AC09, AC09A and AC09A1. Datum SIRGAS 2000 UTM - Zone 23S. (B) The stratigraphic column from Quadrilátero Ferrífero modified from Farina et al. (2016) and Endo et al. (2019). The lithostratigraphic unit are represented by the colours shown in (A), while the red stars indicate the studied stratigraphic units. Depositional ages are from [1]Koglin et al. (2014); [2]Babinski, et al. (1994) and [3]Machado et al. (1996).

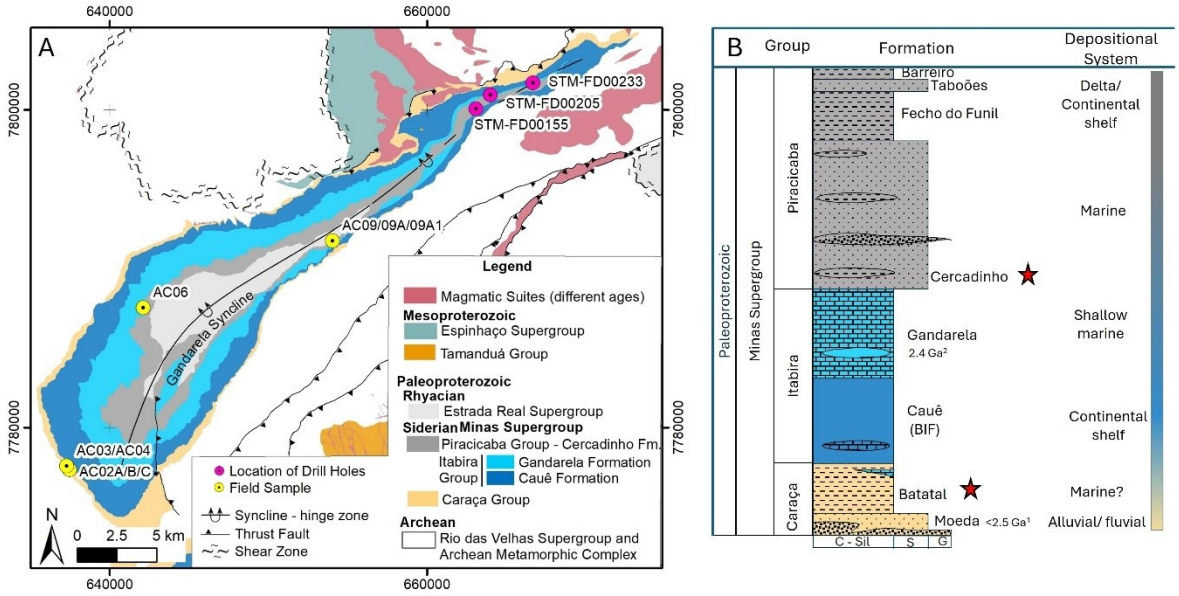

Source: modified from Endo et al., 2019 and Dutra et al. 2020

The Itabira Group records chemical precipitation within a passive margin basin (Dorr, 1969; Alkmim and Marshak, 1998). At the base, the Cauê Formation features BIF deposition on the continental shelf (Klein and Ladeira, 2000). Overlying this, the Gandarela Formation comprises carbonate rock, including dolostone and limestone, locally stromatolitic, dolomitic BIF, and minor phyllite and intraformational breccia (Dorr, 1969; Souza and Müller, 1984; de Paula, 2023). The carbonate rocks were deposited in a shallow marine environment (Dorr, 1969; Babinsky et al., 1995) within a tidal depositional system characterized by high-energy intertidal to shallow subtidal zones (Bekker et al., 2003). They were deposited ca. 2,420 ±19 Ma, according to a Pb/Pb whole

rock isochron age dating of stromatolitic facies from the Gandarela Formation (Babinsky et al., 1995). Furthermore, Cabral et al. (2012) obtained a U-Pb zircon age of 2,655 ± 6 Ma for a purported meta-volcanic layer overlying the Cauê Formation, proposing an Archean age for it. However, this interpretation is contentious as it contradicts published detrital zircon data for the underlying Moeda Formation, which suggests a maximum depositional age of around 2.5 Ga and could represent an inherited population (Koglin et al., 2014; Farina et al., 2016; Nunes, 2016; Dopico et al., 2017).

The uppermost stratigraphic unit, the Piracicaba Group, consists of clastic sedimentary rocks (phyllite, quartzite and minor carbonates rocks) interpreted to represent marine deposition (Dorr, 1969). Detrital zircon $^{207}Pb/^{206}Pb$ dates constrain the maximum sedimentation age for the lowermost Cercadinho Formation to 2.6 Ga (Mendes et al., 2014; Dopico et al., 2017; Dutra et al., 2020). However, based on chemostratigraphy (Bekker et al., 2003) and a 2,110 ± 10 Ma Pb-Pb carbonate whole rock isochron for the Fecho do Funil Formation (Babinski et al., 1995), the age of deposition of the Piracicaba Group could be younger than that, straddling the Rhyacian. The Quadrilátero Ferrífero Province underwent greenschist metamorphism associated with Rhyacian (2.2-2.0 Ga) and Ediacaran/Cambrian (Brasiliano, 570-480 Ma) orogenesis (Chemale et al., 1994; Alkmim and Marshak, 1998; Oliveira et al., 2010; Seixas et al., 2013; Gonçalves-Dias et al., 2022).

5.4 Sampling and Methods

5.4.1 Sample Collection and Mineralogy

We collected a total of 27 samples from the Gandarela syncline, divided into two sets to represent the Batatal and Cercadinho Formation (Figure 5.2B). The first set comprises three drill cores obtained from the Serra do Tamanduá, situated in the northeastern part of the syncline (Figure 5.2A). This set includes 19 phyllite samples, provided by the Vale S.A: STM-FD00155 (591 meters deep), STM-FD00205 (376 meters deep), and STM-FD00233 (266 meters deep) (Figure 5.3). The second set consists of 8 samples collected from well-preserved outcrops: GAD-SW, GAD-Central, and GAD-NE,

each representing a different structural area within the Gandarela Syncline. GAD-SW is situated in the southwest, near the hinge zone; GAD-Central represents the normal flank in the central region; and GAD-NE is in the northeast, corresponding to the inverse flank of the syncline (Figure 5.2). Rocks exhibiting evident hydrothermal alteration, such as carbonate and quartz veins, were excluded from analysis. From the selected samples, we obtained 27 elemental concentrations (major and trace elements), 12 TOC analyses, 7 X-ray diffraction (XRD) analyses of mineral composition and 19 results for Fe speciation.

Different stratigraphic levels of the Minas Supergroup were sampled. The lower stratigraphic unit comprises metasedimentary rocks from the Batatal Formation, representing the deposition before the Cauê BIF. The GAD-SW outcrop (Figure 5.2) has nearly 200 meters of sericitic phyllite. The upper stratigraphic unit is represented by the Cercadinho Formation, which records the deposition following the Cauê BIF and Gandarela dolostone. This unit contains quartz-rich, micaceous and ferruginous phyllites, along with fine-grained quartzite, which is exposed on both limbs of the Gandarela syncline (GAD-Central and GAD-NE) and was also observed in drill core STM-FD00155 (Figure 5.3). The GAD-Central outcrop includes the sample AC06, while samples AC09, AC09A and AC09A1 were taken from the overturned flank (GAD-NE), near the bottom contact with the Cauê BIF (Figure 5.2). The Cercadinho Formation reached a thickness of 280 meters thick in the drill core, but its actual thicknesses may exceed 1,000 meters. No clastic interbeds were found within any of the studied sections of Cauê BIF and Gandarela dolostone.

The samples were characterized by X-ray diffraction (XRD) at the XRD Laboratory of the University of Alberta in Canada. The powdered samples were analyzed using a Bruker D8 Advance diffractometer with a cobalt radiation source (λ = 1.78897 Å) operated at 35 kV and 40 mA. Mineral phases were identified using DIFFRAC.EVA software (Bruker) and the PDF-4 database from the International Centre for Diffraction Data (ICDD).

Figure 5.3 — Stratigraphic column of the drill holes STM-FD00155, STM-FD00205 and STM-FD00233. The order of logs represents the direction NW-SE profile, and the distance between the drill holes is not scaled.

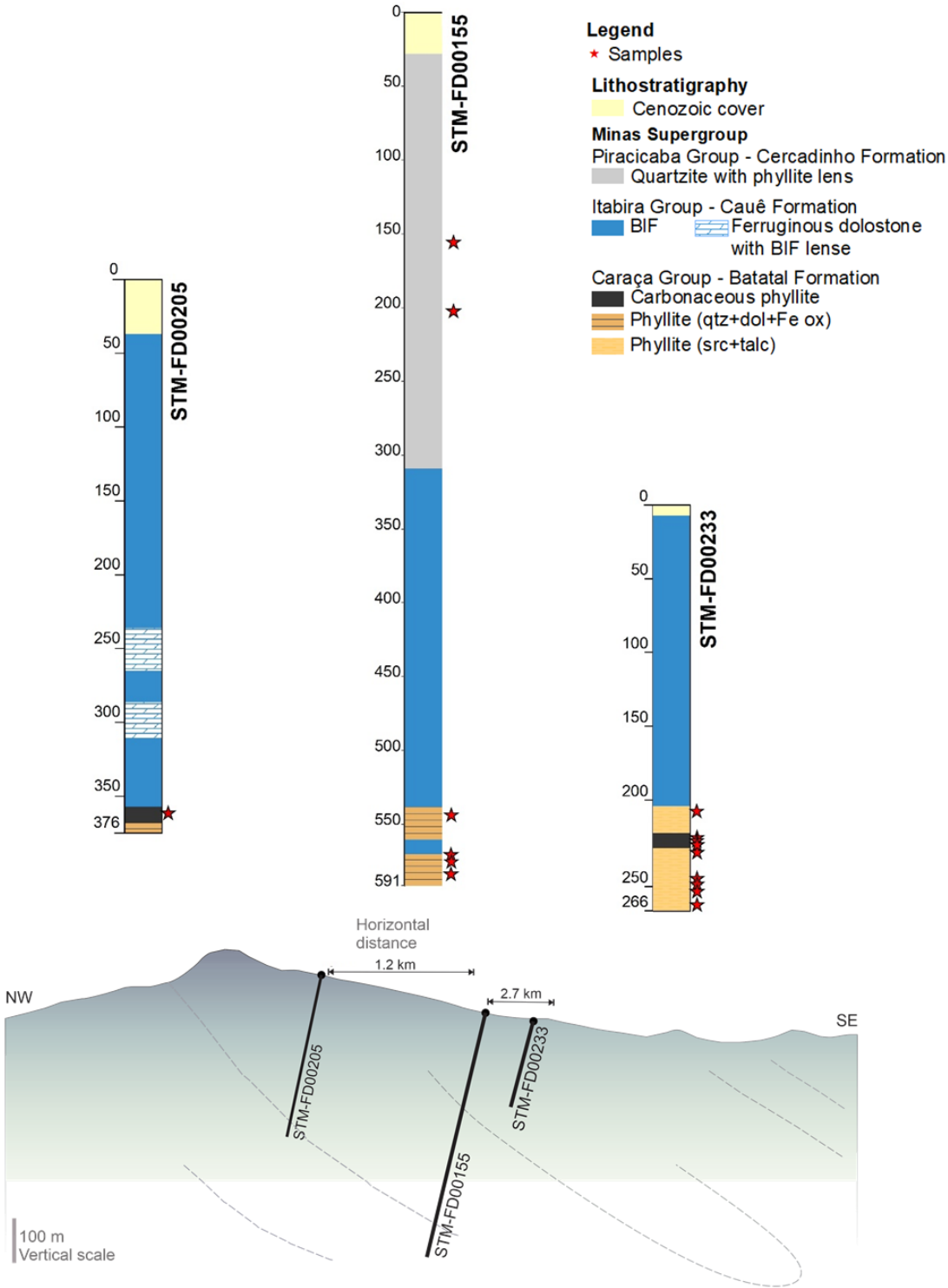

Source: Elaborated by the author

5.4.2 Multi-elemental geochemistry

Major and Trace elements

The geochemistry analyses were performed at SGS Geosol Laboratory Ltd, Belo Horizonte, Brazil. The samples were first dried at 100ºC, then pulverized to achieve 95% <106 µm particle size. A 10 g portion of each sample was designated for either fusion or acid digestion. In the fusion method, the sample underwent lithium metaborate fusion at 950°C, followed by the addition of a solution containing nitric and tartaric acids. In the acid digestion method, the samples were subjected to four acid digestion processes involving the combination of nitric, hydrochloric, hydrofluoric, and perchloric acids. Elemental content was measured using inductively coupled plasma-mass spectrometry (ICP-MS, model Agilent 7800/7850) or optical emission spectrometry (ICP-OES, model Agilent 5110 e 5800). The loss on ignition (LOI) values were determined by measuring the relative difference in mass after roasting at 1,000 °C. Analytical errors are less than 5% for most major oxides and 10% and 15% for most trace elements.

Boron analyses

Boron concentrations were analyzed in the Geobiology laboratory at the University of Alberta. Boron was extracted from these samples via partial digestion using concentrated aqua regia (a 3:1 mixture of hydrochloric and nitric acid). Then, 100 milligrams of dried and homogenized powder were weighed out and placed in a sterile 50 mL centrifuge tube, where 3 mL of 37% HCl and 1 mL of 70% HNO_3 were mixed into each sample and left to react at room temperature. After 1 hour, each sample was remixed, placed in an aluminum block and heated to 130ºC for an additional 3 hours. Each sample was left to cool at room temperature, and then diluted for analysis. The diluted solution was analyzed using an Agilent 8800 Triple Quadrupole ICP-MS/MS with a deviation of less than 5%.

Organic carbon content

Total organic carbon analyses were conducted at the Natural Resources Analytical Laboratory, University of Alberta (Canada). Samples were weighed into open silver

capsules and acidified through sequential additions of 50 µL of 1M HCl to remove inorganic carbon. Subsequently, the samples were dried at 70ºC overnight, sealed and analyzed using a Thermo FLASH 2000 Organic Elemental Analyzer. During analysis, the samples were exposed to an extremely oxidizing environment, promoting an exothermic reaction responsible for the complete combustion of organic matter at temperatures reaching approximately 1800 °C. The resulting gases (N_2, CO_2, and H_2O) were separated using a chromatographic column, and the organic carbon content was quantified using a thermal conductivity detector. The analytical precision for TOC measurements was ±0.5 wt.%.

5.4.3 Iron Speciation

Iron speciation analyses were performed at the Sedimentary Geochemistry Laboratory, Stanford Doerr School of Sustainability, Stanford University, United States. The technique, as described by Poulton and Canfield (2005) and Alcott et al. (2020), quantifies the Fe contents in distinct phase pools that are highly reactive (Fe_{HR}) towards sulfide on early diagenetic timescales (Poulton and Canfield, 2005, 2011; Lyons and Severmann, 2006; Raiswell et al., 2018). Operationally defined phase pools include carbonate iron (Fe_{car}), ferric oxides (Fe_{ox}), magnetite (Fe_{mag}), pyrite (Fe_{py}), and unreactive silicate iron (Fe_U), whose concentrations are determined through a sequential reagent attack process. Highly reactive iron (Fe_{HR}) is calculated as the sum of the iron mineral phases: Fe_{car} (extracted using a 48-h sodium acetate reaction at 50ºC), Fe_{ox} (2-h sodium dithionite reaction at room temperature), Fe_{mag} (6-h ammonium oxalate reaction at room temperature) and Fe_{py} (chromium reduction of sulfur (CRS) method, Canfield et al., 1986). Iron contents in each sequential extraction pool were determined using the ferrozine spectrophotometric method (Stookey, 1970; with the colour allowed to develop overnight) and calculated through gravimetric measurements for Fe_{py}. Detailed methods and estimates of precision can be found in the Supplementary Material of Sperling et al. (2021). Total Fe contents used in the calculation of Fe_{HR}/Fe_T were obtained from SGS Geosol as described above. Fe_{HR}/Fe_T ratios are generally below 0.22 for samples deposited under oxic bottom water conditions, and above 0.38 for anoxic bottom waters, with ambiguous samples plotting in between (Raiswell et al., 2018). The Fe_{py}/Fe_{HR} ratio

further allows for the distinction of anoxic samples, which may have been deposited under ferruginous (nonsulfidic) or euxinic (anoxic with free sulfide) conditions, with a threshold of about 0.7 (März et al., 2008). Pasquier et al. (2022) challenged these proxy thresholds; however, the compilation used by the authors included a number of samples inappropriate for iron speciation according to Raiswell et al. (2018) criteria. Several caveats exist for iron speciation in ancient and metamorphosed rocks (see Raiswell et al., 2018 and Slotznick et al., 2018) and these are discussed further below.

5.5 Results

5.5.1 Petrological and Petrographic Observations

The basal unit of the Batatal Formation is primarily composed of phyllites, with minor occurrences of dolomitic BIF (Figure 5.3). The GAD-SW outcrop is composed of a dark gray, fine-grained sericite-phyllite, mainly consisting of , quartz, minor muscovite, organic matter, and rutile (Figure 5.4A). These phyllites are lepidoblastic and display both laminated and non-laminated structures (Figure 5.4B). Samples from the drill hole STM-FD00155 presented secondary crystals of magnetite, pyrite, carbonate, and quartz overgrowing the foliation. In contrast, the fine-grained metasiliciclastic rocks of the Batatal Formation observed in the drill cores show significant compositional variations, ranging from chloritic, micaceous, and ferruginous to dolomitic phyllites, which may or may not contain organic matter. Accessory minerals include pyrite, rutile, and apatite. A specific occurrence of carbonaceous phyllite (Figure 5.4C), which is less than 3 meters thick, is identified in this unit. This rock is characterized by alternating organic matter-rich layers and rhythmic dolomite-quartz laminae, with secondary dolomite and quartz veining, shear zones, and intrafolial folds also present.

The upper layer of the Cercadinho Formation is predominantly fine-grained quartzite, which may be ferruginous and interbedded with phyllite (Figure 5.3). The phyllite, which is the focus of this study, varies from white or silver to reddish in colour and is composed of quartz, sericite and muscovite, with minor Fe-oxide, kaolinite, and rare occurrences of plagioclase, serpentine, and talc. Toward the lower contact, the

quartzite becomes iron-rich. Common structures include compositional laminae, pervasive schistosity, banding, intrafolial folds, and shear zones.

Figure 5.4 — Photomicrography. (A) Dolomitic phyllite with quartz laminae (*155-29B) in contact with dolomitic phyllite under crossed polarized light (XPL). (B) Chloritic phyllite finely laminated with quartz (XPL). (C) Carbonaceous phyllite from sample *233-A10 showing the organic matter layers (black) under parallel polarized light (PPL). (D) The same sample displaying the compositional variations in the carbonaceous phyllite (XPL).

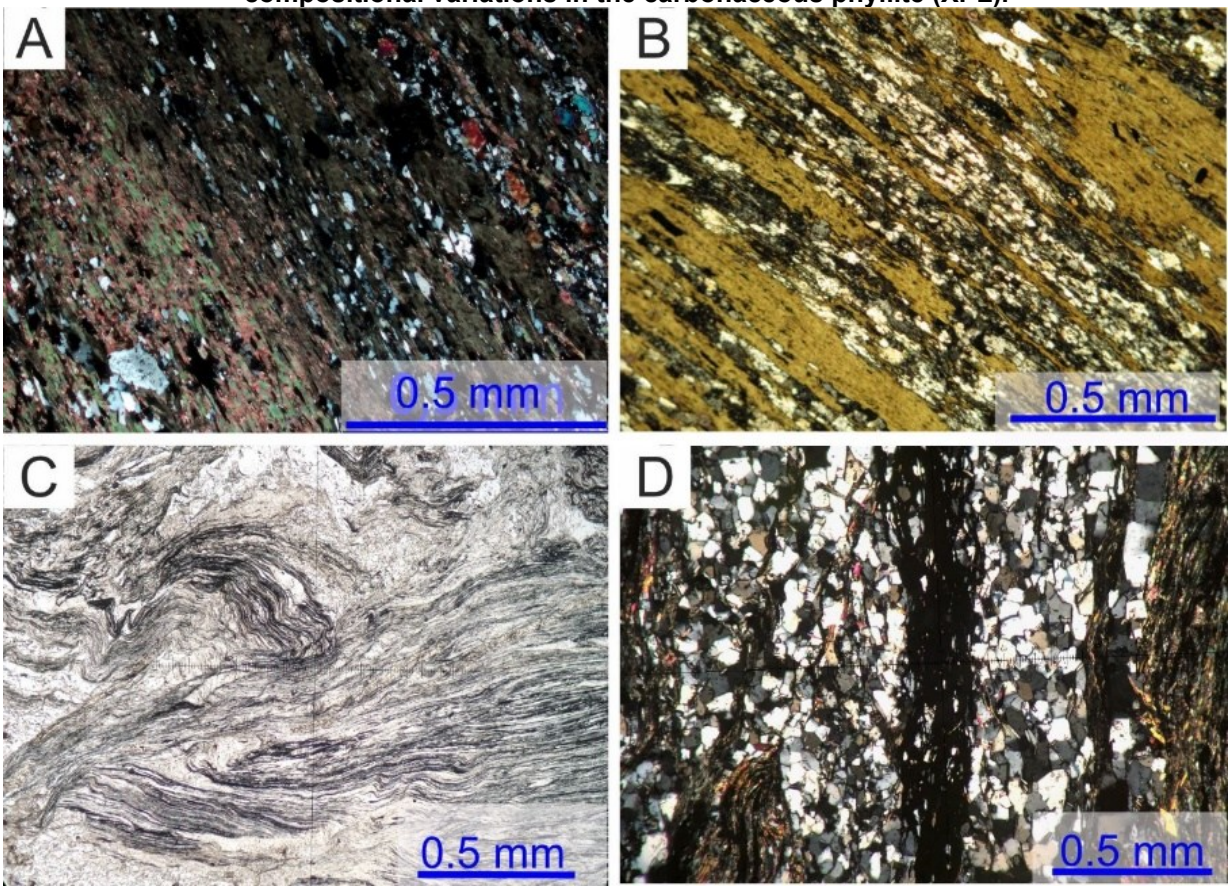

Source: Elaborated by the author

5.5.2 Geochemistry

5.5.2.1 Major elements

Whole-rock major oxide and trace element geochemical analyses were conducted on twenty-seven samples (Tables 5.1 and 5.2). Compositional variation of major elements in the phyllites of the Batatal Formation are shown in Tab. 5.1 and Figure 5.5. The drill core samples display median values (range) of 17.7 wt.% (11.3-24.1 wt.%) for Al_2O_3, 0.7

wt.% (0.2-3.4 wt.%) for CaO, 7.8 wt.% (2.3-18.7 wt.%) for Fe_2O_3, 3.1wt.% (0.5-4.3 wt.%) for K_2O and 57.1 wt.% (47.0-72.0 wt.%) for SiO_2. In contrast, phyllites in the southwest area (GAD-SW) are more compositionally homogeneous, with Al_2O_3 ranging from 21.3-33.9 wt.%, CaO < 0.12 wt.%, Fe_2O_3 <5.6 wt.%, SiO_2 between 44.0-65.2 wt.%. Additionally, K_2O concentrations are notably higher in the southwest, ranging from 6.5-9.7 wt.%. The variation in LOI is similar for both, ranging from 2.9 to 12.4 wt.%.

The upper stratigraphic unit, the Cercadinho Formation, displays a wider compositional range (Figure 5.5), which can be divided into two groups. The first group, represented by the ferruginous phyllite (n=3), is characterized by elevated concentrations of Al_2O_3 (~25 wt.%), Fe_2O_3 (11.6-14.6 wt.%) and K_2O (4.8-6.7 wt.%). In contrast, the second group consists of quartz-rich phyllite (n=2), which is dominated by SiO_2 (~80.5 wt.%) and lower contents of Fe_2O_3 (2.9 and 8.7 wt.%), Al_2O_3 (<2.7 wt.%), and K_2O (<0.7 wt.%).

Figure 5.5 — Box plot representing the major elements in the phyllite from different stratigraphic layers. Boxes represent 25% and 75% of the data from each core, with the median value for each parameter shown within the box and the full range of data bracketed above and below the box.

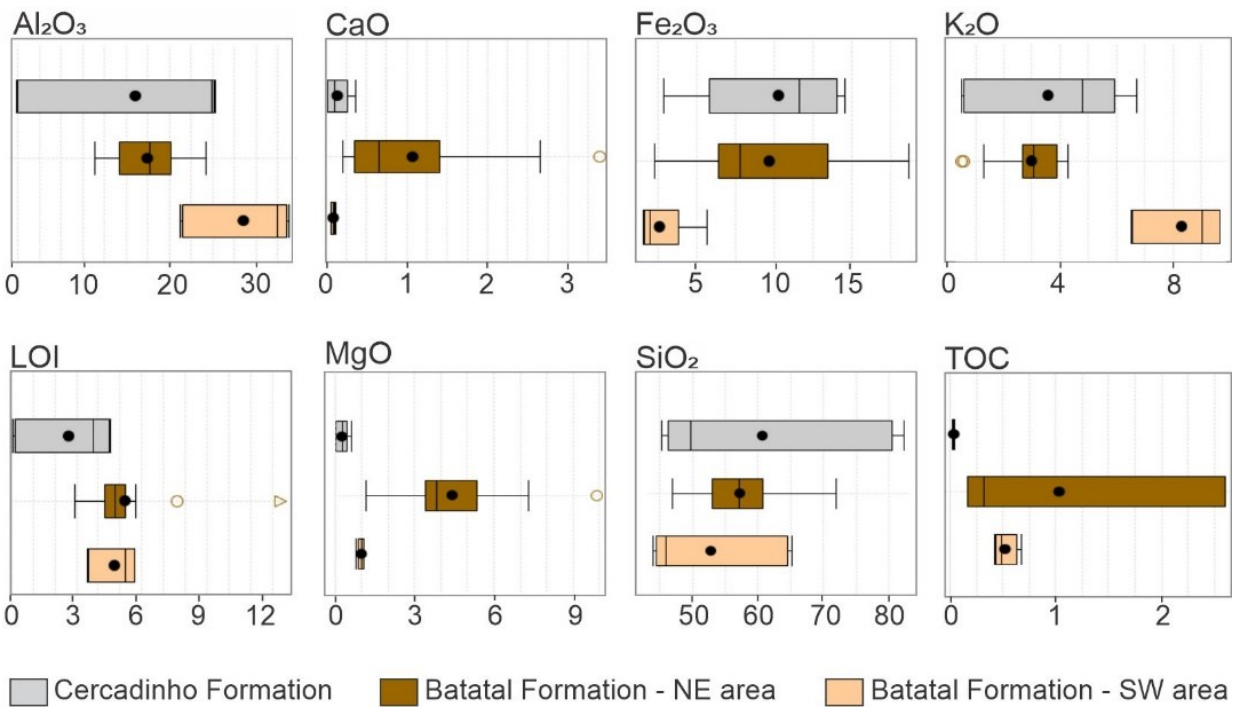

Source: Elaborated by the author

Table 5.1 — Chemical analyses of phyllites samples from the Gandarela syncline. Reference: 1, AC06; 2, AC09; 3, AC09A1; 4, *155-A001; 5, *155-A004; 6, AC02A ; 7, AC02B; 8, AC02C; 9, AC03; 10, AC04; 11, *155-A019; 12, *155-A024; 13, *155-A025; 14, *155-A029B; 15, *205-A024; 6, *233-A006; 17, *233-A009; 18, *233-A010-06; 19, *233-A010-17; 20, *233-A010-22; 21, *233-A010-26; 22, *233-A010-29; 23, *233-A011; 24, *233-A012; 25, *233-A013; 26, *233-A014; 27, *233-A016. *Prefix of drill hole identification: STM-FD00

	Cercadinho Formation					Batatal Formation SW					Batatal Formation NE															
	1	2	3	4	5	6	7	8	9	10	11	12	13	14	15	16	17	18	19	20	21	22	23	24	25	26	27
Major Elements (%)																											
SiO_2	45.3	47.2	49.7	78.7	82.4	44.0	44.9	45.9	64.0	65.2	67.8	48.1	57.6	47.0	49.2	72.0	60.0	62.8	57.1	61.4	59.4	56.7	54.2	52.8	54.6	58.4	53.4
Al_2O_3	25.0	24.9	25.3	2.7	2.3	32.4	33.3	33.9	21.3	21.7	17.0	13.7	17.7	14.4	11.8	11.3	19.2	15.8	21.1	20.6	19.7	21.8	24.1	14.1	18.9	15.7	19.0
Fe_2O_3	14.6	13.5	11.6	8.7	2.9	5.6	2.1	2.0	1.7	1.6	2.3	18.0	7.8	14.0	17.7	5.5	8.5	7.1	6.0	5.9	6.8	6.9	6.8	18.7	8.8	12.9	10.7
K_2O	6.7	4.8	5.2	0.7	0.5	9.0	9.7	9.7	6.5	6.6	4.0	0.5	3.8	3.4	3.1	4.3	3.8	3.0	4.2	3.9	2.6	2.7	3.0	0.6	3.0	1.3	3.3
LOI	3.8	4.4	4.6	0.3	0.1	5.6	5.2	5.7	3.6	3.5	5.7	7.6	4.9	4.4	12.4	2.9	5.0	5.1	5.4	4.8	4.2	4.3	4.6	4.3	4.8	3.7	4.7
MgO	0.6	0.3	0.3	0.0	0.0	1.1	1.1	1.0	1.0	0.8	2.2	9.9	5.8	7.3	3.9	1.2	4.0	3.5	3.3	3.4	3.6	3.5	3.4	4.9	5.1	4.6	5.6
CaO	0.4	0.2	0.1	0.0	0.0	0.1	0.1	0.1	0.1	0.1	2.5	2.7	1.1	3.4	1.4	1.0	1.1	0.4	0.2	0.3	0.6	0.3	0.3	0.5	1.4	0.4	0.7
Na_2O	1.9	1.6	1.4	0.1	0.0	0.5	0.5	0.4	0.1	0.2	0.6	<0.01	0.2	3.4	0.2	0.1	0.5	0.5	0.9	0.9	1.3	1.6	1.9	1.1	2.3	2.2	0.6
TiO_2	0.9	0.7	0.8	0.1	0.2	1.0	1.1	1.1	0.7	0.7	0.2	2.8	0.7	2.8	1.4	0.3	0.7	0.6	0.7	0.7	0.7	0.8	0.9	0.5	0.7	0.5	0.6
P_2O_5	0.2	0.1	0.1	<0.01	<0.01	0.1	0.1	0.1	0.0	0.0	0.1	0.5	0.1	0.4	0.1	0.1	0.1	0.1	0.1	0.1	0.1	0.1	0.1	0.1	0.2	0.1	0.1
MnO	0.0	0.0	<0.01	<0.01	<0.01	0.0	<0.01	<0.01	<0.01	<0.01	0.0	0.1	0.1	0.1	0.6	0.0	0.1	0.1	0.0	0.1	0.1	0.1	0.1	0.1	0.1	0.1	0.1
N	0.06	0.08	0.08	0.07	0.08	0.12	0.12	0.13	0.09	-	-	0.09	-	-	-	-	-	0.10	-	-	-	-	-	-	-	-	0.07
C	0.04	0.04	0.03	0.05	0.04	0.75	0.66	0.69	0.47	-	-	0.88	-	-	-	-	-	2.79	-	-	-	-	-	-	-	-	0.37
TOC	0.04	0.03	0.03	0.04	0.02	0.47	0.51	0.67	0.42	-	-	0.16	-	-	-	-	-	2.61	-	-	-	-	-	-	-	-	0.32
S	<0.01	<0.01	<0.01	<0.01	<0.01	<0.01	<0.01	<0.01	<0.01	<0.01	0.02	<0.01	<0.01	0.81	1.69	0.09	0.11	0.66	0.34	0.26	0.13	0.13	0.14	0.02	0.07	<0.01	<0.01
Trace Elements (ppm)																											
B	25	22	37	24	22	63	72	70	47			21						31									26
Ba	1249	637	809	128	95	481	545	563	305	368	339	94	1327	255	164	1004	480	551	750	688	445	486	535	114	468	274	366
Cd	0	0	0	0	0	0	0	0	0	0	0	0	0	0	0	0	0	16	1	4	1	0	0	0	0	0	0
Co	3	3	2	1	1	37	2	7	1	2	2	45	30	76	20	4	34	58	57	47	35	42	40	37	43	41	47
Cr	119	92	81	54	13	114	87	67	51	54	1	23	86	52	83	4	147	172	177	147	125	120	138	199	191	207	266
Cs	3	6	5	<0.05	0	15	15	16	11	10	3	0	1	31	2	3	3	3	4	4	3	3	3	1	3	2	4
Cu	3	3	13	3	4	32	12	42	8	13	3	5	4	102	262	17	73	534	216	141	78	85	102	7	64	7	19
Ga	37	31	32	5	4	38	39	36	27	28	19	22	22	19	15	19	23	43	51	39	27	28	30	20	24	20	24
Hf	4	3	4	3	3	4	4	4	3	4	2	2	3	1	4	4	3	3	4	4	3	4	4	2	2	2	2
Mo	0	0	0	0	0	3	1	2	2	2	1	1	2	1	2	0	2	3	4	3	2	2	3	1	2	2	2
Nb	23	11	17	3	3	18	21	21	10	13	5	15	10	13	10	17	10	10	12	15	9	13	13	6	10	7	7
Ni	36	52	38	7	8	178	50	66	27	39	6	37	81	66	65	6	198	376	331	259	161	189	160	246	281	288	359
Pb	22	43	41	8	5	32	65	58	11	32	9	2	3	3	10	9	17	95	36	143	30	30	32	7	48	14	22
Rb	185	144	159	20	17	252	280	262	205	210	165	12	60	218	66	104	85	90	139	124	67	78	81	13	97	38	79
Sc	10	7	11	3	3	21	18	17	16	15	2	27	13	35	13	4	11	12	13	13	12	14	14	18	16	16	17
Sr	218	398	322	74	48	54	59	48	27	34	39	42	49	116	10	37	75	68	90	94	134	152	184	40	88	58	63
Ta	2	1	2	<0.05	<0.05	2	2	2	0	1	1	1	1	0	0	2	1	1	1	1	1	1	1	1	1	1	1
Th	18	16	21	5	4	25	33	32	17	22	5	2	13	1	9	11	11	10	12	14	10	13	13	8	10	7	8
U	3	3	4	2	1	5	5	5	3	6	4	1	4	0	3	2	3	3	4	4	3	4	4	2	3	2	2
V	218	148	786	61	29	212	457	335	136	160	LD	384	159	441	165	30	168	157	283	174	155	269	194	148	247	183	170
W	<0.1	1	<0.1	6	3	5	5	<0.1	4	2	2	1	5	3	4	<0.1	2	<0.1	2	2	2	3	<0.1	<0.1	4	<0.1	0
Zr	237	119	221	172	159	164	201	193	156	150	96	208	140	168	179	298	156	144	190	206	138	178	192	105	151	103	116

Source: Elaborated by the author

Table 5.2 — Trace metal elements and relevant ratios for the samples from the Gandarela syncline. Reference: 1, AC06; 2, AC09; 3, AC09A1; 4, *155-A001; 5, *155-A004; 6, AC02A ; 7, AC02B; 8, AC02C; 9, AC03; 10, AC04; 11, *155-A019; 12, *155-A024; 13, *155-A025; 14, *155-A029B; 15, *205-A024; 6, *233-A006; 17, *233-A009; 18, *233-A010-06; 19, *233-A010-17; 20, *233-A010-22; 21, *233-A010-26; 22, *233-A010-29; 23, *233-A011; 24, *233-A012; 25, *233-A013; 26, *233-A014; 27, *233-A016. *Prefix of drill hole identification: STM-FD00

	Cercadinho Formation					Batatal Formation SW					Batatal Formation NE															
	1	2	3	4	5	6	7	8	9	10	11	12	13	14	15	16	17	18	19	20	21	22	23	24	25	26	27
Rare Earth Elements + Y																											
La	125.6	53.4	80.3	11.0	10.0	74.1	123.7	120.6	47.9	66.9	14.3	21.7	32.8	14.9	22.2	56.1	34.8	31.7	42.1	44.6	35.5	42.4	43.6	24.7	34.7	25.6	29.0
Ce	185.2	94.7	146.2	21.6	18.3	134.6	236.6	238.4	86.5	126.7	26.3	51.2	62.9	35.3	44.7	117.3	65.5	59.7	82.9	85.7	66.7	73.4	81.7	47.1	63.3	45.6	54.7
Pr	29.1	10.0	15.1	2.4	2.1	13.3	25.6	25.1	9.6	13.2	2.9	6.9	7.1	5.0	5.4	13.5	6.6	6.6	11.0	9.5	7.4	7.7	8.9	5.2	7.0	5.2	5.7
Nd	105.0	36.3	55.7	9.1	7.9	47.8	95.2	92.6	33.7	51.5	11.1	33.4	26.1	23.1	22.2	54.3	26.6	24.9	38.9	34.4	25.4	29.3	33.2	20.0	25.2	17.7	22.9
Sm	20.4	6.1	8.8	2.0	1.4	7.7	16.1	14.4	6.3	9.0	2.0	8.5	5.3	6.5	4.9	10.3	4.5	4.6	4.4	5.1	4.3	5.2	5.9	3.2	4.0	2.6	3.2
Eu	4.1	1.3	1.9	0.4	0.3	1.8	2.7	3.7	1.2	2.1	0.6	2.4	1.8	2.3	1.1	1.2	1.0	1.0	0.8	1.1	0.9	1.2	1.3	1.2	1.2	0.8	0.9
Gd	17.8	4.5	9.4	2.1	1.5	6.8	11.4	12.7	4.7	7.3	2.0	9.6	4.9	7.1	5.2	11.2	3.8	3.9	5.1	5.7	4.2	5.1	5.2	3.1	3.8	2.5	3.8
Tb	2.6	0.9	1.4	0.4	0.3	1.2	1.9	1.8	0.8	1.1	0.3	1.4	0.8	1.1	0.9	2.0	0.7	0.7	0.9	1.0	0.8	0.8	0.9	0.6	0.8	0.6	0.8
Dy	13.0	5.2	8.5	2.3	1.8	7.0	9.3	9.0	4.7	5.2	1.3	7.8	4.2	6.7	5.3	12.0	4.2	4.3	4.7	6.1	4.3	5.0	5.0	3.6	4.4	3.2	3.9
Ho	2.6	1.1	1.6	0.5	0.4	1.5	1.7	1.7	0.9	1.0	0.3	1.7	0.9	1.3	1.1	2.5	0.8	0.8	1.1	1.2	0.9	1.0	0.8	0.7	0.9	0.7	0.7
Y	69.1	28.6	44.7	14.4	12.7	39.7	47.4	45.5	22.6	29.1	7.7	43.8	25.1	36.8	33.5	66.4	24.4	22.4	28.3	35.5	25.5	29.1	25.3	18.1	24.6	17.1	20.0
Er	6.9	2.9	4.5	1.6	1.3	3.8	5.0	5.4	2.5	3.0	0.8	4.5	2.5	3.9	3.7	6.9	2.1	1.9	2.8	3.2	2.2	2.9	2.5	1.6	2.3	2.1	1.9
Tm	1.1	0.5	0.7	0.2	0.2	0.5	0.7	0.7	0.4	0.5	0.1	0.6	0.3	0.5	0.5	1.1	0.4	0.3	0.5	0.5	0.3	0.4	0.5	0.3	0.4	0.3	0.3
Yb	5.7	2.9	4.6	1.7	1.3	3.9	4.3	3.9	2.8	2.8	0.8	4.2	2.4	3.3	3.6	6.5	2.2	2.2	2.7	3.1	2.3	2.7	2.7	1.5	2.2	1.8	1.8
Lu	0.6	0.2	0.4	0.3	0.2	0.5	0.6	0.7	0.4	0.5	0.3	0.8	0.4	1.0	0.7	1.0	0.4	0.4	0.6	0.4	0.2	0.4	0.4	0.3	0.4	0.4	0.3
Relevant Ratios																											
B/Ga	0.7	0.7	1.1	4.5	5.6	1.6	1.8	1.9	1.8	-	-	0.9	-	-	-	-	-	0.7	-	-	-	-	-	-	-	-	1.1
S/TOC	0.3	0.3	0.3	0.3	0.4	0.0	0.0	0.0	0.0	-	-	0.1	-	-	-	-	-	0.3	-	-	-	-	-	-	-	-	0.0
Sr/Ba	0.2	0.6	0.4	0.6	0.5	0.1	0.1	0.1	0.1	0.1	0.1	0.5	0.0	0.5	0.1	0.0	0.2	0.1	0.1	0.1	0.3	0.3	0.3	0.3	0.2	0.2	0.2
Cr_{EF}	1.4	1.2	0.8	3.0	0.9	1.1	0.8	0.7	0.7	0.7	0.0	0.3	1.2	0.6	1.6	0.1	2.4	3.0	2.7	2.1	2.0	1.9	1.9	2.5	2.6	2.8	3.0
Cu_{EF}	0.1	0.1	0.2	0.2	0.4	0.4	0.2	0.6	0.1	0.2	0.1	0.1	0.1	1.7	6.8	0.4	1.6	12.4	4.5	2.7	1.7	1.8	1.8	0.1	1.2	0.1	0.3
Mo_{EF}	0.4	0.5	0.2	2.3	2.0	2.8	1.0	2.4	2.6	3.0	1.0	1.3	2.1	0.8	4.2	0.8	3.5	6.1	6.4	4.6	3.5	3.6	3.4	1.7	2.5	2.1	2.0
Ni_{EF}	0.7	1.1	0.6	0.6	0.9	2.8	0.8	1.2	0.6	0.9	0.1	0.9	1.8	1.4	2.1	0.2	5.3	10.9	8.6	6.2	4.3	5.0	3.6	5.1	6.3	6.4	6.8
U_{EF}	3.5	4.7	4.1	11.6	9.3	4.7	5.0	5.9	3.9	8.5	6.2	0.9	6.2	0.6	6.7	3.9	5.7	5.5	6.3	6.1	4.8	6.2	5.6	2.7	4.2	2.6	2.7
V_{EF}	1.8	1.3	5.3	2.4	1.4	1.4	3.2	2.7	1.3	1.5		3.9	1.5	3.9	2.3	0.4	1.9	2.0	3.1	1.8	1.8	3.0	1.9	1.3	2.4	1.7	1.4
Zn_{EF}	0.1	0.1	0.1	0.3	0.7	0.2	0.1	0.1	0.2	0.2	0.3	2.9	1.0	1.4	0.5	1.2	2.7	104.8	3.9	10.6	7.5	4.6	5.0	2.8	1.8	1.9	1.5
Mo_{EF}/	0.1	0.1	0.1	0.2	0.2	0.6	0.2	0.4	0.7	0.4	0.2	1.4	0.3	1.4	0.6	0.2	0.6	1.1	1.0	0.7	0.7	0.6	0.6	0.6	0.6	0.8	0.7
Fe/Al	1.4	1.4	0.9	4.0	1.6	0.4	0.2	0.2	0.2	0.2	0.3	2.1	0.9	1.4	2.9	0.9	1.1	1.0	0.8	0.7	0.9	0.9	0.8	1.9	1.0	1.4	1.0
Y/Ho	26.6	26.5	28.3	29.9	31.7	27.4	28.7	26.3	25.1	28.5	28.6	26.4	28.9	28.3	29.4	26.3	31.7	27.0	26.2	30.3	28.3	29.1	31.6	26.6	28.6	24.5	28.9
C_{org}/P	1.2	1.4	0.7	7.0	-	12.5	14.4	19.7	37.8	-	-	0.8	-	-	-	-	-	97.9	-	-	-	-	-	-	-	-	10.8

Source: Elaborated by the author

5.5.2.2 Redox-Sensitive Proxies

The trace metal abundances of analyzed phyllite samples are presented in Table 5.2. To quantify the authigenic enrichment of Cu, Ni, Mo, U and V in the rocks, the elemental concentrations in the samples were compared to the average composition of the Post-Archean Australian Shale (PAAS) (Taylor and Mclennan, 1985; Tribovillard et al. 2006). The enrichment factor (EF) was calculated using the formula: $EF_{element\ X} = (X/Al)_{sample} / (X/Al)_{PAAS}$, where X represents the RSE element (e.g. Mo and U) and Al represents the aluminum abundance (Tribovillard et al., 2006).

The lower stratigraphic phyllites of the Batatal Formation exhibit significant enrichment in RSE, such as $Cr_{EF,}$ Cu_{EF}, Ni_{EF} and Zn_{EF}, as well as elevated Mo_{EF}/U_{EF} ratios (Figures 5.6 and 5.9). Drill core samples from the northeastern extremity of the study area reveal elevated RSE concentrations, with median values of Cr at 138 ppm (range 1-266 ppm), Cu at 73 ppm (range 3-534 ppm), Ni at 189 ppm (range 6-376 ppm), and Zn at 135 ppm (range 17-4821 ppm) where the EF values range as follows (median values) Cr_{EF}, 0.01-3.0 (2); Cu_{EF}, 0.1-12.4 (1.6); Mo_{EF}, 0.7-6.4 (2.5) Ni_{EF}, 0.2-10.9 (5), and Zn_{EF}, 0.3-104.8 (2.7). The Mo_{EF}/U_{EF} ratio has a median of 0.6 (range 0.2-1.4). The highest RSE concentrations are primarily associated with carbonaceous phyllite.

In contrast, the southwestern region (GAD-SW) of the Batatal phyllites shows lower RSE concentrations when compared to the northeastern area (Figures 5.6 and 5.9). The median (range) values for Cr, Cu, Mo, Ni and Zn are 67 ppm (51-114 ppm), 13 ppm (8-42 ppm), 2 ppm (1-3 ppm), 50 ppm (27-178 ppm), and 12 ppm (10-20 ppm), respectively. The EF values show the following range (median): Cr_{EF}, 0.7-1.1 (0.7); Cu_{EF}, 0.1-0.6 (0.2); Mo_{EF} 0.1-3.0 (2.6); Ni_{EF}, 0.6-2.8 (0.9), and Zn_{EF}, 0.1-0.2 (0.2). The Mo_{EF}/U_{EF} ratio has a median of 0.4 (range: 0.2 to 0.7), while the C_{org}/P ratio varies from 12.5 to 37.8, with a median of 17.1.

In the younger stratigraphic unit, the Cercadinho Formation, trace metal abundance decreases (Figures 5.6 and 5.9). Chromium, Cu, Mo, Ni and Zn show a median (range) are: 81 ppm (13-119 ppm); 3.4 ppm (2.9-12.6 ppm); 0.4ppm (0.2-0.4 ppm), 36 ppm (7-52 ppm) and 8 ppm (5-9 ppm), respectively. In general, the EF values represent the lower enrichment levels observed in the studied samples and are expressed as ranges (median): Cr_{EF}, 0.7-3.0 (1.2); Cu_{EF}, 0.05-0.4 (0.2); Mo_{EF} 0.2-2.3 (0.5); Ni_{EF}, 0.6-1.1 (0.7), and Zn_{EF}, 0.1-0.7 (0.1). The Mo_{EF}/U_{EF} ratio ranges from 0.1

to 0.2, with a median of 0.12. C_{org}/P ratios range from 0.72 to 6.96, with a median of 1.3.

Figure 5.6 — Box plot representing the trace metal elements in the phyllite from different stratigraphic layers. Boxes represent 25% and 75% of the data from each core, with the median value for each parameter shown within the box and the full range of data bracketed above and below the box.

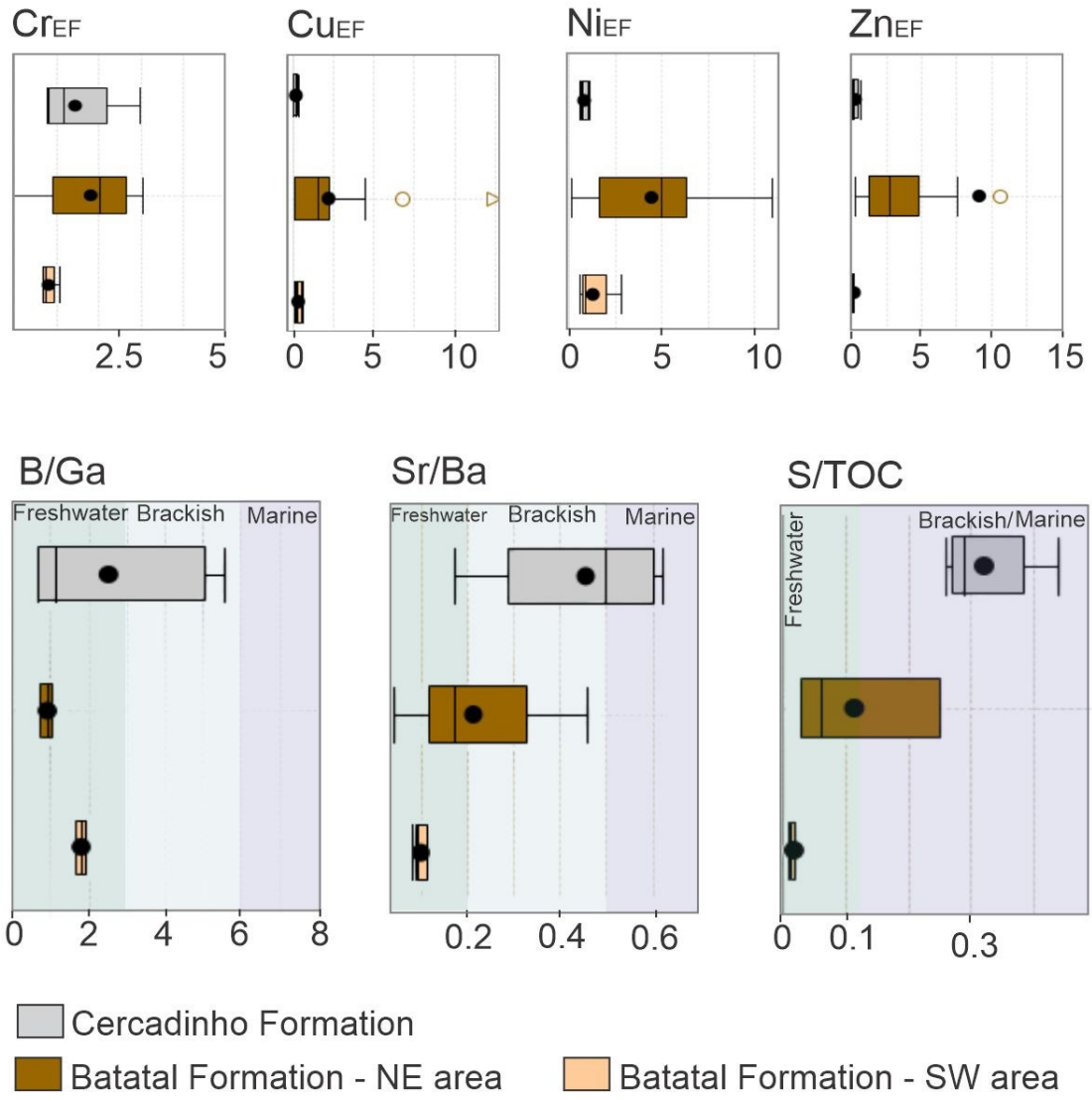

Source: Elaborated by the author

5.5.2.3 Paleosalinity proxies

Elemental paleosalinity proxies expressed by the relative concentration of B/Ga, Sr/Ba and S/TOC were analyzed in the studied samples. Because Sr can substitute for Ca^{2+} in carbonates, and thus record the presence of carbonate rather than a

paleosalinity signal in Sr/Ba proxy reconstructions, all studied samples contain < 5 wt.% CaO in carbonate content (Brand and Veizer, 1980; Wei and Algeo, 2020).

B/Ga values increase upwards in the stratigraphic section (Figure 5.6). At the base, Batatal phyllite samples from the GAD-SW, southwestern area, show a median value of 0.9 (range: 0.7-1.1). This value rises in the northeastern region, where the median B/Ga reaches 1.8 (range: 1.6-1.9). In contrast, the upper stratigraphic unit, represented by the Cercadinho phyllite, exhibits a wider range of B/Ga values, from 0.7 to 5.6, with a median of 1.1.

The Sr/Ba ratio in the Batatal samples from the GAD-SW outcrop ranges from 0.08 to 0.11, with a median of 0.09. In the northeastern region, the Batatal phyllites show greater variability, with Sr/Ba values between 0.04 and 0.46 and a median of 0.17 (Figure 5.6). Conversely, samples from the uppermost stratigraphic unit, the Cercadinho Formation, reveal the highest Sr/Ba values, with a maximum of 0.62, with a median of 0.50 and minimum of 0.17 (Figure 5.6).

Regarding S/TOC ratios, all analyzed phyllite samples from the Batatal and Cercadinho formations show low S concentrations, ranging from 0.01 wt.% to 0.26 wt.%, except the Batatal carbonaceous phyllite (e.g., samples STM-FD00155-A29B, STM-FD00205-A24, STM-FD00205-A10-06, and STM-FD00233-A10-17), where S concentration reaches up to 1.69 wt.%. Consequently, the Batatal phyllites exhibit S/TOC values ranging from 0.01 to 0.25, with a median of 0.02. In contrast, the Cercadinho Formation, which corresponds to the upper stratigraphy, displays higher S/TOC values, ranging from 0.3 to 0.4, with a median of 0.3.

5.5.2.4 Iron Speciation

In the studied stratigraphic section, unreactive iron (Fe_U) is the predominant phase across all samples, with concentrations ranging from 0.77 to 8.85 wt.% (Table 5.3). In contrast, the abundance of highly reactive iron (Fe_{HR}), which includes the Fe-oxide, Fe-carbonate, magnetite and pyrite pools, varies from 0.13 to 2.0 wt.% (Figure 5.7).

In the lower unit, consisting of phyllite from the Batatal Formation in the southwestern area (GAD-SW outcrop), the ratio of Fe_{HR} to total iron (Fe_T) ratio ranges from 0.29 to 0.46, with a median of 0.37. The Fe_{Py}/Fe_{HR} ratio is zero, indicating an absence of Fe_{Py} in the rocks. Conversely, the Batatal Formation in the northeastern

area displays greater variability, with Fe_{HR}/Fe_T values ranging from 0.01 to 0.49, and a median of 0.22. In this area, the Fe_{Py}/Fe_{HR} ratio ranges from 0 to 0.55, with a median of 0.14. Notably, the protocol of Canfield et al. (1986) used here for Chromium Reducible Sulfur (i.e., Fe_{Py}) will also extract Acid Volatile Sulfur including pyrrhotite. Pyrrhotite can commonly form in metamorphic phases at the expense of pyrite or other highly reactive forms and cause erroneous interpretations (Slotznick et al., 2018). The general absence of Fe_{Py} as measured by chromium reduction, indicates that conversion to pyrrhotite is not unduly affecting our interpretations.

In the uppermost stratigraphic succession, comprising the metasedimentary rocks from the Cercadinho Formation, the Fe_{HR}/Fe_T values are 0.06, 0.14 and 0.17 wt.%, with a median of 0.12. Similar to the Batatal phyllite, the Fe_{Py}/Fe_{HR} ratio in this unit is also zero, indicating the absence of pyrite and/or pyrrhotite.

Table 5.3 — Sequential iron extraction data.
*** FeT and Al were calculated from the average of the following intervals. The total interval is 1.5 meters.**

Sample	Lithostatigraphy	Fe_{carb} (wt%)	Fe_{ox} (wt%)	Fe_{mag} (wt%)	Fe_{Py} (wt%)	FeHR (wt%)	FeU (wt%)	FeT (wt%)	Fe_{Py}/FeHR	FeHR/ FeT	Fe/Al
AC06	Cercadinho Formation	0.01	0.96	0.02	0.00	0.99	9.20	10.19	0.00	0.10	1.44
AC09		0.02	1.48	0.05	0.00	1.55	7.91	9.46	0.00	0.16	1.43
AC09A		0.01	1.84	0.04	0.00	1.90	16.56	18.46	0.00	0.10	6.26
AC09A1		0.01	1.06	0.02	0.00	1.09	7.00	8.09	0.00	0.14	0.91
STM-FD00155-A01		0.02	0.99	0.02	0.00	1.03	5.06	6.09	0.00	0.17	3.98
STM-FD00155-A04		0.01	0.11	0.01	0.00	0.13	1.91	2.04	0.00	0.06	1.64
AC02A	Batatal Formation - SW area	0.03	1.75	0.02	0.00	1.80	2.14	3.94	0.00	0.46	0.44
AC02B		0.06	0.48	0.04	0.00	0.59	0.88	1.47	0.00	0.40	0.17
AC02C		0.03	0.36	0.02	0.00	0.41	1.01	1.42	0.00	0.29	0.19
AC03		0.03	0.34	0.04	0.00	0.41	0.77	1.17	0.00	0.35	0.19
STM-FD0015-A19	Batatal Formation - NE area	0.31	0.01	0.01	0.00	0.32	1.30	1.62	0.00	0.20	0.28
STM-FD00155-A24		0.78	0.03	0.15	0.00	0.96	11.66	12.62	0.00	0.08	2.14
STM-FD00155-A25		0.10	0.01	0.03	0.00	0.14	5.33	5.47	0.00	0.02	0.88
STM-FD00233-A06		0.78	0.09	0.04	0.08	0.99	2.87	3.85	0.08	0.26	0.89
STM-FD00233 A010-06		0.41	0.11	0.12	0.33	0.97	4.00	4.97	0.34	0.19	1.03
STM-FD00233 A010-08*		0.20	0.06	0.08	0.42	0.76	3.82	4.58	0.55	0.17	0.89
STM-FD00233 A010-17		1.07	0.23	0.24	0.33	1.87	2.32	4.20	0.18	0.45	0.78
STM-FD00233 A010-22		1.04	0.23	0.39	0.33	2.00	2.10	4.10	0.16	0.49	0.70
STM-FD00233 A010-26		0.17	0.02	0.09	0.08	0.38	4.37	4.75	0.23	0.08	0.91
STM-FD00233 A010-29		0.52	0.17	0.33	0.17	1.20	3.61	4.80	0.14	0.25	0.90
STM-FD00233-A11		0.12	0.04	0.05	0.17	0.38	4.34	4.72	0.44	0.08	0.76
STM-FD00233-A12		0.37	0.05	0.32	0.00	0.73	12.33	13.06	0.00	0.06	1.95
STM-FD00233-A14		0.08	0.01	0.05	0.00	0.13	8.85	8.99	0.00	0.01	1.43
STM-FD00233-A16		0.10	0.01	0.06	0.00	0.17	7.30	7.48	0.00	0.02	1.02

Source: Elaborated by the author

Figure 5.7 — (A) and (B) Iron speciation parameters used to evaluate ocean redox conditions based on metapelitic rock samples from the Batatal Formation (pre-Cauê BIF) and the Cercadinho Formation (post-Cauê BIF). (C) The FeT/Al and FeHR/FeT ratios serve as proxies for iron enrichment in the paleoenvironment. In this case, the inverse correlation between these parameters suggests that FeHR/FeT, which is sensitive to the conversion of FeU (poorly reactive iron) to FeHR (highly reactive iron), may be influenced by depositional processes. Fe/Al ratios between 0.5 and 1 are generally indicative of anoxic conditions. Abbreviations: FeHR = highly reactive iron; FeT = total iron; Fepy = pyritic iron

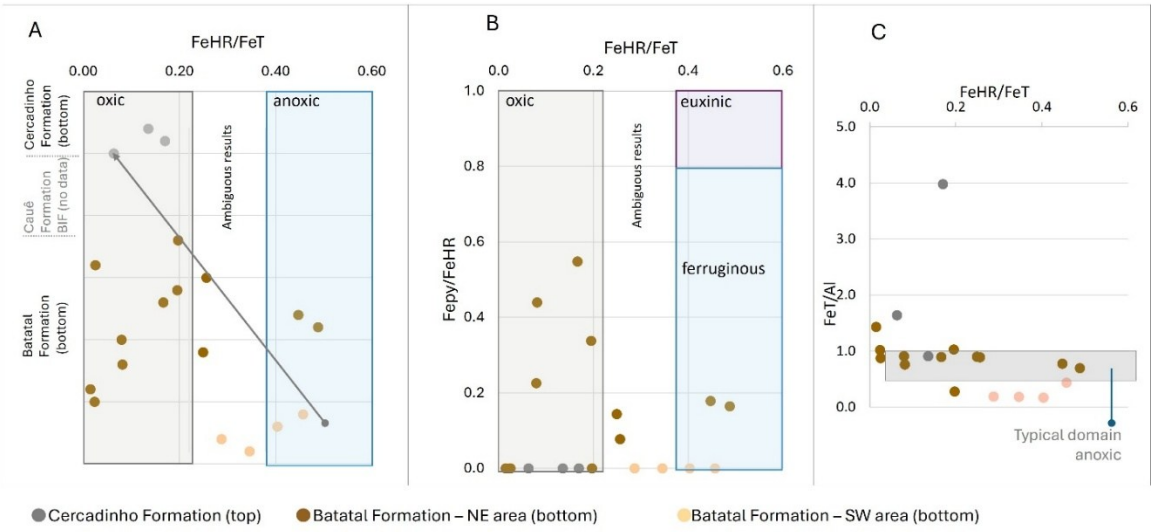

Source: Elaborated by the author

5.6 Discussion

5.6.1 Paleosalinity Reconstruction

Paleosalinity proxies potentially record temporal changes in the water salinity, providing estimates of fresh, brackish, and marine conditions in ancient basins (Potter et al., 1963; Wei et al., 2018; Gilleaudeau et al., 2021; Remìrez et al., 2024). As indicated by Wei and Algeo (2020), salinity levels are classified using multiple geochemical ratios, such as B/Ga, Sr/Ba and S/TOC, obtained from fine-grained sediments like shale or mudstone. These ratios represent the preferential concentration of certain elements under varying water salinities. For example, B and Sr exhibit conservative behaviour in saline water, while Ga and Ba are readily absorbed by clay minerals in freshwater sediments (Sirocko, 1995; Millero et al., 2008; Wei et al., 2018) and their abundance is usually related closely to the detrital and freshwater input (Wei and Algeo, 2020; Schier et al., 2021). The relative concentrations of buried

S and TOC also differ between marine and non-marine sedimentary facies primarily because sulfate is present at extremely low concentrations in freshwaters as compared to marine waters (Berner, 1985).

Reference values from Wei and Algeo (2020) provide a guideline for interpreting paleosalinity proxies: (i) B/Ga <3 is freshwater; 3 to 6 is brackish; and >6 is marine; (ii) Sr/Ba <0.2 is freshwater; 0.2 to 0.5 is brackish; and >0.5 is marine; (iii) S/TOC <0.1 is freshwater, and >0.1 indicates brackish or marine. Liu et al. (2025) updated that Sr abundance in Proterozoic rocks is significantly lower than in modern seawater and suggested adjusting the Sr/Ba parameter for Proterozoic depositional systems, redefining freshwater (<0.08), brackish (0.08–0.20), and marine (>0.20) salinity facies. The analyzed samples from the Quadrilátero Ferrífero reveal a salinity gradient in the Batatal Formation, as indicated by the three paleosalinity proxies. Broadly, salinity increases from the southwestern to the northeastern areas, a pattern likely reflecting either greater freshwater input in the southwest or better connectivity to the open ocean in the northeast. Within the Cercadinho Formation, at the top of the stratigraphy, paleosalinity data confirms that these fine-grained sedimentary rocks were deposited in a marine environment. A detailed discussion of each paleosalinity proxy and its preservation is provided in the following section.

5.6.1.1 Potential effects of post-depositional alteration

Given that many of the elements used as paleosalinity proxies are initially adsorbed onto clay mineral, which recrystallize during metamorphic transformation into phyllite, there is a high likelihood of elemental mobility that could affect the proxies and their interpretive framework (which is based on modern sediments that have not even undergone diagenesis; Wei and Algeo, 2020). However, the crystalline structure and composition of clay minerals may play an important role in limiting the mobility of elements during diagenesis and low-grade metamorphism (Dohmeier et al., 1996; Liu et al., 2025). For example, several studies have discussed the potential preservation of paleosalinity proxies during burial and low-grade metamorphism (Środoń, 2010; Retallack, 2020; Cheng et al., 2021; Wang et al., 2021; Yu et al., 2022; Wei et al., 2024). Liu et al. (2005) reported no evidence of significant gain or loss of B, Ba, Ga, and Sr in clay minerals after burial diagenesis. This work demonstrated that paleosalinity ratios remained consistent despite variations in burial temperature, from

125–150ºC in metasiliciclastic rocks of the Nonesuch Formation (Michigan, USA) to 260–330ºC in the Datangpo Formation (Guizhou Province, China), suggesting that they can be preserved during diagenesis and metamorphic processes.

In the Quadrilátero Ferrífero, Paleoproterozoic rocks exhibit evidence for the preservation of geochemical and isotopic signals in metasedimentary rocks, as demonstrated through i) the consistent carbon isotopic signatures obtained in dolostones (Bekker et al., 2003; de Paula et al., 2023), ii) REE concentrations in BIFs (e.g. Spier et al., 2007; Alkmim, 2014; Teixeira et al., 2017) and iii) minimal deformation observed in the area, as evidenced by well-preserved primary structures (Madureira et al., 2021), stromatolites and oncolites (Souza and Müller, 1984; Babinski et al., 1995). In addition, fluid inclusion studies conducted in the eastern part of the province indicate that fluid-rock interactions in hematite from BIF layers recorded temperatures between 140–205ºC, suggesting minimal metamorphic alteration, while quartz grains reached higher temperatures of 280–351ºC (Rosière and Rios, 2004; Rosière et al., 2008).

Therefore, the integration of geochemical datasets with a well-constrained regional stratigraphic and sedimentological framework in the Quadrilátero Ferrífero (e.g., Madureira et al., 2021; Gonçalves and Uhlein, 2022) supports the interpretation and validates the application of these proxies, demonstrating that the signal shows consistency in a directional sense and is present across multiple proxies, which enhances confidence in the overall interpretation.

5.6.1.2 B-Ga proxy

Within the Batatal Formation, southwestern phyllites (GAD-SW) have lower B/Ga values (median 0.9), increasing toward the northeastern region (median 1.8). The southwestern phyllites exhibit a higher median Ga value of 36 ppm (range 27–39 ppm), while the northeast area shows a wider range of 24 ppm (15–51 ppm). These variations in Ga concentration may reflect more significant freshwater input from the southwestern than from the northeastern.

In the Cercadinho Formation, the upper stratigraphic unit, B/Ga values increase (median/range: 1.1 / 0.7–5.6), among which, two out of five samples acquire B/Ga of 4.5 and 5.6, indicating close to fully marine conditions as defined by Wei and Algeo (2020). This trend aligns with the slight decrease in Ga concentrations (median: 31 ppm; range: 4–37 ppm), indicating increasing salinity levels. The similarity in B/Ga

ratios between the Cercadinho Formation and modern sediments suggests that Paleoproterozoic seawater salinity may have been comparable to that of the modern ocean, consistent with the parameters proposed by Knauth (2005), who argued that the most significant decline in ocean salinity occurred during the Neoproterozoic, coinciding with the formation of the first known large salt deposits. However, the observed secular variations in water mass correspond closely with the depositional evolution of the Minas Basin, reflecting dynamic changes in paleoenvironmental conditions during its formation. Therefore, the B/Ga values indicate a transition from freshwater-brackish facies in the Batatal Formation to fully marine conditions in the Cercadinho Formation from the bottom up (Figures 5.6 and 5.8).

Figure 5.8 — Profile of B/Ga, Sr/Ba, S/TOC, and Mo_{EF}/U_{EF} represents the modern reference values for paleosalinity reconstruction applied to the studied metamorphic fine-grained sedimentary rocks. The horizontal datum (base contact of the Cauê and Batatal formations) was used to calculate the relative depth (see Figure 5.3).

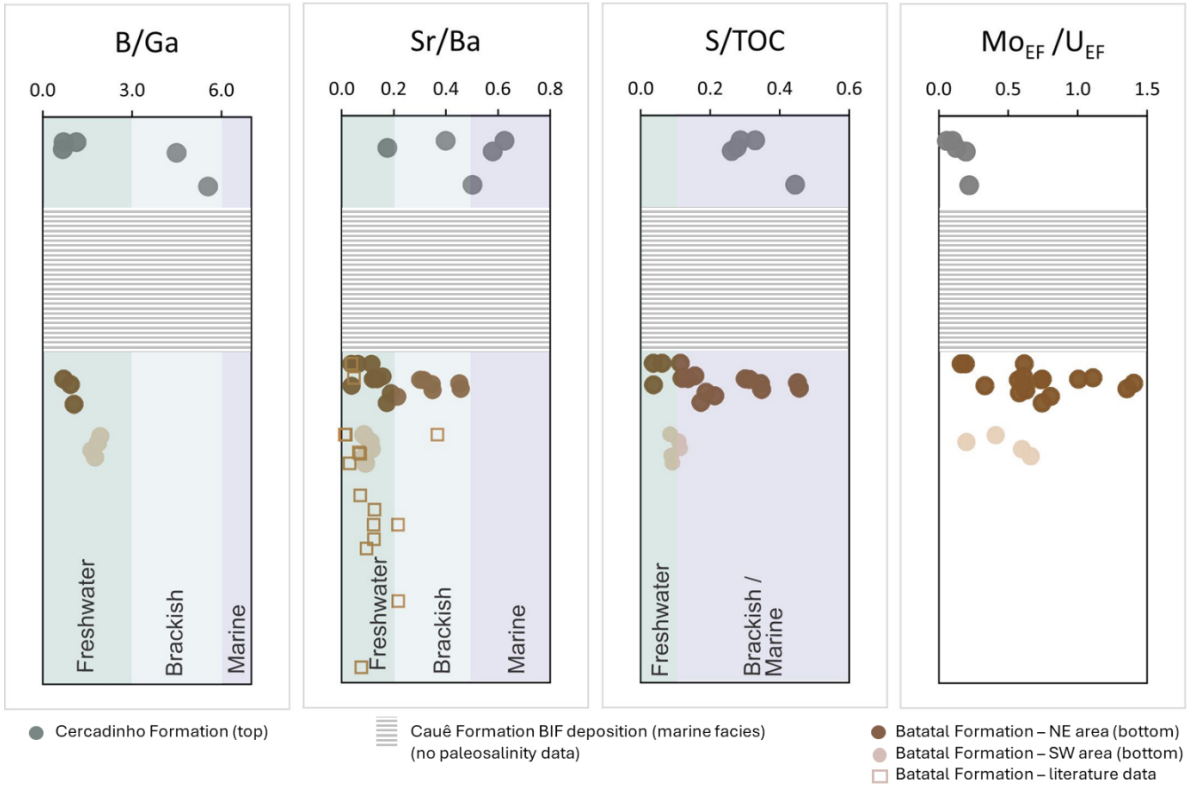

Source: Elaborated by the author

5.6.1.3 Sr-Ba proxy

The Sr/Ba data show an upward trend in younger rocks, ranging from 0.04 to 0.62 (Figure 5.8). In the southwestern Batatal phyllites (GAD-SW), Sr/Ba values are

low (median 0.09, range 0.08–0.11), while northeastern samples show more variability (median 0.17, range 0.04–0.46), indicating freshwater to brackish conditions. These paleosalinity results are consistent with the rock assemblages found in each specific area. In GAD-SW, homogeneous sericitic phyllites dominate, whereas GAD-NE represents a transitional environment with contributions from chemical sedimentary rocks. Other studies (Spier et al., 2007; Alkmim, 2014; Hensler et al., 2017) report similarly low Sr/Ba values in Batatal phyllites, supporting the interpretation of a predominantly freshwater environment during their deposition (Figure 5.8). Interestingly, these reference data, which indicate low Sr/Ba ratios characteristic of freshwater facies (Figure 5.8), come from locations only 30 km away from the study area of this work (Figure 5.1).

In the Cercadinho Formation, Sr/Ba values rise to a median of 0.50 (range 0.40–0.62), with one outlier (0.17). These values suggest marine facies sedimentation during a transgressive phase following the deposition of the Cauê BIF and Gandarela carbonate rocks (Dorr, 1969; Gonçalves and Uhlein, 2022).

Overall, the Sr/Ba proxy reveals a transition in the paleosalinity conditions. Initially, the sediments at the base of the stratigraphy reflect freshwater to low brackish conditions suggesting a weak circulation with the open ocean, and transgression shifted the environment to marine deposition within the Itabira and Piracicaba Groups (Figure 5.8).

5.6.1.4 S-TOC proxy

Sulfur and TOC concentrations are key indicators of paleosalinity, as S is more abundant in marine sediments due to microbial sulfate reduction and pyrite formation (Gilleaudeau et al., 2021). On the other hand, the abundance of TOC in the sedimentary rocks is associated with large microbial populations, sedimentation taxes, and biomass preservation in estuarine, deltaic or coastal settings (Berner, 1985; Playter et al., 2017). The S/TOC ratio is about 13 times higher in marine than in freshwater sediments, making it a reliable paleosalinity proxy (Wei and Algeo, 2020). The S-TOC results align with other proxies (e.g. Sr/Ba ratio and B/Ga ratios), showing increasing salinity toward the Cercadinho Formation (Figures 5.6 and 5.8). In contrast, the Cercadinho Formation's S/TOC values indicate fully marine facies, reinforcing a marine transgressive scenario.

It is possible that the results of TOC in the present day doesn't represent for the original content, as part of the organic matter may have migrated out of the rock during burial and thermal maturation (Hart and Hofmann, 2022; Olson et al., 2025). Similarly, S abundance may have been affected by mobilization from the rocks (Hart and Hofmann, 2022). Reconstructing the original TOC content using Jarvie (2012) method is challenging in this study due to the low TOC abundance. Despite the uncertainties related to post-depositional alterations in the studied samples, the S/TOC results remain consistent with other paleosalinity proxies and align with the evolution of the Minas Basin.

In summary, these paleosalinity proxies (B/Ga, Sr/Ba, and S/TOC) indicate a transition from freshwater to low-brackish conditions in the Batatal Formation to fully marine conditions in the Cercadinho Formation.

5.6.2 Paleoredox variation in the Minas Basin

Iron speciation results indicate a wide range of values associated with ferruginous to oxic conditions, with Fe_{HR}/Fe_T values ranging from 0.49 to 0.06, peaking in the Batatal formation (Figure 5.7A). The inverse relationship between Fe_{HR}/Fe_T and Fe_T/Al (Figures 5.7C and 5.7D) suggests that the Fe_{HR}/Fe_T ratio, which is sensitive to the conversion of Fe_U to Fe_{HR}, may be influenced by post-depositional processes. For example, some highly reactive ($_{HR}$) iron pools may have been converted to silicates or carbonates during metamorphism, thereby transferring it to the Fe_U pool and causing the Fe_{HR}/Fe_T ratio to drop below 0.2 in some samples (Slotznick et al., 2018; Raiswell et al., 2018). Furthermore, samples that were deposited rapidly may not exhibit the authigenic enrichments that the iron speciation proxy attempts to fingerprint, yielding spuriously low Fe_{HR}/Fe_T. Thus, considering the factors mentioned above, samples with $Fe_{HR}/Fe_T > 0.38$ are interpreted as deposited under anoxic bottom water conditions, while lower values suggest oxic conditions (Poulton and Canfield, 2011; Caxito et al., 2024). However, due to the discrepancy between Fe_T/Al and Fe_{HR}/Fe_T ratios (Figure 5.7C), the iron speciation data cannot be directly taken at face value to confirm oxic bottom water conditions.

The low Fe_{Py}/Fe_{HR} ratio (<0.55 wt.%) indicates an overall absence of euxinic conditions (Figure 5.7B). In contrast, the high Fe_T/Al and high Fe_{HR}/Fe_T ratios strongly suggest anoxic bottom water conditions. It is important to note that the iron speciation proxy reflects redox conditions at the sediment/water interface (i.e., bottom water conditions) rather than in surface waters (Poulton and Canfield, 2011; Raiswell et al., 2018). This means that the Minas Basin was probably stratified, with a shallow oxic layer where dissolved ferrous iron (FeII) was oxidized and precipitated, overlying ferruginous bottom waters where the iron accumulated. This stratification aligns with existing models for BIF deposition in the Minas Basin (Teixeira et al., 2017). Our study also highlights the challenges in applying iron-speciation redox proxies to ancient basins, particularly in iron-rich intervals and basins that have experienced substantial metamorphism.

The EF values of the RSE in phyllite samples (Figure 5.6) indicate significant enrichment in the Batatal phyllites at the base of the stratigraphy, with maximum values of Cr_{EF} (3), V_{EF} (3.9), U_{EF} (6.7), and Mo_{EF} (6.3). Notably, the Batatal carbonaceous phyllite in the NE area exhibits a pronounced increase in RSEs (Figure 5.6). Additionally, the distribution of Mo_{EF}/U_{EF} values, as outlined by Algeo and Tribovillard (2009), serves as another redox proxy. This proxy is valuable for identifying reducing conditions, as Mo is preferentially scavenged in euxinic (oxygen-depleted, sulfur-rich) environments, while U is more likely to be scavenged in anoxic settings more broadly (irrespective of sulfide levels) (Algeo and Maynard, 2008; Tostelvin and Mills, 2020). This differentiation provides critical insight into the predominantly suboxic redox conditions during deposition of the Batatal and Cercadinho formations (Figures 5.6, 5.9). The EF values of RSE (e.g. Mo, U, Cu and Ni), along with Mo_{EF}/U_{EF}, indicate generally suboxic-anoxic conditions during the Batatal Formation deposition. In contrast, the Cercadinho Formation seems to exhibit more distinctly suboxic conditions, likely reflecting increased O_2 levels in surface waters while maintaining persistent anoxic conditions at the seafloor.

The C_{org}/P ratio serves as a proxy for tracking redox changes in the Minas Basin, as low O_2 levels promote the preservation of organic carbon and P release, whereas oxygenated conditions lead to organic carbon degradation and P retention (Algeo and Ingall, 2007). According to thresholds proposed by Ingall and Van Cappellen (1990) and Remirez et al. (2024), a $C_{org}/P< 50$ indicates oxic-suboxic conditions. Samples

from the Batatal Formation, located at the base of the stratigraphy, exhibit a wider range of C_{org}/P values, with a median of 14.4 (0.8–97.6). This suggests lower O_2 levels compared to the Cercadinho Formation, which exhibits a lower median C_{org}/P value of 1.3 (0.7–6.7). These findings are consistent with the interpretation that Batatal Formation represents more reduced conditions than of the Cercadinho Formation.

The reconstruction of water mass conditions based on the correlation between redox and paleosalinity proxies has been previously demonstrated by Falkner et al. (1993), Remírez et al. (2024) and Wei et al. (2024). The relationship between the B/Ga ratio versus U_{EF} suggests dynamic water column conditions (Figure 5.10) and a close correlation between salinity and redox condition. An integrated analysis of paleoredox proxies and paleosalinity proxies reveals the evolution of the water mass condition in the Minas Basin. Initially, during a suboxic-anoxic phase, limited connection to the open ocean resulted in a strongly stratified water column with oxygen-depleted deep waters. However, during the deposition of Cercadinho Formation, the basin became better connected to the open ocean, achieving fully marine salinity. Improved water circulation and ventilation led to increased O_2 levels in the water column.

Figure 5.9 — Variation of enrichment of U and Mo in the Minas Basin (Algeo and Tribovillard, 2009). The gray circles represent the Cercadinho Formation, the dark brown, Batatal Formation – area NE and light brown, the Batatal Formation – area SW.

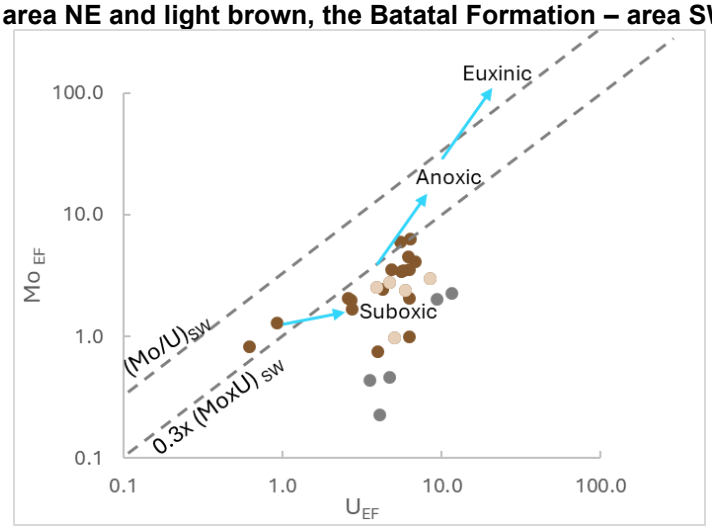

Source: Elaborated by the author

Figure 5.10 — Correlation between paleosalinity and redox proxies.

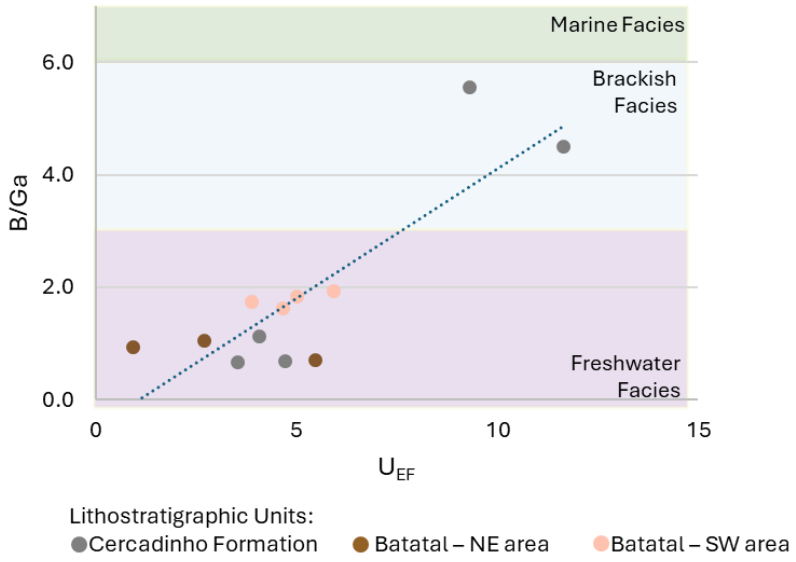

Source: Elaborated by the author

5.6.3 Evidence for bioproductivity in the Batatal phyllite

The Batatal phyllite exhibits enrichment of Cu, Ni and Zn, particularly in the carbonaceous phyllite layers in the northeastern area. This elemental enrichment, along with the sedimentary record, serves as evidence of significant microbial phytoplankton activity in the surface water of the Minas paleobasin, as these trace elements are essential for bacterial cellular functions (e.g. Tribovillard et al., 2006; Scott et al., 2013; Han et al., 2021). Moreover, sedimentary records suggest the paleoenvironmental conditions were reducing, allowing for the accumulation and degradation of biomass. This process, combined with burial fluxes, contributed to the trace element enrichment observed in the sediments (Tribovillard et al., 2006; Algeo and Maynard, 2008; Playter et al., 2017).

Phosphorus is another essential element for life, yet it is not a reliable indicator of paleoproductivity because it can be extensively recycled within the water column under anoxic conditions (Tribovillard et al., 2006). Nevertheless, Algeo and Ingall (2007) discuss variations in the C_{org}/P ratio as a proxy reflecting benthic redox conditions in depositional systems. Accordingly, the elevated C_{org}/P ratio values (97.9) found in the carbonaceous phyllites of the Batatal Formation suggest anoxic benthic redox conditions during their deposition.

This, coupled with other evidence, indicates elevated bioproductivity in the Minas Basin prior to the GOE and the precipitation of the Cauê BIF. This interpretation is consistent with the presence of free O_2 in the photic zone, which would have supported phytoplankton growth by providing essential nutrients derived from chemical weathering of terrestrial rocks (Hsi and Langmuir, 1985; Konhauser et al., 2011; Teixeira et al., 2017; Scott et al., 2008; Tostevin and Mills, 2020). The observed decrease of Cu, Ni and Zn abundance in the younger rocks from the Cercadinho Formation likely indicates a transition period where the paleoenvironmental changes impacted the biogeochemical cycling of trace elements.

5.6.4 Depositional model

The Caraça Group outlines a record of the tectonic evolution of the Minas Basin, transitioning from a continental rift to a passive margin setting (Dorr, 1969). This sequence reflects a shift from continental sedimentation (Gonçalves and Uhlein, 2022; Madureira et al. 2021) to deposition on an extensive continental shelf (Dorr, 1969). In this context, the alluvial-fluvial deposits of the Moeda Formation are conformably overlain by fine-grained siliciclastic rocks of the Batatal Formation (Dorr, 1969; Gonçalves and Uhlein, 2022).

Our findings suggest that the Batatal Formation comprises both detrital and chemical rocks deposited in freshwater to slightly brackish environments (Figures 5.11A and 5.11B). Fluvial influx transported continental sediments into a large freshwater body, interpreted as a lacustrine system, owing to the mixed siliciclastic-dolomitic deposition. Comparable examples can be found in other Brazilian sedimentary basins, such as the Cretaceous-aged Campos and Santos Basins, which both record the tectonic evolution from rift to post rift stage (e.g. Strugale and Cartwright, 2022). This progression is characterized by the initial deposition of fine-grained sediments in continental lacustrine environments, followed by a transition to marine sedimentation on shallow to deep marine platforms (Moreira et al. 2007; Winter et al. 2007).

Figure 5.11 — Proposed depositional model for Batatal Formation and Cercadinho Formation.

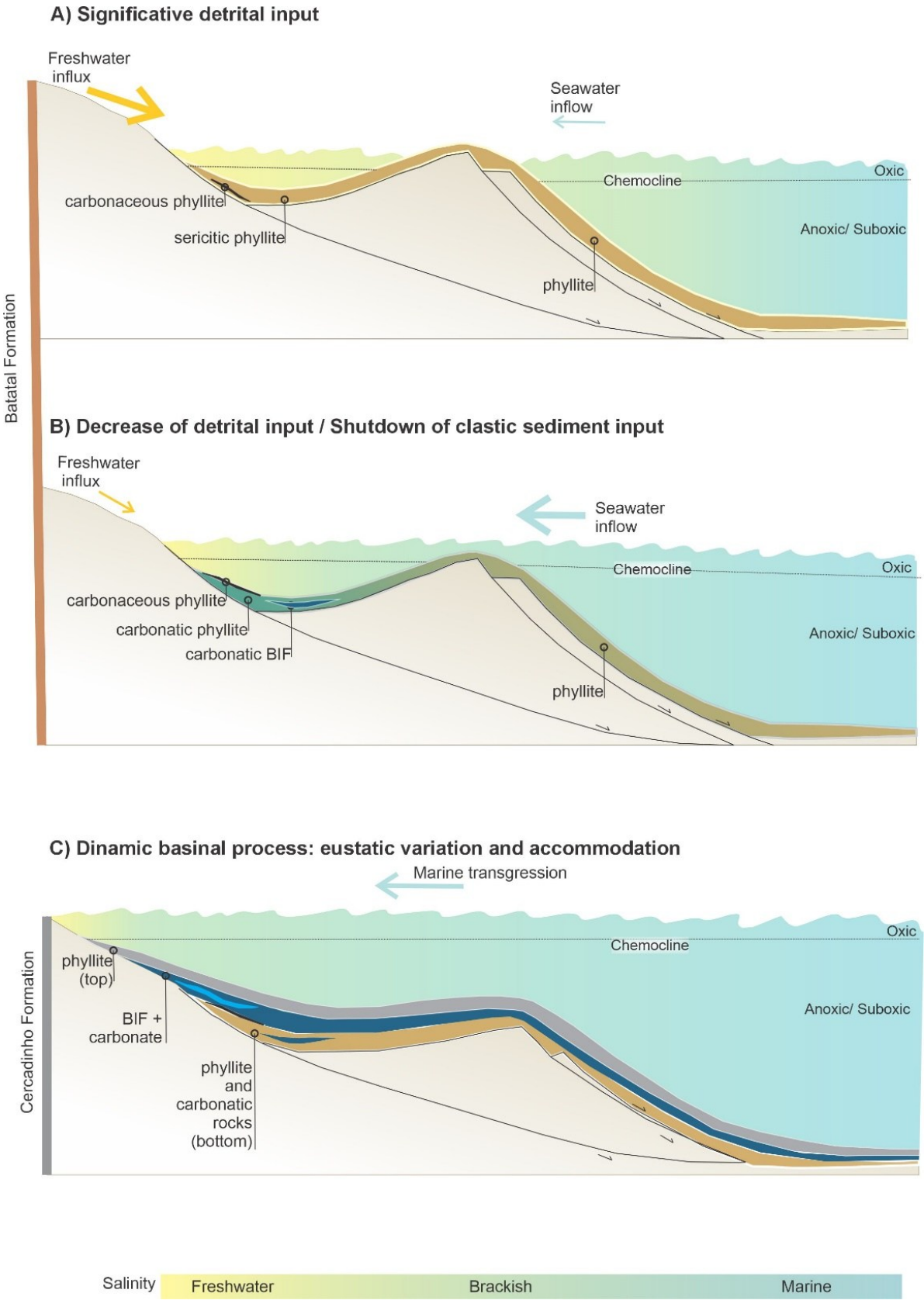

Source: Elaborated by the author

In the studied profile, the Batatal phyllite records a salinity gradient increase from the southwest to the northeast, based on the current orientation of the sedimentary layers in the Gandarela Syncline (Figure 5.2A). This observation suggests that, in the northeastern portion, the freshwater body may have a partial connection with the ocean, leading to water mixing and the development of brackish conditions (Fig 5.11B). During this stage of the sedimentary basin's evolution, the water column likely exhibited suboxic conditions within a stratified basin, characterized by a (sub)oxygenated surface layer overlying anoxic bottom water. Subsequently, as the transgressive system advanced, deposition transitioned to a fully marine environment, marked by the deposition of BIF (Cauê Formation) and carbonate rocks (Gandarela Formation). At the top of the stratigraphic sequence, the Cercadinho Formation reflects sedimentation in a marine environment under less-reducing conditions, indicative of improved ventilation and oxygenation in the basin (Figure 5.11C).

Therefore, the Minas Basin provided localized conditions conducive to the deposition of Fe-mineral precursors of BIF, prior to the Cauê BIF, in a transitional paleoenvironment influenced by a mix of waters with varying salinities, as evidenced by the Batatal Formation. In contrast, the formation of the giant BIF-hosted iron systems in the Quadrilátero Ferrífero, represented by the Cauê BIF (~350 m thick), followed by the Gandarela dolostones (~350 m thick), reflects a period of stable water mass conditions. These conditions facilitated the accumulation of these massive iron deposits over a timespan of approximately 100 million years.

5.7 Conclusion

Comprehensive paleosalinity studies using multiple salinity proxies (B/Ga, Sr/Ba and S/TOC ratios) reveal dynamic changes in water mass conditions throughout the formation of the Minas Basin. The fine-grained sediments of the Batatal Formation, located at the base of the stratigraphy, record a transition from freshwater to low-brackish facies, with limited marine influence. This suggests that the depositional paleoenvironment of the Batatal Formation was dominated by continental sedimentation. As a marine transgression advanced, the depositional environment shifted toward fully marine conditions, coinciding with the deposition of the Cauê BIF, Gandarela carbonate rocks, and fine-grained sediments of the Cercadinho Formation.

Therefore, the onset of BIF deposition is linked to a transitional paleoenvironment subject to mixed-salinity waters (Batatal Formation), while the giant BIF-hosted iron systems of the Quadrilátero Ferrífero, including the Cauê BIF, likely formed under stable water mass conditions sustained for ~100 million years.

This study indicates that paleosalinity proxies (B/Ga, Sr/Ba, and S/TOC) can provide reliable results even in metamorphic rocks, serving as valuable tools for reconstructing depositional environments. It underscores their potential for investigating Paleoproterozoic rocks while also highlighting the need for further research on how these proxies behave during metamorphism.

Paleoredox reconstructions suggest that the Batatal phyllites were deposited under anoxic and ferruginous (non-euxinic) bottom-water conditions. On the other hand, the younger Cercadinho Formation phyllites, found at the top of the stratigraphy, exhibit depleted RSE abundances, and lower Fe_{HR}/Fe_T ratios, but high Fe/Al ratios suggest iron re-partitioning due to post-depositional processes. Further investigation is needed to determine whether the fine-grained sediments of the Cercadinho Formation reflect less-reducing waters, with enhanced water column ventilation leading to improved deep-water oxygenation.

5.8 Acknowledgments

The authors would like to thank the mining company VALE S.A. for its collaboration and financial support, especially through ADIMB collaborative project: VALE - UNIVERSITIES - INSTITUTIONS. JRP was supported by CAPES and FAPEMIG scholarships, and by Instituto Serrapilheira scholarship to promote diversity in science. FAC is a recipient of a Research Productivity Grant from the Conselho Nacional de Pesquisa Científica (CNPq) and acknowledge for the support received through grants nb. 408815/2021-3 and 304509/2021-3. This is a contribution to Project MOBILE (geolifemobile.com), supported by Instituto Serrapilheira, Brazil (grant nb Serra-1912-31510). KOK was funded by the Natural Sciences and Engineering Research Council of Canada (NSERC). EAS was funded by a National Science Foundation grant EAR-2143164. The project was supported by the “CUG Scholar” Scientific Research Funds at China University of Geosciences (Wuhan) (Project No. 2022153).

6 SCIENTIFIC CONTRIBUTIONS III

This study presents detailed lithostratigraphic data on the Itabira Group in the Gandarela Syncline, integrating geochemical and isotopic proxies to reconstruct its paleodepositional evolution and the mechanisms which drove the precipitation of Fe-mineral precursors to the giant BIF-hosted Fe system in the Quadrilátero Ferrífero province. The manuscript is currently in progress, with nitrogen isotope analyses still incomplete and further refinement of the discussion and conclusions underway. The figures and tables included are preliminary drafts. Upon completion, the paper will be submitted to *Precambrian Research*.

C-N-O ISOTOPIC STRATIGRAPHY AND GEOCHEMICAL INSIGHTS INTO BIF AND DOLOSTONE FROM THE GANDARELA SYNCLINE, QUADRILÁTERO FERRÍFERO, BRAZIL

Janaina Rodrigues de Paula[1*], Fabricio A. Caxito[1], Kurt O. Konhauser[2], Alcides N. Sial[3], Leonardo B. Nogueira[4], Hermínio A. Nalini Jr.[4] Xueqi Liang[2], Long Li[2]

[1] Federal University of Minas Gerais, Belo Horizonte, Brazil, janainarpaula@gmail.com[*] and caxito@ufmg.br

[2] Department of Earth and Atmospheric Sciences, University of Alberta, kurtk@ualberta.ca; xueqi5@ualberta.ca; long4@ualberta.ca

[3] Federal University of Pernambuco – LABISE, Recife, Brazil, alcides.sial@ufpe.br

[4] Federal University of Ouro Preto, Ouro Preto, Brazil, leonardo.nogueira@ufop.edu.br and herminio.nalini@gmail.com

[*]Corresponding author: Janaina R. de Paula
Email address: janainarpaula@gmail.com

6.1 Abstract

Banded Iron Formation (BIF) represents a marine chemical precipitate deposited in the ocean during specific intervals of the Earth's history, coinciding with significant changes in the atmosphere, hydrosphere, and biosphere. This study examines the mineralogy, petrography, and geochemistry of BIF and associated carbonate rocks

from the Paleoproterozoic succession of the Itabira Group. The Cauê BIF exhibits compositional variations, including quartz-BIF, dolomite-quartz-BIF, and dolomite-BIF which reflect changes in precipitation and sedimentation patterns within the paleo sedimentary basin. The mineralogy of the BIF is primarily composed of magnetite, hematite, quartz, and dolomite. The geochemical signature indicates a hydrothermal contribution to seawater, as evidenced by a positive Eu anomaly. Additionally, the presence of both positive and negative Ce anomalies suggests localized oxygenated conditions. The carbon isotopic composition of iron-rich rocks reveals negative fractionation, supporting a genetic model involving Dissimilatory Iron Reduction (DIR) as a key process to transform iron-bearing minerals, the precursors of the BIF. The nitrogen isotopic composition corresponds to the expected range for Paleoproterozoic records and may be interpreted as a result of metabolic isotopic fractionation under anoxic conditions. Post-depositional processes, such as devolatilization, can influence geochemical and isotopic signatures. However, the results of this study demonstrate a robust dataset that aligns well with previous research on other giant IF-hosted Fe systems.

Keywords: carbon isotope, nitrogen isotope, BIF, Paleoproterozoic

6.2 Introduction

The Precambrian was marked by significant transformations in Earth's atmosphere and oceans, particularly due to the elevation in free oxygen levels (Cloud, 1973; Lyons et al., 2014). This event, known as the Great Oxygenation Event (GOE), unfolded in two phases: an initial increase around ~2.5 Ga, followed by a major peak at ~1.9 Ga (Large et al., 2022). The impact of this geochemical evolution is potentially recorded in BIF and carbonate rocks, as these marine chemical precipitates can preserve the chemical signature of the water column at the time of deposition (e.g. Morgan et al., 2013; Gumsley et al., 2017; Li et al., 2023).

Several genetic models have been proposed to explain the formation of giant IF-hosted Fe system. One of the most widely accepted models highlights the role of early microbial activity in facilitating the precipitation of primary Fe(III) minerals, such as Fe-oxyhydroxides, followed by the later reduction of iron-bearing minerals (Morris, 1993;

Kappler et al., 2005; Konhauser et al., 2002, 2011). In this process, the oxidation of dissolved Fe(II) was driven either by oxygen produced through the photosynthesis of cyanobacteria (Cloud, 1965; 1973) or by metabolic mechanisms that functioned with or without oxygen (Konhauser et al., 2002, 2011). Subsequently, Fe(III) was recycled through DIR, resulting in the formation of the mixed valence state Fe(II)-Fe(III) minerals (Walker, 1984; Vargas et al., 1998; Konhauser et al., 2005).

To reconstruct the biogeochemical cycles and paleoenvironmental evolution of the Precambrian, chemical and isotopic proxies have been applied to BIF and carbonate rocks (e.g., Pecoits et al., 2009; Bekker et al., 2010; Hensler et al., 2017). For instance, these geochemical investigations can focus on the abundance of redox-sensitive elements (e.g., Cr, Mo, U, and V) to delimitate redox conditions in the ancient atmosphere and ocean, the Ni/Fe ratio as an indicator of microbial activity, and the Y/Ho ratio as a proxy for detrital input into the ocean (Bau et al., 1997; Kamber and Webb, 2001; Konhauser et al., 2009; Tostevin and Mills, 2020). The rare earth elements and yttrium (REEY) concentration can reveal Eu enrichment, indicating hydrothermal Fe(II) inputs and negative Ce anomalies, suggesting local oxidizing conditions during deposition (Klein and Beukes, 1992; Bekker et al., 2010; Mendes et al., 2016). In addition, stable isotope signatures (C, O, Cr, Fe, and N) may provide insights into biogeochemical cycles and the redox state in ancient environments (e.g., Thomazo et al., 2009; Caxito et al., 2019; Mozart et al., 2024).

The Quadrilátero Ferrífero province (QFe) (Figure 6.1) in southeastern Brazil hosts one of the world's largest Paleoproterozoic Fe deposits (Hagemann et al. 2016). The Lake Superior-type BIF comprises over 350 meters of iron-rich sediments, followed by a carbonate rocks succession approximately 600 meters thick (Dorr, 1969; Endo et al., 2020). The province has undergone greenschist metamorphism; however, some of the rocks have preserved marine geochemical and isotopic signatures, which serve as valuable tools for interpreting ancient seawater conditions (e.g. Sial et al., 2000; Bekker et al., 2003; Spier et al., 2007; Nogueira et al., 2019). Previous studies have shown that BIF from the QFe exhibits positive Eu, La, and Y anomalies, along with both positive and negative Ce anomalies, indicating chemical precipitation influenced by low detrital input and hydrothermal contributions to the water column (Spier et al., 2007; Alkmim, 2014; Hensler et al., 2017). In addition, $\delta^{13}C$ ranges from -12.2‰ to -0.2‰ (Spier et al., 2007; Morgan et al., 2013; Teixeira et al., 2017; de Paula et al., 2023),

evidencing the negative fractionation of ^{12}C. Meanwhile, positive fractionated $\delta^{56}Fe$ values, varying between 0.5‰ and 1.3‰ in conjunction with the negative $\delta^{13}C$ were interpreted as evidence for DIR mechanisms in the formation of Fe-minerals precursors of BIF (Teixeira et al., 2017). These geochemical data closely resemble those observed in other Paleoproterozoic BIF-hosted Fe systems, such as the Transvaal Basin (South Africa) and Hamersley Basin (Australia) (Renger et al., 1994; Rosière et al., 2008; Mendes et al., 2016; Teixeira et al., 2017).

This study presents new geochemical and stable isotope data, including C, N, and O isotopes, from Paleoproterozoic BIF and carbonate rock from Caraça, Cauê and Gandarela formations in the Gandarela region, northeastern QFe (Figure 6.1). This area has limited available geochemical data, and its well-preserved outcrops provide an opportunity to investigate the geochemical evolution from both local and regional perspectives. To achieve this, samples collected from deep drill cores and outcrops were analyzed in detail, including novel N-isotope composition in the province. Furthermore, this study helps to contextualize the QFe within global events such as the GOE and world-class BIF-hosted Fe systems (e.g., Hamersley Province, Australia).

Figure 6.1 — Geological map of the Quadrilátero Ferrífero province.

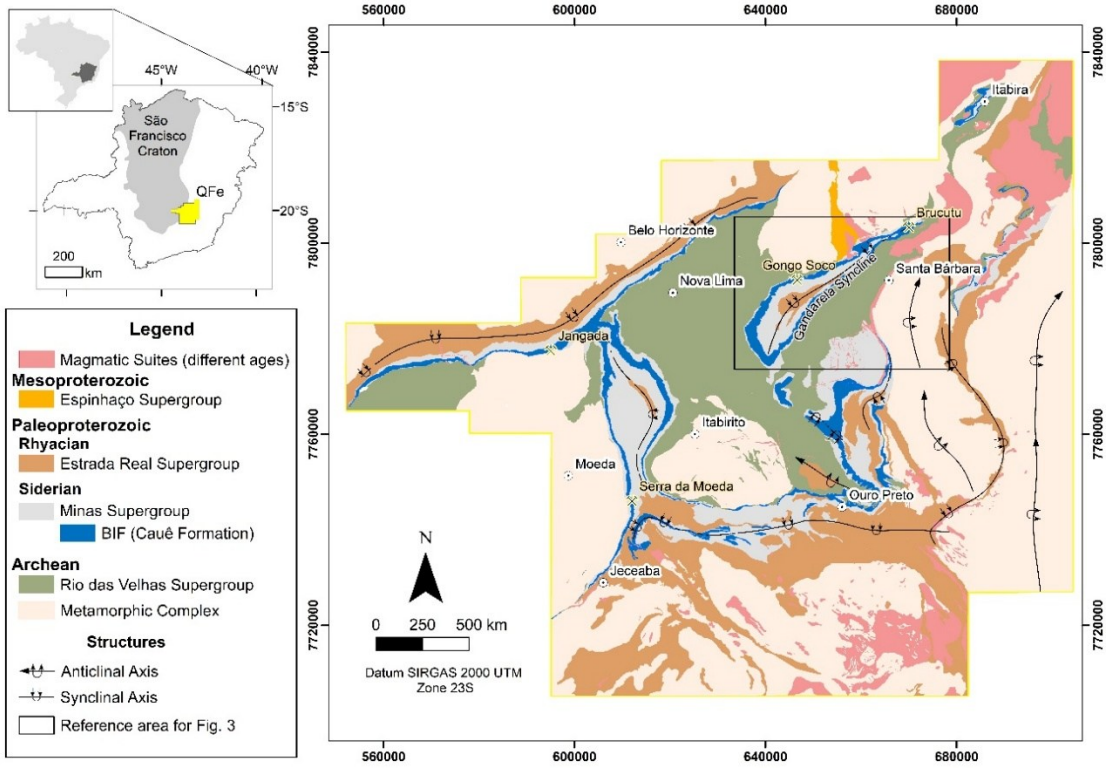

Source: Modified from Endo et al., 2019

6.3 Geologic Setting

The QFe province, southeastern Brazil, overlays the southernmost portion of the São Francisco Craton (Figure 6.1), one of the major cratonic areas of the South American platform. The region shows a succession of Precambrian rocks and hosts significant iron, gold and manganese deposits (Dorr, 1969; Lobato, et al., 2001; Rosière et al., 2008; Dias and Caxito, 2018; Dias et al., 2022). The QFe stratigraphy consists of four lithostratigraphic units, represented from bottom up: the Archean metamorphic complex, the Rio das Velhas Supergroup, the Minas Supergroup, and the Estrada Real Supergroup (Figure 6.2). The Archean metamorphic complex is primarily composed of gneisses, migmatites, and granitoids, formed between 3.2 to 2.7 Ga (Farina et al., 2016 and references therein). The Rio das Velhas Supergroup, characterized by a greenstone belt succession, comprises ca. 6 km of metavolcanic and metasedimentary rocks deposited during the Neoarchean, with a maximum depositional age of 2.7 Ga (Machado et al., 1992; Baltazar and Zucchetti et al., 1997; Hartmann et al., 2006). Above this, the Minas Supergroup, with approximately 3 km of metasedimentary rocks (Dorr, 1969) was deposited between 2.5 and 2.2 Ga (Babinski et al., 1995; Bekker et al., 2003; Hartmann et al., 2006; Koglin et al., 2014; Nunes et al., 2016; Dopico et al., 2017; Rossignol et al., 2020). The youngest lithostratigraphic unit, the Estrada Real Supergroup (~2.0 Ga), is characterized by metasedimentary rocks with an estimated thickness of more than 3 km (Machado et al., 1996; Endo et al., 2020).

The Minas Supergroup succession (Figure 6.2) represents the transition from a rift basin to a passive margin (Renger et al., 1994; Alkmim and Marshak, 1998). The basal units include the Caraça group, which is subdivided in the Moeda and Batatal formations, and its lateral equivalent, the Tamanduá group, which comprises the Cambotas and Morro Grande Formation. These basal units consist predominantly of clastic rocks with minor chemical rocks (Dorr et al., 1969; Endo et al., 2020). Endo et al. (2019) identified a local occurrence of the Tamanduá Group in the studied area, but its extent, timing, and stratigraphic context remain debated (e.g., Simmons and Maxwell, 1961; Marshak and Alkmim, 1989; Daher et al., 2020; Dutra et al., 2020). Therefore, this study classifies fine-grained sedimentary rocks deposited before the Itabira Group BIFs as part of the Batatal Formation. Conformally overlying these units,

the Itabira Group, first defined by Dorr et al. (1957), consists mainly of a package of chemical sedimentary rocks (Figure 6.2). Its basal unit, the Cauê Formation, contains quartz-, dolomite-, and amphibolitic-BIF, with minor phyllite and dolostones. This is followed by the Gandarela Formation, composed of carbonate rocks, including dolostones (locally with spheroids and stromatolites), dolomitic BIF, and brecciated carbonates (e.g., Bekker et al., 2003; Almeida and Sousa Jorge, 2022). An erosional unconformity separates the Itabira from the overlying Piracicaba Group (Dorr, 1969; Gonçalves and Uhlein, 2022), which, in the studied area, is represented by the Cercadinho Formation, consisting of quartzite, ferruginous quartzite, schist, and phyllite.

Figure 6.2 – Stratigraphic column of QFe, with emphasis on the Minas Supergroup. References: [1] Machado et al. (1996), Lana et al. (2013), Farina et al. (2015); [2] Machado et al. (1992), Noce et al. (2005); [3] Hartmann et al. (2006); [4] Cabral et al. (2012); [5] Babinski et al. (1995); [6] Machado et al. (1996) and [7] Machado et al. (1996), Dopico et al. (2019).

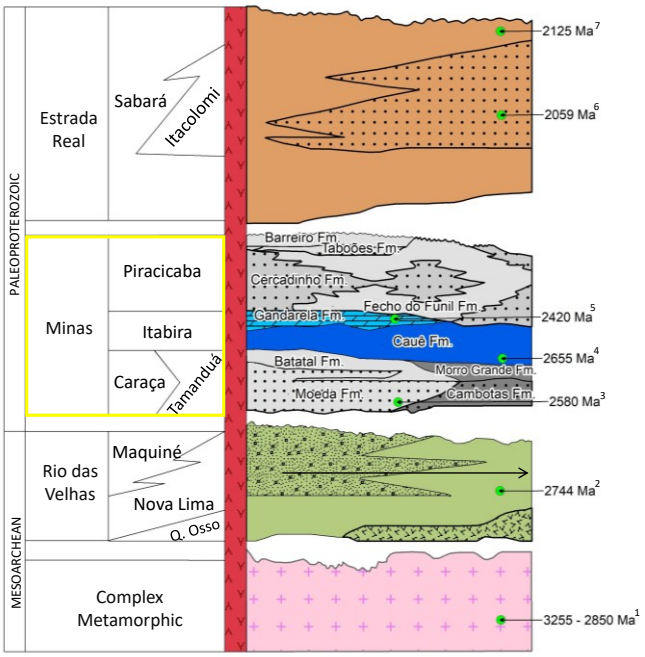

Source: Modified from Dorr (1969) and Endo et al. (2022).

The QFe underwent two main phases of deformation, during the Rhyacian orogeny (~2.0 Ga) and the Brasiliano Orogeny (~0.5 Ga) (Marshak and Alkmim, 1989). As a result, the Gandarela syncline (Figure 6.3) exhibits a reclined fold geometry with an NE-SW trending axial trace (Dorr, 1969) and hinge at 110/45 (Oliveira et al., 2005).

This study focuses on the metasedimentary chemical rocks of the Minas Supergroup, particularly those associated with the Batatal, Cauê and Gandarela Formations in the Gandarela region (Figure 6.3). Through the analysis and interpretation of geochemical proxies and C-O-N isotopic composition, this study aims to contribute to paleoenvironmental reconstructions by evaluating the evolution of the redox state of the water column, as well as identifying biogeochemical signatures associated with Fe deposition in the QFe. These results provided insights into the role of microbial activity, hydrothermal influence, and seawater conditions in the formation of the giant BIF-hosted Fe systems, further contextualizing the QFe within global Paleoproterozoic environmental changes.

Figure 6.3 — Geological map of the Gandarela syncline (modified by Endo et al. 2019), showing the studied drill holes and field samples. Vertical sections illustrate the lithostratigraphic units intersected by the sampled drill holes.

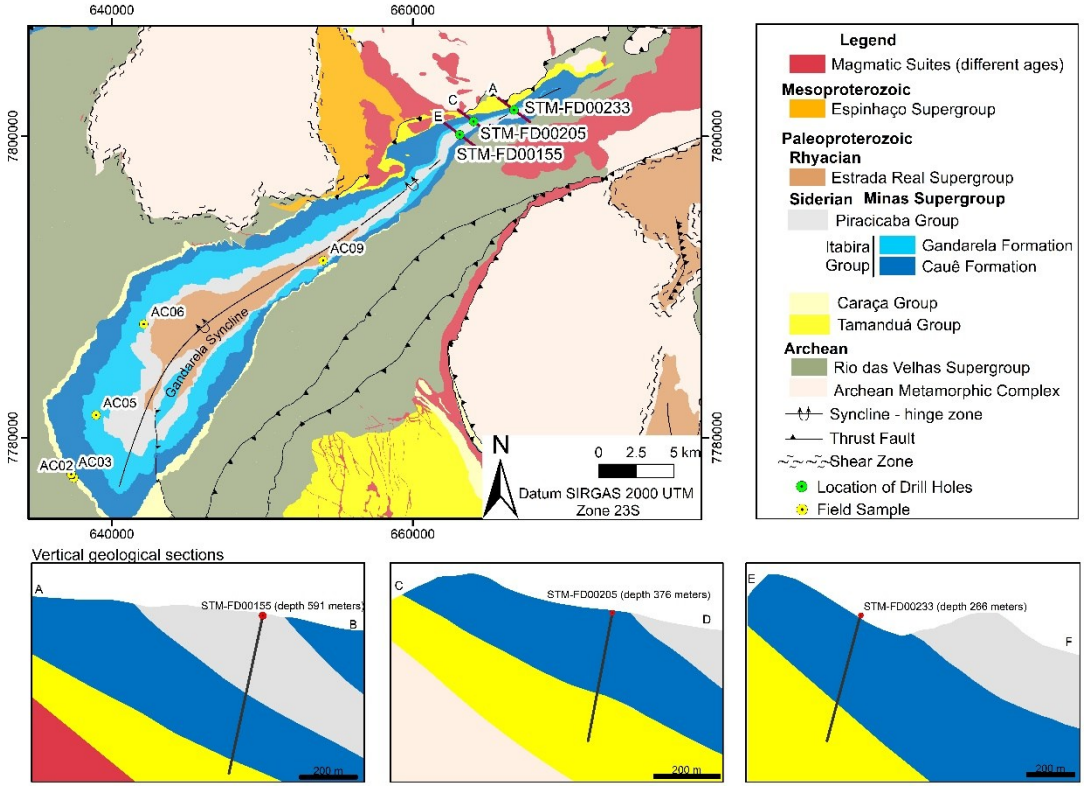

Source: Elaborated by the author

6.4 Sampling and Analytical Methods

This study investigates three deep drill cores provided by Vale S.A., identified as STM-FD00155 (591-meters depth), STM-FD00205 (376-meters depth) and STM-FD00233 (233-meters depth), along with well-preserved outcrops samples from the Gandarela syncline (Figure 6.3). In total, 54 samples were collected, comprising 39 from drill cores and 15 from outcrops, representing BIF and carbonate rocks from different layers within the Minas Supergroup, from the base to top: Caraça Group (Batatal Formation) and Itabira Group (Cauê and Gandarela formations).

After a detailed macroscopic examination, petrographic observations were made on sixteen thin sections from representative samples using an optical microscope in the Microscopy Laboratory at the Federal University of Minas Gerais, Brazil, and the University of Alberta, Canada.

X-ray diffraction (XRD) analyses were performed on five samples to determine mineral phase identification. At the X-Ray Diffraction Laboratory, University of Alberta (Canada). The powdered samples were examined using a Bruker D8 Advance X-ray diffractometer with a cobalt radiation source - 35 kV and 40 mA. The XRD data were processed with the DIFFRAC.EVA software was developed by Bruker. Mineral phase identification was conducted using the PDF 4+ database from the International Center for Diffraction.

Geochemical analyses were performed on 54 samples at SGS Geosol Laboratory Ltd., Brazil and 21 samples at Bureau Veritas Laboratory, Canada. Sample preparation included drying, crushing, homogenization, and pulverization to 150# mesh. Powdered aliquots were digested either with lithium metaborate or a multi-acid mix (nitric, hydrochloric, hydrofluoric, and perchloric acids). Major oxide and trace element concentrations were determined using an inductively coupled plasma with a mass spectrometer (ICP-MS) or optical emission spectrometer (ICP-OES). Analytical errors are less than 5% for major oxides and range from 10% to 15% for trace elements. Loss on Ignition (LOI) values were calculated based on the relative mass difference after ignition at 1000°C. Rare Earth Element (REEY) concentrations were normalized using the Post Archean Average Australian Shale (PAAS), as proposed by Pourmand et al. (2012), which revised the REE patterns established by Taylor and McLennan (1985). Cerium and Eu anomalies were calculated using the following equations: $Ce/Ce^* = [Ce]_{SN}/([Pr]_{SN}^2)/[Nd]_{SN})$, as developed by Lawrence et al. (2006) to minimize influence from anomalous La behavior. $Eu/Eu^* = [Eu]_{SN}/([Sm]_{SN}$ x

$[Gd]_{SN})0.5$, where Eu* represents a hypothetical concentration of Eu^{+3} (Taylor and McLennan, 1985).

A total of 76 carbon and oxygen isotopic analyses were performed on dolomitic rocks, including dolomitic BIF and dolostones. Samples were obtained through micro-drilling (4 mm diameter) or carefully grinding in an agate mortar to avoid contaminations. The sampling avoided highly deformed zones to minimize the effects of metamorphic overprinting. The analyses were conducted at three laboratories: the NEG-LABISE Laboratory at the Federal University of Pernambuco (UFPE), the Geochemistry Laboratory at the Federal University of Ouro Preto (UFOP), and the Stable Isotope Laboratory at the University of Alberta (UofA). At NEG-LABISE, CO_2 extraction was carried out using a high-vacuum line, where samples reacted with 100% orthophosphoric acid at 25°C over three days—an approach suited for Ca-Mg carbonates. The released CO_2 was analyzed using a Thermo Finnigan Delta V Advantage mass spectrometer. At the Geochemistry Laboratory, CO_2 extraction followed an online method in which 500 µg of powdered samples reacted with 100% orthophosphoric acid in a closed-tube system at 72°C for one hour. The resulting CO_2 was analyzed using a Thermo Finnigan Delta V Advanced mass spectrometer, coupled with a GasBench II system. Both Brazilian laboratories achieved analytical accuracy better than ±0.1‰. At the UofA, powdered samples were reacted with 100% orthophosphoric acid in glass tubes under a vacuum at 50°C overnight. The released CO_2 gas was cryogenically purified, collected into sample tubes, and analyzed using a Thermo Finnigan MAT 253 isotope ratio mass spectrometer in dual-inlet mode. An acid fractionation correction was applied for aragonite. The analytical precision was ±0.2‰ (2σ) for both $\delta^{13}C$ and $\delta^{18}O$. All isotopic values are reported relative to the Vienna Pee Dee Belemnite (VPDB) standard.

Nitrogen extraction and isotopic analysis were conducted on 21 BIF samples at the Stable Isotope Laboratory, University of Alberta, Canada. As described by Li et al. (2021), the method used a sealed-tube offline combustion technique with two combustion stages (1200°C for 2 h and 900°C for 8 h) and cooling at 600°C for 2 h. A CuO reagent was added in the second combustion step. Following vacuum conditions, the nitrogen released was cryogenically purified and analyzed using a Thermo MAT 253 isotope ratio mass spectrometer.

6.5 Results

6.5.1 Core Descriptions

The following describes the lithologic successions observed in the three analyzed drill cores (Figure 6.4).

The deepest drill core, STM-FD00155, reaches 591 meters. The uppermost 28 meters consist of a laterite crust, succeeded by the Piracicaba Group, composed predominantly of quartzite with minor phyllite lenses, extending to 308 meters in depth. Then, the Itabira Group begins with chemical sedimentary rocks, which comprise friable BIF in the next 100 meters (Figure 6.5A). Between 411 and 538 meters, a thick (127m) compact quartz-BIF is present. Lastly, a 53-meter succession of ferruginous dolostone, quartz-carbonate-BIF (Figure 6.5B and C), and phyllite marks the bottommost section, continuing to the end of the core at 591.

Drill core STM-FD00205 has a depth of 376 meters and is notably characterized by a higher concentration of carbonate rocks than the other studied drill holes. In brief, the drill hole begins with a 37-meters ferruginous lateritic crust. This is followed by 68 meters of friable manganesiferous and aluminous BIF and Mn-rich rocks, which represent a typical feature of weathered carbonate rocks in the QFe province and were classified as Gandarela Formation. From a depth of 105 meters to the end of the drill core at 376 meters, there is a predominant succession of dolomite-quartz-BIF. During this interval, it becomes less evident to discern the lower boundary of the Cauê Formation due to a gradual decrease in the Fe content of BIF. Additionally, from 237 meters, intercalations of ferruginous dolostone, dolomite-BIF and dolomite-quartz-BIF layers are found within the ferruginous package. Finally, the last 18 meters of the drill core consist of carbonaceous phyllite and ferruginous dolostone and these have been correlated with the Batatal Formation.

The final drill core, designated as STM-FD00233, is in the westernmost area and reaches a depth of 266 meters. The succession of the drill core begins with an 8-meter lateritic. Subsequently, there is a persistent layer of quartz-BIF, belonging to the Cauê Formation, that spans 180 meters of thickness, extending down to 188 meters. The lithological contact between the BIF Cauê Formation and metasedimentary rocks from the Batatal Formation is marked by a 7-meter deep weathered friable quartzite.

Then, from 195 to 266 meters, the core comprises a succession of rocks including quartzite, carbonaceous phyllite, and sericitic phyllite.

Figure 6.4 — Lithostratigraphic column of drill cores STM-FD00155 (A), STM-FD00205 (B) and STM-FD00233 (C).

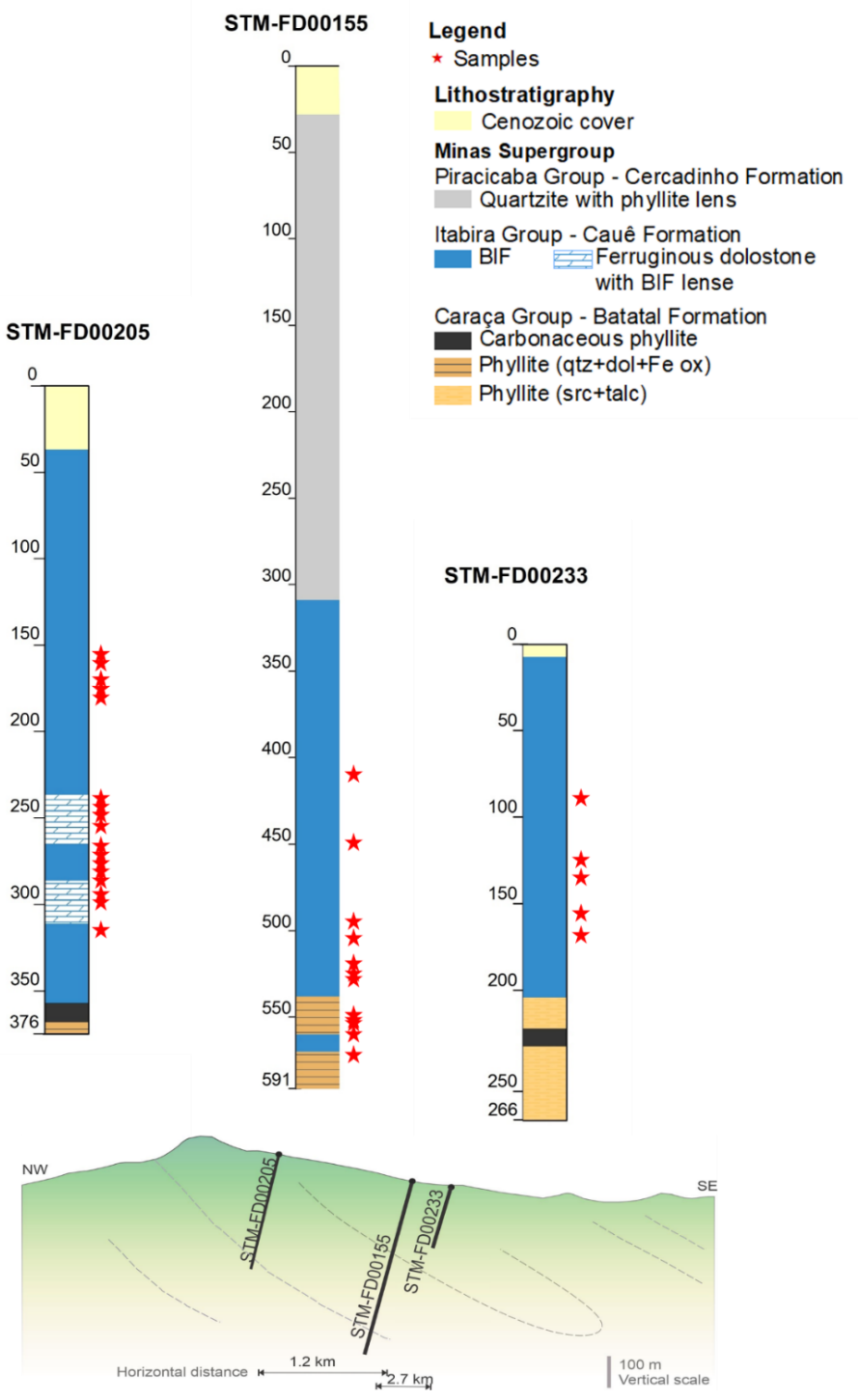

Source: Elaborated by the author

Figure 6.5 — Drill core STM-FD00155 A) BIF from the main layer of Cauê Formation (depth ~ 516 meters), B) BIF lenses into the dolostone (depth ~ 557 meters) and C) Texture of the dolomitic BIF (depth ~565 meters).

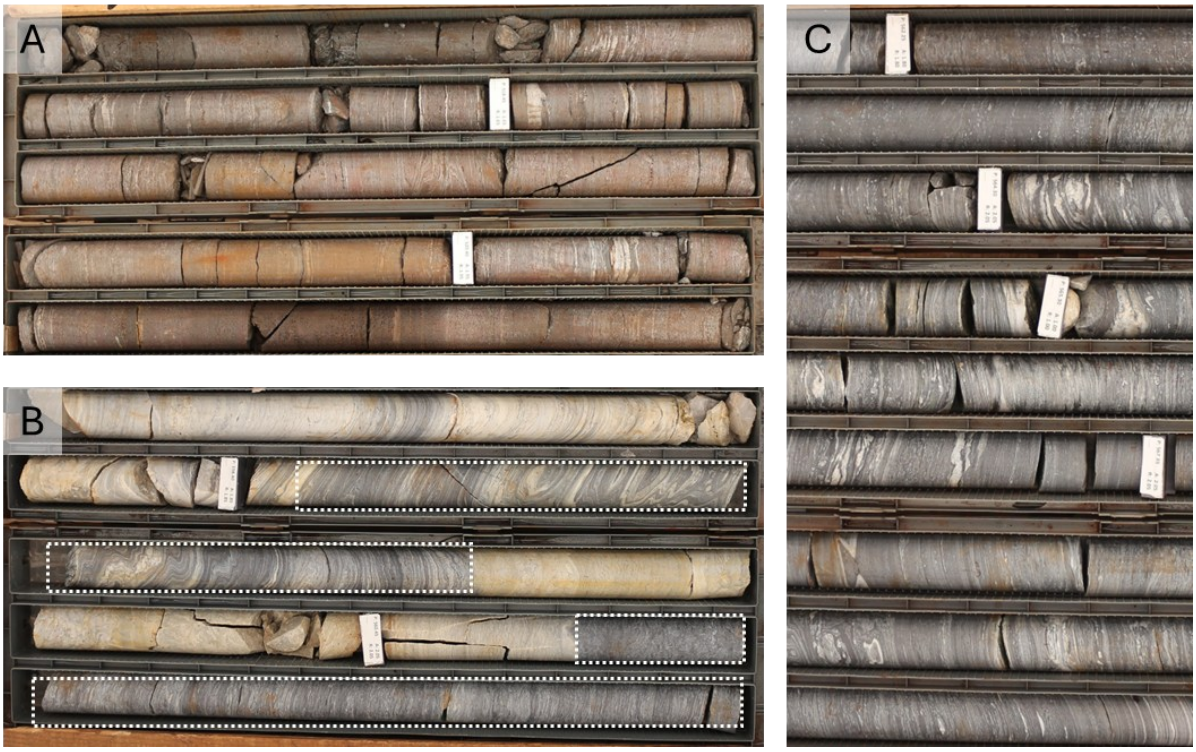

Source: Elaborated by the author

6.5.2 Petrographic Description and Mineralogy

The petrographic description of chemical sedimentary rocks is based on the stratigraphic units.

6.5.2.1 Batatal Formation

The phyllite of the Batatal Formation can reach up to 300 meters in thickness and is primarily composed of homogeneous sericitic phyllite, with variations including ferruginous, dolomitic, chloritic, micaceous, and carbonaceous types, as well as impure dolostones and dolomitic BIF lenses. This study focuses on carbonate-rich intervals. The dolomitic phyllite consists of chlorite, quartz, dolomite, Fe-oxides, and muscovite, with accessory pyrite, rutile, and apatite. It may exhibit lamination with magnetite, pyrite, carbonate, and quartz overgrowing the schistosity. Impure dolostone is commonly composed of dolomite, quartz, chlorite, varying amounts of Fe-oxides, and accessory pyrite. The dolomitic interval is intercalated with Dolomite-Quartz-BIF

layers, in which the main Fe-oxide is magnetite. The banding varies from well-laminated to more diffuse in some sections (Figure 6.5 B and C).

6.5.2.2 Itabira Group

The BIF layers are primarily associated with the Cauê Formation, where they exceed 250 meters in thickness. The BIF composition varies between Quartz-BIF and dolomite-BIF. The quartz-BIF, observed in drill cores STM-FD00155 and STM-FD00233, is the most Fe-rich BIF, consists of microbands (<0.5 cm thick) alternating between white quartz and gray Fe-oxide (magnetite) laminae, with minor hematite, goethite and kaolinite. Localized features include secondary porosity, folds, and microfaults within the microbands. Dolomite-Quartz-BIF, found in drill cores STM-FD00205 and STM-FD00155, has an intermediate Fe content and consists of alternating magnetite-rich Fe-oxide laminae and quartz-dolomite laminae, with minor hematite, apatite, and chlorite. Its microband structure varies from regular wavy textures (STM-FD00205) to more heterogeneous patterns with intrafolial folds and quartz-carbonate veins (STM-FD00155).

The Gandarela Formation is represented by fresh carbonate rocks found in two rare outcrops within the Gandarela syncline (Figure 6.6 A). These rocks show dolomitic and calcitic compositions, with accessory minerals such as Fe-oxide, chlorite, pyrite, and rare muscovite. Microfractures filled with calcite and/or quartz occasionally intersect the carbonates. Based on texture and mineral composition, six distinct dolostone lithotypes can be identified:

1) Massive white or gray dolostone: composed of micrite carbonate with low or absent magnetism (Figure 6.6 B).

2) Laminated red and white dolostone: a rhythmic micritic dolostone formed by alternating white and red bands (Figure 6.6 C). The red bands contain magnetite microcrystals and dust-like Fe-oxide inclusions, imparting a reddish colour. In contrast, the white bands primarily consist of carbonate minerals.

3) Gray ferruginous dolostone: composed of micritic dolostone with medium to high magnetism with Fe-oxide and pyrite as accessory minerals (Figure 6.6 D). In sample AC05-08, gray dolostone is interlayered with green talc-phyllite. The texture is mainly laminated but occasionally massive.

4) Banded limestone with spheroids and stromatolites: characterized by alternating white bands (predominantly calcite and occasional muscovite) and dark

gray bands (mainly calcite with minor quartz and hematite). Figure 6.6 E illustrates black spheroid and stromatolite structures within this lithotype, previously described in studies by Souza and Muller (1984), Bekker et al. (2003), and Almeida and Sousa Jorge (2022).

Figure 6.6 — A) Outcrop of dolostone from Gandarela Formation, showing compositional variations: (B) massive white, (C) laminated, D) ferruginous with disseminated pyrite crystals and E) dolostone with spheroid and stromatolite structures.

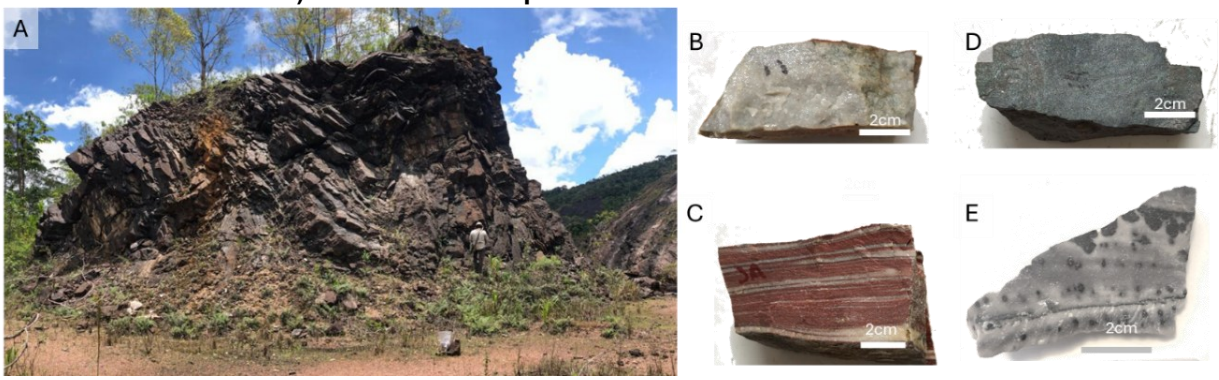

Source: Elaborated by the author

6.5.3 Geochemical analyses

Geochemical analyses of major oxides from BIF and carbonate rock are presented in Table 6.1. A ternary diagram (Figure 6.7) illustrates the major composition of BIF samples, highlighting the compositional variability of the iron-rich rocks. The trace elements and REEY abundance are shown in Table 6.2. PAAS normalization follows the parameters defined by Marshak and Alkmim (1989) and updated by Pourmand et al. (2012).

Figure 6.7 — A) Ternary diagram showing the main composition of the BIF types. B) Folded quartz-BIF, C) Laminated dolomite-quartz-BIF and (D) Dolomite-BIF with macrocrystals of magnetite.

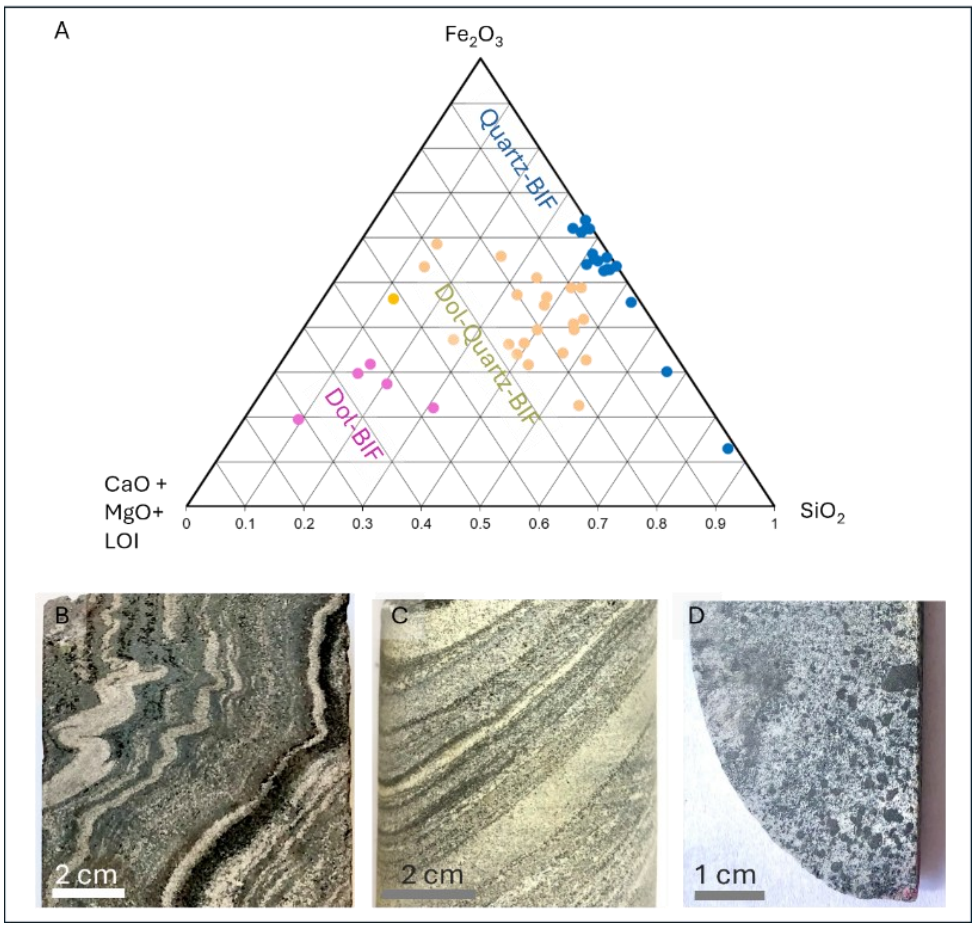

Source: Elaborated by the author

Table 6.1 — Results of major elements of the studied samples from the Gandarela Syncline.

				Oxides (wt.%)										
Type	Sample ID	Lithology	Lithostratigraphy	Al_2O_3	CaO	Fe_2O_3	K_2O	MgO	MnO	Na_2O	P_2O_5	SiO_2	TiO_2	LOI
Outcrop samples	AC05-00	Dolostone	Gandarela	0.81	26.33	4.84	0.29	17.44	1.13	<0.01	0.02	4.82	0.04	41.66
	AC05-01	Dolostone	Gandarela	0.90	28.55	3.54	0.30	18.26	1.33	0.04	0.02	3.24	0.04	44.39
	AC05-02	Dolostone	Gandarela	0.41	28.30	5.99	0.18	18.29	1.32	0.02	0.02	2.57	0.01	42.66
	AC05-03	Dolostone	Gandarela	0.31	28.54	5.07	0.16	18.12	1.87	0.03	0.02	2.50	0.01	43.30
	AC05-04	Dolostone	Gandarela	0.20	28.57	4.90	0.11	18.09	1.80	0.03	0.02	2.75	-	43.44
	AC05-05	Dolostone	Gandarela	0.50	28.73	6.67	0.17	17.68	2.01	0.04	0.02	2.18	0.02	42.50
	AC05-06	Ferrug. dolostone	Gandarela	0.22	16.43	25.27	0.10	13.18	0.56	<0.01	0.06	21.54	0.01	23.28
	AC05-07	Ferrug. dolostone	Gandarela	0.17	20.58	21.26	0.08	13.77	0.68	0.02	0.04	17.88	-	29.03
	AC05-09	Dolostone	Gandarela	0.06	28.97	8.47	0.03	16.61	0.77	0.02	0.01	2.15	-	43.85
	AC05-10	Dolostone	Gandarela	0.04	28.75	7.95	0.03	17.86	0.64	<0.01	0.02	3.51	-	42.54
	AC05-11	Dolostone	Gandarela	0.06	29.37	6.25	0.04	18.39	0.63	0.02	0.02	4.07	-	43.08
	AC05-12	Dolostone	Gandarela	0.04	28.73	5.04	0.03	18.44	0.56	<0.01	0.01	3.85	-	43.31
	AC05-13	Dolostone	Gandarela	0.04	25.65	9.17	0.03	17.03	0.64	0.03	0.02	7.50	0.01	38.62
	AC05-14	Ferrug. dolostone	Gandarela	0.14	20.86	21.16	0.03	13.95	0.76	<0.01	0.06	11.82	0.01	30.57
	AC05-15	Ferrug. dolostone	Gandarela	0.11	24.69	10.88	0.05	16.04	1.62	0.02	0.05	10.53	-	36.90
	AC-17-01A	Dolomitic BIF	Cauê	0.23	10.06	53.18	<0.01	7.34	0.32	<0.01	0.07	13.58	0.02	15.10
	AC-17-01B	Dolomitic BIF	Cauê	0.21	8.82	58.08	<0.01	6.05	0.30	<0.01	0.11	13.25	0.02	13.00
Drill core STM-FD00155	A011	Quartz-BIF	Cauê	0.85	0.13	29.77	0.10	0.19	0.04	<0.01	0.09	65.92	0.15	2.85
	A011_BV	Quartz-BIF	Cauê	0.31	<0.01	12.83	0.06	0.02	0.01	0.01	0.06	85.18	0.02	1.40
	A012	Quartz-BIF	Cauê	0.39	<0.01	61.37	0.02	0.04	0.01	<0.01	0.11	36.56	0.06	0.93
	A013	Quartz-BIF	Cauê	0.23	<0.01	56.52	0.02	0.01	0.01	<0.01	0.14	40.98	0.03	2.60
	A013_BV	Quartz-BIF	Cauê	0.05	0.01	52.68	<0.01	0.02	0.01	<0.01	0.12	44.89	<0.01	2.20
	A015	Quartz-BIF	Cauê	0.21	<0.01	53.43	<0.01	0.07	0.06	<0.01	0.13	45.43	0.02	2.60
	A016	Quartz-BIF	Cauê	0.18	<0.01	53.75	<0.01	<0.1	0.12	<0.01	0.04	46.40	0.01	0.01
	A017_BV	Dol-Quartz-BIF	Cauê	6.52	1.79	37.46	0.31	6.01	0.03	0.01	0.24	41.67	0.94	4.80
	A017B	Quartz-BIF	Cauê	0.46	0.27	50.96	0.05	0.25	0.02	<0.01	0.13	45.06	0.03	-0.39
	A018	Impure Dolostone	Batatal	13.61	2.47	16.74	1.76	6.80	0.09	4.84	0.43	36.42	2.48	16.05
	A020A	Dol-Quartz-BIF	Batatal	6.81	3.55	23.96	1.21	4.00	0.10	1.56	0.16	47.88	0.48	11.93
	A021	Impure Dolostone	Batatal	1.37	17.29	16.51	0.36	9.90	0.56	0.07	0.07	25.18	0.07	30.96
	A022	Dol-Quartz-BIF	Batatal	0.49	3.14	48.83	0.06	3.41	0.10	0.02	0.09	41.00	0.03	3.56
	A023	Dol-Quartz-BIF	Batatal	0.36	5.37	46.29	0.06	3.09	0.08	<0.01	0.07	37.56	0.01	6.76
	A023_BV	Dol-Quartz-BIF	Batatal	0.14	6.48	44.62	<0.01	2.46	0.07	<0.01	0.32	38.25	<0.01	7.60
	A027B	Impure Dolostone	Batatal	10.31	5.72	10.07	2.66	9.82	0.19	0.22	0.10	43.75	0.75	18.32
Drill core STM-FD00205	A001	Dol-Quartz-BIF	Cauê	0.50	1.47	46.44	0.06	3.03	0.09	<0.01	0.16	40.60	0.05	3.56
	A002	Dol-Quartz-BIF	Cauê	0.43	6.90	39.86	0.06	4.67	0.13	0.07	0.12	40.25	0.06	9.18
	A002A_BV	Dol-Quartz-BIF	Cauê	0.04	8.62	31.46	<0.01	5.10	0.14	<0.01	0.13	42.11	<0.01	12.20
	A002B_BV	Dol-Quartz-BIF	Cauê	0.02	4.76	39.31	<0.01	3.50	0.08	<0.01	0.10	45.91	<0.01	6.00
	A004	Dol-Quartz-BIF	Cauê	0.40	8.29	36.82	0.06	5.13	0.15	<0.01	0.13	39.62	0.05	11.20
	A004A_BV	Dol-Quartz-BIF	Cauê	0.04	1.44	61.88	0.02	1.44	0.03	<0.01	0.13	34.64	<0.01	0.30
	A004B_BV	Dol-Quartz-BIF	Cauê	0.04	2.12	54.00	0.01	1.35	0.04	<0.01	0.09	40.92	<0.01	1.40
	A006	Dol-Quartz-BIF	Cauê	0.34	4.78	48.83	0.03	3.01	0.07	<0.01	0.18	32.57	0.03	6.46
	A007	Dol-Quartz-BIF	Cauê	0.21	6.21	48.56	<0.01	5.97	0.62	<0.01	0.12	33.54	0.02	8.49
	A007A_BV	Dol-BIF	Cauê	0.07	22.94	18.98	<0.01	11.43	2.05	<0.01	0.03	9.10	<0.01	35.20
	A007B_BV	Dol-Quartz-BIF	Cauê	0.21	2.20	41.53	<0.01	5.90	0.25	<0.01	0.17	46.26	<0.01	3.30
	A008A_BV	Dol-Quartz-BIF	Cauê	0.22	0.63	54.73	0.02	5.24	1.54	<0.01	0.07	25.12	0.03	12.30
	A008B_BV	Dol-Quartz-BIF	Cauê	0.44	0.25	22.19	0.02	6.94	1.17	<0.01	0.04	54.44	<0.01	14.40
	A009	Ferrug. dolostone	Cauê	0.47	23.22	11.82	<0.01	13.94	0.28	<0.01	0.03	8.58	0.03	45.04
	A010	Ferrug. dolostone	Cauê	0.53	25.88	12.74	<0.01	15.30	0.34	<0.01	0.02	2.12	0.04	41.86
	A011	Dol-BIF	Cauê	0.34	17.19	27.28	<0.01	9.87	0.30	<0.01	0.05	20.28	0.03	24.90
	A012	Dol-BIF	Cauê	0.41	17.76	28.79	0.01	9.96	0.26	<0.01	0.07	13.87	0.03	26.41
	A013	Dol-Quartz-BIF	Cauê	0.18	4.72	34.25	0.04	4.68	0.45	0.45	0.11	46.84	0.02	9.45
	A014	Dol-BIF	Cauê	0.45	16.15	30.43	<0.01	8.94	0.42	<0.01	0.04	14.72	0.03	25.33
	A015	Dol-Quartz-BIF	Cauê	0.82	15.84	22.33	0.12	8.82	0.31	<0.01	0.06	31.40	0.04	23.08
	A016	Dol-Quartz-BIF	Cauê	0.34	9.32	36.54	0.01	5.41	0.19	0.01	0.09	37.11	0.02	12.64
	A016_BV	Dol-Quartz-BIF	Cauê	0.15	5.31	32.56	<0.01	2.99	0.10	<0.01	0.08	51.39	<0.01	7.30
	A017	Dol-Quartz-BIF	Cauê	0.26	8.80	33.39	0.01	4.74	0.31	<0.01	0.08	38.46	0.02	12.71
	A017A_BV	Dol-BIF	Cauê	0.51	13.73	45.75	<0.01	7.60	0.50	<0.01	0.08	11.86	0.04	19.80
	A017B_BV	Dol-Quartz-BIF	Cauê	0.42	11.98	36.83	<0.01	6.49	0.43	<0.01	0.06	26.47	0.05	17.10
	A018	Ferrug. dolostone	Cauê	0.41	15.38	17.67	<0.01	9.07	0.20	<0.01	0.04	34.34	0.02	22.99
	A019	Ferrug. dolostone	Cauê	1.01	21.18	19.52	<0.01	13.15	0.28	<0.01	0.06	16.99	0.09	30.63
	A020	Ferrug. dolostone	Cauê	0.71	17.81	18.79	<0.01	11.03	0.23	<0.01	0.03	25.93	0.04	26.76
	A021	Ferrug. dolostone	Cauê	0.51	20.31	22.13	<0.01	12.06	0.23	<0.01	0.05	14.12	0.03	31.13
	A022	Ferrug. dolostone	Cauê	0.59	21.63	16.77	<0.01	12.22	0.33	<0.01	0.03	17.72	0.05	31.82
	A023	Ferrug. dolostone	Cauê	0.36	14.84	23.62	<0.01	9.03	0.61	<0.01	0.08	30.41	0.02	22.04
Drill core STM-FD00233	A001	Quartz-BIF	Cauê	0.25	0.46	51.63	0.04	0.32	0.03	0.02	0.12	44.59	0.01	0.73
	A001A_BV	Quartz-BIF	Cauê	0.17	<0.01	63.73	<0.01	0.02	0.01	<0.01	0.05	35.72	<0.01	0.20
	A001B_BV	Quartz-BIF	Cauê	0.19	<0.01	61.80	<0.01	0.02	0.01	<0.01	0.06	37.43	<0.01	0.40
	A002	Quartz-BIF	Cauê	0.21	0.28	44.75	0.03	0.21	0.03	0.02	0.15	51.90	0.01	1.11
	A003	Quartz-BIF	Cauê	0.49	0.05	53.12	0.05	0.14	0.07	0.26	0.15	45.15	0.02	1.67
	A003_BV	Quartz-BIF	Cauê	0.09	0.01	60.93	<0.01	0.10	0.07	<0.01	0.16	36.40	<0.01	2.20
	A004	altered Quartz-BIF	Cauê	0.09	0.17	55.04	0.02	0.56	0.03	0.01	0.05	43.35	-	-0.05
	A005	altered Quartz-BIF	Cauê	0.10	0.08	54.79	0.01	3.47	0.08	0.03	0.03	42.45	-	-0.96
	A005_BV	Quartz-BIF	Cauê	0.08	<0.01	55.12	<0.01	3.58	0.08	<0.01	0.03	41.60	<0.01	-0.60

Source: Elaborated by the author

Table 6.2 — Abundance of trace elements and REEY of the studied samples from the Gandarela Syncline. *Normalized to PAAS

					Trace elements (ppm)													REE (ppm)														Relevant ratios			
Type	Sample ID	Lithology	Lithostrati-graphy	Ba	Cr	Co	Cu	Mo	Ni	Sr	Ti	Th	Zn	Zr	V	U	W	La	Ce	Pr	Nd	Sm	Eu	Gd	Tb	Dy	Y	Ho	Er	Tm	Yb	Lu	ΣREEY	Y/Ho	U/Th	Eu/ Eu*	Ce/ Ce*
Outcrop samples	AC05-00	Dolostone	Gandarela	20	5.0	1.3	8.7	0.1	12.0	21.6	0.0	2.2	9.0	-	90	0.4	<0.1	6.3	8.3	0.9	3.9	0.3	<0.05	<0.05	0.1	0.7	6.0	0.1	0.1	<0.05	0.3	0.1	27.09	100	-	-	1.2
	AC05-01	Dolostone	Gandarela	25	2.0	0.8	6.1	<0.05	10.0	21.3	-	0.9	7.0	-	143	0.3	0.8	6.9	6.1	0.6	2.7	<0.1	<0.05	<0.05	0.1	0.5	5.3	0.1	0.1	0.1	0.2	0.1	22.64	89	-	-	1.4
	AC05-02	Dolostone	Gandarela	14	<1	2.8	6.4	<0.05	5.0	21.6	-	0.3	8.0	-	<5	0.2	<0.1	0.9	1.2	0.3	0.8	<0.1	<0.05	<0.05	<0.05	0.2	3.4	<0.05	<0.05	<0.05	0.2	0.1	7.04	-	0.3	-	0.3
	AC05-03	Dolostone	Gandarela	14	2.0	1.0	6.6	<0.05	<5	24.9	-	0.1	18.0	-	<5	0.2	<0.1	0.4	1.2	0.3	1.1	<0.1	<0.05	<0.05	0.1	0.2	3.2	<0.05	<0.05	<0.05	<0.1	0.1	6.54	-	-	-	0.6
	AC05-04	Dolostone	Gandarela	<10	2.0	1.1	5.4	<0.05	5.0	24.3	-	<0.1	13.0	-	<5	0.2	<0.1	0.9	1.1	0.3	1.4	<0.1	<0.05	<0.05	<0.05	0.2	3.5	0.1	<0.05	<0.05	0.2	0.1	7.69	69	-	-	0.6
	AC05-05	Dolostone	Gandarela	16	3.0	1.3	6.1	0.1	8.0	23.4	-	0.2	13.0	-	<5	0.2	0.2	1.4	2.3	0.4	1.5	<0.1	<0.05	<0.05	<0.05	0.3	4.0	<0.05	<0.05	<0.05	0.2	<0.05	10.06	-	-	-	0.7
	AC05-06	Ferrug. dolostone	Gandarela	31	2.0	0.8	11.6	0.1	8.0	16.4	-	0.4	8.0	-	72	0.2	3.1	4.5	5.6	0.6	3.4	<0.1	<0.05	0.2	0.1	0.6	8.5	0.2	0.3	0.1	0.6	0.2	24.82	42	-	-	1.5
	AC05-07	Ferrug. dolostone	Gandarela	15	3.0	0.8	6.8	0.1	<5	22.2	-	<0.1	11.0	-	<5	0.1	<0.1	3.5	5.0	0.6	2.6	<0.1	<0.05	<0.05	0.1	0.8	8.4	0.2	0.2	0.1	0.6	0.1	22.09	42	-	-	1.2
	AC05-09	Dolostone	Gandarela	<10	2.0	0.4	14.9	0.1	<5	19.8	-	<0.1	9.0	-	110	0.2	0.4	5.0	4.7	0.5	2.4	<0.1	<0.05	<0.05	0.1	0.6	7.1	0.1	0.1	<0.05	0.2	0.1	20.86	88	-	-	1.5
	AC05-10	Dolostone	Gandarela	<10	2.0	0.8	7.3	0.1	5.0	57.9	-	<0.1	8.0	-	9	0.1	<0.1	1.1	1.6	0.2	1.2	<0.1	<0.05	<0.05	<0.05	0.1	0.3	3.2	<0.05	<0.05	<0.05	0.2	0.1	7.93	-	-	-	2.1
	AC05-11	Dolostone	Gandarela	<10	3.0	0.3	5.0	<0.05	<5	17.8	-	<0.1	9.0	-	30	0.2	<0.1	1.9	2.2	0.3	1.7	<0.1	<0.05	<0.05	<0.05	0.4	3.4	<0.05	<0.05	<0.05	0.2	0.1	10.16	-	-	-	1.1
	AC05-12	Dolostone	Gandarela	<10	3.0	1.2	6.5	<0.05	6.0	19.6	-	<0.1	7.0	-	36	0.1	<0.1	1.7	1.8	0.3	1.5	<0.1	<0.05	<0.05	0.1	0.2	3.0	0.1	<0.05	<0.05	0.1	0.3	8.92	43	-	-	1.2
	AC05-13	Dolostone	Gandarela	<10	2.0	3.1	6.2	0.1	9.0	17.4	-	<0.1	10.0	-	66	0.3	<0.1	3.3	3.4	0.4	2.2	<0.1	<0.05	<0.05	0.1	0.5	4.7	0.1	<0.05	<0.05	0.2	0.1	15.03	79	-	-	1.5
	AC05-14	Ferrug. dolostone	Gandarela	<10	3.0	1.9	8.0	<0.05	9.0	17.9	-	1.3	10.0	-	168	0.3	<0.1	6.4	24.5	8.0	27.9	<0.1	<0.05	0.7	0.2	0.8	6.7	0.3	0.1	0.1	0.3	0.1	76.13	20	-	-	0.3
	AC05-15	Ferrug. dolostone	Gandarela	<10	1.0	1.1	10.1	0.1	13.0	39.1	-	0.7	15.0	-	160	0.2	<0.1	4.6	4.6	0.4	2.2	<0.1	<0.05	<0.05	0.1	0.3	4.5	0.1	<0.05	<0.05	0.2	<0.05	17.06	34	0.8	-	1.7
	AC-17-01A	Dolomitic BIF	Cauê	16	-	12.1	1.1	0.4	4.6	29	-	0.2	10	3.8	56	3.3	98.6	1.4	1.9	0.3	1.3	0.28	0.12	0.4	0.08	0.52	4.7	0.12	0.42	0.06	0.45	0.07	12.12	39	-	1.8	0.9
	AC-17-01B	Dolomitic BIF	Cauê	5	-	10	0.9	0.4	4.3	24.7	-	<0.2	8	3.9	46	3.2	69.6	1.5	2	0.3	1.3	0.3	0.1	0.46	0.07	0.49	4.4	0.12	0.42	0.06	0.41	0.06	11.99	37	-	1.5	0.9
Drill core STM-FD00155	A011	Quartz-BIF	Cauê	33	3.0	3.2	16.3	0.3	39.0	17.3	0.1	0.4	27.0	19	34	0.4	2.4	3.2	4.3	0.7	3.3	0.6	0.3	0.8	0.1	0.7	8.1	0.2	0.5	0.1	0.4	0.3	23.45	48	-	1.9	1.0
	A011_BV	Quartz-BIF	Cauê	25	-	46.2	4.9	0.1	57.3	<0.5	-	0.3	9	4	22	0.6	653.9	3.6	1.9	0.67	2.6	0.45	0.13	0.57	0.07	0.46	4	0.11	0.34	0.04	0.28	0.05	15.27	36	-	1.5	0.3
	A012	Quartz-BIF	Cauê	10	<1	0.7	2.0	0.3	6.0	17.0	-	0.2	6.0	19	19	0.1	1.8	1.3	1.8	0.2	1.2	0.2	0.1	0.3	0.1	0.3	4.7	0.1	0.3	<0.05	0.4	<0.05	10.94	59	-	1.7	1.7
	A013	Quartz-BIF	Cauê	<10	<1	0.6	3.2	0.3	7.0	14.6	-	<0.1	11.0	20	13	<0.05	0.6	1.7	2.1	0.2	1.3	0.2	0.1	0.4	0.1	0.3	7.0	0.1	0.5	0.1	0.6	0.3	14.98	54	-	2.5	1.8
	A013_BV	Quartz-BIF	Cauê	2	-	47.5	5.8	<0.1	2.8	<0.5	-	<0.2	3	2.2	20	<0.1	411	1	1.5	0.21	0.8	0.2	0.11	0.39	0.06	0.44	5.7	0.13	0.49	0.07	0.53	0.09	11.72	44	-	2.3	0.9
	A015	Quartz-BIF	Cauê	<10	<1	1.1	<0.5	0.3	7.0	8.5	-	<0.1	9.0	19	8	0.1	0.2	1.8	2.5	0.3	1.4	0.4	0.1	0.5	0.1	0.4	7.5	0.1	0.5	0.1	0.5	0.2	16.48	58	0.2	1.6	1.1
	A016	Quartz-BIF	Cauê	14	<1	1.8	3.2	0.8	8.0	7.8	-	<0.1	7.0	-	68	3.1	5.4	1.7	3.0	0.3	1.5	0.4	0.2	0.5	0.1	0.6	7.8	0.2	0.5	0.1	0.6	0.1	17.35	49	10.4	1.9	1.4
	A017_BV	Dol-Quartz-BIF	Cauê	102	-	41.5	6.3	<0.1	30.1	5	-	1.7	43	76.8	175	2.9	301.2	11.9	23.1	2.89	11.3	2.55	0.8	2.9	0.46	2.89	17.3	0.63	1.81	0.25	1.64	0.24	80.66	27	-	1.6	1.0
	A017B	Quartz-BIF	Cauê	<10	<1	4.5	<0.5	0.2	9.0	7.0	0.0	<0.1	35.0	20	70	1.3	2.0	3.3	23.7	8.5	27.4	0.4	0.2	1.9	0.2	1.0	7.8	0.4	0.6	0.1	0.5	<0.05	75.85	22	-	1.5	0.3
	A018	Impure Dolostone	Batatal	282	14.0	28.1	2.5	0.3	38.0	76.2	0.3	3.7	89.0	181	209	1.3	1.8	19.8	43.9	5.9	25.6	6.1	1.9	7.0	1.1	6.7	38.3	1.4	3.9	0.6	3.4	1.0	166.35	28	3.2	1.6	1.0
	A020A	Dol-Quartz-BIF	Batatal	360	8.0	9.3	67.3	4.5	15.0	53.8	0.2	2.5	38.0	68	63	0.9	0.5	9.8	18.7	2.3	9.3	2.1	0.6	2.2	0.3	1.9	13.4	0.4	1.4	0.2	1.3	0.3	64.08	30	3.1	1.5	1.0
	A021	Impure Dolostone	Batatal	43	4.0	2.3	10.1	0.1	12.0	124.7	0.0	0.9	13.0	19	18	0.4	1.5	4.8	9.0	1.1	4.6	1.1	0.4	1.4	0.2	1.4	14.2	0.4	1.1	0.2	1.0	0.3	41.06	41	-	1.6	1.2
	A022	Dol-Quartz-BIF	Batatal	16	<1	0.7	5.1	0.1	5.0	51.6	-	0.3	8.0	20	44	0.1	0.6	2.7	3.2	0.3	1.5	0.5	0.1	0.5	0.1	0.4	6.1	0.2	0.5	0.1	0.5	0.5	17.23	34	0.3	1.3	1.5
	A023	Dol-Quartz-BIF	Batatal	<10	<1	0.4	<0.5	0.2	5.0	66.1	-	<0.1	1.0	-	7	0.1	1.2	1.7	2.5	0.3	1.3	0.4	0.1	0.3	0.1	0.4	5.4	0.1	0.4	0.1	0.6	0.2	13.91	45	0.4	1.4	1.3
	A023_BV	Dol-Quartz-BIF	Batatal	3	-	10.9	0.7	<0.1	2.5	69	-	<0.2	3	4.7	20	<0.1	147.5	1.5	2.5	0.34	1.3	0.35	0.12	0.55	0.09	0.64	6.8	0.16	0.53	0.08	0.57	0.1	15.63	43	-	1.5	0.9
	A027B	Impure Dolostone	Batatal	204	219.0	40.9	113.4	0.4	128.0	131.3	0.2	0.6	51.0	56	183	0.3	5.2	4.6	10.2	1.3	6.2	1.7	0.7	2.1	0.4	2.3	15.6	0.5	1.6	0.3	1.7	<0.05	49.16	29	-	1.8	1.1
Drill core STM-FD00205	A001	Dol-Quartz-BIF	Cauê	15	<1	1.2	4.1	0.1	17.0	17.8	-	<0.1	2.0	-	11	<0.05	2.8	1.2	1.7	0.2	1.2	0.3	0.1	0.3	0.1	0.4	4.9	0.1	0.5	0.1	0.5	0.4	11.90	41	-	1.7	1.3
	A002	Dol-Quartz-BIF	Cauê	23	1.0	0.4	<0.5	0.1	9.0	77.3	-	<0.1	3.0	-	44	0.1	1.8	1.9	2.3	0.3	1.4	0.3	0.1	0.4	0.1	0.4	5.1	0.1	0.4	0.1	0.5	0.5	13.81	39	0.1	2.0	1.5
	A002A_BV	Dol-Quartz-BIF	Cauê	293	-	24.4	1.2	<0.1	1.4	103.4	-	<0.2	4	1.5	13	<0.1	318	1.2	1.5	0.2	0.8	0.21	0.13	0.35	0.06	0.44	5	0.11	0.4	0.05	0.41	0.07	10.93	45	-	2.6	0.9
	A002B_BV	Dol-Quartz-BIF	Cauê	1499	-	19.9	1.1	<0.1	1.6	105.5	-	<0.2	5	1.3	14	<0.1	285.2	0.9	1.1	0.16	0.6	0.18	0.11	0.27	0.04	0.35	4.2	0.09	0.36	0.05	0.43	0.07	8.91	47	-	2.8	0.8
	A004	Dol-Quartz-BIF	Cauê	16	2.0	0.6	1.0	0.1	9.0	79.3	0.0	<0.1	13.0	-	24	0.1	0.6	2.3	2.7	0.4	1.8	0.4	0.1	0.4	0.1	0.4	5.9	0.1	0.5	0.1	0.5	0.3	16.06	42	0.2	1.7	1.1
	A004A_BV	Dol-Quartz-BIF	Cauê	<1	-	21.2	1.2	<0.1	1.6	10.9	-	<0.2	7	2.3	21	<0.1	281.8	1	1.3	0.16	0.8	0.17	0.05	0.25	0.05	0.35	3.9	0.1	0.33	0.05	0.35	0.06	8.92	39	-	1.2	1.3
	A004B_BV	Dol-Quartz-BIF	Cauê	<1	-	17.4	0.9	<0.1	1.2	17.6	-	<0.2	6	1.1	24	<0.1	205	0.6	0.7	0.11	0.4	0.11	0.05	0.2	0.03	0.26	2.7	0.07	0.24	0.03	0.22	0.04	5.76	39	-	1.9	0.7
	A006	Dol-Quartz-BIF	Cauê	13	<1	0.5	3.0	0.1	7.0	28.3	0.0	<0.1	3.0	-	30	0.1	2.9	2.4	3.0	0.4	1.8	0.4	0.2	0.4	0.1	0.4	6.5	0.2	0.5	0.1	0.5	0.2	16.86	40	0.7	1.7	1.2
	A007	Dol-Quartz-BIF	Cauê	<10	<1	0.4	<0.5	0.2	6.0	16.5	-	<0.1	6.0	-	13	0.1	1.3	1.4	1.7	0.2	1.1	0.3	0.1	0.3	0.1	0.2	3.1	0.1	0.3	<0.05	0.3	0.1	9.37	31	0.8	1.1	1.1
	A007A_BV	Dol-BIF	Cauê	18	-	7.1	1.9	<0.1	0.5	35.5	-	<0.2	4	1.6	18	<0.1	125.1	0.9	1.2	0.15	0.5	0.12	0.06	0.21	0.03	0.22	2.7	0.06	0.2	0.03	0.19	0.03	6.60	45	-	2.2	0.8
	A007B_BV	Dol-Quartz-BIF	Cauê	5	-	15.3	1.2	<0.1	1.5	5.7	-	<0.2	7	2.3	19	<0.1	212.4	1.2	1.6	0.24	0.8	0.21	0.05	0.34	0.06	0.38	3.7	0.1	0.31	0.05	0.35	0.05	9.44	37	-	1.0	0.7
	A008A_BV	Dol-Quartz-BIF	Cauê	15	-	12.2	0.7	<0.1	3.3	1	-	0.3	7	7.9	37	0.1	151.3	3.1	4.7	0.52	2	0.28	0.05	0.35	0.06	0.45	5	0.12	0.4	0.06	0.53	0.08	17.70	42	-	0.8	1.1
	A008B_BV	Dol-Quartz-BIF	Cauê	<1	-	20.9	24.6	<0.1	2.9	<0.5	-	<0.2	7	1.6	16	<0.1	276	1.2	1.9	0.23	0.8	0.12	0.03	0.16	0.03	0.24	3.4	0.07	0.31	0.05	0.41	0.07	9.02	49	-	1.1	0.9
	A009	Ferrug. dolostone	Cauê	<10	5.0	0.7	1.2	0.1	7.0	32.9	0.0	<0.1	5.0	-	<5	0.2	0.3	1.8	3.1	0.3	1.3	0.3	0.1	0.3	0.1	0.2	1.6	0.1	0.2	<0.05	0.2	0.6	10.14	23	-	1.1	1.4
	A010	Ferrug. dolostone	Cauê	<10	2.0	1.2	8.9	0.1	10.0	34.6	0.0	<0.1	10.0	-	11	0.2	1.1	2.5	3.6	0.4	1.8	0.4	0.1	0.3	<0.05	0.2	1.9	0.1	0.3	<0.05	0.2	0.7	12.49	28	-	-	1.7
	A011	Dol-BIF	Cauê	<10	4.0	0.7	1.9	0.1	7.0	22.6	-	<0.1	9.0	-	11	0.1	0.9	2.0	2.7	0.3	1.2	0.3	0.1	0.3	0.1	0.2	2.1	0.1	0.3	<0.05	0.2	0.7	10.36	26	-	1.0	1.1
	A012	Dol-BIF	Cauê	28	3.0	0.9	2.6	0.1	7.0	28.1	0.0	<0.1	10.0	-	7	0.3	0.4	2.1	2.8	0.3	1.3	0.2	0.1	0.3	0.1	0.3	2.6	0.1	0.3	<0.05	0.3	0.1	10.91	29	-	1.6	1.0
	A013	Dol-Quartz-BIF	Cauê	51	<1	0.6	<0.5	0.1	6.0	10.4	-	0.5	21.0	-	24	0.2	3.0	2.0	2.4	0.3	1.2	0.3	0.1	0.4	0.1	0.2	3.1	0.1	0.3	0.1	0.4	<0.05	10.97	28	-	1.3	0.8
	A014	Dol-BIF	Cauê	<10	<1	1.0	0.8	0.1	5.0	55.7	-	0.5	10.0	-	10	0.2	5.6	2.9	4.2	0.5	2.0	0.5	0.1	0.5	0.1	0.4	3.5	0.1	0.4	0.1	0.3	0.1	15.49	35	-	1.3	1.1
	A015	Dol-Quartz-BIF	Cauê	65	4.0	1.0	6.2	0.1	8.0	32.6	0.0	0.7	10.0	-	13	0.2	<0.1	2.5	3.9	0.4	2.0	0.5	0.2	0.4	0.1	0.2	3.2	0.1	0.3	<0.05	0.3	0.2	14.27	29	-	1.7	1.3
	A016	Dol-Quartz-BIF	Cauê	13	<1	0.6	<0.5	0.1	8.0	43.5	0.0	0.3	12.0	-	14	0.1	2.7	1.9	2.7	0.3	1.7	0.3	0.1	0.3	0.1	0.2	3.2	0.1	0.3	0.1	0.3	0.1	11.59	36	-	0.9	2.1
	A016_BV	Dol-Quartz-BIF	Cauê	9	-	22.5	0.8	0.3	2.1	11.7	-	<0.2	8	2.4	18	<0.1	410.4	1	1.6	0.2	0.8	0.17	0.05	0.22	0.04	0.29	2.6	0.07	0.24	0.03	0.25	0.07	7.63	37	-	1.3	1.0
	A017	Dol-Quartz-BIF	Cauê	<10	<1	1.0	17.1	0.1	11.0	15.3	-	<0.1	12.0	-	32	0.2	4.6	2.3	2.6	0.4	1.3	0.2	0.1	0.3	0.1	0.3	4.2	0.1	0.4	0.1	0.4	<0.05	12.77	42	-	2.0	0.7
	A017A_BV	Dol-BIF	Cauê	<1	-	8.9	3.7	0.2	2.9	19.9	-	0.4	14	7.6	28	0.2	100.4	2.7	3.8	0.52	1.7	0.38	0.13	1.08	0.09	0.69	7.1	0.18	0.58	0.09	0.58	0.1	19.72	39	-	1.5	0.7
	A017B_BV	Dol-Quartz-BIF	Cauê	<1	-	9.8	19.1	0.1	2	17.1	-	0.3	11	7.5	29	0.2	109.3	2.1	3.1	0.37	1.3	0.31	0.11	0.48	0.07	0.52	5.9	0.14	0.49	0.07	0.46	0.08	15.50	42	-	1.6	0.9
	A018	Ferrug. dolostone	Cauê	<10	4.0	0.6	0.9	0.3	6.0	28.3	0.0	<0.1	18.0	-	<5	0.1	5.2	1.4	2.1	0.3	1.3	0.3	0.1	0.2	<0.05	0.1	1.3	0.1	0.2	<0.05	0.2	<0.05	7.54	22	-	-	1.3
	A019	Ferrug. dolostone	Cauê	<10	5.0	1.7	<0.5	0.1	11.0	53.0	0.1	0.4	36.0	20	26	0.3	<0.1	3.0	5.7	0.7	2.9	0.8	0.1	0.7	0.1	0.7	5.2	0.2	0.5	0.1	0.6	0.2	21.41	30	-	0.9	1.2
	A020	Ferrug. dolostone	Cauê	<10	5.0	0.8	1.6	0.1	8.0	21.9	0.0	0.2	26.0	-	<5	0.2	3.9	2.9	4.8	0.6	2.3	0.4	0.1	0.3	0.1	0.3	2.8	0.1	0.4	0.1	0.3	0.6	15.98	25	-	1.4	0.9
	A021	Ferrug. dolostone	Cauê	<10	6.0	1.0	20.2	0.1	11.0	59.2	0.0	0.2	26.0	-	27	0.2	1.4	3.0	4.3	0.5	2.0	0.4	0.1	0.4	0.1	0.3	2.5	0.1	0.3	<0.05	0.2	0.6	14.73	36	-	1.3	1.1
	A022	Ferrug. dolostone	Cauê	<10	2.0	1.7	1.2	0.1	8.0	54.5	0.0	<0.1	13.0	-	6	0.2	1.4	2.4	3.7	0.5	2.1	0.5	0.2	0.5	0.1	0.5	3.9	0.1	0.4	0.1	0.4	0.7	16.14	30	-	1.5	1.1
	A023	Ferrug. dolostone	Cauê	<10	<1	0.6	<0.5	0.2	7.0	25.0	0.0	<0.1	6.0	-	24	0.3	0.6	3.4	3.6	0.4	2.0	0.4	0.1	0.5	0.1	0.3	3.6	0.1	0.4	<0.05	0.3	0.8	15.96	40	-	1.6	1.3
Drill core STM-FD00233	A001	Quartz-BIF	Cauê	13	6.0	1.0	1.9	0.2	9.0	10.8	-	0.5	11.0	-	16	0.1	<0.1	2.0	3.9	0.4	1.7	<0.1	<0.05	<0.05	<0.05	0.5	6.2	0.1	0.2	0.1	0.5	0.1	15.71	69	-	-	1.5
	A001A_BV	Quartz-BIF	Cauê	<1	-	33.3	3.1	<0.1	1.6	0.5	-	<0.2	6	2.8	22	<0.1	489.4	1.5	2.3	0.25	1	0.19	0.07	0.28	0.05	0.44	5.3	0.11	0.41	0.06	0.49	0.08	12.53	48	-	1.6	1.2
	A001B_BV	Quartz-BIF	Cauê	2	-	45	3	<0.1	2.6	0.6	-	<0.2	6	2.8	24	<0.1	658.6	1.6	2.5	0.27	0.9	0.21	0.08	0.32	0.05	0.45	5.5	0.12	0.45	0.07	0.54	0.09	13.15	46	-	1.7	1.0
	A002	Quartz-BIF	Cauê	10	5.0	0.9	2.3	0.2	9.0	14.3	-	0.3	2.0	-	39	0.4	<0.1	2.3	3.6	0.4	2.0	<0.1	0.1	<0.05	0.1	0.5	6.6	0.1	0.2	0.1	0.5	0.1	16.54	51	-	-	1.3
	A003	Quartz-BIF	Cauê	16	3.0	0.5	2.6	0.3	7.0	15.3	-	0.2	5.0	27	31	0.1	<0.1	1.2	2.4	0.3	0.7	<0.1	<0.05	<0.05	0.1	0.5	6.5	0.1	0.1	0.1	0.5	0.1	12.54	59	-	-	0.8
	A003_BV	Quartz-BIF	Cauê	<1	-	32.7	3.8	0.2	5.2	<0.5	-	<0.2	6	2.4	31	0.1	430.8	1.1	1.6	0.21	0.8	0.24	0.05	0.43	0.07	0.53	6.6	0.14	0.46	0.07	0.46	0.08	12.84	47	-	0.9	0.9
	A004	altered Quartz-BIF	Cauê	10	5.0	0.7	2.8	0.5	9.0	13.4	-	0.1	2.0	-	37	0.1	<0.1	1.3	2.4	0.3	1.5	<0.1	<0.05	<0.05	0.2	1.3	18.7	0.3	0.8	0.2	1.0	0.2	28.16	64	-	-	1.7
	A005	altered Quartz-BIF	Cauê	11	4.0	0.7	3.1	0.2	<5	15.1	-	0.1	14.0	-	28	0.1	<0.1	5.8	2.1	0.9	4.1	<0.1	0.2	0.4	0.2	1.5	24.3	0.3	1.2	0.2	1.1	0.2	42.55	74	-	-	0.3
	A005_BV	Quartz-BIF	Cauê	8	-	20.6	4.1	<0.1	2.3	1.4	-	<0.2	9	2.6	19	<0.1	266.2	4.5	1.1	0.6	2.6	0.54	0.18	1.08	0.16	1.13	16.7	0.3	1.03	0.14	0.85	0.14	31.05	56	-	1.4	0.2

Source: Elaborated by the author

6.5.4 Stable Isotope Composition (C-N-O)

Table 6.3 presents the results of the C-N-O isotopic ratio for carbonate rocks and dolomite-rich BIF samples. The carbon and oxygen isotope compositions display a positive trend towards the younger rocks, particularly the dolostones of the Gandarela Formation. The results of the N-isotopic ratio represent partial data, as the quality control analyses, including duplicates and triplicates, are still pending.

Table 6.3 — Whole rock carbon, nitrogen and oxygen isotopic composition for studied samples. * Waiting for results

Type	Sample ID	X	Y	Z	Lab	C_{TOTAL} ppm	δC^{13}_{VPDB} ‰	δO^{18}_{VPDB} ‰	N ppm	δN^{15}_{VPDB} ‰	Lithology	Lithostratigraphy
Outcrop Sample	AC05-00	638949	7781499	1352	UFPE	-	0.54	-9.35	-	-	Dolostone	Gandarela
	AC05-01	638949	7781499	1352	UFPE	-	0.54	-8.65	-	-	Dolostone	Gandarela
	AC05-02	638949	7781499	1352	UFPE	-	0.57	-9.17	-	-	Dolostone	Gandarela
	AC05-03	638949	7781499	1352	UFPE	-	0.51	-8.94	-	-	Dolostone	Gandarela
	AC05-03A	638949	7781499	1353	UFPE	-	0.62	-9.04	-	-	Dolostone	Gandarela
	AC05-04	638949	7781499	1352	UFPE	-	0.50	-9.31	-	-	Dolostone	Gandarela
	AC05-05	638949	7781499	1352	UFPE	-	0.41	-8.86	-	-	Ferruginous dolostone	Gandarela
	AC05-06	638949	7781499	1352	UFPE	-	-2.30	-11.37	-	-	Ferruginous dolostone	Gandarela
	AC05-07	638949	7781499	1352	UFPE	-	-2.44	-10.49	-	-	Ferruginous dolostone	Gandarela
	AC05-08	638949	7781499	1352	UFPE	-	-1.74	-11.30	-	-	Ferruginous dolostone	Gandarela
	AC05-09	638949	7781499	1352	UFPE	-	-0.09	-10.04	-	-	Dolostone	Gandarela
	AC05-10	638949	7781499	1352	UFPE	-	0.52	-8.76	-	-	Dolostone	Gandarela
	AC05-11	638949	7781499	1352	UFPE	-	0.60	-9.70	-	-	Dolostone	Gandarela
	AC05-12	638949	7781499	1352	UFPE	-	0.65	-9.47	-	-	Dolostone	Gandarela
	AC05-13	638949	7781499	1352	UFPE	-	0.43	-8.24	-	-	Dolostone	Gandarela
	AC05-14	638949	7781499	1352	UFPE	-	-0.74	-8.37	-	-	Ferruginous dolostone	Gandarela
	AC05-15	638949	7781499	1352	UFPE	-	-0.55	-11.10	-	-	Ferruginous dolostone	Gandarela
	AC-16-01A	638924	7781033	1264	UofA	-	-1.15	-11.32	-	-	Dolostone	Gandarela
	AC-16-01B	638924	7781033	1264	UofA	-	-1.19	-11.48	-	-	Dolostone	Gandarela
Drill core STM-FD00155	-A011	663073	7800177	454.1	UofA	0.03	-	-	3.48	2.64	Quartz-BIF	Cauê
	-A013	663059	7800190	376.7	UofA	<0.02	-	-	3.37	-4.01	Quartz-BIF	Cauê
	-A017	663051	7800196	336.3	UofA	0.32	-	-	6.24	-5.55	Dol-Quartz-BIF	Cauê
	-A018	663050	7800198	329	UFOP	-	-6.70	-18.11	-	-	Impure Dolonate	Batatal
	-A019	663049	7800198	327	UFOP	-	-2.66	-18.75	-	-	Dolomite-rich phyllite	Batatal
	-A020A	663048	7800199	319	UFOP	-	-5.52	-18.22	-	-	Dol-Quartz-BIF	Batatal
	-A020B	663048	7800199	319	UFOP	-	-6.18	-17.98	-	-	Dol-Quartz-BIF	Batatal
	-A021	663046	7800200	313	UFOP	-	-2.75	-18.73	-	-	Impure Dolostone	Batatal
	-A023	663044	7800202	302.5	UofA	2.57	-	-	1.80	4.04	Dol-Quartz-BIF	Batatal
	-A027A	663041	7800204	291	UFOP	-	-6.83	-18.40	-	-	Impure Dolostone	Batatal
	-A027B	663041	7800204	291	UFOP	-	-6.09	-18.12	-	-	Impure Dolostone	Batatal
	-A028A	663041	7800204	290	UFOP	-	-5.98	-19.90	-	-	Dolomite-rich phyllite	Batatal
	-A028B	663041	7800204	290	UFOP	-	-5.38	-18.95	-	-	Dolomite-rich phyllite	Batatal
	-A029A	663041	7800204	289	UFOP	-	-5.04	-20.04	-	-	Dolomite-rich phyllite	Batatal
	-A029B	663041	7800204	289	UFOP	-	-4.91	-20.09	-	-	Dolomite-rich phyllite	Batatal
	-A030	663041	7800204	282	UFOP	-	-2.87	-20.35	-	-	Impure Dolonate	Batatal
Drill core STM-FD00205	-A002	664029	7801009	773	UFOP	-	-6.59	-15.74	-	-	Dol-Quartz-BIF	Cauê
	-A002_A	664029	7801009	773	UofA	3.67	-6.64	-16.89	1.77	0.65	Dol-Quartz-BIF	Cauê
	-A002_B	664029	7801009	773	UofA	1.95	-6.68	-16.97	*	*	Dol-Quartz-BIF	Cauê
	-A004	664028	7801010	766	UFOP	-	-6.74	-16.28	-	-	Dol-Quartz-BIF	Cauê
	-A004_A	664028	7801010	766	UofA	0.54	-7.07	-17.42	*	*	Dol-Quartz-BIF	Cauê
	-A004_B	664028	7801010	766	UofA	0.81	-6.80	-17.14	*	*	Dol-Quartz-BIF	Cauê
	-A007_A	664028	7801010	761	UofA	10.14	-3.67	-13.95	2.08	-1.56	Dol-BIF	Cauê
	-A007_B	664028	7801010	761	UofA	0.95	-4.69	-14.69	*	*	Dol-Quartz-BIF	Cauê
	-A008	664026	7801012	746	UFOP	-	-5.70	-12.68	-	-	Dol-Quartz-BIF	Cauê
	-A008_A	664026	7801012	746	UofA	3.77	-6.64	-13.14	*	*	Dol-Quartz-BIF	Cauê
	-A008_B	664026	7801012	746	UofA	3.92	-5.78	-14.28	*	*	Dol-Quartz-BIF	Cauê
	-A009	664018	7801018	696	UFPE	-	-1.98	-9.45	-	-	Ferruginous dolostone	Cauê
	-A009	664018	7801018	696	UFOP	-	-1.88	-10.64	-	-	Ferruginous dolostone	Cauê
	-A010	664017	7801019	692	UFPE	-	-2.00	-9.81	-	-	Ferruginous dolostone	Cauê
	-A010	664017	7801019	692	UFOP	-	-1.45	-9.54	-	-	Ferruginous dolostone	Cauê
	-A010V	664017	7801019	692	UFPE	-	-2.06	-9.39	-	-	Vein	Cauê
	-A011	664016	7801019	688	UFPE	-	-1.78	-10.11	-	-	Dol-BIF	Cauê
	-A011	664016	7801019	688	UFOP	-	-1.57	-10.26	-	-	Dol-BIF	Cauê
	-A012	664015	7801020	683	UFPE	-	-1.33	-11.29	-	-	Dol-BIF	Cauê
	-A012	664015	7801020	683	UFOP	-	-1.20	-11.88	-	-	Dol-BIF	Cauê
	-A013	664014	7801021	674	UFPE	-	-2.67	-12.31	-	-	Dol-Quartz-BIF	Cauê
	-A013	664014	7801021	674	UFOP	-	-2.48	-12.11	-	-	Dol-Quartz-BIF	Cauê
	-A014	664013	7801022	669	UFPE	-	-3.36	-14.26	-	-	Dol-BIF	Cauê
	-A014	664013	7801022	669	UFOP	-	-2.43	-13.25	-	-	Dol-BIF	Cauê
	-A015	664012	7801023	666	UFOP	-	-1.69	-13.09	-	-	Dol-Quartz-BIF	Cauê
	-A015	664012	7801023	666	UFPE	-	-1.53	-12.31	-	-	Dol-Quartz-BIF	Cauê
	-A016	664012	7801023	661	UFOP	-	-1.94	-12.79	-	-	Dol-Quartz-BIF	Cauê
	-A016	664012	7801023	661	UFPE	-	-1.93	-11.92	-	-	Dol-Quartz-BIF	Cauê
	-A016	664012	7801023	661	UofA	2.26			*	*	Dol-Quartz-BIF	
	-A017	664011	7801024	656	UFOP	-	-2.28	-13.52	-	-	Dol-Quartz-BIF	Cauê
	-A017	664011	7801024	656	UFPE	-	-2.04	-12.59	-	-	Dol-Quartz-BIF	Cauê
	-A017A	664011	7801024	656	UofA	5.64	-	-	2.70	3.56	Dol-Quartz-BIF	Cauê
	-A017B	664011	7801024	656	UofA	4.93	-	-	*	*	Dol-Quartz-BIF	Cauê
	-A018	664010	7801025	651	UFPE	-	-0.98	-10.13	-	-	Ferruginous dolostone	Cauê
	-A018	664010	7801025	651	UFOP	-	-0.89	-9.98	-	-	Ferruginous dolostone	Cauê
	-A019	664009	7801025	647	UFPE	-	-1.14	-10.11	-	-	Ferruginous dolostone	Cauê
	-A019	664008	7801025	647	UFOP	-	-1.07	-10.43	-	-	Ferruginous dolostone	Cauê
	-A020	664009	7801025	647	UFOP	-	-1.66	-11.36	-	-	Ferruginous dolostone	Cauê
	-A020	664008	7801026	643	UFPE	-	-1.34	-9.97	-	-	Ferruginous dolostone	Cauê
	-A021	664007	7801027	639	UFPE	-	-1.12	-10.13	-	-	Ferruginous dolostone	Cauê
	-A021	664007	7801027	639	UFOP	-	-0.94	-10.58	-	-	Ferruginous dolostone	Cauê
	-A022	664007	7801027	634	UFOP	-	-0.95	-12.04	-	-	Ferruginous dolostone	Cauê
	-A023	664006	7801028	630	UFOP	-	-0.24	-13.19	-	-	Ferruginous dolostone	Cauê
	-A024	663996	7801036	581	UFPE	-	-0.43	-11.96	-	-	Carbonaceous phyllite	Batatal
	-A025	663995	7801037	576	UFPE	-	-1.12	-14.51	-	-	Carbonaceous phyllite	Batatal
Drill core STM-FD00233	-A001A	666718	7801769	801	UofA	<0.02	-	-	*	*	Quartz-BIF	Cauê
	-A001B	666718	7801769	801	UofA	0.03	-	-	1.22	1.31	Quartz-BIF	Cauê
	-A003	666712	7801780	754	UofA	0.02	-	-	2.77	-1.40	Quartz-BIF	Cauê
	-A005	666710	7801784	735	UofA	<0.02	-	-	3.10	0.25	Quartz-BIF	Cauê

Source: Elaborated by the author

6.6 Perspectives

The geochemical and isotopic data from the BIF and carbonate rocks provide insights into the dynamics of biogeochemical conditions in the Minas paleobasin. The transition from the clastic-dominated deposits of the Batatal Formation to the chemical rocks of the Cauê and Gandarela Formations reflects a progressive deepening of the paleobasin (Gonçalves and Uhlein, 2022), with significant paleogeographic evolution along with changes in water salinity and redox conditions in the Minas paleobasin (e.g., de Paula et al., 2023; 2025, under review at Chemical Geology Journal).

Some laboratory issues caused delays in obtaining the N isotope composition results, which affected the timeline for completing this paper. Therefore, the discussions outlined here will be fully developed once the remaining analyses are completed. The following topics will be included:

1) **Reconstruction of paleoredox conditions and the mechanisms of Fe-mineral deposition** in the QFe, precursors of the BIF, through REE signatures (Eu, La, and Ce anomalies) and the Y/Ho ratio. The REE concentrations show that most BIF samples exhibit positive Eu anomalies, a tracer of hydrothermal contribution (Bekker et al., 2010). The Ce anomaly, an indicator of redox conditions, varies between absent and weak, suggesting that there was not enough oxygen to oxidize dissolved Ce(III) to Ce(IV) (Lawrence et al., 2006), associated with a suboxic to anoxic water column. In contrast, the strong negative Ce anomaly (maximum 2.1) found in some BIF and carbonate rocks samples is considered evidence for a locally oxygenated Minas paleobasin.

Additionally, the unnormalized Y/Ho ratio distinguishes two BIF populations: one with lower values (22–29) and another with values above 30. The lower values are typically found near the basal contact or adjacent to dolomite layers interbedded the BIF, suggesting that these rocks may have been influenced by a mixture of waters with different Y/Ho ratios or by specific conditions that favored the preferential fractionation of HREE (e.g., Nozaki et al., 1997; Lawrence et al., 2006).

2) **The influence of biogenic pathways on Fe-mineral deposition and the evolution of redox conditions** in the Minas paleobasin, analyzed through isotopic

proxies (C-N-O). Additionally, this study will compare the redox conditions of the Minas Basin with those of other BIF-hosting regions (e.g., Hamersley Province). Carbon isotope data indicate negative fractionation for Fe-rich rocks, providing evidence of Fe reduction via microbial metabolism (DIR) (e.g., Konhauser et al., 2011). The nitrogen isotope ratios indicate a reducing basin, potentially with even more reducing conditions than those recorded in the Hamersley Basin (Liang, verbal communication). The completion of nitrogen analyses will allow for a more detailed interpretation of this proxy.

3) **Evaluate the contribution of oxidative weathering** during Fe-mineral deposition by analyzing the distribution of RSE such as Cr, Mo, V, and U in BIF from the QFe. The abundance of these elements can indicate the presence of atmospheric O_2, which plays a key role in the chemical weathering of continental landmasses, leading to the mobilization of RSE that are subsequently transported by river flux into to seawater (e.g., Teixeira et al., 2017). Additionally, Mo abundance is an essential element for biological activity and is therefore interpreted as evidence of primitive life (e.g., Konhauser et al., 2017).

7 GENERAL CONCLUSIONS AND PERSPECTIVES

This thesis brings new field, petrographic, geochemical, isotopic and geochronological data on rocks of the Minas Supergroup, Quadrilátero Ferrífero region of eastern Brazil, with special emphasis on the chemical precipitates (BIF and carbonate rocks) and fine-grained siliciclastic rocks and their geochemical signatures in order to reconstruct past redox, salinity, and overall paleoenvironmental conditions in the Minas Basin. Amongst the proxies used, trace element geochemistry, carbon and oxygen isotopes, and specially proxies never applied before in the Quadrilátero Ferrífero, such as Fe speciation and N isotopes, stand out for their novelty and wealth of data that can be used for reconstruction of the depositional conditions, specially during BIF deposition.

The results, based on new lithostratigraphic, petrographic, elemental geochemistry, and isotopic data of the Paleoproterozoic rocks from the Minas Supergroup, provide insights into the depositional and paleoenvironmental evolution of the Quadrilátero Ferrífero. The Cauê Formation BIF are characterized by a minimal detrital component and REEY signatures with local Ce and Eu anomalies indicating periodic oxygenation pulses and hydrothermal contributions. These geochemical signatures reinforce their importance as natural archives of seawater conditions during the formation of the large Lake Superior-type deposits during the Paleoproterozoic.

The carbon isotopic composition of the Itabira Group shows a gradual increase in $\delta^{13}C$ (-7.1 to 0.7‰) and $\delta^{18}O$ (-20.4 to -8.2‰) values from the Cauê to the Gandarela Formation, indicating isotopic fractionation likely driven by microbial processes (DIR) involved in the formation of Fe-mineral precursors of the BIF. Otherwise, the values are typical of Paleoproterozoic seawater and similar to other major Lake Superior-type BIF-hosted Fe system throughout the world.

Paleosalinity proxies such as B/Ga, Sr/Ba, and S/TOC ratios reveal dynamic changes in the watermass conditions in the Minas paleobasin. The Batatal Formation at the stratigraphic base shows a transition from freshwater to low-brackish facies, with a lacustrine depositional system suggested. The subsequent marine transgression led to saline conditions associated with the deposition of Cauê BIF, Gandarela carbonate rocks, and Cercadinho fine-grained siliciclastic rocks. These data and interpretations support the development of the Minas Supergroup in a basin that evolved from

continental to fully marine (passive margin) marking a typical rift to drift transition in a classic Wilson cycle scenario.

Paleoredox proxies, especially Fe speciation, indicate that the Batatal Formation phyllites were deposited under anoxic and ferruginous bottom water conditions, while the Cercadinho Formation phyllites show geochemical signs of post-depositional Fe re-partitioning, requiring further study to assess potential deep-water oxygenation. Overall, the paleoredox proxies indicate the formation of the BIF under a stratified water column, with a shallow oxic layer capping a predominantly anoxic, ferruginous, deeper ocean. Preliminary N isotope data support the interpretation of predominantly anoxic conditions.

Some remaining questions to be addressed include:

- Conducting high-resolution geochemical studies to evaluate geochemical and isotopic variations between well-preserved and weathered rocks.
- Expanding paleosalinity data and analysis in the Quadrilátero Ferrífero to refine the paleoenvironmental reconstruction of the Minas Basin.
- Applying Fe speciation techniques in a larger number of well-preserved rocks to demonstrate redox variations in the Minas Basin.
- Obtaining new geochronological data for the BIF of the Cauê Formation, as their age remains controversial.
- Conducting isotopic studies, such as Cr and Cd, in the carbonate rocks of the Gandarela Formation to investigate the evolution of bioproductivity and redox conditions in the Minas paleobasin.

REFERENCES

Agilent Technologies (2024). Available at: What is ICP-MS? Principles & Technique | Agilent. Accessed on: December 19, 2024

Agilent Technologies (2024). Available at: What Is ICP-OES? Principles & Technique | Agilent. Accessed on: December 19, 2024

Aguilar, C., Alkmim, F.F., Lana, C., & Farina, F. (2017). Palaeoproterozoic assembly of the São Francisco craton, SE Brazil: New insights from U–Pb titanite and monazite dating. *Precambrian Research*, **289**: 95-115. https://doi.org/10.1016/j.precamres.2016.12.001

Alcott, L.J., Krause, A.J., Hammarlund, E.U., Bjerrum, C.J., Scholz, F., Xiong, Y., ... & Poulton, S.W. (2020). Development of iron speciation reference materials for palaeoredox analysis. *Geostandards and Geoanalytical Research*, **44**(3): 581-591. https://doi.org/10.1111/ggr.12342

Algeo, T.J., & Ingall, E. (2007). Sedimentary Corg: P ratios, paleocean ventilation, and Phanerozoic atmospheric pO_2. *Palaeogeography, Palaeoclimatology, Palaeoecology*, **256**(3-4): 130-155. https://doi.org/10.1016/j.palaeo.2007.02.029

Algeo, T.J., & Maynard, J.B. (2008). Trace-metal covariation as a guide to water-mass conditions in ancient anoxic marine environments. *Geosphere*, **4**(5): 872-887. https://doi.org/10.1130/GES00174.1

Algeo, T.J., & Tribovillard, N. (2009). Environmental analysis of paleoceanographic systems based on molybdenum–uranium covariation. *Chemical Geology*, **268**(3-4): 211-225. https://doi.org/10.1016/j.chemgeo.2009.09.001

Alkmim, A.R. (2014). Investigação geoquímica e estratigráfica da Formação Ferrífera Cauê na porção centro–oriental do Quadrilátero Ferrífero, MG. *Dissertation on Graduate Departament in Geology,* Escola de Minas, Universidade de Ouro Preto, Ouro Preto. 178p.

Alkmim, F.F., & Marshak, S. (1998). Transamazonian orogeny in the Southern Sao Francisco craton region, Minas Gerais, Brazil: evidence for Paleoproterozoic collision and collapse in the Quadrilátero Ferrífero. *Precambrian Research*, **90**(1): 29-58. https://doi.org/10.1016/S0301-9268(98)00032-1

Alkmim, F.F., & Martins-Neto, M. A. (2012). Proterozoic first-order sedimentary sequences of the São Francisco craton, eastern Brazil. *Marine and Petroleum Geology*, ***33***(1), 127-139. https://doi.org/10.1016/j.marpetgeo.2011.08.011

Almeida, A.S.F. and Sousa Jorge, L. M. (2022). Investigação petrográfica de carbonatos possivelmente microbiais da Formação Gandarela, Paleoproterozoico do Quadrilátero Ferrífero, MG. *Trabalho geológico de Graduação, Instituto de Geociências*, Universidade de Minas Gerais, Belo Horizonte, 84 p.

Almeida, F.F.M. (1977). O cráton do São Francisco. *Revista Brasileira de Geociências*, **7**(4): 349-364.

Almeida, L.G., Castro, P.D., Endo, I., Fonseca, M.A. (2005). Grupo Sabará no sinclinal Dom Bosco, Quadrilátero Ferrifero: uma revisão estratigráfica. *Revista Brasileira de Geociências*, **35**(2): 177-186.

ANM. (2022). Anuário Mineral Brasileiro: 2 (ano base 2021) principais substâncias metálicas: produção bruta, beneficiada e comercializada. https://www.gov.br/anm/pt-br/centrais-de-conteudo/publicacoes/serie-estatisticas-e-economia-mineral/anuario-mineral/anuario-mineral-brasileiro/PreviaAMB2022.pdf

Babinski, M., Chemale Jr, F., & Van Schmus, W. (1995). The Pb/Pb age of the Minas Supergroup carbonate rocks, Quadrilátero Ferrífero, Brazil. *Precambrian Research*, **72**(3-4): 235-245. https://doi.org/10.1016/0301-9268(94)00091-5

Baltazar, O. F., & Zucchetti, M. (2007). Lithofacies associations and structural evolution of the Archean Rio das Velhas greenstone belt, Quadrilátero Ferrífero, Brazil: A review of the setting of gold deposits. *Ore Geology Reviews*, ***32***(3-4), 471-499. https://doi.org/10.1016/j.oregeorev.2005.03.021

Barley, M.E., Pickard, A.L., & Sylvester, P.J. (1997). Emplacement of a large igneous province as a possible cause of banded iron formation 2.45 billion years ago. *Nature*, **385**(6611): 55-58. https://doi.org/10.1038/385055a0

Bau, M., and Dulski, P. (1996). Distribution of yttrium and rare-earth elements in the Penge and Kuruman iron-formations, Transvaal Supergroup, South Africa. *Precambrian Research*, ***79***(1-2), 37-55. https://doi.org/10.1016/0301-9268(95)00087-9

Bau, M., and Möller, P. (1993). Rare earth element systematics of the chemically precipitated component in Early Precambrian iron formations and the evolution of the terrestrial atmosphere-hydrosphere-lithosphere system. *Geochimica et Cosmochimica Acta*, ***57***(10), 2239-2249. https://doi.org/10.1016/0016-7037(93)90566-F

Bau, M., Höhndorf, A., Dulski, P., & Beukes, N. J. (1997). Sources of rare-earth elements and iron in Paleoproterozoic iron-formations from the Transvaal Supergroup, South Africa: evidence from neodymium isotopes. *The Journal of Geology*, ***105***(1), 121-129. https://doi.org/10.1086/606152

Baur, M.E., Hayes, J.M., Studley, S.A., and Walter, M.R., 1985, Millimeterscale variations of stable isotope abundances in carbonates from banded iron-formations in the Hamersley Group of Western Australia: Economic Geology **80**, p. 270–282. https://doi.org/10.2113/gsecongeo.80.2.270

Bekker, A., Sial, A.N., Karhu, J.A., Ferreira, V.P., Noce, C.M., Kaufman, A.J., ... & Pimentel, M.M. (2003). Chemostratigraphy of carbonates from the Minas Supergroup, Quadrilátero Ferryífero (Iron Quadrangle), Brazil: A stratigraphic

record of early Proterozoic atmospheric, biogeochemical and climactic change. *American Journal of Science*, **303**(10): 865-904. https://doi.org/10.2475/ajs.303.10.865

Bekker, A., Slack, J., Planavsky, N., & Krapez, B. (2010). Iron formation: the sedimentary product of a complex interplay among mantle, tectonic, oceanic, and biospheric processes. *Economic Geology*, **105**(3): 467-508. https://doi.org/10.2113/gsecongeo.105.3.467

Berner, R.A. (1985). Sulphate reduction, organic matter decomposition and pyrite formation. *Philosophical Transactions of the Royal Society of London. Series A, Mathematical and Physical Sciences*, **315**(1531): 25-38. https://doi.org/10.1098/rsta.1985.0027

Beukes, N. J., & Gutzmer, J. E. N. S. (2008). Origin and paleoenvironmental significance of major iron formations at the Archean-Paleoproterozoic boundary. https://doi.org/10.5382/Rev.15.01

Beukes, N.J., Gutzmer, J. and Mukhopadhyay, J. (2003). The geology and genesis of high-grade hematite iron ore deposits. *Applied Earth Science*, 112(1): 18-25. https://doi.org/10.1179/037174503225011243

Beukes, N.J., Klein, C., Kaufman, A.J., & Hayes, J.M. (1990). Carbonate petrography, kerogen distribution, and carbon and oxygen isotope variations in an early Proterozoic transition from limestone to iron-formation deposition, Transvaal Supergroup, South Africa. *Economic Geology and the Bulletin of the Society of Economic Geologists*, **85**(4): 663-690. https://doi.org/10.2113/gsecongeo.85.4.663

Borchert, H. (1960). Genesis of marine sedimentary iron ores. *Transactions of the Institution of Mining and Metallurgy*, **69**: 261-279.

Boyd SR, Philippot P. (1998). Precambrian ammonium biogeochemistry: A study of the Moine metasediments, Scotland. *Chem Geol*. **144**:257-268.

Brand, U., & Veizer, J. (1980). Chemical diagenesis of a multicomponent carbonate system; 1, Trace elements. *Journal of Sedimentary Research*, **50**(4): 1219-1236. https://doi.org/10.1306/212F7BB7-2B24-11D7-8648000102C1865D

Bryce, C., N. Blackwell, C. Schmidt, J. Otte, Y.-M. Huang, S. Kleindienst, E. Tomaszewski, M. Schad, V. Warter, C. Peng, et al. 2018. Microbial anaerobic Fe(II) oxidation—Ecology, mechanisms and environmental implications. *Environmental Microbiology* **20**(10): 3462–3483. https://doi.org/10.1111/1462-2920.14328

Cabral, A. R., & Zeh, A. (2015). Celebrating the centenary of “The geology of central Minas Gerais, Brazil”: an insight from the Sítio Largo amphibolite. *The Journal of Geology*, *123*(4), 337-354. https://doi.org/10.1086/682047

Cabral, A.R., Zeh, A., Koglin, N., Gomes Jr, A.A.S., Viana, D.J., & Lehmann, B. (2012). Dating the Itabira iron formation, Quadrilátero Ferrífero of Minas Gerais, Brazil, at

2.65 Ga: depositional U–Pb age of zircon from a metavolcanic layer. *Precambrian Research*, **204:** 40-45. https://doi.org/10.1016/j.precamres.2012.02.006

Cairns-Smith, A.G., 1978, Precambrian solution photochemistry, inverse segregation, and banded iron formations: Nature, v. 76, p. 807–808. https://doi.org/10.1038/276807a0

Canfield, D.E., Raiswell, R., Westrich, J.T., Reaves, C.M., & Berner, R.A. (1986). The use of chromium reduction in the analysis of reduced inorganic sulfur in sediments and shales. *Chemical Geology*, **54**(1-2): 149-155. https://doi.org/10.1016/0009-2541(86)90078-1

Canuto, J.R. (2010). Estratigrafia de sequências em bacias sedimentares de diferentes idades e estilos tectônicos. *Revista Brasileira de Geociências*, **40**(4): 537-549.

Caxito, F.A., Hagemann, S., Dias, T.G., Barrote, V., Dantas, E.L., de Oliveira Chaves, A., ... & Campos, F.C. (2020). A magmatic barcode for the São Francisco Craton: Contextual in-situ SHRIMP U-Pb baddeleyite and zircon dating of the Lavras, Pará de Minas and Formiga dyke swarms and implications for Columbia and Rodinia reconstructions. *Lithos*, **374**: 105708. https://doi.org/10.1016/j.lithos.2020.105708

Caxito, F.A., Sperling, E., Fazio, G., Adorno, R.R., Denezine, M., Do Carmo, D.A., ... & Sial, A.N. (2024). A shift in redox conditions near the Ediacaran/Cambrian transition and its possible influence on early animal evolution, Corumbá Group, Brazil. *Geoscience Frontiers*, **15**(4): 101810. https://doi.org/10.1016/j.gsf.2024.101810

Caxito, F.A., Uhlein, G.J., Uhlein, A., Pedrosa-Soares, A.C., Kuchenbecker, M., Reis, H., ... & Paula, J.R. (2019). Isotope stratigraphy of Precambrian sedimentary rocks from Brazil: Keys to unlock Earth's hydrosphere, biosphere, tectonic, and climate evolution. In *Stratigraphy & Timescales*. Academic Press. **4**: 73-132. https://doi.org/10.1016/bs.sats.2019.08.002

Chemale Jr, F., Rosière, C.A., & Endo, I. (1994). The tectonic evolution of the Quadrilátero Ferrífero, Minas Gerais, Brazil. *Precambrian Research*, **65**(1-4): 25-54. https://doi.org/10.1016/0301-9268(94)90098-1

Cheng, M., Zhang, Z., Algeo, T.J., Liu, S., Liu, X., Wang, H., ... & Li, C. (2021). Hydrological controls on marine chemistry in the Cryogenian Nanhua Basin (South China). *Earth-Science Reviews*, **218**: 103678. https://doi.org/10.1016/j.earscirev.2021.103678

Cloud Jr, P.E. (1965). Significance of the Gunflint (Precambrian) Microflora: Photosynthetic oxygen may have had important local effects before becoming a major atmospheric gas. *Science*, *148*(3666), 27-35. https://www.science.org/doi/10.1126/science.148.3666.27

Cloud, P. (1973). Paleoecological significance of the banded iron-formation. *Economic Geology*, *68*(7), 1135-1143. https://doi.org/10.2113/gsecongeo.68.7.1135

Daher, A.P., Costa, M.A., & Novo, T.A. (2020). A Serra das Cambotas: terminação Meridional do Supergrupo Espinhaço no Quadrilátero Ferrífero, MG. *Geonomos*., **28**(1):15-24.

De Paula, J.R. (2020). Estratigrafia e geoquímica do Supergrupo Minas na Mina de Segredo, Quadrilátero Ferrífero, Brasil Master Dissertation. *Universidade Federal de Minas Gerais*. 79p.

De Paula, J.R., Caxito, F.A., Sial, A.N., Ribeiro, D.T., Alkmim, A.R., Lana, C., & Endo, I. (2023). Trace elements, C–O isotopes and U–Pb geochronology of the Minas Supergroup in the Segredo deposit, Quadrilátero Ferrífero, Brazil. *Journal of South American Earth Sciences*, **129**: 104525. https://doi.org/10.1016/j.jsames.2023.104525

De Paula, J.R., Wei, W., Caxito, F. A., Snihur, K. N., Lazowski, C. N., Konhauser, K. O., Sperling, E. A., Alessi, D. S. (2025). Under review at *Chemical Geology* (Paper number: CHEMGE18144) on February 28, 2025.

Derry, L. A., & Jacobsen, S. B. (1990). The chemical evolution of Precambrian seawater: evidence from REEs in banded iron formations. *Geochimica et Cosmochimica Acta*, *54*(11), 2965-2977. https://doi.org/10.1016/0016-7037(90)90114-Z

Dias, T. G., & Caxito, F. (2018). Manganês. *CODEMGE – Companhia de Desenvolvimento de Minas Gerais. Disponível em: http://recursomineralmg. codemge. com. br/substanciasminerais/manganes/. Acesso em*, *12*(11), 2021.

Dias, T.G., e Silva, R.C.F., Lobato, L.M., Caxito, F.A., Hagemann, S., Santos, J.O.S., & Barrote, V. (2022). Ediacaran-Cambrian fluid flow in Archean orogenic gold deposits: Evidence from U–Pb SHRIMP hydrothermal monazite ages of the metaturbidite-hosted Córrego do Sítio and Pilar deposits, Quadrilátero Ferrífero, Brazil. *Journal of South American Earth Sciences*, 103844. https://doi.org/10.1016/j.jsames.2022.103844

Dopico, C.I.M., Lana, C., Moreira, H.S., Cassino, L.F., & Alkmim, F.F. (2017). U–Pb ages and Hf-isotope data of detrital zircons from the late Neoarchean-Paleoproterozoic Minas Basin, SE Brazil. *Precambrian Research*, **291**: 143-161. https://doi.org/10.1016/j.precamres.2017.01.026

Dorr, J.V.N. (1969). Physiographic, stratigraphic, and structural development of the Quadrilátero Ferrífero, Minas Gerais, Brazil. *US Government Printing Office*. **641**-A: 118p.

Dorr, J.V.N., 2d, Gair, J. E., Pomerene, J. B., and Rynearson, G. A. (1957). Revisão da estratigrafia Pré-cambriana do Quadrilátero Ferrífero: Brazil Dept. Nac. Produção Mineral, Div. Fomento Produção Mineral, Avulso **81**, 31 p.

Dreher, C. L., Schad, M., Robbins, L. J., Konhauser, K. O., Kappler, A., & Joshi, P. (2021). Microbial processes during deposition and diagenesis of Banded Iron Formations. *PalZ*, ***95***(4), 593-610. https://doi.org/10.1007/s12542-021-00598-z

Dutra, L.F., Dias, S.P., Martins, M., Lana, C., Batista, A.C., & Tavares, T.D. (2020). Detrital zircon records of the Paleo-Mesoproterozoic rift-sag Tamanduá Group in its type-section, Northern Quadrilátero Ferrífero, Minas Gerais, Brazil. *Brazilian Journal of Geology*, **50**: e20190069. https://doi.org/10.1590/2317-4889202020190069

Endo, I.; Fonseca, M.A. Sistema de cisalhamento Fundão-Cambotas no Quadrilátero Ferrífero, MG : geometria e cinemática. REM. Revista Escola de Minas, Ouro Preto, v. 45 1/2, p. 15-17, 1992.

Endo, I., Galbiatti, H.F., Delgado, C.E.R., Oliveira, M.M.F. de, Zapparoli, A. de C., Moura, L.G.B. de, ... & Carlos, D.U. (2019). Mapa geológico do Quadrilátero Ferrífero, Minas Gerais, Brasil. Escala 1:150.000. Ouro Preto, Departamento de Geologia, Escola de Minas – UFOP - Centro de Estudos Avançados do Quadrilátero Ferrífero: www.qfe2050.ufop.br.

Endo, I., Machado, R., Galbiatti, H.F., Rossi, D.Q., Zapparoli, A. de C., Delgado, C.E.R., ... & Oliveira, M.M.F. (2020). Estratigrafia e evolução estrutural do Quadrilátero Ferrífero, Minas Gerais. In: Castro, P.T.A., Endo, I., & Gandini, A.L. (Eds.), Quadrilátero Ferrífero: Avanços do conhecimento nos últimos 50 anos, Belo Horizonte, pp. 70-113.

Endo. I., Silva L. G., Zavaglia G., Rocha, F., O G., Guimarães M. L. V., Rosas C. F., Lagoeiro L. E., Santos, G. J. I. (2004). Arcabouço estrutural e modelo evolutivo do Sinclinal Gandarela, Quadrilátero Ferrífero, MG. *Resumo, XLII Cong. Bras. de Geol.*, Araxá.

Falkner, K.K., Bowers, T.S., Todd, J.F., Lewis, B.L., Landing, W.M., & Edmond, J.M. (1993). The behavior of barium in anoxic marine waters. *Geochimica et Cosmochimica Acta*, **57**(3): 537-554. https://doi.org/10.1016/0016-7037(93)90366-5

Farina, F., Albert, C., & Lana, C. (2015). The Neoarchean transition between medium- and high-K granitoids: Clues from the Southern São Francisco Craton (Brazil). *Precambrian Research*, ***266***, 375-394. https://doi.org/10.1016/j.precamres.2015.05.038

Farina, F., Albert, C., Dopico, C., Moreira, H., Hippertt, J., ..., & Lana, C. (2016). The Archean–Paleoproterozoic evolution of the Quadrilátero Ferrífero (Brasil): Current models and open questions. *Journal of South American Earth Sciences*, **68**: 4-21. https://doi.org/10.1016/j.jsames.2015.10.015

Fischer, W. W., and Valentine, J. S. (2019). How did life come to tolerate and thrive in an oxygenated world? *Free Radical Biology and Medicine*, ***140***, 1-3. https://doi.org/10.1016/j.freeradbiomed.2019.07.021

Fitzsimmons, J.N., John, S.G., Marsay, C.M., Hoffman, C.L., Nicholas, S.L., Toner, B.M., German, C.R., Sherrell, R.M. (2017). Iron persistence in a distal hydrothermal plume supported by dissolved–particulate exchange. *Nat. Geosci*. **10**, 195–201. https://doi.org/10.1038/ngeo2900

Franco, A. S. P., & Endo, I. (2004). Sinclinal ouro fino revisitado, Quadrilátero Ferrífero, Minas Gerais: uma hipótese sobre a sua origem e evolução. *Rev Bras Geoc*, ***34***, 167-174.

Fryer, B.J., Fyfe, W.S., & Kerrich, R. (1979). Archaean volcanogenic oceans. *Chemical Geology*, **24**(1-2): 25-33. https://doi.org/10.1016/0009-2541(79)90010-X

Garrels, R.M., E.A. Perry Jr., and F.T. MacKenzie. 1973. Genesis of Precambrian Iron-Formations and the Development of Atmospheric Oxygen. *Economic Geology* **68**(7): 1173–1179. https://doi.org/10.2113/gsecongeo.68.7.1173

German, C.R., Seyfried Jr., W.E., (2014). Hydrothermal processes. In: Holland, H.D., Turekian, K.K. (Eds.), Treatise of Geochemistry, second ed. v. 8. Elsevier, pp. 191–233.

Gilleaudeau, G.J., Algeo, T.J., Lyons, T.W., Bates, S., & Anbar, A.D. (2021). Novel watermass reconstruction in the Early Mississippian Appalachian Seaway based on integrated proxy records of redox and salinity. *Earth and Planetary Science Letters*, **558**: 116746. https://doi.org/10.1016/j.epsl.2021.116746

Gole, M.J., and Klein, C., 1981, Banded iron-formation through much of Precambrian time: Journal of Geology, v. 89, p. 169−183. https://doi.org/10.1086/628578

Gonçalves, G.F., & Uhlein, A. (2022). Depositional systems, sequence stratigraphy, and sedimentary provenance of the Palaeoproterozoic Minas Supergroup and Itacolomi Group, Quadrilátero Ferrífero, Brazil. *Brazilian Journal of Geology*, **52**(4):e20210081. https://doi.org/10.1590/2317-4889202220210081

Gonçalves-Dias, T.G., e Silva, R.C.F., Lobato, L.M., de Andrade Caxito, F., Hagemann, S., Santos, J.O.S., & Barrote, V. (2022). Ediacaran-Cambrian fluid flow in Archean orogenic gold deposits: Evidence from U–Pb SHRIMP hydrothermal monazite ages of the metaturbidite-hosted Córrego do Sítio and Pilar deposits, Quadrilátero Ferrífero, Brazil. *Journal of South American Earth Sciences*, **116**: 103844. https://doi.org/10.1016/j.jsames.2022.103844

Graf, J.L. (1977). Rare earth elements as hydrothermal tracers during the formation of massive sulfide deposits in volcanic rocks. *Economic Geology*, **72**(4): 527-548. https://doi.org/10.2113/gsecongeo.72.4.527

Gross, G. A. (1965). Geology of iron deposits in Canada. I. General geology and evaluation of iron deposits. Geol. *Surv. Can. Econ. Geol. Rep*., **22**:181

Gross, G. A. (1973). Genesis of Precambrian Iron and Manganese Deposits *Unesco Earth Sci*., **9**:15-2. In: M.P. Semenenko (Editors) Proc. Kiev Symp.

Gross, G. A. (1980). A classification of iron formations based on depositional environments. *The Canadian Mineralogist*, *18*(2), 215-222.

Gross, G.A. (1993). Element distribution patterns as metallogenetic indicators in siliceous metalliferous sediments: International Geological Congress, 29th, Kyoto, Japan, Proceedings, v. 17C, p. 96–106.

Guild, P. (1957). Geology and mineral resources of the Congonhas district, Minas Gerais, Brazil. *USGS Numbered Series - Professional Paper 290*, 90p.

Gumsley, A.P., Chamberlain, K.R., Bleeker, W., Söderlund, U., de Kock, M.O., Larsson, E.R., & Bekker, A. (2017). Timing and tempo of the Great Oxidation Event. *Proceedings of the National Academy of Sciences*, **114**(8): 1811-1816. https://doi.org/10.1073/pnas.1608824114

Hagemann, S.G., Angerer, T., Duuring, P., Rosière, C.A., e Silva, R.F., Lobato, L., ... & Walde, D.H.G. (2016). BIF-hosted iron mineral system: A review. *Ore Geology Reviews*, **76**: 317-359. https://doi.org/10.1016/j.oregeorev.2015.11.004

Halverson, G. P., Wade, B. P., Hurtgen, M. T., & Barovich, K. M. (2010). Neoproterozoic chemostratigraphy. *Precambrian Research*, *182*(4), 337-350. https://doi.org/10.1016/j.precamres.2010.04.007

Han, X., Tomaszewski, E.J., Schoenberg, R., Konhauser, K.O., Amor, M., Pan, Y., ... & Byrne, J.M. (2021). Using Zn and Ni behavior during magnetite precipitation in banded iron formations to determine its biological or abiotic origin. *Earth and Planetary Science Letters*, **568**: 117052. https://doi.org/10.1016/j.epsl.2021.117052

Hart, B.S., & Hofmann, M.H. (2022). Revisiting paleoenvironmental analyses and interpretations of organic-rich deposits: The importance of TOC corrections. *Organic Geochemistry*, **170**: 104434. https://doi.org/10.1016/j.orggeochem.2022.104434

Hartman, H. 1984. The evolution of photosynthesis and microbial mats: a speculation on banded iron formations. In *Microbial Mats: Stromatolites*, eds. Y. Cohen, and R.W. Castenholz, 451–453. New York: Alan Liss.

Hartmann, L.A., Endo, I., Suita, M.T.F., Santos, J.O.S., Frantz, J.C., Carneiro, M.A., McNaughton, N.J., & Barley, M.E. (2006). Provenance and age delimitation of Quadrilátero Ferrífero sandstones based on zircon U–Pb isotopes. *Journal of South American Earth Sciences*, **20**(4): 273-285. https://doi.org/10.1016/j.jsames.2005.07.015

Hensler, A.S., Rosière, C.A., & Hagemann, S.G. (2017). Iron oxide mineralization at the contact zone between phyllite and itabirite of the Pau Branco deposit, Quadrilátero Ferrífero, Brazil—implications for fluid-rock interaction during iron ore formation. *Economic Geology*, **112**(4): 941-982. https://doi.org/10.2113/econgeo.112.4.941

Herz, N. (1978). Metamorphic rocks of the Quadrilátero Ferrífero, Minas Gerais, Brazil. *US Geological Survey Professional Paper*, 641-C.

Hoefs, J., Müller, G., & Schuster, A.K. (1982). Polymetamorphic relations in iron ores from the Iron Quadrangle, Brazil: the correlation of oxygen isotope variations with deformation history. *Contributions to Mineralogy and Petrology*, **79**(3): 241-251.

Hoffman, P.F. (2013). The Great Oxidation and a Siderian snowball Earth: MIF-S based correlation of Paleoproterozoic glacial epochs. *Chemical Geology*, **362**: 143-156. https://doi.org/10.1073/pnas.2003090117

Hoffman, P.F., Kaufman, A.J., Halverson, G.P., & Schrag, D.P. (1998). A Neoproterozoic snowball earth. *Science*, **281**(5381): 1342-1346. https://doi.org/10.1126/science.281.5381.1342

Holland, H.D. (1973). The oceans: A possible source of iron in iron formations. *Economic Geology* **68**: 1169–1172. https://doi.org/10.2113/gsecongeo.68.7.1169

Holland, H.D. (1984). The Chemical Evolution of the Atmosphere and Oceans. Princeton University Press, Princeton, NJ, pp. 1–598.

Holland, H.D. (2002). Volcanic gases, black smokers, and the Great Oxidation Event. *Geochimica et Cosmochimica acta*, ***66***(21), 3811-3826. https://doi.org/10.1016/S0016-7037(02)00950-X

Holland, H.D. (2006). The oxygenation of the atmosphere and oceans. Philosophical *Transactions of the Royal Society B: Biological Sciences*, **361**(1470): 903-915. https://doi.org/10.1098/rstb.2006.1838

Honma H, Itihara Y. (1981) Distribution of ammonium in minerals of metamorphic and granitic rocks. *Geochim Cosmochim Acta* **45**: 983-988.

Hsi, C.K.D., & Langmuir, D. (1985). Adsorption of uranyl onto ferric oxyhydroxides: application of the surface complexation site-binding model. *Geochimica et Cosmochimica Acta*, **49**(9): 1931-1941. https://doi.org/10.1016/0016-7037(85)90088-2

Hudson, J.D. (1977). Stable isotopes and limestone lithification. *Journal of the Geological Society of London*, **133**: 637-660. https://doi.org/10.1144/gsjgs.133.6.0637

Ingall, E.D., & Van Cappellen, P. (1990). Relation between sedimentation rate and burial of organic phosphorus and organic carbon in marine sediments. *Geochimica et Cosmochimica Acta*, **54**(2): 373-386. https://doi.org/10.1016/0016-7037(90)90326-G

Isley, A.E. (1995). Hydrothermal plumes and the delivery of iron to banded iron formation. *The Journal of Geology*, **103**(2): 169-185. https://doi.org/10.1086/629734

Isley, A.E. and Abbott, D.H. (1999). Plume-related mafic volcanism and the deposition of banded iron formation. *Journal of Geophysical Research: Solid Earth*, **104**(B7): 15461-15477. https://doi.org/10.1029/1999JB900066

James, H.L. (1954). Sedimentary facies of iron-formations. *Economic Geology*, **49**: 235-293. https://doi.org/10.2113/gsecongeo.49.3.235

Jarvie, D. (2012). Shale Resource Systems for Oil and Gas— Giant Resources for the 21st Century, *AAPG Memoir*, **97**:1-19. https://doi.org/10.1306/13321446M973489

Jones, C., S. Nomosatryo, S.A. Crowe, C.J. Bjerrum, and D.E. Canfield. 2015. Iron oxides, divalent cations, silica, and the early earth phosphorus crisis. *Geology* 43(2): 135–138. https://doi.org/10.1130/G36044.1

Kamber, B. S., and Webb, G. E. (2001). The geochemistry of late Archaean microbial carbonate: implications for ocean chemistry and continental erosion history. *Geochimica et Cosmochimica Acta*, *65*(15), 2509-2525. https://doi.org/10.1016/S0016-7037(01)00613-5

Kappler A., Pasquero C., Konhauser K. O. and Newman D. K. (2005). Deposition of banded iron formations by anoxygenic phototrophic Fe (II)-oxidizing bacteria. Geology **33**, 865–868. https://doi.org/10.1130/G21658.1

Kendall, B., Reinhard, C.T., Lyons, T.W., Kaufman, A.J., Poulton, S.W., Anbar, A.D., 2010. Pervasive oxygenation along late Archaean ocean margins. *Nat. Geosci.* **3**, 647–652. https://doi.org/10.1038/ngeo942

Klein, C. (2005). Some Precambrian banded iron-formations (BIFs) from around the world: Their age, geologic setting, mineralogy, metamorphism, geochemistry, and origins. *American Mineralogist*, *90*(10), 1473-1499.

Klein, A.J. and Knoll, A.H. (1995). Neoproterozoic variations in the C-isotopic composition of seawater: stratigraphic and biogeochemical implications. *Precambrian Research*, **73**(1-4): 27-49. https://doi.org/10.1016/0301-9268(94)00070-8

Klein, C. and Beukes, N.J., (1989). Geochemistry and sedimentology of a facies transition from limestone to iron-formation deposition in the early Proterozoic Transvaal Supergroup, South Africa. *Econ. Geol*. **84**, 1733–1774. https://doi.org/10.2113/gsecongeo.84.7.1733

Klein, C. and Beukes, N.J. (1992). Proterozoic Iron-Formations. In: *Developments in Precambrian geology*: 10, pp. 383-418. https://doi.org/10.1016/S0166-2635(08)70124-5

Klein, C., Beukes, N. J., & Schopf, J. W. (1992). Models for iron-formation deposition. *The proterozoic bioshere: a rnultidisciplinary study, University Press, Cambridge*, 147-151.

Klein, C., and Ladeira, E.A. (2000). Geochemistry and petrology of some Proterozoic banded iron-formations of the Quadrilátero Ferrífero, Minas Gerais, Brazil. *Economic Geology*, **95**(2): 405-427. https://doi.org/10.2113/gsecongeo.95.2.405

Knauth, L. P. (2005). Temperature and salinity history of the Precambrian ocean: implications for the course of microbial evolution. In Geobiology: Objectives, concepts, perspectives (pp. 53-69). Elsevier.

Koglin, N., Zeh, A., Cabral, A.R., Gomes Jr, A.A.S., Neto, A.V.C., Brunetto, W.J., & Galbiatti, H. (2014). Depositional age and sediment source of the auriferous Moeda Formation, Quadrilátero Ferrífero of Minas Gerais, Brazil: New constraints from U–Pb–Hf isotopes in zircon and xenotime. *Precambrian Research*, **255**: 96-108. https://doi.org/10.1016/j.precamres.2014.09.010

Konhauser, K.O., Hamade, T., Raiswell, R., Morris, R.C., Ferris, F.G., Southam, G., & Canfield, D.E. (2002). Could bacteria have formed the Precambrian banded iron formations?. *Geology*, ***30***(12), 1079-1082. https://doi.org/10.1130/0091-7613(2002)030%3C1079:CBHFTP%3E2.0.CO;2

Konhauser, K.O., Kappler, A., and Roden, E.E. (2011). Iron in microbial metabolisms. *Elements*, **7**(2): 89-93. https://doi.org/10.2113/gselements.7.2.89

Konhauser, K.O., Newman, D.K., & Kappler, A. (2005). The potential significance of microbial Fe (III) reduction during deposition of Precambrian banded iron formations. *Geobiology*, ***3***(3), 167-177. https://doi.org/10.1111/j.1472-4669.2005.00055.x

Konhauser, K.O., Pecoits, E., Lalonde, S. V., Papineau, D., Nisbet, E. G., Barley, M. E., ... & Kamber, B. S. (2009). Oceanic nickel depletion and a methanogen famine before the Great Oxidation Event. *Nature*, *458*(7239), 750-753. https://doi.org/10.1038/nature07858

Konhauser, K.O., Planavsky, N.J., Hardisty, D.S., Robbins, L.J., Warchola, T.J., Haugaard, R., ... & Johnson, C.M. (2017). Iron formations: A global record of Neoarchaean to Palaeoproterozoic environmental history. *Earth-Science Reviews*, **172**: 140-177. https://doi.org/10.1016/j.earscirev.2017.06.012

Kopp, R.E., Kirschvink, J.L., Hilburn, I.A., & Nash, C.Z. (2005). The Paleoproterozoic snowball Earth: a climate disaster triggered by the evolution of oxygenic photosynthesis. *Proceedings of the National Academy of Sciences*, **102**(32): 11131-11136. https://doi.org/10.1073/pnas.0504878102

Krapež, B., M.E. Barley, and A.L. Pickard. (2003). Hydrothermal and resedimented origins of the precursor sediments to banded iron formation: Sedimentological evidence from the Early Palaeoproterozoic Brockman Supersequence of Western Australia. *Sedimentology* 50(5): 979–1011. https://doi.org/10.1046/j.1365-3091.2003.00594.x

Köhler, I., Konhauser, K.O., Papineau, D., Bekker, A., Kappler, A., 2013. Biological carbon precursor to diagenetic siderite with spherical structures in iron formations. *Nat. Commun*. **4**, 1741. https://doi.org/10.1038/ncomms2770

Lana, C., Alkmim, F.F., Armstrong, R., Scholz, R., Romano, R., Nalini, H.A., (2013). The ancestry and magmatic evolution of Archaean TTG rocks of the Quadrilátero Ferrífero province, southeast Brazil. Precambrian Res. 231, 157e173. https://doi.org/10.1016/j.precamres.2013.03.008

Lana, C., Farina, F., Gerdes, A., Alkmim, A., Gonçalves, G.O., Jardim, A.C., ... & Lana, C. (2017). Characterization of zircon reference materials via high precision U-Pb LA-MC-ICPMS. *Journal of Analytical Atomic Spectrometry*, **32**(10): 1-13. https://doi.org/10.1039/c7ja00167c

Large, R.R., Hazen, R.M., Morrison, S.M., Gregory, D.D., Steadman, J.A., & Mukherjee, I. (2022). Evidence that the GOE was a prolonged event with a peak around 1900 Ma. *Geosystems and Geoenvironment*, **1**(2): 100036. https://doi.org/10.1016/j.geogeo.2022.100036

Lawrence, M. G., Greig, A., Collerson, K. D., & Kamber, B. S. (2006). Rare earth element and yttrium variability in South East Queensland waterways. *Aquatic Geochemistry*, *12*, 39-72. https://doi.org/10.1007/s10498-005-4471-8

Li, L., Li, K., Li, Y., Zhang, J., Du, Y., & Labbe, M. (2021). Recommendations for offline combustion-based nitrogen isotopic analysis of silicate minerals and rocks. *Rapid Communications in Mass Spectrometry*, *35*(10), e9075. https://doi.org/10.1002/rcm.9075

Li, Z., Konhauser, K. O., Zhou, Y., Adlakha, E., Button, M., Lazowski, C., ... & Robbins, L. J. (2023). How does weathering influence geochemical proxies in Paleoproterozoic banded iron formations? A case study from outcrop samples of 2.46 Ga banded iron formation, Hamersley Basin, Western Australia. *Geological Society of America Bulletin*, *136*(7-8), 2735-2752. https://doi.org/10.1130/B37152.1

Liu, W., Hao, J., Elzinga, E. J., Piotrowiak, P., Nanda, V., Yee, N., & Falkowski, P. G. (2020). Anoxic photogeochemical oxidation of manganese carbonate yields manganese oxide. *Proceedings of the National Academy of Sciences*, *117*(37), 22698-22704. https://doi.org/10.1073/pnas.2002175117

Lima N.P., Ferreira, A..S, Ruffei, M., Ferreira, R.F., Piret, W., Galbiatti, H.F. (2020). Quadrilátero Ferrífero: cinco décadas de histórias, descobertas, importância econômica e tecnológica e novas fronteiras para a mineração de ferro. In: Castro, P.T.A., Endo, I., & Gandini, A.L. (Eds.), Quadrilátero Ferrífero: Avanços do conhecimento nos últimos 50 anos, Belo Horizonte, pp. 319-342.

Lobato, L.M., Ribeiro-Rodrigues, L.C., & Vieira, F.W. (2001). Brazil's premier gold province. Part II: geology and genesis of gold deposits in the Archean Rio das Velhas greenstone belt, Quadrilátero Ferrífero. *Mineralium Deposita*, **36**: 249-277. https://doi.org/10.1007/s001260100180

Lovley, D. R., & Phillips, E. J. (1987). Rapid assay for microbially reducible ferric iron in aquatic sediments. *Applied and Environmental Microbiology*, *53*(7), 1536-1540. https://doi.org/10.1128/aem.53.7.1536-1540.1987

Ludwig, K. R. (2008). User's manual for Isoplot 3.6. A geochronological toolkit for Microsoft Excel. *Berkeley Geochronology Center Special Publication*, **4**: 77p.

Lyons, T.W., & Severmann, S. (2006). A critical look at iron paleoredox proxies: New insights from modern euxinic marine basins. *Geochimica et Cosmochimica Acta*, **70**(23): 5698-5722. https://doi.org/10.1016/j.gca.2006.08.021

Lyons, T.W., Reinhard, C.T., & Planavsky, N.J. (2014). The rise of oxygen in Earth's early ocean and atmosphere. *Nature*, **506**(7488): 307-315. https://doi.org/10.1038/nature13068

Machado, M. M. M. (2009). Construindo a imagem geológica do Quadrilátero Ferrífero: conceitos e representações. Universidade Federal de Minas Gerais. Tese de Doutorado. 238p.

Machado, N., Noce, C. M., Ladeira, E., & Belo de Oliveira, O. (1992). U-Pb geochronology of Archean magmatism and Proterozoic metamorphism in the Quadrilátero Ferrífero, southern São Francisco craton, Brazil. *Geological Society of America Bulletin*, **104**(9): 1221-1227.

Machado, N., Schrank, A., Noce, C. M., & Gauthier, G. (1996). Ages of detrital zircon from Archean-Paleoproterozoic sequences: implications for Greenstone Belt setting evolution of a Transamazonian foreland basin in Quadrilátero Ferrífero, southeast Brazil. *Earth and Planetary Science Letters*, **141**: 259-276. https://doi.org/10.1016/0012-821X(96)00054-4

Machel, H. G. (2003). Dolomites and dolomitization. In: *Encyclopedia of Sediments and Sedimentary Rocks*. Kluwer Academic Publishers, Dordrecht, pp. 235-243.

Madeira, M.R., de Souza Martins, M., Martins, G.P., & Alkmim, F.F. (2019). Caracterização faciológica e evolução sedimentar da Formação Moeda (Supergrupo Minas) na porção noroeste do Quadrilátero Ferrífero, Minas Gerais. *Geologia USP. Série Científica*, **19**(3): 129-148. https://doi.org/10.11606/issn.2316-9095.v19-148467

Madureira, R.D.S., Martins, M., Queiroga, G., Lana, C., Dutra, L.F., & Alkmim, A.R. (2021). Depositional setting and U-Pb detrital record of rift-related deposits in the Moeda Formation (Minas Supergroup) at the Gandarela and Ouro Fino synclines, Quadrilátero Ferrífero, Brazil. *Brazilian Journal of Geology*, **51**(03): e20200023. https://doi.org/10.1590/2317-4889202120200023

Maheshwari, A., Sial, A.N., Gaucher, C., Bossi, J., Bekker, A., Ferreira, V.P., Romano, A.W., ... & Romano, A.W. (2010). Global nature of the Paleoproterozoic Lomagundi carbon isotope excursion: A review of occurrences in Brazil, India, and Uruguay. In: Karhu, J., Sial, A.N., & Ferreira, V.P. (Eds.), *Precambrian Isotope Stratigraphy,*

special issue, Precambrian Research, **182**(4): 274-299. https://doi.org/10.1016/j.precamres.2010.06.017

Maliva R. G., Knoll A. H. and Simonson B. M. (2005) Secular change in the Precambrian silica cycle: insights from chert petrology. *Geol. Soc. Am. Bull*. **117**, 835–845. https://doi.org/10.1130/B25555.1

Marshak, S., & Alkmim, F.F. (1989). Proterozoic contraction/extension tectonics of the southern São Francisco region, Minas Gerais, Brazil. *Tectonics*, **8**(3): 555-571. https://doi.org/10.1029/TC008i003p00555

Mendes, M., Lobato, L.M., Kunzmann, M., Halverson, G.P., & Rosière, C.A. (2016). Iron isotope and REE+ Y composition of the Cauê banded iron formation and related iron ores of the Quadrilátero Ferrífero, Brazil. *Mineralium Deposita*, **52**: 159-180. https://doi.org/10.1007/s00126-016-0649-9

Mendes, M.D.C.O., Lobato, L.M., Suckau, V., & Lana, C. (2014). Datação U-Pb in situ por LA-ICPMS em zircões detríticos da Formação Cercadinho, Supergrupo Minas. *Geologia USP. Série Científica*, **14**(1): 55-68. https://doi.org/10.5327/Z1519-874X201400010004

Millero, F.J., Feistel, R., Wright, D.G., & McDougall, T.J. (2008). The composition of Standard Seawater and the definition of the Reference-Composition Salinity Scale. *Deep-Sea Research Part I*, **55**(1): 50-72. https://doi.org/10.1016/j.dsr.2007.10.001

Mloszewska A. M., Cole D. B., Planavsky N. J., Kappler A., Whitford D. S., Owttrim G. W. and Konhauser K. O. (2018) UV radiation limited the expansion of cyanobacteria in early marine photic environments. *Nat. Commun*. **9**, 1–8. https://doi.org/10.1038/s41467-018-05520-x

Moreira, J.L.P., Madeira, C.V., Gil, J.A., & Machado, M.A.P. (2007). Bacia de Santos. *Boletim de Geociências da Petrobras*, **15**(2): 531-549.

Morgan, R., Orberger, B., Rosière, C.A., Wirth, R., da Mota Carvalho, C., & Bellver-Baca, M.T. (2013). The origin of coexisting carbonates in banded iron formations: a micro-mineralogical study of the 2.4 Ga Itabira Group, Brazil. *Precambrian Research*, **224**: 491-511. https://doi.org/10.1016/j.precamres.2012.10.013

Morris, R. C. (1993). Genetic modelling for banded iron-formation of the Hamersley Group, Pilbara Craton, Western Australia. *Precambrian Research*, *60*(1-4), 243-286. https://doi.org/10.1016/0301-9268(93)90051-3

Morris, R.C., and Horwitz, R.C. (1983). The origin of the iron-formation-rich Hamersley Group of Western Australia—deposition on a platform. *Precambrian Research* 21(3–4): 273–297. https://doi.org/10.1016/0301-9268(83)90044-X

Morris, R.C., & Kneeshaw, M. (2011). Genesis modelling for the Hamersley BIF-hosted iron ores of Western Australia: a critical review. *Australian Journal of Earth Sciences*, *58*(5), 417-451. https://doi.org/10.1080/08120099.2011.566937

Mozart, M. S., Neto, A. V. C., Soares, M. B., & Silva-Alves, G. P. (2024). Geochemistry of BIF in the Quadrilátero ferrífero, Brazil, as a proxy to neoarchean paleoenvironmental and depositional conditions. *Journal of South American Earth Sciences*, *143*, 105009. https://doi.org/10.1016/j.jsames.2024.105009

März, C., Poulton, S.W., Beckmann, B., Küster, K., Wagner, T., & Kasten, S. (2008). Redox sensitivity of P cycling during marine black shale formation: dynamics of sulfidic and anoxic, non-sulfidic bottom waters. *Geochimica et Cosmochimica Acta*, **72**(15): 3703-3717. https://doi.org/10.1016/j.gca.2008.04.025

Nelson, C.S., & Smith, A.M. (1996). Stable oxygen and carbon isotope compositional fields for skeletal and diagenetic components in New Zealand Cenozoic nontropical carbonate sediments and limestones: a synthesis and review. *New Zealand Journal of Geology and Geophysics*, **39**(1): 93-107. https://doi.org/10.1080/00288306.1996.9514697

Neri, M.E.N.V. (2012). Supergrupo Minas na Serra de Bom Sucesso, extremo sudoeste do Quadrilátero Ferrífero – Minas Gerais: Petrografia, geoquímica e isótopos de U-Pb. *Programa de Pós-Graduação em Geologia - Instituto de Geociências da Universidade Federal de Minas Gerais. Dissertação de Mestrado*. 163p. https://doi.org/10.5327/Z1519-874X2013000200010

Noce, C. M., Zuccheti, M., Baltazar, O. F., Armstrong, R., Dantas, E., Renger, F. E., & Lobato, L. M. (2005). Age of felsic volcanism and the role of ancient continental crust in the evolution of the Neoarchean Rio das Velhas Greenstone belt (Quadrilátero Ferrífero, Brazil): U–Pb zircon dating of volcaniclastic graywackes. *Precambrian Research*, *141*(1-2), 67-82. https://doi.org/10.1016/j.precamres.2005.08.002

Noce, C.M., (1995). Geocronologia dos eventos magmáticos, sedimentares e metamórficos na região do Quadrilátero Ferrífero, Minas Gerais. Doctoral Thesis, Instituto de Geociências, University of São Paulo, São Paulo. https://doi.org/10.11606/T.44.2016.tde-05012016-154125

Nogueira, L.B., Oliveira, V.Q., Araújo, L.P., Leão, L.P., Ali, A., Leite, M.G.P., ... & Banerjee, N.R. (2019). Geochemistry and C and O isotope composition of carbonate rocks from Bemil and Lagoa Seca quarries, Gandarela Formation, Quadrilátero Ferrífero-Brazil. *Journal of South American Earth Sciences*, **92**: 609-630. https://doi.org/10.1016/j.jsames.2019.04.001

Nozaki, Y., Zhang, J., & Amakawa, H. (1997). The fractionation between Y and Ho in the marine environment. *Earth and Planetary Science Letters*, *148*(1-2), 329-340. https://doi.org/10.1016/S0012-821X(97)00034-4

Nunes, F.S. (2016). Contribuição à estratigrafia e geocronologia U-Pb de zircões detríticos da Formação Moeda (Grupo Caraça, Supergrupo Minas) na Serra do Caraça, Quadrilátero Ferrífero, Minas Gerais. *Dissertation on Graduate Program in Geology, Escola de Minas, Universidade de Ouro Preto, Ouro Preto*. 77p.

Ohmoto, H., Watanabe, Y., Yamaguchi, K. E., Naraoka, H., Haruna, M., Kakegawa, T., ... & Kato, Y. (2006). Chemical and biological evolution of early Earth: constraints from banded iron formations. https://doi.org/10.1130/2006.1198(17)

Olesik, J. W. (1991). Elemental analysis using ICP-OES and ICP/MS. *Analytical Chemistry*, ***63***(1), 12A-21A.

Oliveira, E.P., Windley, B.F., & Araújo, M.N.C. (2010). The Neoproterozoic Sergipano orogenic belt, NE Brazil: a complete plate tectonic cycle in western Gondwana. *Precambrian Research*, **181**(1): 64-84. https://doi.org/10.1016/j.precamres.2010.05.014

Oliveira, N.V.D., Endo, I., & Oliveira, L.G.S.D. (2005). Geometria do Sinclinal Gandarela baseada na deconvolução Euler 2D e 3D: Quadrilátero Ferrífero (MG). *Revista Brasileira de Geofísica*, **23**: 221-232. https://doi.org/10.1016/j.precamres.2010.05.014

Olson, H.C., Scheirer, A.H., Ritzer, S.R., & Sperling, E.A. (2025). Prediction of organic geochemical parameters from inorganic geochemical data in the Cretaceous-Danian Moreno Formation, San Joaquin Basin, California. *Chemical Geology*, **674**: 122551. https://doi.org/10.1016/j.chemgeo.2024.122551

Olson, S.L., Kump, L.R., Kasting, J.F., 2013. Quantifying the areal extent and dissolved oxygen concentrations of Archean oxygen oases. *Chem. Geol*. **362**, 35–43. https://doi.org/10.1016/j.chemgeo.2013.08.012

Pasquier, V., Fike, D.A., Révillon, S., & Halevy, I. (2022). A global reassessment of the controls on iron speciation in modern sediments and sedimentary rocks: A dominant role for diagenesis. *Geochimica et Cosmochimica Acta*, **335**: 211-230. https://doi.org/10.1016/j.gca.2022.08.037

Pavlov, A.A., Kasting, J.F., Brown, L.L., Rages, K.A., & Freedman, R. (2000). Greenhouse warming by CH4 in the atmosphere of early Earth. *Journal of Geophysical Research: Planets*, **105**(E5): 11981-11990. https://doi.org/10.1029/1999JE001134

Pecharsky, V. K., & Zavalij, P. Y. (2003). Fundamentals of diffraction. *Fundamentals of powder diffraction and structural characterization of materials*, 99-260.

Pecoits, E., Gingras, M. K., Barley, M. E., Kappler, A., Posth, N. R., & Konhauser, K. O. (2009). Petrography and geochemistry of the Dales Gorge banded iron formation: Paragenetic sequence, source and implications for palaeo-ocean chemistry. *Precambrian Research*, *172*(1-2), 163-187. https://doi.org/10.1016/j.precamres.2009.03.014

Pellerin, A., Thomazo, C., Ader, M., Marin-Carbonne, J., Alleon, J., Vennin, E., & Hofmann, A. (2023). Iron-mediated anaerobic ammonium oxidation recorded in the early Archean ferruginous ocean. https://doi.org/10.1111/gbi.12540

Pinho, F.A., & Neiva, I.K. de A. de. (2012). 200 anos Fábrica Patriótica: A primeira indústria de ferro do Brasil - Belo Horizonte: Vale. 112p.

Pires, F.R.M., & Bertolino, L.C. 1991. Estudo do metamorfismo nas formações proterozóicas no Quadrilátero Ferrífero, Minas Gerais. *Anuário do Instituto de Geociências*, **14**: 1-9. https://doi.org/10.11137/1991_0_1-9

Planavsky, N., Bekker, A., Rouxel, O.J., Kamber, B., Hofmann, A., Knudsen, A., ... & Lyons, T.W. (2010). Rare earth element and yttrium compositions of Archean and Paleoproterozoic Fe formations revisited: new perspectives on the significance and mechanisms of deposition. *Geochimica et Cosmochimica Acta*, **74**(22): 6387-6405. https://doi.org/10.1016/j.gca.2010.07.021

Playter, T., Konhauser, K., Owttrim, G., Hodgson, C., Warchola, T., Mloszewska, A.M., ... & Gingras, M. (2017). Microbe-clay interactions as a mechanism for the preservation of organic matter and trace metal biosignatures in black shales. *Chemical Geology*, **459**: 75-90. https://doi.org/10.1016/j.chemgeo.2017.04.007

Potter, P.E., Shimp, N.F., & Witters, J. (1963). Trace elements in marine and fresh-water argillaceous sediments. *Geochimica et Cosmochimica Acta*, **27**(6): 669-694. https://doi.org/10.1016/0016-7037(63)90019-X

Poulton, S. W. (2021). The iron speciation paleoredox proxy. Cambridge University Press. https://doi.org/10.1017/9781108847148

Poulton, S.W., and Canfield, D.E. (2005). Development of a sequential extraction procedure for iron: implications for iron partitioning in continentally derived particulates. *Chemical Geology*, **214**(3-4): 209-221. https://doi.org/10.1016/j.chemgeo.2004.09.003

Poulton, S.W., and Canfield, D.E. (2011). Ferruginous conditions: a dominant feature of the ocean through Earth's history. *Elements*, **7**(2): 107-112. https://doi.org/10.2113/gselements.7.2.107

Pourmand, A., Dauphas, N., & Ireland, T. J. (2012). A novel extraction chromatography and MC-ICP-MS technique for rapid analysis of REE, Sc and Y: Revising CI-chondrite and Post-Archean Australian Shale (PAAS) abundances. *Chemical Geology*, *291*, 38-54. https://doi.org/10.1016/j.chemgeo.2011.08.011

Raiswell, R., Hardisty, D.S., Lyons, T.W., Canfield, D.E., Owens, J.D., Planavsky, N.J., ... & Reinhard, C.T. (2018). The iron paleoredox proxies: A guide to the pitfalls, problems and proper practice. *American Journal of Science*, **318**(5): 491-526. https://doi.org/10.2475/05.2018.03

Rasmussen, B., Bekker, A., Fletcher, I.R., (2013). Correlation of Paleoproterozoic glaciations based on U-Pb zircon ages for tuff beds in the Transvaal and Huronian supergroups. *Earth Planet. Sci. Lett.* **382**, 173–180. https://doi.org/10.1016/j.epsl.2013.08.037

Rasmussen, B., Krapez, B. and Meier D.B. (2014). Replacement origin for hematite in 2.5 Ga banded iron formation: Evidence for postdepositional oxidation of iron-bearing minerals. *Geological Society of America Bulletin* 126(3–4): 438–446. https://doi.org/10.1130/B30944.1

Rasmussen, B., Muhling, J. R., and Krapež, B. (2021). Greenalite and its role in the genesis of early Precambrian iron formations–A review. *Earth-Science Reviews*, *217*, 103613. https://doi.org/10.1016/j.earscirev.2021.103613

Rasmussen, B., Muhling, J.R., Suvorova, A., Krapež, B., (2016). Dust to dust: evidence for the formation of “primary” hematite dust in banded iron formations via oxidation of iron silicate nanoparticles. *Precambrian Res.* **284**, 49–63. https://doi.org/10.1016/j.precamres.2016.07.003

Rasmussen, B., Muhling, J.R., Suvorova, A., Krapež, B., (2017). Greenalite precipitation linked to the deposition of banded iron formations downslope from a late Archean carbonate platform. *Precambrian Research*, **290**, 49–62. https://doi.org/10.1016/j.precamres.2016.12.005

Reis, L.A., Martins-Neto, M.A., Gomes, N.S., Endo, I., 2002. A bacia de antepaís paleoproterzóica Sabará, Quadrilátero Ferrífero, MG. Revista Brasileira de Geociências 32, 43e58.

Remírez, M.N., Algeo, T.J., Shen, J., Liu, J., Gilleaudeau, G.J., & Zhou, L. (2024). Low-salinity conditions in the "marine" Late Triassic-Early Jurassic Neuquén Basin of Argentina: Challenges in paleosalinity interpretation. *Palaeogeography, Palaeoclimatology, Palaeoecology*, **646**: 112216. https://doi.org/10.1016/j.palaeo.2024.112216

Renger, F.E., Noce, C.M., Romano, A.W., & Machado, N. (1994). Evolução sedimentar do Supergrupo Minas: 500 Ma. de registro geológico no Quadrilátero Ferrífero, Minas Gerais, Brasil. *Revista Geonomos*, **2**(1): 1-11. https://doi.org/10.18285/geonomos.v2i1.227

Retallack, G.J. (2020). Boron paleosalinity proxy for deeply buried Paleozoic and Ediacaran fossils. *Palaeogeography, Palaeoclimatology, Palaeoecology*, 540:109536. https://doi.org/10.1016/j.palaeo.2019.109536

Ribeiro, D.T., Moraes, I., Kwitko-Ribeiro, R., Braga, D., Spier, C., & Santos, P. (2021). From Fresh Itabirites and Carbonates to Weathered Iron Ore: Mineral Composition, Density and Porosity of Different Fresh and Altered Rocks from the Quadrilátero Ferrífero, Brazil. *Minerals*, **11**: 29-59. https://doi.org/10.3390/min11010029

Ribeiro, D.T., Pires, F.R., & Carvalho, R.M. (2002). Supergene iron ore and disorder. *Proceedings of Iron Ore 2002 Conference*, pp. 81-90. Perth: Australasian Institute of Mining and Metallurgy.

Rosière, C.A., & Chemale Jr, F. (2000). Brazilian iron formations and their geological setting. *Revista Brasileira de Geociências*, **30**(2): 274-278.

Rosière, C.A., Spier, C.A., Rios, F.J., & Suckau, V.E. (2008). The itabirites of the Quadrilátero Ferrífero and related high-grade iron ore deposits: an overview. *Reviews in Economic Geology*, **15**: 223-254. https://doi.org/10.5382/Rev.15.09

Rossignol, C., Lana, C., & Alkmim, F. (2020). Geodynamic evolution of the Minas Basin, southern São Francisco Craton (Brazil), during the early Paleoproterozoic: Climate or tectonic? *Journal of South American Earth Sciences*, **101**: 102628. https://doi.org/10.1016/j.jsames.2020.102628

Sampaio, G.M.S., Pufahl, P.K., Raye, U., Kyser, K.T., Abreu, A.T., Alkmim, A.R., & Nalini Jr, H.A. (2018). Influence of weathering and hydrothermal alteration on the REE and δ^{56}Fe composition of iron formation, Cauê Formation, Iron Quadrangle, Brazil. *Chemical Geology*, **497:** 27-40. https://doi.org/10.1016/j.chemgeo.2018.08.014

Scanning Electron Microscope Laboratory (2024). Available at: https://www.eas.ualberta.ca/sem/. Accessed on December 19, 2024.

Schad, M., Halama, M., Bishop, B., Konhauser, K. O., & Kappler, A. (2019). Temperature fluctuations in the Archean ocean as trigger for varve-like deposition of iron and silica minerals in banded iron formations. *Geochimica et Cosmochimica Acta*, *265*, 386-412. https://doi.org/10.1016/j.gca.2019.08.031

Schier, K., Ernst, D. M., de Sousa, I. M. C., Garbe-Schoenberg, D., Kuhn, T., Hein, J. R., & Bau, M. (2021). Gallium-aluminum systematics of marine hydrogenetic ferromanganese crusts: Inter-oceanic differences and fractionation during scavenging. Geochimica et Cosmochimica Acta, 310, 187-204. https://doi.org/10.1016/j.gca.2021.05.019

Scott, C., Lyons, T.W., Bekker, A., Shen, Y., Poulton, S.W., Chu, X., & Anbar, A.D. (2008). Tracing the stepwise oxygenation of the Proterozoic ocean. *Nature*, **452**: 456-459. https://doi.org/10.1038/nature06811

Scott, C., Planavsky, N.J., Dupont, C.L., Kendall, B., Gill, B.C., Robbins, L.J., ... & Lyons, T.W. (2013). Bioavailability of zinc in marine systems through time. *Nature Geoscience*, **6**(2): 125-128. https://doi.org/10.1038/ngeo1679

Seixas, L.A.R., Bardintzeff, J.M., Stevenson, R., & Bonin, B. (2013). Petrology of the high-Mg tonalites and dioritic enclaves of the ca. 2130 Ma Alto Maranhão suite: Evidence for a major juvenile crustal addition event during the Rhyacian orogenesis, Mineiro Belt, southeast Brazil. *Precambrian Research*, **238**: 18-41. https://doi.org/10.1016/j.precamres.2013.09.015

Sial, A.N., Ferreira, V.P., de Almeida, A.R., Romano, A.W., Parente, C.V., da Costa, M.L., & Santos, V.H. (2000). Carbon isotope fluctuations in Precambrian carbonate sequences of several localities in Brazil. *Anais da Academia Brasileira de Ciências*, **72**(4): 539-558. https://doi.org/10.1590/S0001-37652000000400006

Sial, A.N., Gaucher, C., Misi, A., Boggiani, P.C., Alvarenga, C.J.S.D., Ferreira, V.P., ... & Cezario, W. D. S. (2016). Correlations of some Neoproterozoic carbonate-dominated successions in South America based on high-resolution chemostratigraphy. *Brazilian Journal of Geology*, *46*, 439-488. https://doi.org/10.1590/2317-4889201620160079

Siever, R. (1992). The silica cycle in the Precambrian. *Geochimica et Cosmochimica Acta* 56(8): 3265–3272. https://doi.org/10.1016/0016-7037(92)90303-Z

Sigman, D. M., Karsh, K. L., & Casciotti, K. L. (2009). Nitrogen isotopes in the ocean. In J. H. Steele, S. A. Thorpe, & K. K. Turekian (Eds.), *Encyclopedia of ocean sciences* (pp. 40–54). Academic Press. https://doi.org/10.1016/B978-012374473-9.00632-9

Silverman MP, Lundgren DG (1959) Studies on the chemoautotrophic iron bacterium *Ferrobacillus ferrooxidans*. II. Manometric studies. *Journal of Bacteriology* **78**: 326-331

Simmons, G.C., & Maxwell, C.H. (1961). Grupo Tamanduá da Série Rio das Velhas. *DNPM*, **211**: 1-31.

Simonson, B.M., Goode, A.D.T., (1989). First discovery of ferruginous chert arenites in the early Precambrian Hamersley Group of Western Australia. *Geology* **17**, 269–272. https://doi.org/10.1130/0091-7613(1989)017%3C0269:FDOFCA%3E2.3.CO;2

Sirocko, F. (1995). Abrupt change in monsoonal climate: evidence from the geochemical composition of Arabian Sea sediments. *Ph.D. dissertation, University of Kiel*.

Slotznick, S.P., Eiler, J.M., & Fischer, W.W. (2018). The effects of metamorphism on iron mineralogy and the iron speciation redox proxy. *Geochimica et Cosmochimica Acta*, **224**: 96-115. https://doi.org/10.1016/j.gca.2017.12.003

Song, Y., Gilleaudeau, G.J., Algeo, T.J., Over, D.J., Lyons, T.W., Anbar, A.D., & Xie, S. (2021). Biomarker evidence of algal-microbial community changes linked to redox and salinity variation, Upper Devonian Chattanooga Shale (Tennessee, USA). *GSA Bulletin*, **133**(1-2): 409-424. https://doi.org/10.1130/B35543.1

Souza, P.C., & Müller, G. (1984). Primeiras estruturas algais comprovadas na Formação Gandarela, Quadrilátero Ferrífero, 13-21.

Sperling, E.A., Melchin, M.J., Fraser, T., Stockey, R.G., Farrell, U.C., Bhajan, L., ... & Strauss, J.V. (2021). A long-term record of early to mid-Paleozoic marine redox change. *Science Advances*, **7**(28): eabf4382. https://doi.org/10.1126/sciadv.abf4382

Spier, C.A., Oliveira, S.M., Sial, A.N., & Rios, F.J. (2007). Geochemistry and genesis of the banded iron formations of the Cauê Formation, Quadrilátero Ferrífero, Minas

Gerais, Brazil. *Precambrian Research*, **152**: 170-206. https://doi.org/10.1016/j.precamres.2006.10.003

Środoń, J. (2010). Evolution of boron and nitrogen content during illitization of bentonites. *Clays and Clay Minerals*, **58**: 743-756. https://doi.org/10.1346/CCMN.2010.0580602

Stookey, L.L. (1970). Ferrozine - A new spectrophotometric reagent for iron. *Analytical Chemistry*, **42**(7): 779-781.

Strugale, M., & Cartwright, J. (2022). Tectono-stratigraphic evolution of the rift and post-rift systems in the Northern Campos Basin, offshore Brazil. *Basin Research*, **34**(5): 1655-1687. https://doi.org/10.1111/bre.12674

Stüeken, E. E., Kipp, M. A., Koehler, M. C., & Buick, R. (2016). The evolution of Earth's biogeochemical nitrogen cycle. *Earth-Science Reviews*, *160*, 220-239. https://doi.org/10.1016/j.earscirev.2016.07.007

Swanner, E.D., A.M. Mloszewska, O.A. Cirpa, R. Schoenberg, K.O. Konhauser, and A. Kappler. 2015a. Modulation of oxygen production in Archean oceans by episodes of Fe(II) toxicity. *Nature Geoscience* **8**(2): 126–130. https://doi.org/10.1038/ngeo2327

Taylor, S.R., & McLennan, S.M. (1985). The Continental Crust: Its Composition and Evolution. *Blackwell, Oxford*, 312pp. https://doi.org/10.1017/S0016756800032167

Teixeira, N.L., Caxito, F.A., Rosière, C.A., Pecoits, E., Vieira, L., Frei, R., ... & Poitrasson, F. (2017). Trace elements and isotope geochemistry (C, O, Fe, Cr) of the Cauê iron formation, Quadrilátero Ferrífero, Brazil: Evidence for widespread microbial dissimilatory iron reduction at the Archean/Paleoproterozoic transition. *Precambrian Research*, **298**: 39-55. https://doi.org/10.1016/j.precamres.2017.05.009

Thermo Fisher, 2024. Avaliable at: https://www.thermofisher.com/br/en/home/materials-science/learning-center/applications/scanning-electron-microscope-sem-electron-column.html. Accessed on December 19, 2024.

Thomazo, C., Pinti, D. L., Busigny, V., Ader, M., Hashizume, K., & Philippot, P. (2009). Biological activity and the Earth's surface evolution: insights from carbon, sulfur, nitrogen and iron stable isotopes in the rock record. *Comptes Rendus Palevol*, *8*(7), 665-678. https://doi.org/10.1016/j.crpv.2009.02.003

Tong, X., Wang, C., Peng, Z., Li, Y., Hao, W., Mänd, K., ... & Konhauser, K. O. (2021). Depositional and environmental constraints on the late Neoarchean Dagushan deposit (Anshan-Benxi area, North China Craton): An Algoma-type banded iron formation. *Economic Geology*, ***116***(7), 1575-1597. https://doi.org/10.5382/econgeo.4841

Tostevin, R., & Mills, B.J. (2020). Reconciling proxy records and models of Earth's oxygenation during the Neoproterozoic and Palaeozoic. *Interface Focus*, **10**(4): 20190137. https://doi.org/10.1098/rsfs.2019.0137

Tostevin, R., Shields, G.A., Tarbuck, G.M., He, T., Clarkson, M.O., & Wood, R.A. (2016). Effective use of cerium anomalies as a redox proxy in carbonate-dominated marine settings. *Chemical Geology*, **438**: 146-162. https://doi.org/10.1016/j.chemgeo.2016.06.027

Trendall, A., Blockley, J., (1970). The iron formations of the Precambrian Hamersley Group, Western Australia with special reference to the associated crocidolite. In: *Western Australia Geological Survey Bulletin* **119**, pp. 1–366.

Tribovillard, N., Algeo, T.J., Lyons, T., & Riboulleau, A. (2006). Trace metals as paleoredox and paleoproductivity proxies: an update. *Chemical Geology*, **232**(1-2): 12-32. https://doi.org/10.1016/j.chemgeo.2006.02.012

Trzaskos, B., Alkmim, F.F., & Zavaglia, G. (2011). Arcabouço estrutural e microestruturas do minério de ferro da jazida Casa de Pedra, Quadrilátero Ferrífero, MG. *Brazilian Journal of Geology*, **41**(3): 486-497.

Tyler, G., & Yvon, J. (1995). ICP-OES, ICP-MS and AAS Techniques Compared. *ICP Optical Emission Spectroscopy Technical Note*, *5*, 1-11.

Urey, H. C. (1947). The thermodynamic properties of isotopic substances. *Journal of the Chemical Society (Resumed)*, 562-58ge

Vale S.A. (2024). Report 20-F. *U.S. Securities and Exchange Commission on April 18, 2024*. 240p. https://ri-vale.mz-sites.com/informacoes-para-o-mercado/relatorios-anuais/relatorio-20-f/ (accessed 5 February 2025).

Vargas, M., Kashefi, K., Blunt-Harris, E. L., & Lovley, D. R. (1998). Microbiological evidence for Fe (III) reduction on early Earth. *Nature*, *395*(6697), 65-67. https://doi.org/10.1038/25720

Veizer, J., Clayton, R., & Hinton, R. (1992). Geochemistry of Precambrian carbonates: IV. Early Paleoproterozoic (2.25±0.25 Ga) seawater. *Geochimica et Cosmochimica Acta*, **56**: 2487-2501. https://doi.org/10.1016/0016-7037(92)90204-V

Veizer, J., Hoefs, J., Lowe, D., & Thurston, P. (1989). Geochemistry of Precambrian carbonates: II. Archean greenstone belts and Archean sea water. *Geochimica et Cosmochimica Acta*, **53**: 859-871. https://doi.org/10.1016/0016-7037(89)90030-6

Walker, J. C. (1984). Suboxic diagenesis in banded iron formations. *Nature*, *309*(5966), 340-342. https://doi.org/10.1038/309340a0

Wang, H.Y., Liu, A., Li, C., Feng, Q., Tang, S., Cheng, M., & Algeo, T.J. (2021). A benthic oxygen oasis in the early Neoproterozoic ocean. *Precambrian Research*, **355**:106085. https://doi.org/10.1016/j.precamres.2020.106085

Warren, J. (2000). Dolomite: occurrence, evolution and economically important associations. *Earth-Science Reviews*, **52**(1-3): 1-81. https://doi.org/10.1016/S0012-8252(00)00022-2

Wei, W., & Algeo, T.J. (2020). Elemental proxies for paleosalinity analysis of ancient shales and mudrocks. *Geochimica et Cosmochimica Acta*, **287**: 341-366. https://doi.org/10.1016/j.gca.2019.06.034

Wei, W., Algeo, T.J., Lu, Y., Lu, Y., Liu, H., Zhang, S., ... & Chen, L. (2018). Identifying marine incursions into the Paleogene Bohai Bay Basin lake system in northeastern China. *International Journal of Coal Geology*, **200**: 1-17. https://doi.org/10.1016/j.coal.2018.10.001

Wei, W., Lu, Y., Ma, Y., Zhang, J., Song, H., Chen, L., ... & Zhang, S. (2021). Nitrogen isotopes as paleoenvironmental proxies in marginal-marine shales, Bohai Bay Basin, NE China. *Sedimentary Geology*, *421*, 105963. https://doi.org/10.1016/j.sedgeo.2021.105963

Wei, W., Yu, W., Du, Y., Algeo, T.J., Li, Z., Cheng, M., ... & Konhauser, K. (2024). A new salinity-based model for Cryogenian Mn-carbonate deposits. *Precambrian Research*, **403**: 107309. https://doi.org/10.1016/j.precamres.2024.107309

Winter, W.R., Jahnert, R.J., & França, A.B. (2007). Bacia de Campos. *Boletim de Geociências da Petrobrás*, **15**(2): 511-529.

Wood, R. A., Poulton, S. W., Prave, A. R., Hoffmann, K. H., Clarkson, M. O., Guilbaud, R., ... & Kasemann, S. A. (2015). Dynamic redox conditions control late Ediacaran metazoan ecosystems in the Nama Group, Namibia. *Precambrian Research*, *261*, 252-271. https://doi.org/10.1016/j.precamres.2015.02.004

Xu, J., Liu, Z., Bechtel, A., Meng, Q., Sun, P., Jia, J., ... & Song, Y. (2015). Basin evolution and oil shale deposition during Upper Cretaceous in the Songliao Basin (NE China): Implications from sequence stratigraphy and geochemistry. *International Journal of Coal Geology*, **149**: 9-23. https://doi.org/10.1016/j.coal.2015.07.005

Yu, W., Algeo, T.J., Zhou, Q., Wei, W., Yang, M., Li, F., Du, Y., Pan, W., & Wang, P. (2022). Evaluation of alkalinity sources to Cryogenian cap carbonates, and implications for cap carbonate formation models. *Global and Planetary Change*, 217:103949. https://doi.org/10.1016/j.gloplacha.2022.103949

Zhang, X., Lin, C., Zahid, M.A., Jia, X., & Zhang, T. (2017). Paleosalinity and water body type of Eocene Pinghu Formation, Xihu Depression, East China Sea Basin. *Journal of Petroleum Science and Engineering*, **158**: 469-478. https://doi.org/10.1016/j.petrol.2017.08.074

APENDIX - A: PHOTOMICROGRAPHS OF THE MAIN SAMPLES, INCLUDING HAND SAMPLE IMAGES, AND THIN SECTION VIEWS UNDER PLANE-POLARIZED AND CROSS-POLARIZED LIGHT.

STM-FD00155 – A23 - Dolomitic BIF

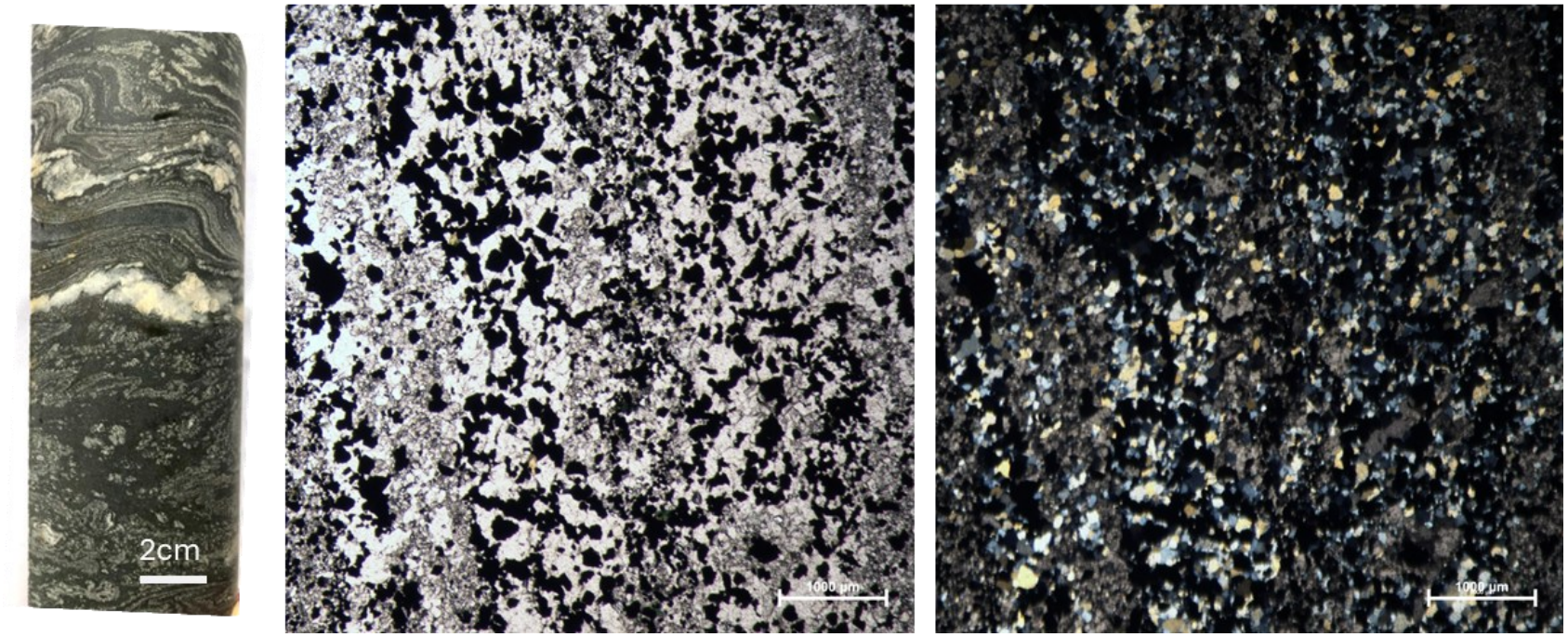

Fonte: Elaborado pelo autor

STM-FD00155 – A29 – Chlorite-dolomite-magnetite phyllite

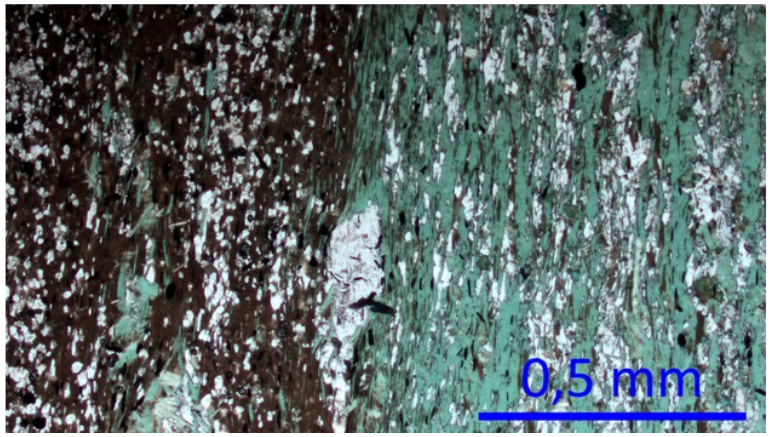

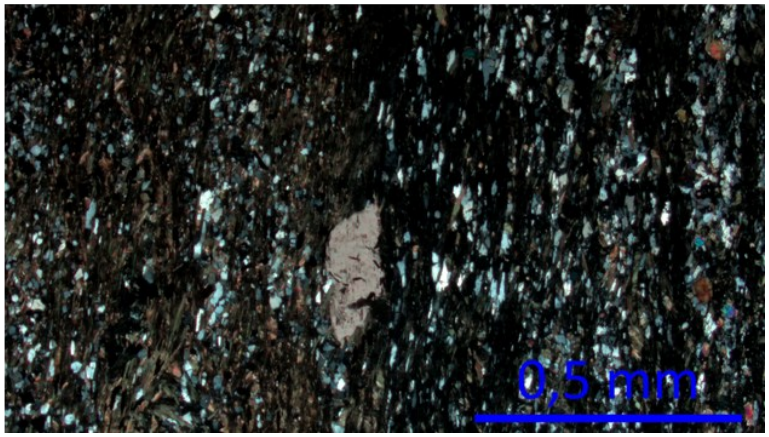

Fonte: Elaborado pelo autor

STM-FD00205 – A02 – Dolomitic BIF

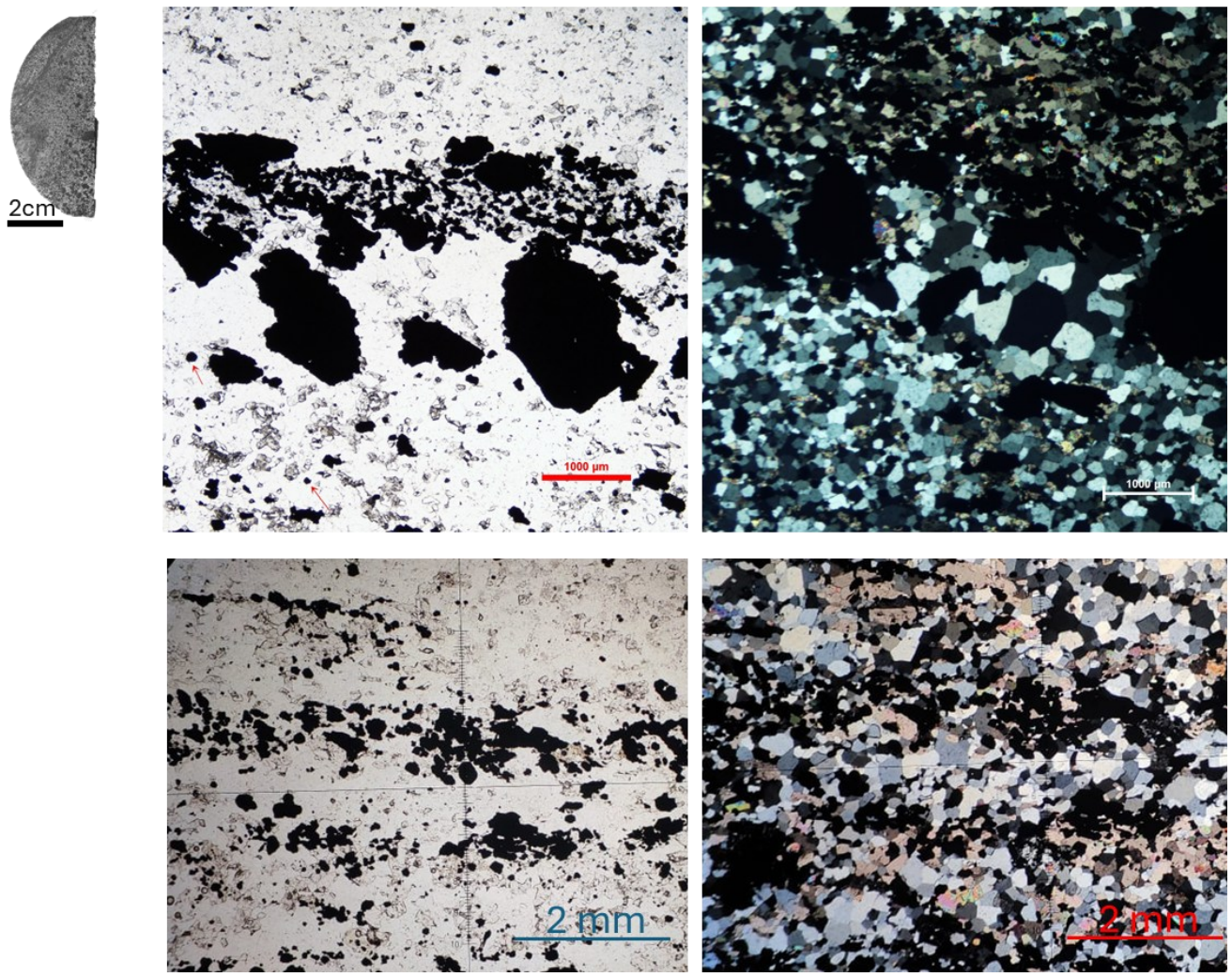

Fonte: Elaborado pelo autor

STM-FD00205 – A08 – Dolomitic BIF and Dolostone

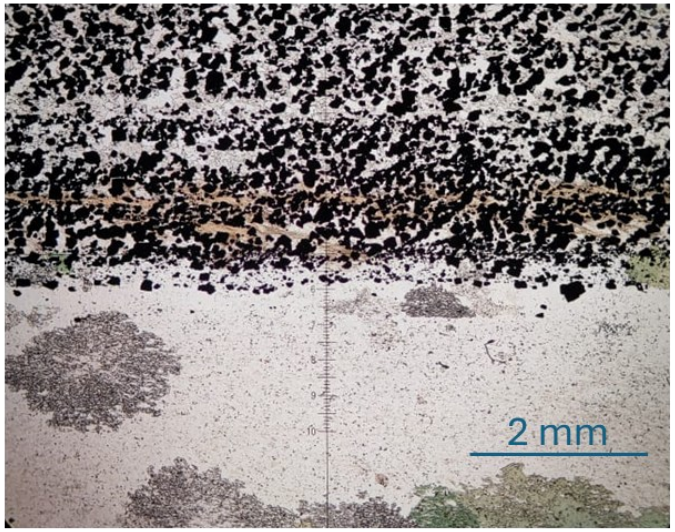

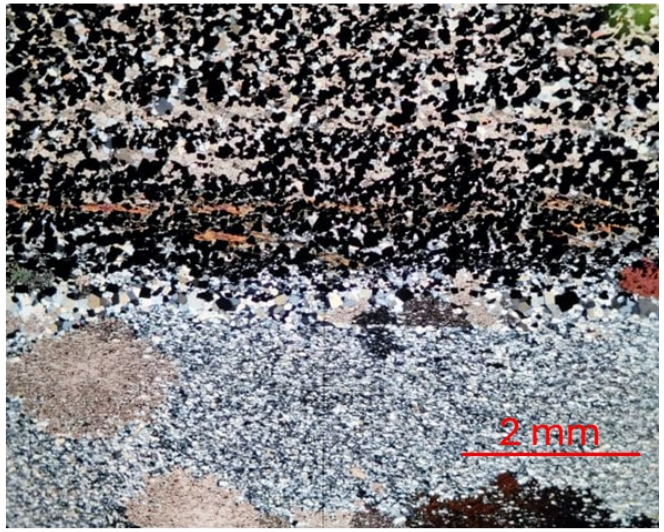

Fonte: Elaborado pelo autor

STM-FD00205 – A25 – Carbonaceous phyllite

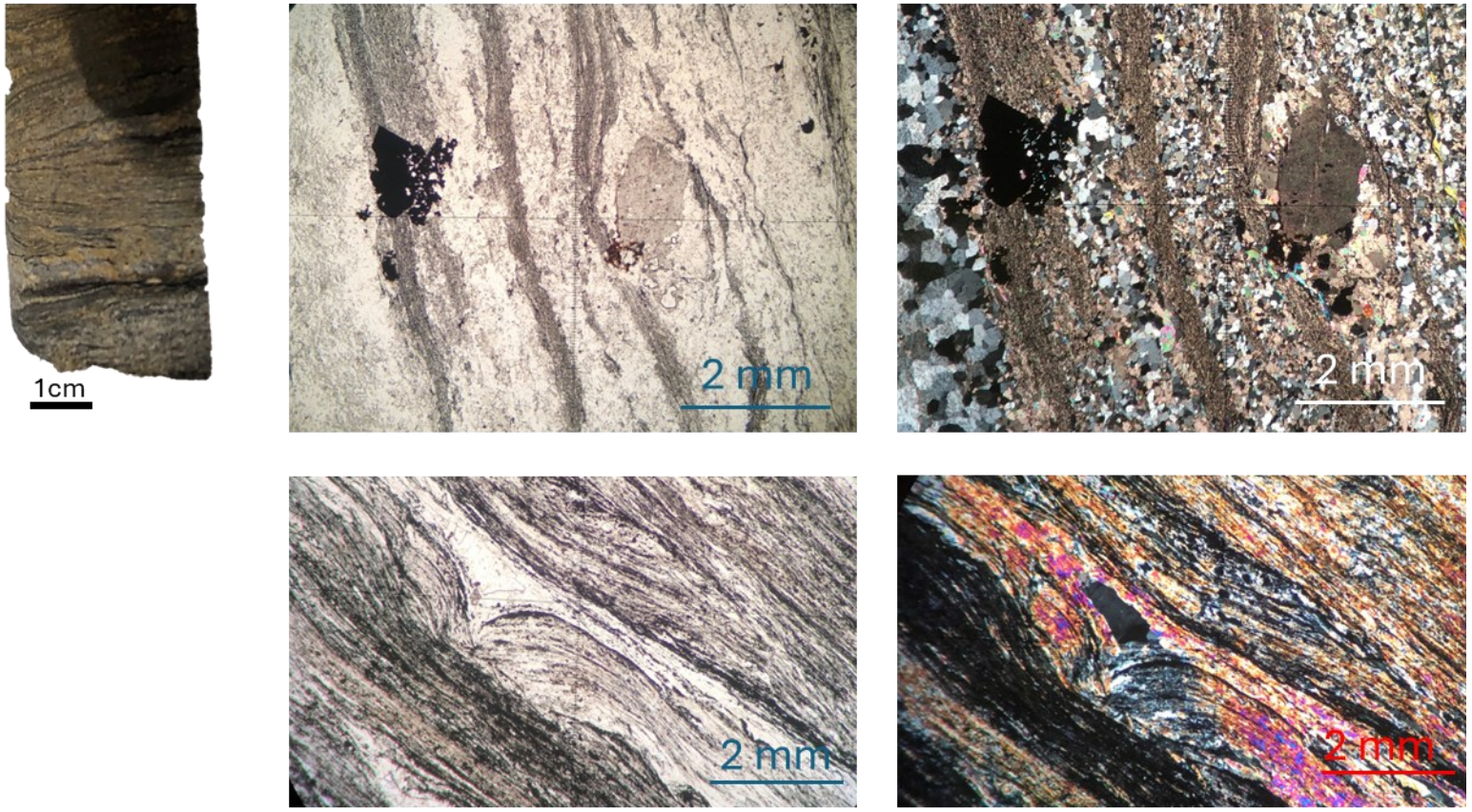

Fonte: Elaborado pelo autor

AC05-03– Ferruginous Dolostone

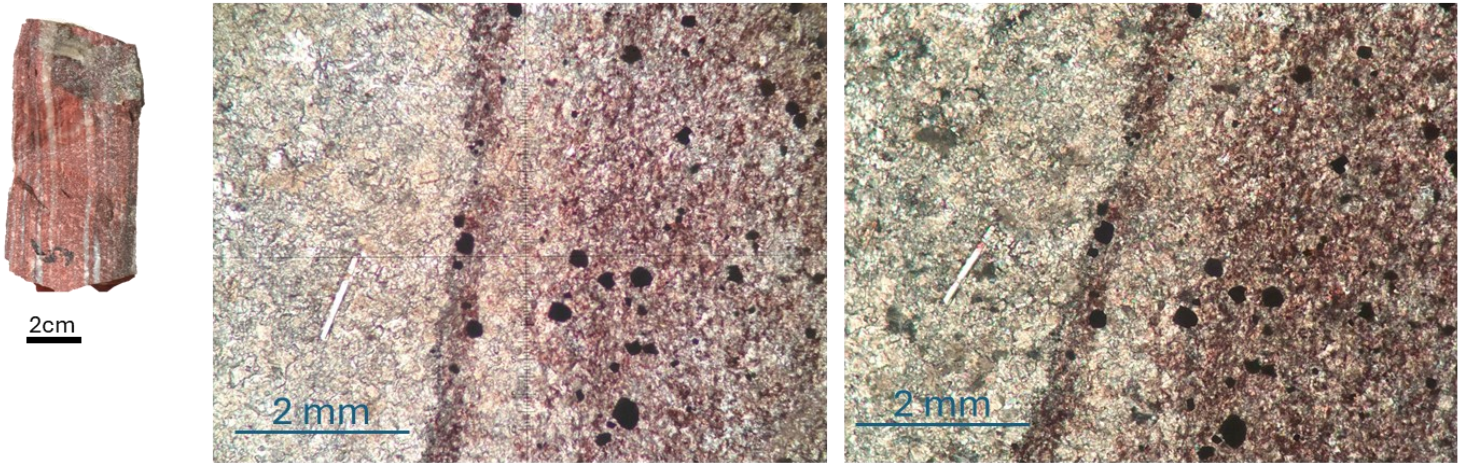

AC05-08 – Ferruginous Dolostone

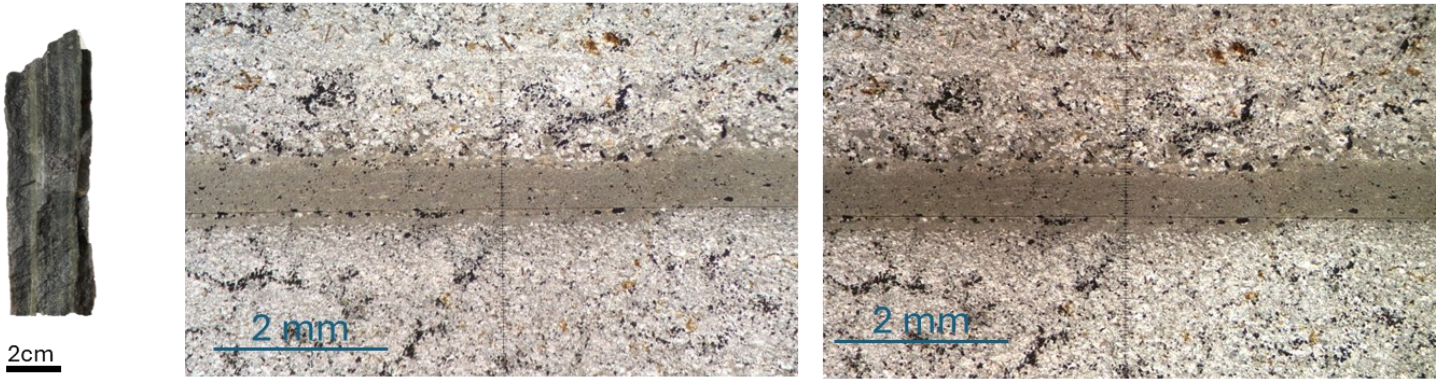

Fonte: Elaborado pelo autor